Dynamic acoustic emission for the characterization of the nonlinear behavior of complex materials

Xiaoyang Yu

UNIVERSITE BRETAGNE SCIENCES LOIRE POUR L'INGENIEUR

Le Mans Université

THESE DE DOCTORAT DE

LE MANS UNIVERSITE

COMUE UNIVERSITE BRETAGNE LOIRE

ECOLE DOCTORALE N° 602

Sciences pour l'Ingénieur

Spécialité : *Acoustique*

Par

Xiaoyang YU

Émission acoustique dynamique pour la caractérisation du comportement non linéaire des matériaux complexes

Dynamic acoustic emission for the characterization of the nonlinear behavior of complex materials

Thèse présentée et soutenue à Le Mans, le 18 Septembre 2020
Unité de recherche : LAUM
Thèse N° : 2020LEMA1019

Rapporteurs avant soutenance :

Olivier BOU MATAR	Professeur, IEMN – École Centrale de Lille
Jérôme FORTINEAU	Professeur, GREMAN - INSA Centre Val de Loire

Composition du Jury :

Président :	Alain LHEMERY	Directeur de recherche, CEA
Examinatrice :	Nathalie GODIN	Maître de Conférence, HDR, MATEIS - INSA de Lyon
Examinateur :	Rachid EL GUERJOUMA	Professeur, Le Mans Université
Dir. de thèse :	Mourad BENTAHAR	Maître de Conférence, HDR, LAUM - Le Mans Université
Co-dir. de thèse :	Silvio MONTRESOR	Maître de Conférence, LAUM - Le Mans Université
Co-dir. de thèse :	Charfeddine MECHRI	PAST, CTTM/LAUM - Le Mans Université

Acknowledgments

First of all, I would like to express my deep gratitude to my three thesis supervisors Dr. Mourad BENTAHAR, Dr. Silvio MONTRESOR and Dr. Charfeddine MECHRI for providing me the opportunity, direction, encouragement, and support to complete my PhD research. Without their help, this work would not have been achieved. It is my honor to work with them.

I want to thank Prof. Olivier BOU MATAR and Prof. Jérôme FORTINEAU for having agreed to be the reviewers of this thesis. I would also like to acknowledge Prof. Rachid EL GUERJOUMA, Dr. Nathalie GODIN and Dr. Alain LHEMERY for having agreed to be the members of my jury committee.

I want to thank Prof. Abderrahim El MAHI for his help provided during all the mechanical experiments. I would like to thank Dr. Marco SCALERANDI from Polytechnic University of Turin (Italy) for his useful suggestions about knowledge of elastic nonlinearity. I would also like to thank Angelo DI BELLA for performing some significant experiments together.

I would also like to thank Hervé MEZIERE, Eric EGON and all of the technical team for their technical support in manufacturing mold and concrete samples.

I would like to thank all the friendly collaborators: thanks to Dr. Aroune DUCLOS, Dr. Jean-Philippe GROBY, and Dr. Wenping BI for helping with various things around the laboratory and university.

I want to thank the director and co-director of LAUM, Dr. Pierrick LOTTON and Prof. Laurent SIMON, respectively. I want to thank them for their warm reception in the laboratory. I want to thank Prof. Manuel MELON, the director of doctoral school for his helping.

I want to thank all the friends from Harbin Engineering University and all the friends I made in Le Mans University who made these years filled with fun and joy. I thank all the people, post-doc, PhD, master students as well as all the staff in University during my thesis.

Thank again all my supervisors for all of their helps and guides during my PhD work.

Finally, to my family for providing encouragement and support during the duration of my PhD and whole my life as well as for their sacrifices.

Contents

General introduction

The characterization and assessment of damage is a key point for controlling the durability and reliability of structures and materials in service. A growing number of concrete structures have shown the appearance of different signs of deterioration. Indeed, the changes in the manufacturing and specifications of different constituents such as cement and the use of alternative materials and admixtures made many international standards inadequate. Consequently, particular attention was given to the development of test methods, which are related to durability performance and integrity. In that sense, the number of scientific and technical contributions to detect the presence of damage within these materials and estimating their remaining lifetime has not stopped growing.

In the past three decades, significant efforts have been made towards the development of structural health monitoring (SHM) systems for concrete structures (bridges, power plants, etc.). Among the proposed techniques, acoustic emission (AE) has been widely used. Indeed, compared with other nondestructive techniques, the advantage of AE is that the creation and propagation of damage can be determined in real-time through the detected AE events. The latter represent the transient elastic waves emitted by the defects during their creation and/or propagation. In addition, based on the detected AE signals, damage mechanisms within the materials of interest can be characterized using either a quantitative or a phenomenological approach. The quantitative approach requires the understanding of the physics related to the AE sources, the propagation of the involved elastic waves (the knowledge of the Green function), the calibration of the sensors and the acquisition system, etc. However, it remains possible to use a phenomenological approach, whose purpose is to establish links between damage mechanisms and the time and/or frequency parameters of the detected AE signals.

In general, complex materials such as concrete (it could also be rocks, composites, or micro-cracked materials) have a particular mechanical behavior at the micro-scale level and are denoted as Nonlinear Mesoscopic Elastic Materials (NMEM). They exhibit a non-classical nonlinear behavior, which is characterized by the presence of hysteresis and memory effects in their stress-strain equation. In the last decades, numerous studies have been developed to characterize the evolution of the microstructural changes (micro-cracks, contacts, etc.) within NMEM with the help of dynamic excitation. According to these studies, which are still relevant, hysteretic elastic nonlinearity is composed of two interlinked effects: the fast dynamics (FD) and the slow dynamics (SD). FD refers to instantaneous changes experimentally observed through harmonics generation, resonance frequency shift or dumping increase. The SD refers to the long-time dependence recovery of the elastic modulus and/or damping to its initial value (relaxation) after being softened by a large amplitude dynamic strain. The materials that exhibit FD and SD are characterized by soft regions within a small volume surrounded by hard regions. Despite the

experiments and modeling developed in this field, the comprehension and experimental evidence of the physics, which lies behind the macroscopic observations are still needed.

There is abundant literature showing the good performances of AE as a tool to monitor the creation and propagation of the micro-cracking created within structural materials during quasi-static or dynamic mechanical tests. By performing adequate signal processing techniques on the detected AE signals, reliable correlations between the different damage mechanisms (e.g. matrix cracking, interface debonding, etc.) and AE events were established. In general, AE data are collected during the creation of the micro-cracks. Beyond the fact that AE cannot be considered as completely nondestructive (from the point of view of the damage creation), AE is never used when it comes to control or to characterize the existing defects (or micro-cracks) within complex materials. In previous work, an interesting correlation between the energy of AE hits, recorded during the progressive damaging of composites, and the evolution of the relaxation time recorded during slow dynamic experiments, has been experimentally proved [Bentahar and El Guerjouma, 2009]. The latter reference showed that AE has great potential to link micromechanisms to macroscopic observations made during nonlinear acoustic experiments.

In order to advance knowledge around the micro-mechanisms involved in the nonlinear behavior of complex materials, this thesis proposes to follow the evolution of the nonlinear relaxation of micro-cracked concrete samples according to an original protocol. The latter is based on the listening of the acoustic activity during passive relaxation by means of calibrated piezoelectric sensors. The thesis is divided into four chapters.

In Chapter 1, as a short review, we introduce the fundamental background of the necessary knowledge for this thesis. This chapter starts by presenting the historical and theoretical basis of the elastic waves and the acoustic emission (AE) technique. In consideration of some general ideas of the relation between AE technique and damage mechanisms identification, our research is focused on the AE source theory, elastic wave propagation, AE source characterization, and AE acquisition system. In the second part of this chapter, from the classical nonlinear theory to non-classical nonlinear theory, theoretical knowledge and experimental observations are presented. Finally, based on existing experimental results of fast dynamics (FD) and the slow dynamics (SD) performed on different materials, the dynamic behavior of nonlinear mesoscopic elastic materials is presented, which leads to the motivation of this research study. To establish the link between nonlinear mesoscopic elasticity and damage mechanisms in the complex materials (polymer concrete and civil engineering concrete), we propose an original approach by using AE to probe the acoustic activity during the quasi-static mechanical tests and the passive relaxation of the same samples.

In Chapter 2, our research is mainly focused on the phenomenological signal-based AE analysis. Each detected AE signal has properties related to the characteristics of the created source. The aim of our work is to propose a relevant method, which can associate AE signals with damage mechanisms. Based on the literature research on the AE feature extraction and signal classification, we proposed an unsupervised pattern recognition process, which is an automated technique to select promising feature combinations for unsupervised clustering of detected AE signals. In addition, by using the time-frequency characteristics of AE signals and the deep learning ability of computer science, we propose a novel 'image-based AE classification' approach to classify AE signals.

Chapter 3 is devoted to the presentation of quasi-static three-point bending tests

performed on different concrete samples. In addition, during the tests, the evolution of damages is monitored. The aim of this study is to analyze the fracture process of samples during the quasi-static mechanical tests and identify the damage mechanism by using the detected AE data. For civil engineering concrete samples, the results of crack mode classification obtained from the unsupervised pattern recognition approach are compared to the ones of the parametric approach (average frequency and RA value of AE signal). For polymer concrete (PC) samples, damage mechanisms are clustered using the proposed unsupervised pattern recognition, which applied on the manufactured specific samples. Then AE data in the PC specimen is also analyzed by using the proposed 'image-based AE classification' approach based on continuous wavelet transform (CWT) and convolutional neural network (CNN). Results show that according to the time-frequency characteristics of AE data and transfer learning technique, retrained AlexNet algorithm has high classification accuracy.

Chapter 4 is dedicated to the characterizing of the hysteretic nonlinear dynamic behavior of polymer concrete (PC) and civil engineering concrete samples around their third flexural resonance modes. Firstly, the experimental device is calibrated to ensure of its linear behavior at the frequencies and amplitudes of excitation applied. By using the calibrated experimental setup, the evolution of dynamic behavior of the samples taken at intact and damaged states are followed during fast and slow nonlinear dynamic experiments. In addition, we proposed a novel passive relaxation monitoring protocol, which uses AE sensors to probe the nonlinear behavior of the materials during the relaxation phase. Compare this passive method with the one using a common low amplitude probe signal (active method) during the relaxation phase, the results show a very good correlation between the two approaches. Furthermore, the signal processing of AE signals recorded during passive relaxation shows that these signals are obviously similar to those obtained from quasi-static mechanical tests performed on the same concrete sample. This approach will certainly help to better identify the damage mechanisms that contribute the most to the evolution of the nonlinear hysteretic behavior of damaged concretes during the relaxation.

Chapter 1

State of the art

This chapter introduces the basic background of the acoustic emission (AE) technique and the nonlinear mesoscopic elastic materials (NMEM). As a short review, the study is focused on the theoretical concepts and experimental research of AE and nonlinear dynamic behavior in complex materials (civil engineering concrete and polymer concrete).

1.1 Theory background of elastic waves

1.1.1 Elastic waves theory

Wave motion is a phenomenon during which the particle motion is dynamically transferred to neighboring particles. It complies that each particle vibrates around its equilibrium position and does not move. The originating wave is defined on the basis of orientations of particle motions and directions of propagations and propagates with its characteristic velocity. In homogenous isotropic solids, the excitation of the medium by a source causes the propagation of two types of transient mechanical bulk waves which propagate in concentric spheres centered on the source:

1 - Longitudinal wave (P-wave): In the case of longitudinal waves, particles vibrate along the direction in which the wave propagates. The longitudinal wave can propagate through all medium types (solids, liquids, and gases) and is the fastest of elastic waves.

2 - Transverse wave (S-wave): In the case of transverse waves, particles vibrate perpendicular to the direction in which the wave propagates. The transverse wave is also called a shear wave and propagates through solids but not through liquids and gases.

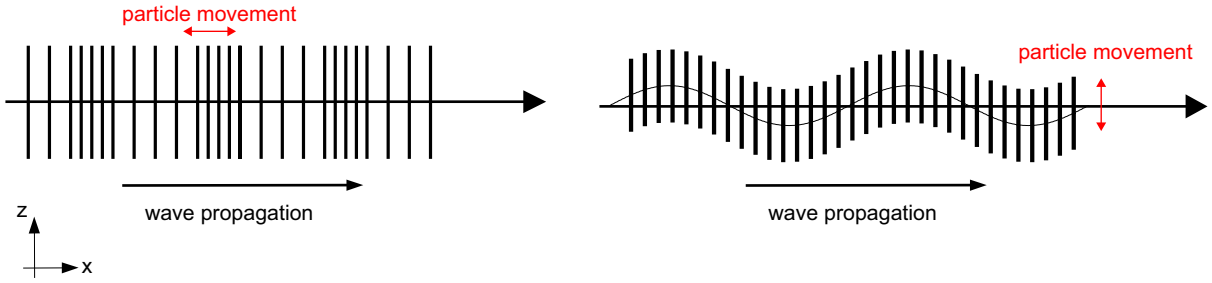

Figure 1.1: Schematic illustration of longitudinal and transverse elastic waves propagating.

The propagation of an elastic wave can thus be described by the independent longitudinal wave and transverse wave propagation as shown in Figure 1.1. The theory of elastic waves describes the propagation of deformations within the solid for small initial deformation. For a homogeneous isotropic medium, the fundamental equation governing the propagation of elastic waves is written as [Royer and Dieulesaint, 1999]:

$$\rho \frac{\partial^2 \mathbf{u}}{\partial t^2} = (\lambda + \mu)\nabla(\nabla \cdot \mathbf{u}) + \mu \nabla^2 \mathbf{u}, \tag{1.1}$$

where $\mathbf{u}$ is the displacement vector, ρ is the material density, λ and μ are the Lamé constants. In general, we consider a time harmonic solution of Equation (1.1) in the form:

$$\mathbf{u} = \mathbf{A} e^{i\omega(S-t)}, \tag{1.2}$$

where S and $\mathbf{A}$ are functions of $\mathbf{x}$ which are to be determined and ω is the constant angular frequency of the solutions. For simplicity, we assume that S is independent of ω and $\mathbf{A}$ has an expansion of the form:

$$\mathbf{A} = \sum_{n=0}^{\infty} (i\omega)^{-n} \mathbf{A}_n. \tag{1.3}$$

The vectors $\mathbf{A}_n$ are functions of $\mathbf{x}$ which needs to be determined. For the case $n = 0$, Equation (1.1) can be represented by the following two equations [Karal Jr and Keller, 1959]:

$$\left[-\rho + (\lambda + 2\mu)(\nabla S)^2\right] \mathbf{A}_0 \cdot \nabla S = 0 \tag{1.4}$$

and

$$\left[-\rho + \mu(\nabla S)^2\right] \mathbf{A}_0 \times \nabla S = 0. \tag{1.5}$$

In the case where neither $\mathbf{A}_0$ nor ∇S is zero, Equations (1.4) and (1.5) show that one of the products $\mathbf{A}_0 \cdot \nabla S$ and $\mathbf{A}_0 \times \nabla S$ is zero. At the same time, on the bracketed expression within the above mentioned equations can also vanish. This will lead to the following equations:

$$\mathbf{A}_0 \cdot \nabla S = 0, \tag{1.6}$$

$$(\nabla S)^2 = \rho/(\lambda + 2\mu), \tag{1.7}$$

$$\mathbf{A}_0 \times \nabla S = 0, \tag{1.8}$$

$$(\nabla S)^2 = \rho/\mu. \tag{1.9}$$

Based on considerations relating to geometric optics, Equations (1.7) and (1.9) determine the phase functions S and the corresponding laws i.e., the original trajectories of $S =$ constant. It comes out that the rays are straight lines in the case of a homogeneous medium. It follows from Equation (1.6) that $\mathbf{A}_0$ is parallel to ∇S which corresponds to the propagation of a longitudinal wave with the velocity c_L:

$$c_L = \sqrt{\frac{\lambda + 2\mu}{\rho}}. \tag{1.10}$$

In this case, S is a linear function of arc length s along a ray and is given by:

$$S = S_0 + \left[\rho(\lambda + 2\mu)^{-1}\right]^{\frac{1}{2}} (s - s_0), \tag{1.11}$$

where S_0 is the value of S at the point s_0 on the ray. Similarity, from Equation (1.8), $\mathbf{A}_0$ is perpendicular to ∇S, which corresponds to the propagation of transverse wave with the velocity c_T:

$$c_T = \sqrt{\frac{\mu}{\rho}}. \tag{1.12}$$

In this case, S is also a linear function of s along a ray and is given by:

$$S = S_0 + \left(\rho\mu^{-1}\right)^{\frac{1}{2}} (s - s_0). \tag{1.13}$$

Finally, we note that the elastic properties of homogeneous isotropic solids can also be expressed as a function of Young's modulus E and Poisson's ratio ν, where:

$$E = \frac{\mu(3\lambda + 2\mu)}{\lambda + \mu} \tag{1.14}$$

and

$$\nu = \frac{\lambda}{2(\lambda + \mu)}. \tag{1.15}$$

1.1.2 Propagation in a semi-infinite space

Longitudinal and transverse waves are always generated within elastic solids. Following their arrival at the surface of a semi-infinite medium, a surface wave called 'Rayleigh wave' is generated. In that case (see Figure 1.2), particles near the surface move elliptically, and their motion decreases exponentially with depth.

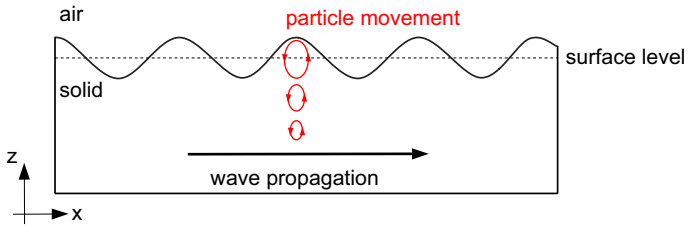

Figure 1.2: Schematic illustration of a Rayleigh wave propagating at the solid-air interface.

Rayleigh wave propagates at a lower rate than bulk waves. Its velocity c_R is often given by an approximation formula such as the one given below [Bergman and Shahbender, 1958]:

$$c_R \approx \frac{0.874 + 1.12\nu}{1+\nu} c_T \tag{1.16}$$

where ν is Poisson's radio. Finally, note that in general, Rayleigh wave velocity is roughly 0.9 times shear wave velocity.

1.1.3 Propagation in a plate

Wave propagation in a plate or 1-D waveguide is different from that in solid materials. In fact, when the plate is thin enough (thickness of the order of involved wavelength). The coupling between longitudinal and transverse waves reflected at the top and bottom of the plate produces additional waves. In such a case, Lamb waves are generated, as

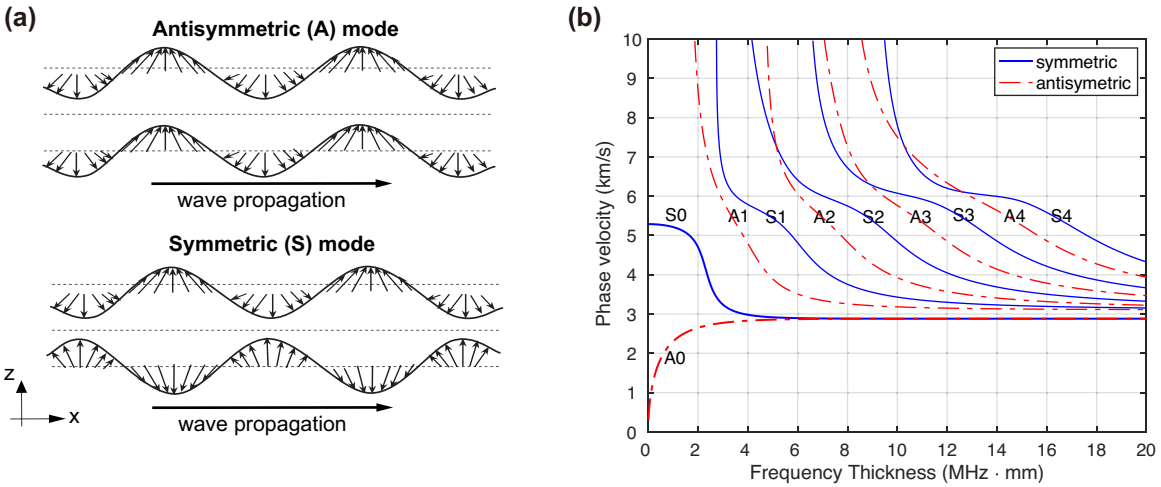

Figure 1.3: (a) Schematic illustration of antisymmetric (A) and symmetric (S) Lamb modes propagating in a plate. (b) Dispersion curves of Lamb modes for an aluminum plate ($C_L = 5940\,\mathrm{m/s}$ and $C_T = 3100\,\mathrm{m/s}$).

the plate vibrates. Lamb waves are therefore guided by the faces of the plate and this leads to two main properties: (a) they are geometrically dispersive, their velocities depend on the wavelength/thickness ratio and (b) they propagate in the form of symmetric (S) and antisymmetric (A) modes. Symmetric modes are modes in which the plate thickness changes symmetrically and antisymmetric modes are modes that interact with the plate anti-symmetrically with respect to the medium plane (the thickness remains constant), as shown in Figure 1.3(a). Lamb waves are described by dispersion curves, which represent the variation of velocity as a function of the product (Frequency×Thickness). Figure 1.3(b) shows an example of phase velocity dispersion curves for an aluminum plate.

1.2 Acoustic emission (AE)

1.2.1 Introduction

Acoustic emission (AE) is the phenomenon of energy release, in the form of transient elastic waves, resulting from micro-local displacements within a material subjected to static or dynamic stress (standard AFNOR NFA 09350). Part of the energy is released as an elastic wave that propagates in all directions to the boundaries of the material. By analyzing the vibration of the elastic waves detected at the surface of the material, it becomes possible to collect information on the event at the origin of these vibrations.

The typical example of AE is the 'tin cry', known since the Middle Ages by blacksmiths. This manifestation of AE in the field of audibility was attributed to the twinning phenomenon (its source mechanism) in 1916 by Czochralski [Czochralski, 1916]. However, AE technology began to be investigated in the middle of the 20th century. Joseph Kaiser [Kaiser, 1950] tested tensile specimens of metallic materials and recorded the AE signals. He discovered a famous phenomenon, which is now called the 'Kaiser effect'. A few years later, Schofield [Schofield, 1963] reexamined Kaiser's works and published pioneering work entitled 'Acoustic Emission', which was the first use of the terminology of AE in history. At present, AE technology applies to different fields: structural health monitoring (SHM), quality control of materials, characterization of damage, etc [Giurgiutiu, 2007, Grosse and Ohtsu, 2008].

1.2.2 Acoustic emission and damage mechanisms

Acoustic emission (AE) can be separated in terms of discrete and continuous emissions. The discrete emission is in the form of damped or sine waves (resonant AE sensors) or very short pulses (broadband AE sensors). It is often associated with damage phenomena such as crack initiation and propagation, stress corrosion, and fiber ruptures. The continuous emission happens when signals are frequent and overlap in a way that they cannot be separated in bursts. They are mainly observed in metallic materials and are associated with dislocations movement due to the plastic deformation [Godin et al., 2018a]. Damage mechanisms as the origin of AE have different properties. They can be divided into two types: chemical sources (e.g., corrosion) and mechanical sources. This thesis mainly studies the mechanical sources of AE created during mechanical tests and/or excited using low-frequency vibrations.

Figure 1.4(a) presents a schematic experimental setup of a tensile test monitored by AE on a glass fiber reinforced polyester composite in laboratory conditions. The created cracks during the tensile test release elastic waves that propagate following one of the presented wave modes. AE sensors capture these elastic waves at the material's surface and transform the energy of the transient elastic wave to an electric waveform, which passes in general through the pre-amplifier. The AE signals are then digitized and recorded by the AE system shown in Figure 1.4(b).

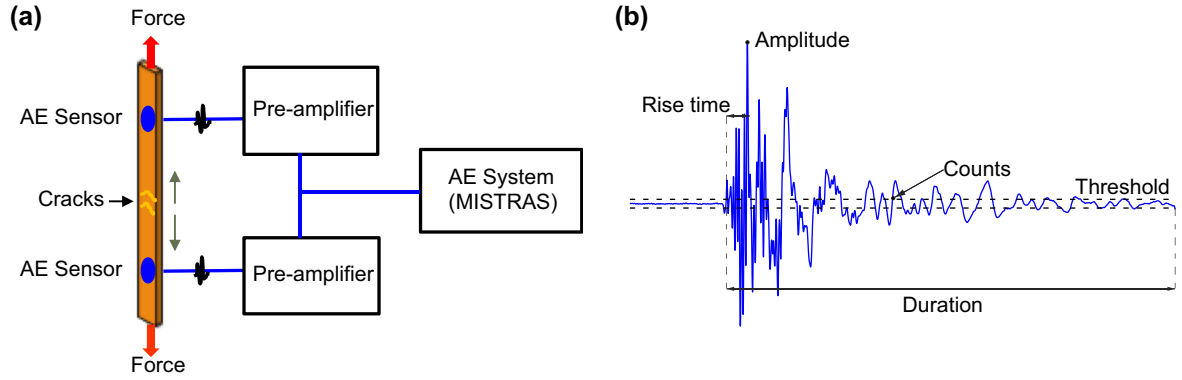

Figure 1.4: (a) Schematic experimental setup of a tensile test with AE monitoring on a glass fibre reinforced polyester composite. (b) A recorded AE signal and some of its associated features.

The AE process is therefore affected by different parameters:

– the physical and geometrical characteristics of the source, represented by $E(t)$;

– the propagation medium, represented by $G(t)$;

– the sensor used for measurement, with its function $R(t)$;

– the acquisition system (pre-amplifier, cable, signal processor system, etc.), with its function $H(t)$.

Finally, the detected AE signal $V(t)$ is a complex signal generated by the following convolution product [Scott, 1991, Godin et al., 2018b]:

$$V(t) = E(t) * G(t) * R(t) * H(t). \tag{1.17}$$

In acoustic emission analysis, the source signal $E(t)$ corresponding to the damage mechanism is always the most interesting. The phenomenological AE approach requires to establish the empirical correlations between the damage mechanism and the measured AE signal. A comprehensive quantitative AE study requires understanding the physical theory of AE source, AE wave propagation, calibration of the sensors, and the acquisition system. These contents will be introduced and discussed in the following sections.

1.3 Sources of acoustic emission

The origin of AE events has been studied by modeling the damage mechanism. Since few decades, many researchers have applied analytical or numerical methods to the simulations of AE source formation. When source characteristics are specified, the AE waveform

can be calculated by convolving the source function with an appropriate Green's function. This method is called a forward problem or simulation analysis. When source characteristics are obtained from measured waveforms and Green's functions, this is referred to as an inverse problem or deconvolution analysis [Breckenridge et al., 1975]. In the practical application of acoustic emission, due to a large number of combinations of feasible source characteristics and possible propagation paths, the inverse problem cannot be easily adopted. In order to completely determine the source characteristics and location, a large number of AE sensors might be needed. Therefore, studies were focused on the source and propagation modeling and validation. The moment tensor analysis (MTA) is the most early used AE analytical method of source modeling representation [Scruby et al., 1983, Ohtsu and Ono, 1986, Ohtsu, 1988]. M.Ohtsu [Ohtsu, 1991] developed an improved MTA technique named Simplified Green's Function (SiGMA) by considering the first motions of AE amplitudes, which was later applied on concrete materials [Shigeishi and Ohtsu, 2001]. In recent years, various studies, such as the AE sources and wave propagations in plates were based on the Finite Element Method (FEM), which is one of the most commonly used numerical methods [Sause and Horn, 2010, Sause and Richler, 2015, Le Gall et al., 2018].

1.3.1 Theory of acoustic emission and moment tensor analysis

Based on a generalized theory of acoustic emission, the displacement field $u_i(\mathbf{x}, t)$ at location $\mathbf{x}$ due to a dislocation in terms of the Burgers vector $b_k(\mathbf{y}, t)$ on a crack surface F is represented by the following equation [Ohtsu and Ono, 1986]:

$$u_i(\mathbf{x}, t) = \int_F T_{ik}(\mathbf{x}, \mathbf{y}, t) * b_k(\mathbf{y}, t) \mathrm{d}S, \tag{1.18}$$

where $*$ indicates a convolution, T_{ik} is the traction associated with Green's function which is called Green's function of the second kind. In the case of small-scale dislocations, time and spatial dependencies of the crack vector $b_k(\mathbf{y}, t)$ can be separated as:

$$\int_F b_k(\mathbf{y}, t) dS = b l_k S(t), \tag{1.19}$$

where b represents the magnitude of the crack displacement, vector l_k denote the direction of the crack movement, and $S(t)$ denotes the time dependence of the crack formation, which is called the source-time function. However, Equation (1.18) can also be represented as [Scruby et al., 1983]:

$$u_i(\mathbf{x}, t) = G_{ip,q}(\mathbf{x}, \mathbf{y}, t) m_{pq} * S(t), \tag{1.20}$$

where $*$ denotes the convolution operation, $G_{ip,q}(\mathbf{x}, \mathbf{y}, t)$ represents the spatial derivatives of Green's functions. m_{pq} is called a moment tensor and is written as:

$$m_{pq} = C_{pqkl} l_k n_l \tag{1.21}$$

where C_{pqkl} are the second order elastic constants and n_l is the normal vector over the crack surface. In addition, symbols p, q, k, l represent the space directions x, y and z. Figure 1.5 depicts the dislocation model of a microcrack and its equivalent tensor components.

In the case of isotropic materials, m_{pq} is expressed as:

$$m_{pq} = b \left[\lambda l_k n_k \delta_{\rho q} + \mu \left(n_\rho l_q + n_q l_\rho \right) \right], \tag{1.22}$$

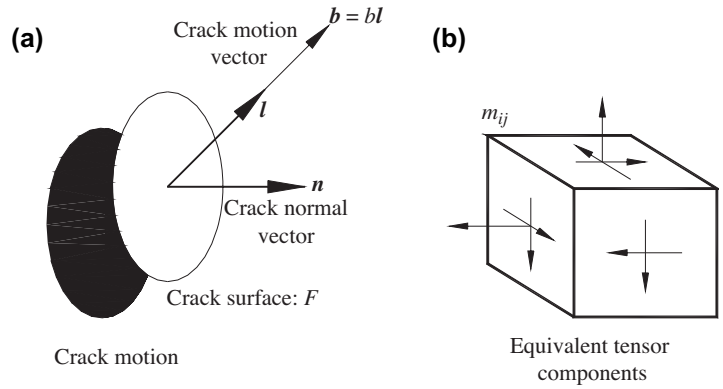

Figure 1.5: Dislocation model for a microcrack and its equivalent tensor components.

where λ and μ are Lamé constants and $\mathbf{M} = [m_{pq}]$ can be represented as a 3×3 symmetrical matrix as shown below:

$$\mathbf{M} = [m_{pq}] = b \begin{bmatrix} \lambda l_k n_k + 2\mu l_1 n_1 & \mu (l_1 n_2 + l_2 n_1) & \mu (l_1 n_3 + l_3 n_1) \\ \mu (l_1 n_2 + l_2 n_1) & \lambda l_k n_k + 2\mu l_2 n_2 & \mu (l_2 n_3 + l_3 n_2) \\ \mu (l_1 n_3 + l_3 n_1) & \mu (l_2 n_3 + l_3 n_2) & \lambda l_k n_k + 2\mu l_3 n_3 \end{bmatrix}, \tag{1.23}$$

where $l_k = (l_1, l_2, l_3)$ and $n_k = (n_1, n_2, n_3)$.

In the model proposed in [Scruby et al., 1983] and [Ohtsu and Ono, 1986], based on Equation (1.23), AE source of tensile crack and shear crack are defined as shown in Figure 1.6.

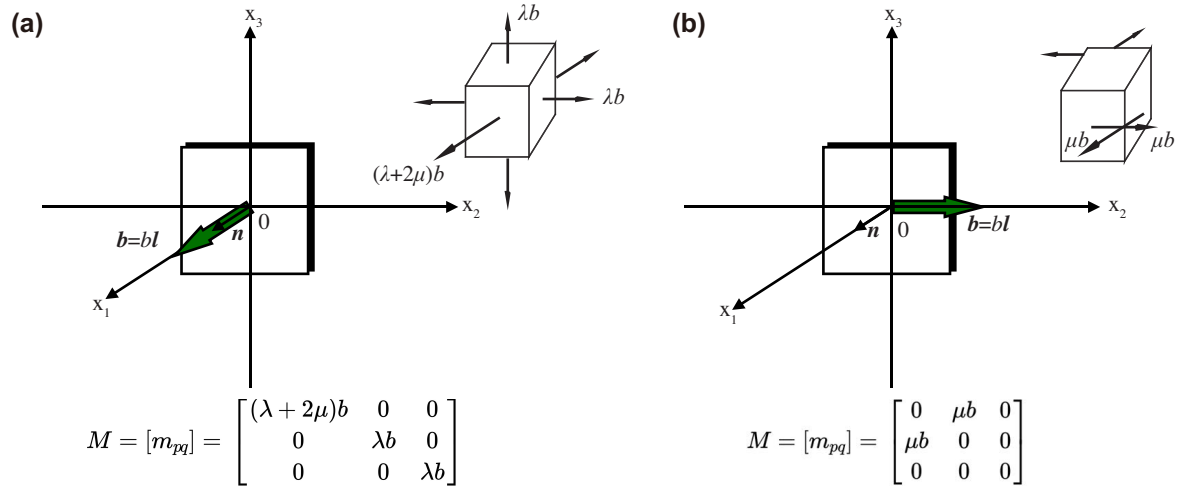

Figure 1.6: Schematic illustration of (a) a tensile dislocation model for a tensile crack on dislocation surface located on the $x_2 - x_3$ plan with the corresponding force components of the moments tensor and moment tensor matrix and (b) a shear dislocation model for a shear crack on dislocation surface located on the $x_2 - x_3$ plan with the corresponding force components of the moments tensor and moment tensor matrix.

Based on the MTA model of AE analysis, crack kinematics, crack classification, and crack volume can be analyzed from the recorded AE signals. In [Rice, 1980], Rice introduced the relationship between the stress and displacement in a homogeneous elastic isotropic solid due to the appearance of a micro-crack or a sliding phenomenon.

Scruby [Scruby et al., 1985] used this model to study the micro-cracking during the propagation of a fatigue crack in aluminum samples. Ohtsu and Ono [Ohtsu and Ono, 1988] proposed that dynamic motions in an elastic medium always generate P-waves which have the faster velocities and are likely to arrive first at any observation point on the surface. Compared with surface waves and other waves generated by diffractions, which are dispersive, AE arrival time differences of P-waves are most suited for the source localization technique. Simplified Green's Function (SiGMA) method is mostly used in concrete applications in order to estimate the size, orientation, crack classification, location, and fracture mode of individual micro-cracking [Chang and Lee, 2004, Uddin et al., 2006]. In SiGMA analysis, the type of crack is classified into three modes, namely shear mode, tensile mode, and mixed mode. Figure 1.7 shows the way the crack motion vector (arrow) is located relative to the crack surface (taken as a circular disc) for the three modes. Results of studies based on the SiGMA technique were compared with AE parametric analysis and experimental observations [Ohno and Ohtsu, 2010].

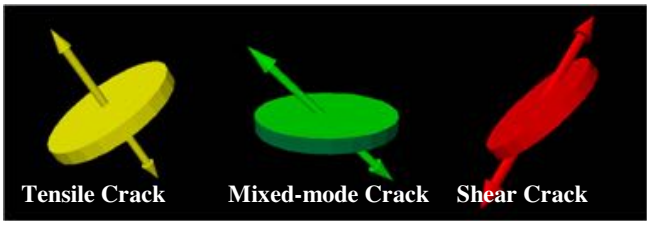

Figure 1.7: Classification of three main modes of cracking. [Ohno and Ohtsu, 2010]

1.3.2 Finite element method analysis

Modeling of AE events was also performed using the Finite Element Method (FEM) analysis. AE sources were therefore simulated by considering, in general, pointed forces to simulate surface sources and force dipoles to simulate internal sources. In the case of AE wave propagation in plates, many studies applied the FEM to simulate the different AE sources at the origins of the detected elastic waves. Results were used to better understand the numerous experiments performed on composites [Sause et al., 2012b, Zelenyak et al., 2015, Le Gall et al., 2018]. In particular, the characteristics of the displacement fields created

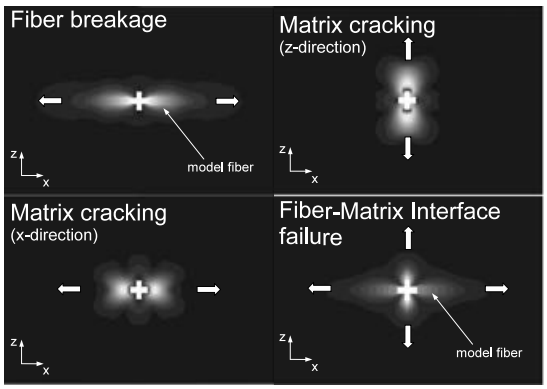

Figure 1.8: Different simulated damage mechanisms obtained using FEM in fiber-reinforced composite. [Sause and Horn, 2010]

by different damage mechanisms (the main ones or the most emissive) were studied in the

case of matrix cracking, fiber breakage, and fiber-matrix interface. In order to illustrate these effects, Figure 1.8 shows the main differences existing in the displacement fields excited by the crack surface displacement of the above-mentioned three main damage mechanisms [Sause and Horn, 2010].

1.4 Acoustic emission waves propagation in inhomogeneous medium

Elastic wave propagation in an inhomogeneous medium is very complex. For an isotropic inhomogeneous elastic medium the equation of motion can be written as:

$$\rho\frac{\partial^2\mathbf{u}}{\partial t^2} = (\lambda+\mu)\nabla(\nabla\cdot\mathbf{u}) + \mu\nabla^2\mathbf{u} + \nabla\lambda(\nabla\cdot\mathbf{u}) + \nabla\mu\times(\nabla\times\mathbf{u}) + 2(\nabla\mu\cdot\nabla)\mathbf{u}, \quad (1.24)$$

where $\mathbf{u}$ is the displacement vector, ρ is the material density, λ and μ are the Lamé constants, respectively.

If we suppose that the elastic wave is produced by a point source Q. First, we must determine the two families of rays (shear and compressional), which emanate from Q. In a homogeneous medium, they will both be straight lines leaving Q in all directions. In an inhomogeneous medium there will be two families of curved lines, also starting from Q in all directions. Next, we compute the phase S and then the amplitudes $\mathbf{A}_0, \mathbf{A}_1$,... on each ray using the formulas for transverse waves on the transverse rays and those for longitudinal waves on the longitudinal rays [Karal Jr and Keller, 1959]. Equations (1.11) and (1.13) will be denoted in the inhomogeneous case as:

$$\text{Longitudinal case} \quad S = S_0 + \int_{s_0}^{s} \left[\rho(\lambda+2\mu)^{-1}\right]^{\frac{1}{2}} \mathrm{d}s \quad (1.25)$$

$$\text{Transverse case} \quad S = S_0 + \int_{s_0}^{s} \left(\rho\mu^{-1}\right)^{\frac{1}{2}} \mathrm{d}s \quad (1.26)$$

where s is measures positively in the direction of propagation and S_0 is the value of S at point s_0 on the ray. However, the wave propagation rays in the inhomogeneous media are no longer straight lines. If the medium has boundaries or contains obstacles or interfaces some of the incident rays from the source will hit them. These rays will produce reflected and refracted rays and possibly diffracted and surface rays. With each new family of rays, a new wave is associated. In this way, reflected, refracted, diffracted, and surface waves arise and all the preceding considerations will also apply to them.

In addition, from the elastodynamics, heterogeneity is dependent on the ratio between the wavelength and the size of heterogeneity (i.e., aggregate in concrete). When the wavelengths are larger than the sizes of aggregates, the effect of heterogeneity becomes minor and vice versa. For example, in [Ohno and Ohtsu, 2010], P-wave velocity in concrete is about 4000 m/s and the wavelength becomes 40 mm at 100 kHz. Therefore, AE waveforms with a frequency range smaller than 100 kHz are supposed to propagate in an isotropic homogeneous medium since the maximum size of aggregate is 20 mm. At the higher frequency range, the wavelength becomes smaller and the scattering due to aggregation becomes important. Therefore, it is necessary to pay attention to the attenuation and in particular to the scattering effects under considering the inhomogeneous nature of materials. The wave scattering within extremely heterogeneous materials such as concrete is

mainly due to the existing pores, air bubbles, sand grain, aggregates as well as distributed cracks [Prosser, 1996, Philippidis and Aggelis, 2005]. In order to highlight their effects, various experimental studies have been performed on concrete and/or mortar specimens. For instance, Aggelis and Shiotani [Aggelis and Shiotani, 2007, Aggelis et al., 2012] studied the influence of scatterers on Rayleigh and longitudinal waves propagating in mortar samples (see Figures 1.9(a)-(c)). They have found that the existing cracks on the path of AE signals disturb their waveforms, which confuses the crack mode (shear mode or tensile mode) identification (see Figures 1.9(d) and (e)).

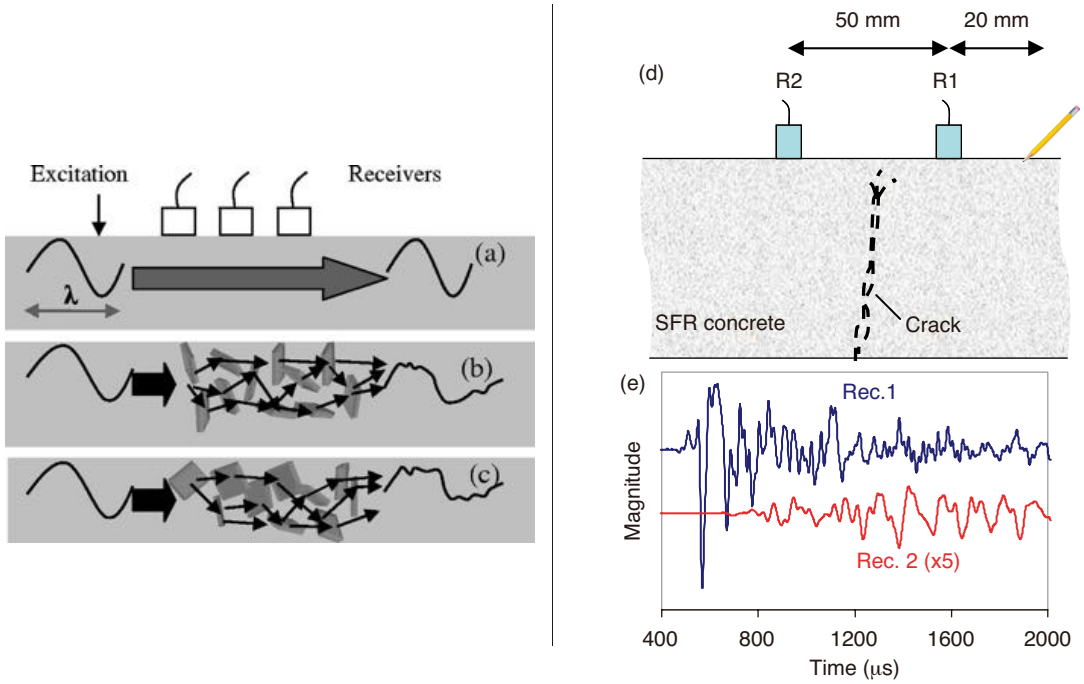

Figure 1.9: Schematic illustration of elastic wave propagation in a mortar specimen with (a) no scatterer, (b) distributed scatterers and (c) different arrangement of distributed scatterer. [Aggelis and Shiotani, 2007] (d) Schematic representation of surface wave measurements in cracked concrete and (e) detected AE waveforms from two different sensors at different positions. [Aggelis et al., 2012]

1.5 Acoustic emission sources characterization

1.5.1 Source localization

The localization technique is required for quantitative methods in AE analysis in order to accurately obtain the spatial source coordinates form the detected AE events. In AE analysis, a longitudinal wave is, in general, non-dispersive, whereas almost all the surface waves and other waves generated by diffraction are dispersive. Since the velocities of dispersive waves depend on the excitation frequency, it becomes appropriate to compare the arrival time difference of longitudinal waves for AE source location technology [Ohtsu and Ono, 1988].

Several works have been developed to study the source localization in different specimen geometries [Grosse et al., 1997, Salinas et al., 2010, Han et al., 2015]. In general,

they recommend verifying if the area near the AE sensors is free of cracks. Then the localization can be one-dimensional to monitor large structures, such as buildings and pipelines, or two-dimensional, which is usually applied in the case of structures with small thicknesses (see Figure 1.10). In this case, only three unknowns (two source coordinates

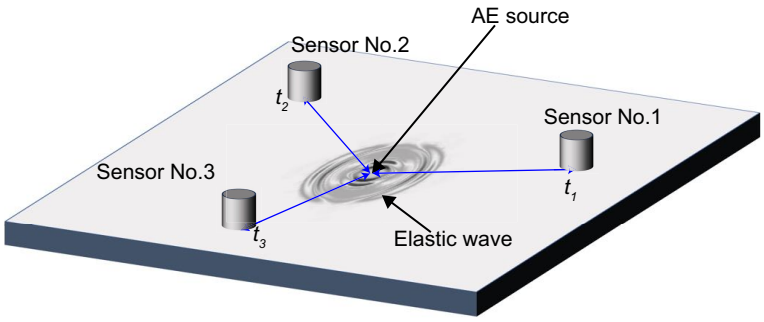

Figure 1.10: Schematic representation of two-dimensional localization method with three AE sensors.

and source time) need to be determined using three sensors' records. Three-dimension localization problem is accurately determined when four travel times are available to calculate the three coordinates and the source time of an AE event which needs at least four sensors and good arrangement.

1.5.2 Acoustic emission signal classification

The present thesis is mainly focused on the characterization of damages created in polymer concrete (PC) and civil engineering concrete samples. When submitted to quasi-static stresses, the forces distribution at the different main constituents (matrix, aggregate, interface) of the concrete samples will play an important role. Indeed, when the local force reaches the fracture limit of one of the constituents, damage starts to develop at the microscopic scale. Micro-cracking, which appears in the matrix will cause cracks to propagate in a direction perpendicular to the stress. The stress at the micro cracks will lead to interface or aggregate cracking [Elaqra et al., 2007, Soulioti et al., 2009, Sagar and Prasad, 2011, Aggelis et al., 2013a].

For civil engineering concrete and mortar specimens, under three-point bending tests, the matrix cracking is the only damage mechanism detected by AE sensors before the macroscopic main crack deformation [Aggelis, 2011, Aggelis et al., 2013b]. Therefore, studies were mainly focused on the crack mode classification by using parametric analysis based on the following characteristics of the detected AE signals, namely rise time, amplitude, and average frequency [Soulioti et al., 2009, Aggelis et al., 2013a]. This approach and these parameters are presented below.

1.5.2.1 Parametric approach of crack mode classification

As presented earlier, the moment tensor analysis (MTA) appears to be the most appropriate method in crack mode classification analysis, while each cracking event needs to be detected by at least six sensors [Ohno and Ohtsu, 2010]. Various researches have shown that some AE features can be used to describe each specific type of crack. For

example, tensile crack deformation caused by the opposing movement of the crack sides is expected to generate AE waveforms with short rise time and high frequency. Instead, shear-type cracks result in signals with a lower frequency and longer rise time. Based on these indicators, the parametric classification approach is established by computing two AE parameters: RA value and average frequency (AF). The RA value is derived from the rise time and peak amplitude of the AE signal and AF is defined as the counts over the AE signal duration.

This classification approach has been highly investigated particularly on concrete and mortar specimens [Ohno and Ohtsu, 2010, Aggelis, 2011, Aldahdooh and Bunnori, 2013], fiber composites [Aggelis et al., 2010] and rocks [Shiotani, 2006]. Experimental results showed the existence of a good agreement between ratios of tensile/shear crack identified by parametric analysis and those obtained using the SiGMA analysis (based on moment tensor analysis). Details of the parametric approach and its application on concrete specimens will be discussed in Chapter 2 and Chapter 3.

1.5.2.2 Pattern recognition of acoustic emission signals clustering

In AE analysis, one of the main objectives is to identify the nature of AE sources. Each detected signal can be considered as an acoustic signature of a damage mechanism. In view of the huge number of unlabeled AE events, the relation between the AE signals and damage mechanisms can be described by a statistic method such a multi-parametric unsupervised pattern recognition analysis [Doan et al., 2015]. This method consists of several relevant AE features and an effective unsupervised clustering approach that overcomes the drawbacks of simplified AE parametric analysis and is more accurate. The proposed unsupervised pattern recognition involves AE feature selection, cluster analysis, and cluster validity. For unsupervised cluster analysis of AE signals, k-means algorithm is the most used method [Godin et al., 2004, Sause et al., 2012a, Pashmforoush et al., 2012]. However, another method for unsupervised data classification is the Kohonen's Self Organizing Map (SOM) [Huguet et al., 2002, Crivelli et al., 2014], which separates AE data by neural network procedures. The SOM is one of the most prominent artificial neural network models adhering to the unsupervised learning example.

In this thesis, we use multi-parametric unsupervised pattern recognition analysis based on the k-means algorithm to cluster AE data, to separate damage mechanisms, and to track their evolution in time. The details of the above-mentioned processing will be introduced and discussed in the next Chapter.

1.6 Acoustic emission sensors and acquisition system

1.6.1 Acoustic emission sensors

There is a large variety of AE sensors available today, which are in general based on the piezoelectric effect which transforms the vibrations detected at the material surface into electric signals. AE sensors could be either resonant or broadband. Resonant sensors with appropriate resonant frequencies are required to supply maximum sensitivity and reduce or eliminate background noise. Broadband sensors are less sensitive compared

with resonant sensors, however, they are capable of responding almost uniformly at the same sensitivity over a large frequency bandwidth [Keprt and Benes, 2009].

Figure 1.11(a) shows the sensitivity of a resonant AE sensor (Mistras R15α with resonance frequency at 150 kHz). When an AE signal reaches the resonance sensor, it is reflected repeatedly inside the piezoelectric element. The reflections interfere constructively around the PZT resonance frequencies, which makes it possible to increase the sensitivity to displacement and/or to stress. In return, using resonant PZT sensors makes the analysis of the characteristics of the incident wave (source) very delicate [Sause et al., 2012c]. In the case of broadband AE sensors, the PZT disc is covered with a damping material such as tungsten-enriched epoxy [Goujon and Baboux, 2003]. In such a case, the received elastic waves pass from the PZT to the damping material by reducing the reflections on the edge of the PZR disc [Boulay, 2017]. Therefore, a loss of sensitivity is generated but with a flat frequency response over a wide frequency bandwidth (see Figure 1.11(b)).

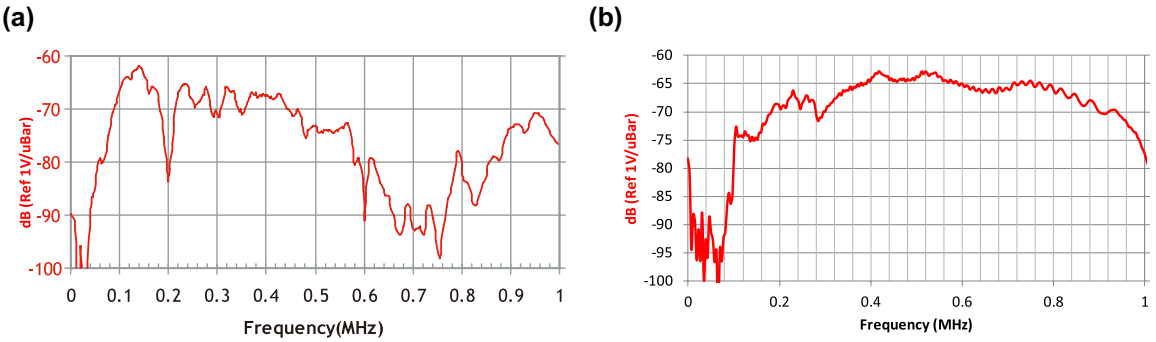

Figure 1.11: Manufacturer's sensitivity curves of (a) the R15α resonant sensor and (b) WSα broadband sensor (from the website of R15a and WSa). Here, 0 dB corresponds to 1 V/μBar.

1.6.2 Acoustic emission acquisition system

Thanks to piezoelectric effect, AE sensors transform strain (or displacement) into voltage. The small amplitude of signals requires the use of significant amplification to better process, where the pre-amplification is 40 dB or 60 dB. In addition, frequency filtering is performed directly on the pre-amplifier a high-pass filter to eliminate the operating noise of the installation. Amplified signals are then transferred into the AE system. In this thesis, we use a Physical Acoustic (MISTRAS) PCI-2 AE system with two measurement channels. The elastic energy freed by cracks initiation and/or propagation is associated with an 'AE event' and can be detected and digitized by the AE system as an 'AE hit'. The detection of AE hits depends on different time windows and parameters: threshold, Peak-Definition-Time (PDT), Hit-Definition-Time (HDT), and Hit-Lockout-Time (HLT) as shown in Figure 1.12.

- Threshold: this parameter is fixed at a suitable value (in dB), which is big enough for filtering the background noise.
- Peak Definition Time (PDT): it enables to determine the time of the true peak in the waveform.

- Hit Definition Time (HDT): it enables the system to determine the end of the AE hit. It is the time of which the acquisition of the AE hit stops.
- Hit Lockout Time (HLT): it inhibits the measurement of reflection and late-arriving parts of the AE signal, so that data from wave arrivals can be acquired.

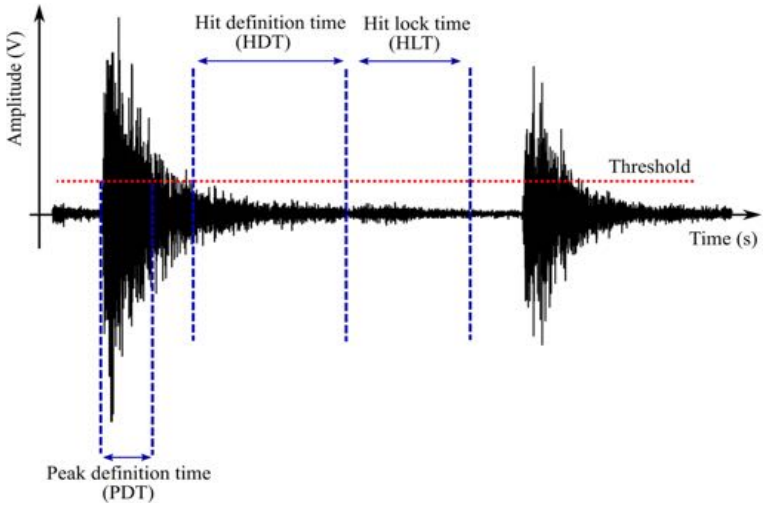

Figure 1.12: Representation of acquisition parameters. [Shateri et al., 2017]

1.6.3 Acoustic emission Q-value analysis

As mentioned in subsection 1.2.2, AE waveforms are achieved as a convolution of source functions $E(t)$, propagation medium function $G(t)$, sensors function $R(t)$ and acquisition system function $H(t)$ in the time domain. The frequency responses can be formulated in the frequency domain as:

$$V(f) = E(f)G(f)R(f)H(f), \tag{1.27}$$

where $V(f)$, $E(f)$, $G(f)$, $R(f)$, $H(f)$ are the Fourier transforms of detected AE waveforms, AE source, propagation medium, sensor and acquisition system, respectively. $G(f)$ in Equation (1.27) is a target to quantify the damage. Therefore, it is very important to identify $G(f)$ irrespective of source time function since $E(f)$ is not easily achievable in the AE technique.

One of the ways to get rid of the effects of the sensor and acquisition system would be to consider two AE signals obtained by two identical sensors for the same AE source. When the frequency responses of AE sensors are the same, the comparison of detected AE signals may conform as:

$$\frac{V_2(f)}{V_1(f)} = \frac{R_2(f)}{R_1(f)} \cdot \frac{G_2(f)}{G_1(f)} = \frac{G_1(f)}{G_2(f)}. \tag{1.28}$$

Furthermore, considering the dependence of $G(f)$ on propagation distance, Equation (1.28) might be introduced as [Shiotani, 2012]:

$$G(f) = \exp\left(-\frac{\pi f}{VQ}d\right) \tag{1.29}$$

where f is the frequency (Hz), V is the P-wave velocity (m/s) and Q is a normalized value of the attenuation rate. By combining Equation (1.28) and Equation (1.29), Equation (1.30) is then obtained:

$$\begin{aligned} &\frac{X_2(f)}{X_1(f)} = \frac{D_i(f)}{D_1(f)} = \exp\left(-\frac{\pi f}{VQ}\Delta d_i\right), \\ &\Delta d_i = d_i - d_1 \,(d_i \geq d) \quad (i = 2, \ldots, n). \end{aligned} \tag{1.30}$$

Equation (1.30) shows that a function of frequency response can be expressed by an exponential function composing from the difference of distance Δd and frequency f.

The frequency response ratios for different propagation distances are shown in Figure 1.13(a). We observe the decrease of the ratio for high frequencies (above 100 kHz) becomes larger as the difference in propagation distances increases. As this trend is in good accordance with Equation (1.30), the slop of the ratios γ in Figure 1.13(b) was calculated as:

$$\gamma = \left(\frac{\pi \Delta d}{VQ}\right). \tag{1.31}$$

Figure 1.13(b) shows the relation between the slope γ and the difference of propagation distances. The relation can be approximated by a linear equation, resulting in good agreement with Equation (1.31). The slope γ correlates well to the difference of propagation distance, but more likely to demonstrate the properties of the propagation medium. However, we note that the frequency range is only under 200 kHz where the wavelength is larger than the size of the aggregates, meaning the propagation can be considered in a homogenous medium.

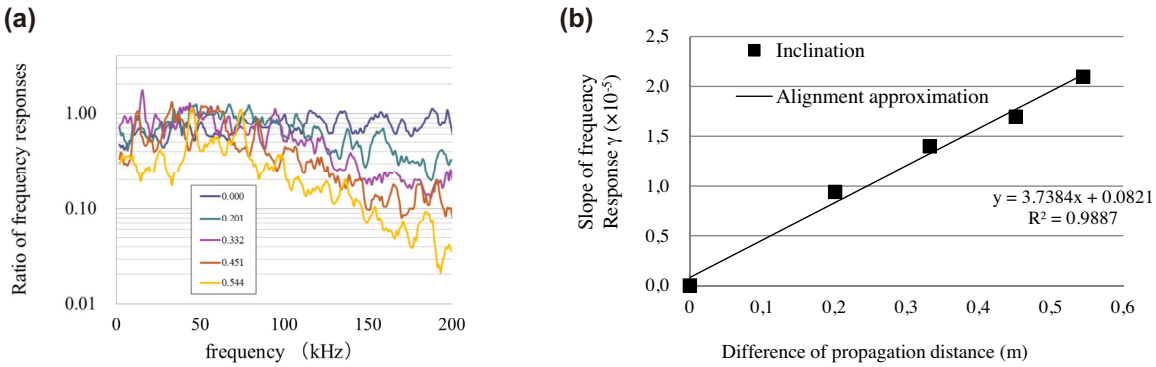

Figure 1.13: (a) Frequency responses ratio as a function of the difference of propagation distances. (b) Linear evolution of frequency response as a function of difference of propagation distances. [Shiotani, 2012]

1.7 Nonlinear acoustic theory and Nonlinear Mesoscopic Elastic theory

In this PhD work, the AE technique is used in two cases: to probe damage creation and propagation in complex samples (polymer concrete and civil engineering concrete) during

quasi-static tests and during the nonlinear relaxation of the same samples. The aim of this section is to present the main characteristics of nonlinear elastic materials when submitted to dynamic excitation. It will therefore include classical and non-classical nonlinear effects.

1.7.1 Classical nonlinear theory

The linear elastic theory is based on the assumption which considers infinitesimal strains and a linear relationship between stress (σ) and strain (ε) which is described by the famous Hook's law:

$$\sigma = K\varepsilon, \tag{1.32}$$

where K is the elastic modulus of the material. However, when the two above-mentioned conditions are not satisfied, classical nonlinearity appears. The latter can be divided into two types: geometric nonlinearity and physical nonlinearity.

The geometric nonlinearity comes from an extrinsic reason, related to deformation. Indeed, when the deformation is big enough, its infinitesimal aspect is no longer valid. In this case, even if the material is perfectly elastic (elastic modulus K remains constant), the linearity between the deformation and the stress is broken by the change of the geometry. This effect is at the origin of the so-called 'geometric nonlinearity'. On the other hand, the physical nonlinearity comes from the intrinsic nonlinearity resulting from the nonlinearity at the smallest scales, such as the nonlinearity of the interaction potential between atoms of a crystal.

In general, studies of the classical nonlinear theory for a one-dimensional system have the stress-strain relation which can be expressed as:

$$\sigma = K_0\left(\varepsilon + \beta\varepsilon^2 + \delta\varepsilon^3 + \cdots\right), \tag{1.33}$$

where K_0 is the linear elastic modulus, β and δ are the quadratic and the cubic nonlinear coefficients, respectively. In Equation (1.33), the first-order term $K_0\varepsilon$ corresponds to linear elastic behavior, while the higher-order terms correspond to the second and the third order nonlinear behaviors, respectively.

In the case of an elastic wave propagating in an isotropic solid, the nonlinear coefficients β and δ are:

$$\beta = \frac{3}{2} + \frac{l+2m}{\lambda+2\mu} \quad \delta = \frac{3l+2m}{2\lambda+2\mu} \tag{1.34}$$

where λ and μ are the Lamé constants, l, m and n are the third order elastic constants of Murnaghan [Ostrovsky and Johnson, 2001].

When materials exhibiting classical nonlinearity are excited with a pure monochromatic wave with angular frequency ω ($\omega = 2\pi f$), they can distort the propagating wave and generate higher-order harmonics (2ω, 3ω, etc.). In such a case, the quadratic nonlinear parameter β, for instance, can be obtained from a measurement of the displacement amplitude A_2 at the second harmonic generated at a distance x as [Meegan Jr et al., 1993]:

$$\beta = \frac{2A_2c^2}{A_1^2\omega^2x}, \tag{1.35}$$

where A_1 is the displacement amplitude at the fundamental frequency and c is the wave velocity.

Besides, the classical nonlinearity could be observed through the resonance frequency shifts as a function of the dynamic strain in the form [Idjimarene, 2013]:

$$\frac{\omega_r - \omega_l}{\omega_l} \propto \frac{1}{2}\delta\epsilon_{\max}^2 \tag{1.36}$$

where ω_l and ω_r are resonance frequency in the linear limit and measured resonance frequency in the nonlinear limit, respectively, $\epsilon_{\max}$ is the maximum strain amplitude and δ is the cubic nonlinear coefficient.

1.7.2 Non classical nonlinear theory

The classical nonlinear theory was used successfully to describe the nonlinear elastic behavior of air, water, and mono-crystalline materials (such as intact metals). In general, the elastic nonlinear behaviors are in accordance with the macroscopic observations of interactions at the microscopic and/or atomic scales [Landau et al., 1986]. However, this theory was unable to describe the nonlinear behavior observed in cracked metals, rocks, concrete, composites, etc., which belong to the class of Nonlinear Mesoscopic Elastic Materials (NMEM) (or micro-inhomogeneous materials) for which micro-inhomogeneities are of the order of 10 μm - 100 μm [Guyer et al., 1999, Guyer and Johnson, 1999]. Indeed, these materials obey generally to the classical nonlinear theory of elasticity for the strain amplitudes corresponding to approximately 10^{-6} and lower. At higher strain amplitudes ($\varepsilon \gtrsim 10^{-6}$), their behavior is no longer adequately described by the classical nonlinear theory of elasticity. Many experimental observations were reported from quasi-static stress-strain experiments [Gist, 1994, Guyer et al., 1997, Darling et al., 2006] and dynamics experiments [Pasqualini et al., 2007, Muller et al., 2005, Remillieux et al., 2016].

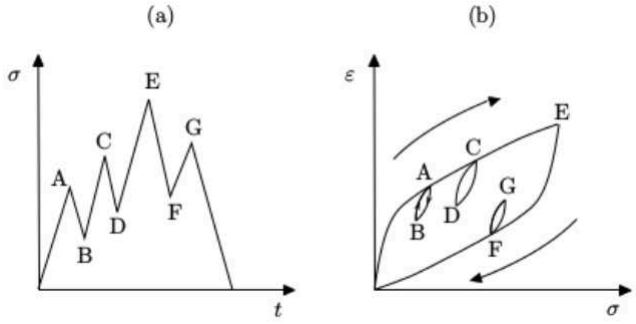

Figure 1.14: (a) Axial quasi-static protocol. (b) Stress-strain curve showing hysteresis loops corresponding to the protocol in subplot(a). [Guyer and Johnson, 1999]

Quasi-static stress-strain experiments allowed to get the first observations of non-classical nonlinearity in solid. Figure 1.14(b) presents the stress-strain curve with hysteresis loops when a given axial stress protocol (see Figure 1.14(a)) is applied to a geological material. The applied stress is varied very slowly to ensure quasi-static (equilibrium) conditions at each strain and the resulting plot shows that tested materials are nonlinear and present hysteresis and discrete memory which can be observed through the inner-loops. For such a material behavior, the stress-strain relationship must take into account the existing hysteresis and discrete memory [Guyer et al., 1995]. The one-dimensional stress-strain relationship can be expressed as [McCall and Guyer, 1994]:

$$\sigma(\varepsilon) = K_0\left(\varepsilon + \beta\varepsilon^2 + \delta\varepsilon^3 + \cdots\right) + H[\varepsilon, \text{sign}(\dot{\varepsilon})], \tag{1.37}$$

where σ is the stress, ε is the strain, K_0 is the linear elastic modulus, β and δ are the classical quadratic and cubic nonlinear parameters, respectively, and H is a function describing the hysteresis where $\dot{\varepsilon}$ is the strain rate, $\text{sign}(\dot{\varepsilon}) = 1$ when $\dot{\varepsilon} > 0$ and $\text{sign}(\dot{\varepsilon}) = -1$ when $\dot{\varepsilon} < 0$ [Guyer and Johnson, 2009]. The function H in Equation (1.37) take into account the fact that hysteresis in the stress-strain relationship cannot be described by an analytic function. For that reason, phenomenological modeling can be performed, for instance, such as the Preisach-Mayergoyz (P-M) space approach [Mayergoyz, 1985] in order to take into account the hysteresis and the memory effect as well [McCall and Guyer, 1994, Guyer et al., 1995, Delsanto and Scalerandi, 2003].

The effects of classical and hysteretic nonlinearity on a sinusoidal waveform are summarized in Figure 1.15.

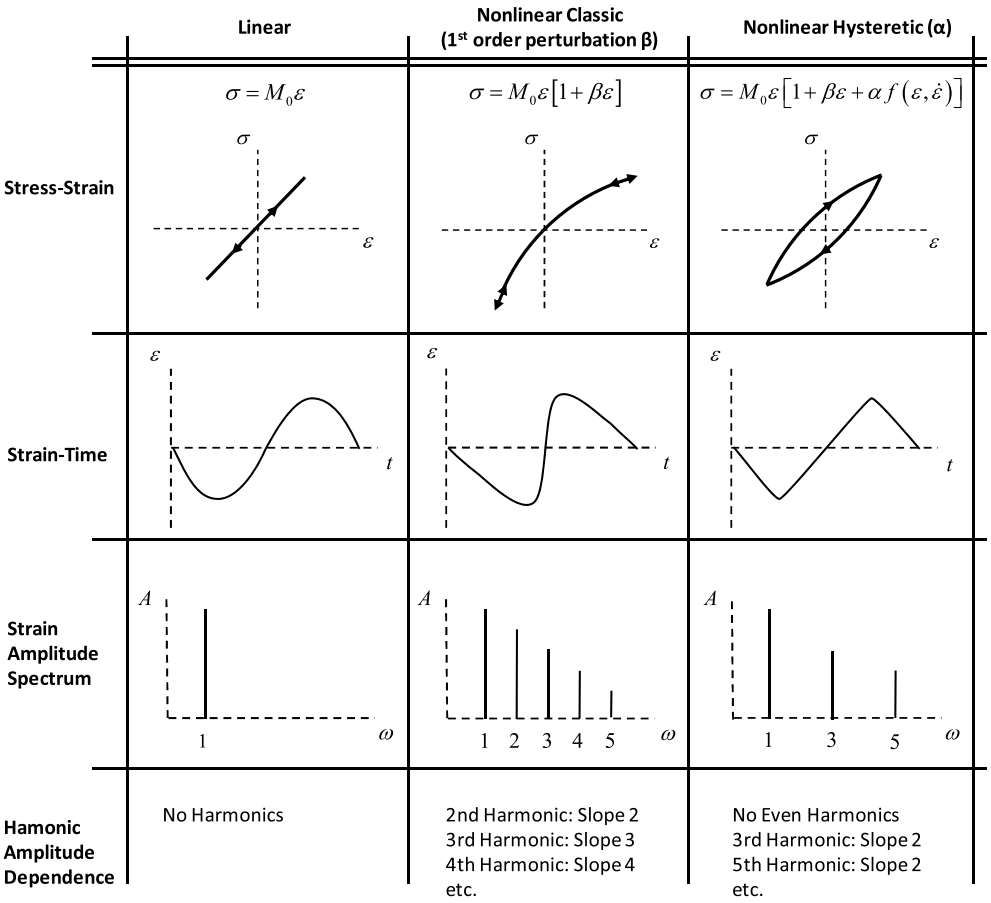

Figure 1.15: Effects of pure classical nonlinearity and pure hysteretic nonlinearity on the evolution of a sinusoidal waveform in the time and frequency domains. [Van Den Abeele et al., 2000]

1.8 Dynamic behavior of Nonlinear Mesoscopic Elastic Materials (NMEM)

The dynamic behavior of Nonlinear Mesoscopic Elastic Materials (NMEM) has been observed and discussed in many references [Guyer and Johnson, 2009, Antonaci et al., 2010]. Most of these experiments are showing an anomalous behavior when a time-dependent per-

turbation is applied. Like it was shown in the classical nonlinear case, the dynamic nonlinear response may manifest itself in a variety of ways (transient regime, standing waves...). Therefore many indicators of nonlinearity could be defined, linking the evolution of strain amplitudes to the generated harmonics [Ostrovsky and Johnson, 2001, Novak et al., 2012, Liu et al., 2012], resonance frequency shift [Muller et al., 2005, Zaitsev et al., 2005], break the superposition principle [Scalerandi et al., 2008, Bruno et al., 2009]. Furthermore, additional indicators related to memory effects can also be introduced exploiting the properties linked to slow dynamics.

In the following, we will mainly focus on two types of experiments called fast and slow dynamics, both based on the memory effect existing within NMEM.

1.8.1 Fast dynamic experiments

Fast dynamic (FD) experiments are performed when the material is excited increasingly in either transient or standing waves conditions. For instance, we often probe the resonance frequency (elastic modulus) and the quality factor Q decrease as a function of the amplitude of excitation. We can also expect a distortion of the propagating waves which is manifested by a decrease in the propagation velocities, and the generation of harmonics (notably odd harmonics) [TenCate et al., 2004, Chen et al., 2011].

Figure 1.16(a) presents an example of the FD behavior of the sandstone sample. The relative change of the resonance frequency and the quality factor of different materials are shown in Figures 1.16(b) and (c).

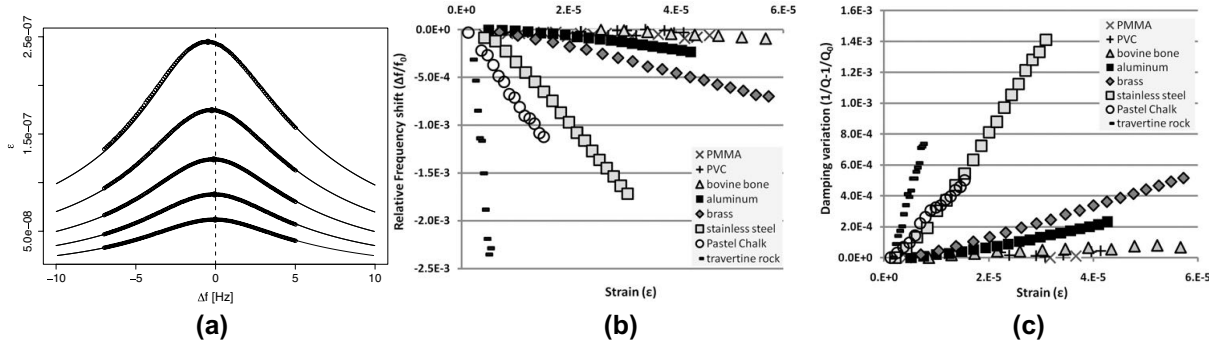

Figure 1.16: (a) Fast dynamics behavior of a sandstone sample: frequency resonance curves in the function of different strain levels. [TenCate et al., 2004] (b) Resonance frequency and (c) damping shifts on different strain level for several tested materials. [Haupert et al., 2011]

Numerous studies [Johnson et al., 2004, Johnson and Sutin, 2005, Haupert et al., 2011, Remillieux et al., 2017] have shown that in the FD experiments, the resonance frequency $f(\varepsilon)$ and the damping $1/Q(\varepsilon)$ change linearly as a function of the strain amplitude ε at high strain rates ($\varepsilon \gtrsim 10^{-6}$). Two parameters α_f and α_Q representing the change of modulus and damping can be defined as:

$$\frac{f(\varepsilon) - f_0}{f_0} = -\alpha_f \varepsilon, \tag{1.38}$$

$$\frac{1}{Q(\varepsilon)} - \frac{1}{Q_0} = -\alpha_Q \varepsilon, \tag{1.39}$$

where f_0 is the linear resonance frequency, Q_0 is the linear quality factor of the tested materials.

1.8.2 Slow dynamic experiments

Slow dynamics (SD) refers to the logarithmic time dependence recovery of the elastic modulus and damping to their initial values after being softened by a large amplitude dynamic strain (10^{-6} or higher). It includes two different time scale mechanisms: conditioning, which takes seconds to minutes and relaxation, which takes a long time of the order of 10^3 seconds to days depending on the configuration [Ten Cate and Shankland, 1996, TenCate et al., 2000b, Shokouhi et al., 2017, Bittner and Popovics, 2019].

As shown in Figure 1.17(a), the illustration of the experimental excitation protocol consists of three phases: preconditioning (low-amplitude excitation), conditioning (high-amplitude excitation) and relaxation (same as preconditioning). Figure 1.17(b) depicts a typical result for the evolution of relative change of resonance frequency (or elastic modulus) as a function of time measured for three measurement conditions on a NMEM sample.

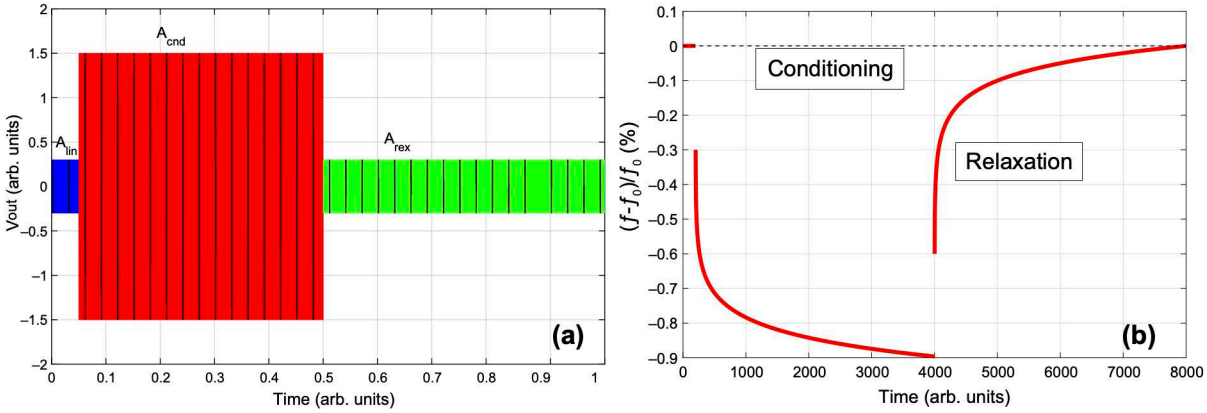

Figure 1.17: (a) Schematic illustration of excitation protocol in three phases: preconditioning (the sample is excited with a low-amplitude signal), conditioning (high excitation amplitudes) and relaxation (the excitation signal is the same as that of the preconditioning). (b) Schematic sketch of the evolution of the relative variation of resonance frequency (or elastic modulus) as a function of time during preconditioning, conditioning and relaxation.

1.8.2.1 Conditioning

The softening of the material, also termed conditioning, occurs at dynamic strain levels ($\varepsilon \gtrsim 10^{-6}$). When a high excitation level is applied to NMEM repeatedly, the material's viscoelastic properties will change depending on the excitation level and the material's state. Under the effect of such a dynamic excitation, the material goes to an out of equilibrium phase until the full conditioning is obtained, meaning the material reached a new equilibrium state [Mechri et al., 2017].

The conditioning effect can be observed through the evolution of the resonance frequency (elastic modulus, wave velocity, etc.) and the quality factor (damping) during

the application of the dynamic excitation. Numerous references [TenCate et al., 2000a, Delsanto and Scalerandi, 2003, Scalerandi et al., 2010, Gliozzi et al., 2010] have shown that the total decrease in elastic modulus (i.e., material softening) becomes greater and when the duration and amplitude of the excitation are significant.

Figure 1.18 shows an example of the conditioning experiment, in which a large-amplitude of excitation is applied to a cylindrical damaged concrete sample during a long time (more than 1500 s). An ultrasonic wave with a weak linear amplitude is used to test the sample by measuring the wave velocity at different times during the conditioning process. The curve shows that the velocity (blue triangle) drops continuously until reaching a stationary state which is a typical observation of conditioning. Simultaneously, the defined nonlinear indicators (red circles - SSM indicator; black squares - harmonics indicator) increase continuously as well, until the new equilibrium state is reached. In the experiment, the temperature (green diamond) and humidity are controlled to separate the conditioning effects from those due to fluctuations in the environmental parameters.

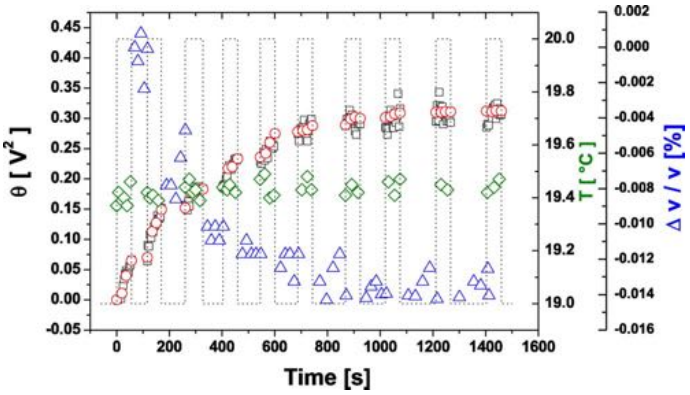

Figure 1.18: Conditioning on a damaged concrete sample. As conditioning time increased, the wave velocity (or elastic modulus) diminishes (blue triangle), while the nonlinearity of the sample (indicator θ) increases and harmonics indicators increase, respectively. [Scalerandi et al., 2010]

1.8.2.2 Relaxation

After the material is conditioned, the high excitation level is turned off and the sample's properties return back slowly to their original values. This slow recovery behavior is probed by a very weak signal to monitor the material's relaxation, which lasts for a long time (minutes to days depending on the strain amplitude used for conditioning and the conditioning duration as well). The recovery evolves in general as the logarithm of time [TenCate et al., 2000b, Johnson and Sutin, 2005, Zaitsev et al., 2014].

As an example, Figure 1.19(a) depicts the relaxation effects on a damaged concrete sample after full conditioning is obtained. During relaxation monitoring, successive sweeps are repeated around the resonance mode at the lowest excitation amplitude and the resonance frequency is monitored over time. Here we observe that immediately after conditioning, a significant recovery is observed in a quasi-continuous way slowly in time, frequency recovery evolves continuously until the elastic modulus returns back to its original value (see Figure 1.19(b)). At the time when the mechanisms at the origin of conditioning and relaxation remain diverse and varied depending on the material studied

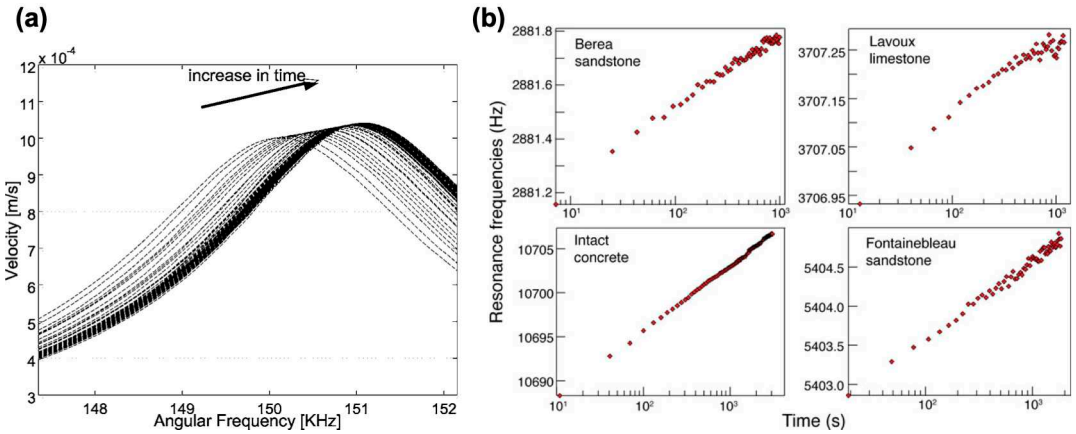

Figure 1.19: (a) Relaxation effects on a damaged concrete sample represented by recovery of resonance curves during the relaxation process. [Bentahar et al., 2006] (b) Resonance frequency versus logarithmic relaxation time for four different materials. [TenCate, 2011]

(rocks, composites, concrete, glass, etc.), it remains very difficult to find a unique reason which explains alone the observed log-time evolution. This is the reason for which, we propose in this thesis to use AE during relaxation in order to provide the necessary evidence to show the link between the damage mechanisms and nonlinear relaxation.

1.9 Conclusions

In this chapter, firstly, the elastic wave theory is shown which leads to the propagation of acoustic emission (AE) events. Acoustic emission has been proved to be a significant technique in damage mechanisms studies. The quantitative AE study requires understanding the physical theory of AE source, AE wave propagation, calibration of the sensors, and the acquisition system, which have been presented. In this thesis, we use the phenomenological AE approach to establish the link between the damage mechanisms and the measured AE signals in complex materials during the mechanical tests. This approach needs knowledge of signal processing, pattern recognition, and deep learning, which will be presented in Chapter 2.

Nonlinear Mesoscopic Elastic Materials (NMEM) always have hysteretic nonlinear behavior in dynamic experiments which has been introduced by literature studies and experimental observations in this chapter. To investigate the link between nonlinear mesoscopic elasticity and damage mechanisms in the complex materials (polymer concrete and civil engineering concrete), we use the AE technique to probe the damage creation and propagation in the complex materials during the quasi-static mechanical tests (Chapter 3) and during the nonlinear dynamic tests of the same samples (Chapter 4).

Chapter 2

Signal based acoustic emission signal analysis

This Chapter presents signal processing tools used to analyze Acoustic Emission (AE) signals and associate each AE signal with corresponding damage mechanisms. In this study, the AE system records AE waveforms instead of several AE parameters (AE feature extraction), the raw signal waveform analysis offers a better interpretation. Thus, the relation between the AE signals and damage mechanisms can be described by the statistic method which is the multi-parametric unsupervised pattern recognition analysis.

Additionally, due to artificial intelligence (AI) technology has made great progress in recent years, we propose a novel approach for AE signal classification combining continuous wavelet transform (CWT) and convolution neural network (CNN). This approach uses the time-frequency representation of the AE signal and deep learning algorithm that may have a good outlook.

2.1 Acoustic emission features extraction

One main purpose of the AE signal analysis is to associate a signal with a source mechanism (damage mechanism). The AE phenomenological approach to the identification of sources of AE is based on a fundamental assumption: each recorded AE signal has properties related to the characteristics of the created source. To analyze AE signals, the most mentioned method is the feature-based approach which is based on that the AE signal is completely described by a set of features [Sikorski, 2012]. The association of damage mechanisms with AE signals is based on the signal features.

2.1.1 Time domain features

An AE signal $x(t)$ with several AE time features is shown in Figure 2.1. It is reasonable to suggest that the energy in the AE waveform is proportional to the energy of the associated events [Curtis, 1975, Landis and Baillon, 2002]. It is reasonably assumed as well that the AE signal depends on its source, specifically the intensity and the damage mode [Sagar and Prasad, 2011, Van Tittelboom et al., 2012]. The shape of the AE waveform is related to the cracking event that gave rise to damage mode. In literature related to AE, feature extraction has been well studied up to now and the features are calculated in real-time by the AE system. However, in this study, by using the Physical Acoustic (MISTRAS) PCI-2 AE system, waveforms of detected AE hits are saved and the features are computed implemented on an external software (Matlab). The MISTRAS

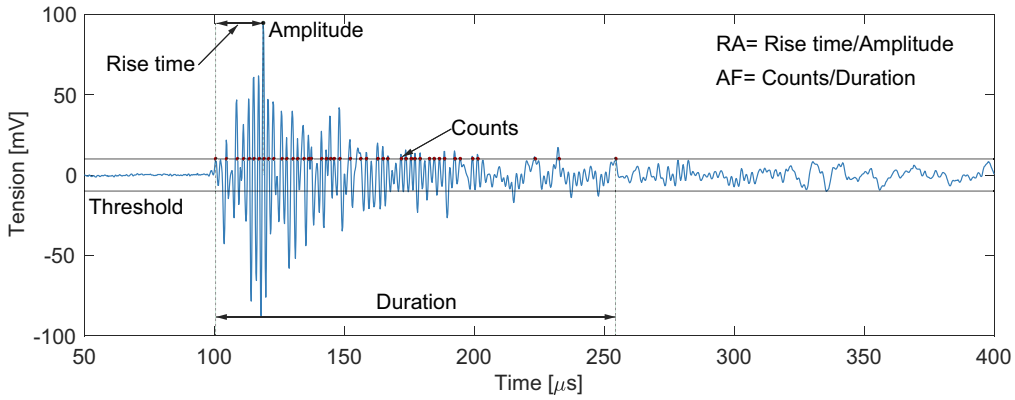

Figure 2.1: Extraction of time features from acoustic emission signal $x(t)$.

AE system uses a fixed threshold to detect a signal arrival time and also to detect the end of the signal. The detected AE events are dependent on this threshold, meaning that the analyzed signal lies between the first and the last threshold crossing. Some of the AE features defined in time domain can be defined as follows [Grosse and Ohtsu, 2008]:

– Amplitude (A) [dB]: calculated by the maximum value of the AE signal and the value of the gain of the pre-amplifier of the AE sensors, with the expression :

$$A = 20 \times \log(\frac{\mathrm{V_{max}}}{\mathrm{V_{ref}}}) - \mathrm{Gain}, \tag{2.1}$$

where $\mathrm{V_{max}}$ is the maximum value of signal in Volts, $\mathrm{V_{ref}}$ is the reference voltage ($1\,\mu$V), Gain is the pre-amplifier's gain (e.g. 40 dB).

– AE Energy (E) [aJ]: the area under the square of voltage-time envelope (aJ, atto Joules with $1\,\mathrm{aJ} = 1 \times 10^{-18}\,\mathrm{J}$).

$$E = \int_{t_d}^{t_f} x(t)^2 \,\mathrm{d}t, \tag{2.2}$$

where t_d is the starting time of the AE signal $x(t)$ and t_f is the ending time of this signal.

– Duration (DU) [µs]: it corresponds to the time between the first and the last crossing of the threshold.

– Rise Time (RT) [µs]: the time interval from the first threshold crossing to the maximum amplitude.

– Count (CNTS) : number of crossing thresholds over the duration of the signal.

– Average Frequency (AF) [kHz]: number of counts divided by duration, which determines number of threshold crossing per unit time over one AE hit.

– RA value (RA) [µs/V]: rise time divided by amplitude (measured in voltage).

In reference [Ni and Iwamoto, 2002], Q.Ni and M.Iwamoto have shown that the frequency component of the AE signals was less changed by the distance between the AE source and the sensor, which can be used as useful feature to represent the signals. Besides, each damage mechanism generates different intrinsic frequencies that has been discovered in many articles. In fiber/resin composites [Bohse, 2000], matrix cracking has low-frequency signal and fiber failure generates high-frequency components. In addition, in concrete, tensile cracks always have higher frequencies than shear cracks [Aggelis, 2011, Farhidzadeh et al., 2014].

In this study, due to the fact that specimens are of small dimension, influence of attenuation can be controlled. In the next subsection, AE features extracted from the frequency domain will be presented.

2.1.2 Frequency domain features

In this section, the Fourier Transform (FT) provides the frequency spectral information of an AE signal which makes it possible to establish its frequency features. The analytical expressions of the Fourier Transform (TF) and the Inverse Fourier Transform (IFT) of signal $x(t)$ are defined as follows:

$$\hat{x}(f) = \int_{-\infty}^{\infty} e^{-2\pi i f t} x(t) \,\mathrm{d}t \tag{2.3}$$

and

$$x(t) = \int_{-\infty}^{\infty} e^{2\pi i f t} \hat{x}(f) \,\mathrm{d}f, \tag{2.4}$$

where the $\hat{x}(f)$ is a complex-valued function of frequency. The frequency spectrum is the distribution of the amplitudes and phases of each frequency component against frequency of signal $x(t)$. For $\hat{x}(f)$, its magnitude component is spectrum amplitude ($|\hat{x}(f)|$) and complex argument is the phase [Bracewell, 1986].

In this study, the spectral analysis of the digital AE signals is calculated using the Fast Fourier Transform (FFT) which is based on the Discrete Fourier Transform (DFT)

by software Matlab [Van Loan, 1992]. For the AE signal $x(t)$, we calculate its FFT. Figure 2.2 shows the spectral amplitude of signal x(t) and some of its associated spectral features. The frequency features are calculated on the frequency spectrum of the signal $x(t)$ with the expressions as [Grosse and Ohtsu, 2008]:

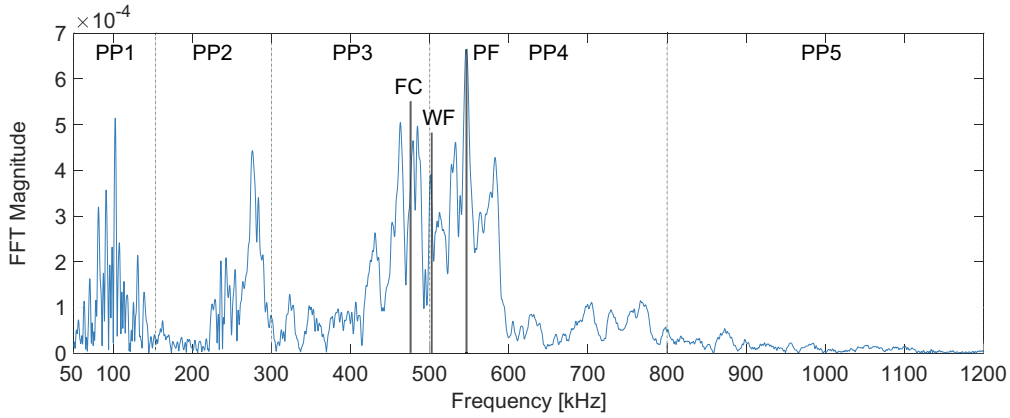

Figure 2.2: Extraction of features from AE signal $x(t)$ in frequency domain.

– Peak Frequency (PF) [kHz]: denoted as PF, which is the frequency corresponding to the maximum of amplitude on the spectrum.

– Frequency Centroid (FC) [kHz]: denoted as FC, it is the average frequency content of the signal expressed as:

$$\mathrm{FC} = \frac{\int_{-\infty}^{\infty} f \cdot |\hat{x}(f)| \, \mathrm{d}f}{\int_{-\infty}^{\infty} |\hat{x}(f)| \, \mathrm{d}f}, \tag{2.5}$$

where for each point of the frequency spectrum, f is the frequency value and $|\hat{x}(f)|$ is the amplitude of spectrum.

– Weighted Frequency (WF) [kHz]: denoted as WF, which is square root of Frequency Centroid and Peak Frequency multiplication, with expression as:

$$\mathrm{WF} = \sqrt{\mathrm{PF} \times \mathrm{FC}} \tag{2.6}$$

– Partial Power [%]: which is the fraction of power with different band of frequency in the band between 0 kHz and 1200 kHz with expression as:

$$\mathrm{PP_n} = \frac{\int_{f_d}^{f_f} |\hat{x}(f)|^2 \, \mathrm{d}f}{\int_{0Hz}^{1200kHz} |\hat{x}(f)|^2 \, \mathrm{d}f}, \tag{2.7}$$

where the number of band $n \in [1{:}5]$ and $|\hat{x}(f)|$ is the spectrum amplitude. They measure the signals frequency contribution within a given interval and are thus used to capture the frequency composition of the signal in more than a single characteristic value. Each Partial Power is computed with frequency range is:

– Partial Power 1 ($\mathrm{PP_1}$): $f_d = 0\,\mathrm{kHz}$; $f_f = 150\,\mathrm{kHz}$;

– Partial Power 2 ($\mathrm{PP_2}$): $f_d = 150\,\mathrm{kHz}$; $f_f = 300\,\mathrm{kHz}$;

– Partial Power 3 ($\mathrm{PP_3}$): $f_d = 300\,\mathrm{kHz}$; $f_f = 500\,\mathrm{kHz}$;

– Partial Power 4 ($\mathrm{PP_4}$): $f_d = 500\,\mathrm{kHz}$; $f_f = 800\,\mathrm{kHz}$;

– Partial Power 5 (PP_5): $f_d = 800\,\text{kHz}$; $f_f = 1200\,\text{kHz}$.

Based on the above-mentioned frequency features, many studies have been performed on the damage mechanisms of composite materials. Gutkin et al. [Gutkin et al., 2011] studied the AE signals in damaged carbon fiber reinforced plastics by using peak frequency analysis. In [Maillet and Morscher, 2015], Maillet and Morscher concluded that frequency centroid takes into account the whole frequency spectrum and as a result gives a finer image of signal's frequency content and is less sensitive than peak frequency to slight variations in the spectrum. In [Li et al., 2014] and [Li et al., 2015], Li et al. used weighted frequency as a frequency feature in the clustering analysis of woven glass fiber reinforced laminate composite. Indeed, in this thesis, for each AE signal, 15 features are computed as shown in Table 2.1.

No.	Features	Dimension	No.	Features	Dimension
1	Peak Amplitude (PA)	dB	9	Frequency Centroid (FC)	kHz
2	AE Energy (E)	aJ	10	Weighted Frequency (WF)	kHz
3	Duration (DU)	µs	11	Partial Power 1	
4	Rise time (RT)	µs	12	Partial Power 2	
5	Counts (CNTS)		13	Partial Power 3	
6	Average Frequency (AF)	kHz	14	Partial Power 4	
7	RA value (RA)	µs/V	15	Partial Power 5	
8	Peak Frequency (PF)	kHz			

Table 2.1: AE Features calculated from AE waveform.

Different works have shown that using AE features in the classification analysis of the AE signal is possible. Since AE signals in complex materials are transient, time-scale methods are used to determine new relevant features to be introduced in the classification process in order to improve the characterization and the discrimination of the damage mechanisms. [De Groot et al., 1995] studied AE signals through a short-time Fourier transform as frequency bands evolving in time, characteristic of each damage mechanism are determined during the tensile tests on carbon/epoxy materials. Marec et al. [Marec et al., 2008] used continuous and discrete wavelet transform to get time-scale features on AE signals of glass-fiber-reinforced plastic composite and they found a better discrimination of damage mechanisms than some time-based features. For this purpose, in section 2.2, the time-frequency analysis of AE signals will be introduced and discussed.

2.2 Time-frequency signal analysis

In this section, the AE signals will be represented in the time-frequency domain. The classification of AE signals to characterize damage is done conventionally from time and frequency features. However, the AE signals are non-stationary, the features resulting from the temporal or frequency analysis are insufficient for the study of damage (source characterization algorithms) in complex materials. Time-frequency features contain more information than time or frequency features [Hamstad et al., 2002, Marec et al., 2008]. The time-frequency features of AE signals can be evaluated using the wavelet transform. The wavelet analysis of AE signals makes it possible to define new features that are more relevant and effective for studying the damage mechanisms [Suzuki et al., 1996,

Ferreira et al., 2004]. The purpose of this part is to give a short introduction to the wavelets used in this study. The more general framework of time-frequency analysis will be presented, some of their main properties will be reminded and its application to AE signals will be shown in this section. First, subsection 2.2.1 presents the energy localization of a signal in time-frequency domain.

2.2.1 Energy localization in time and frequency

In signal processing, the total energy E_x of a signal $x(t)$ is defined as the area under the squared magnitude of the considered signal, expressed as follows:

$$E_x = \langle x(t), x(t) \rangle = \int_{-\infty}^{\infty} |x(t)|^2 \, \mathrm{d}t, \tag{2.8}$$

Parseval's theorem gives an alternate expression for the energy of the signal $x(t)$ in the frequency domain as:

$$E_x = \int_{-\infty}^{\infty} |x(t)|^2 \, \mathrm{d}t = \int_{-\infty}^{\infty} |\hat{x}(f)|^2 \, \mathrm{d}f, \tag{2.9}$$

where $\hat{x}(f)$ is the Fourier transform of $x(t)$ and $S_{xx}(f) = |\hat{x}(f)|^2$ is the spectral density of signal $x(t)$ [Daubechies, 1990].

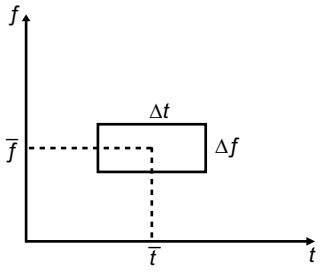

Figure 2.3: Localization of a signal in the time-frequency plane.

However, the energy E_x of signal $x(t)$ can be localized in the time-frequency plane. Figure 2.3 shows this energy localization. In this plane, the representation of the signal shows the localization of its energy in time and frequency [Auger and Flandrin, 1995]. The time location depends on the center time $\overline{t}$ and frequency location depends on the center frequency $\overline{f}$ which are given respectively by:

$$\overline{t} = \frac{1}{E_x} \int_{-\infty}^{\infty} t \, |x(t)|^2 \, \mathrm{d}t, \;\; \overline{f} = \frac{1}{E_x} \int_{-\infty}^{\infty} f \, |\hat{x}(f)|^2 \, \mathrm{d}f, \tag{2.10}$$

which means energy E_x is localized in time $\overline{t}$ and frequency $\overline{f}$. The time resolution Δt and frequency resolution Δf are defined respectively by:

$$\Delta t = \sqrt{\frac{1}{E_x} \int_{-\infty}^{\infty} (t - \overline{t})^2 \, |x(t)|^2 \, \mathrm{d}t}, \;\; \Delta f = \sqrt{\frac{1}{E_x} \int_{-\infty}^{\infty} (f - \overline{f})^2 \, |\hat{x}(f)|^2 \, \mathrm{d}f} \tag{2.11}$$

which presents the spread around $\overline{t}$ and $\overline{f}$. The representation of the signal in the time-frequency plane introduces a frequency dependence on time. The rectangle centered at $(\overline{t}, \overline{f})$, has a size $(2\Delta t \times 2\Delta f)$. This energy localization in time and frequency is the core of time-frequency analysis of signal [Shafi et al., 2009].

2.2.2 Short-time Fourier transform

Before the description of the Wavelet transform, there is another Fourier-related transform that represents signals in time and frequency domain. The short-time Fourier transform (STFT) overcomes the drawback of FT to some extent. It consists of multiplying a signal $x(t)$ with a short window function $w(t-\tau)$, centered at time τ in which the window shifts along with the signal duration with the same size of all frequency and computing the Fourier transform of product $x(t)w(t-\tau)$ [Rioul and Vetterli, 1991]. The expression of the STFT is:

$$\mathrm{STFT}_x(\tau, f) = \int_{-\infty}^{\infty} x(t)w(t-\tau)e^{-2\pi ift}\mathrm{d}t, \tag{2.12}$$

where the window function $w(t-\tau)$, is short relative to the signal duration. When the window function is Gaussian as:

$$w(t-\tau) = e^{-(t-\tau)^2}/\sigma, \tag{2.13}$$

with a constant σ, the STFT is also called Gabor transform. The analysis depends critically on the choice of window $w(t)$.

Spectrogram The STFT is defined as complex-valued functions and thus include both modulus and phase information. The spectrogram is defined as the energy distribution associated with the STFT, that is:

$$S(\tau, f) = \left|\mathrm{STFT}_x(\tau, f)\right|^2. \tag{2.14}$$

The spectrogram is based on the squared modulus of STFT that represents how the energy of signal $x(t)$ is distributed in the time-frequency plane. It means that the energy $x(t)$ is measured in position of (τ, f) but in a Heisenberg rectangle [Cohen, 1989]. Figure 2.4(a) shows that for a given window $w(t)$, the two Heisenberg rectangles centered at (t_1, f_1) and (t_2, f_2), have the same time resolution σ_t and frequency resolution σ_f with respective expressions as:

$$\sigma_t = \sqrt{\int_{-\infty}^{\infty} t^2|w(t)|^2\mathrm{d}t}; \quad \sigma_f = \sqrt{\int_{0}^{\infty} f^2|\hat{w}(f)|^2\mathrm{d}f}, \tag{2.15}$$

where the $\hat{w}(f)$ is the Fourier transform of $w(t)$ [Cohen, 1995, Mallat, 1999]. The time resolution σ_t and frequency resolution σ_f are independent of position of the Heisenberg rectangle. Thus, $w_{(t_1,f_1)}(t) = w(t-t_1)e^{2\pi f_1 t}$ corresponds to a Heisenberg rectangle of area $(\sigma_t \times \sigma_f)$ centered at (t_1, f_1), the same as $w_{(t_2,f_2)}(t)$ centered at (t_2, f_2).

There is a classical time-frequency resolution problem in time-frequency analysis, which underlies the structure of spectrogram because of the Heisenberg inequality:

$$\sigma_t\sigma_f \geq \frac{1}{4\pi}. \tag{2.16}$$

The choice of the window of short duration ensures a good time resolution but at the expense of a poor frequency resolution and vice-versa. It means that once an analyzing window has been chosen, the resolution capabilities of the spectrogram remain fixed for all time and frequency parameters (see Figure 2.4(a)).

2.2.3 Wavelet transform and continuous wavelet transform

The wavelet transform (WT) is a time-frequency representation of the signal that is described as a time-scale transform [Qi, 2000, Zitto et al., 2012]. The WT is an alternative to the STFT and has been applied in several areas, including data compression [Chang et al., 2000], image processing [Bovik, 2010], time-frequency spectral estimation and in the field of acoustic emission [Ni and Iwamoto, 2002]. The WT is useful in analyzing the frequency component of an AE signal as a function of time, denoising low-amplitude AE signals on the tensile test of cross-ply composite [Satour et al., 2014] and locate the source of AE signals in plate-type structures [Mostafapour et al., 2014]. Compared with the TF and the STFT, the WT is superior due to its ability to measure the time-frequency variations of a signal at different time-frequency resolutions. In [Tang, 2000], Tang et al. slated that in AE signal analysis, WT improves remarkably the ability to locate short time energy variation of AE signals while saving main frequencies characteristics.

A wavelet is a function ψ ($\psi(t) \in L^2(\mathbb{R})$) with zero average ($\int_{-\infty}^{\infty} \psi(t)dt = 0$), normalized ($\|\psi\| = 1$) and centered in the neighborhood of $t = 0$. Its Fourier Transform $\hat{\psi}(f)$ satisfies the admissibility condition as :

$$\int_0^{\infty} \frac{\left|\hat{\psi}(f)\right|^2}{f} \mathrm{d}f < \infty \tag{2.17}$$

which ensures the convergence of the integral in the reconstruction formula. Scaling ψ by a positive factor a and translating it by $b \in \mathbb{R}$, we define a family of time-frequency atoms, $\psi_{a,b}$, as

$$\psi_{a,b}(t) = \frac{1}{\sqrt{a}} \psi(\frac{t-b}{a}), a, b \in \mathbb{R}, a > 0. \tag{2.18}$$

These atoms remain normalized as $\|\psi_{a,b}\| = 1$. The variable a ($a \in \mathbb{R}$ and $a > 0$) is the scaling parameter who presents the scale and determines the dilation ($a > 1$) and compression ($a < 1$) of the wavelet $\psi(t)$. The variable b ($b \in \mathbb{R}$) is a translation parameter that allows to delay or advance the wavelet in time. The wavelet $\psi(t)$ can be called a mother wavelet.

Continuous Wavelet Transforms (CWT) is used to analyze non-stationary signals by using a time-scale representation of signal. For a given signal $x(t)$, its wavelet coefficients $\mathrm{CWT}_x(a, b)$ at time b and scale a is defined as its scalar product with the wavelet $\psi_{a,b}(t)$ as follows:

$$\mathrm{CWT}_x(a, b) = \langle x(t), \psi_{a,b}(t) \rangle = \frac{1}{\sqrt{a}} \int_{-\infty}^{\infty} x(t)\psi^*(\frac{t-b}{a})\mathrm{d}t. \tag{2.19}$$

It provides the frequency component of signal $x(t)$ corresponding to the scale a and time location b and $*$ represents the complex conjugate. Varying b for the fixed scale a, a wavelet is sliding with a fixed bandwidth B_a and with some fixed center frequency f_a along the analyzed signal $x(t)$.

The relationship between the scale a and the real frequency content at this scale of the particular analyzing wavelet is established by defining two frequency characteristics of mother wavelet [Mallat, 1999]:

– The center frequency:

$$f_0 = \int_0^\infty f \left|\hat{\psi}(f)\right|^2 \mathrm{d}f \tag{2.20}$$

– The Bandwidth $B_0 = \sigma_f$, centered around f_0, with:

$$\sigma_f = \sqrt{\int_0^\infty (f - f_0)^2 \left|\hat{\psi}(f)\right|^2 \mathrm{d}f} \tag{2.21}$$

For a wavelet at scale a, its center frequency (f_a) and the bandwidth (B_a) are respectively defined by following equations:

$$f_a = \frac{f_0}{a};\ \ B_a = \frac{B_0}{a} = \frac{f_{max} - f_{min}}{a}, \tag{2.22}$$

with $f_{max} = f_0 + B_0/2$ and $f_{min} = f_0 - B_0/2$. The large scales correspond to low frequencies of signals which present a global information of this signal, whereas small scales (high frequencies) correspond to a detailed information of the signal [Giurgiutiu, 2007].

When representing wavelet atoms $\psi_{a,b}(t)$ in the frequency domain, most of the energy is in the frequency interval of length $B_a = \sigma_f/a$, centered at $f_a = f_0/a$ or in the time domain around $b \in \mathbb{R}$ in the interval of length $a\sigma_t$ with the standard deviation σ_t defined by the following integral:

$$\sigma_t = \sqrt{\int_{-\infty}^\infty t^2 \left|\psi(t)\right|^2 \mathrm{d}t}. \tag{2.23}$$

With this definition, for every wavelet $\psi_{a,b}(t)$, the time-frequency resolution can be considered as a Heisenberg rectangle, which is centered at $(b, f_0/a)$ with the dimension of $a\sigma_t$ along the time axis and σ_f/a along the frequency axis. Its area $\sigma_t \times \sigma_f$ is independent of frequency or scale, and its sides represent time resolution and frequency resolution. For a fixed scale (or frequency), in the time direction, the time-frequency resolution is constant. For a fixed time, frequency resolution decreases (time resolution increases) as frequency increases (scale decreases) [Bialasiewicz et al., 2012].

Figure 2.4(b) shows that the resolution in time and frequency depends on different a. This illustration presents two atoms ψ_{a_1,b_1} and ψ_{a_2,b_2} ($a_2 > a_1$) and the variables b_1 and b_2 don't influence the resolution. When using the variable a_2, the wavelet covers greater temporal support of the signal making it possible to extract the long-term behavior of the signal and has a better frequency resolution. Conversely, the smaller variable a_1 presents the temporal support decreasing and allows to study local variations at high frequencies. Comparing with STFT which has a constant time-frequency resolution (see Figure 2.4(a)), this tunable time-frequency resolution of the CWT obviously suits for the analysis of signals containing shorts high-frequency components and extended low-frequency components, which is often the case for AE signals. For this reason, the CWT can reach better time-frequency resolution in AE analysis [Suzuki et al., 1996].

There are many admissible mother wavelets ψ, the choice of optimal mother wavelet depends on the local properties of the analyzed signal. In this thesis, the mother wavelet chosen for the analysis is a 'Complex Morlet wavelet'. This wavelet achieves the best compromise between time-resolution and frequency-resolution and it is widely used for detection and identification of transient AE events [Lin and Qu, 2000, Ni and Iwamoto, 2002].

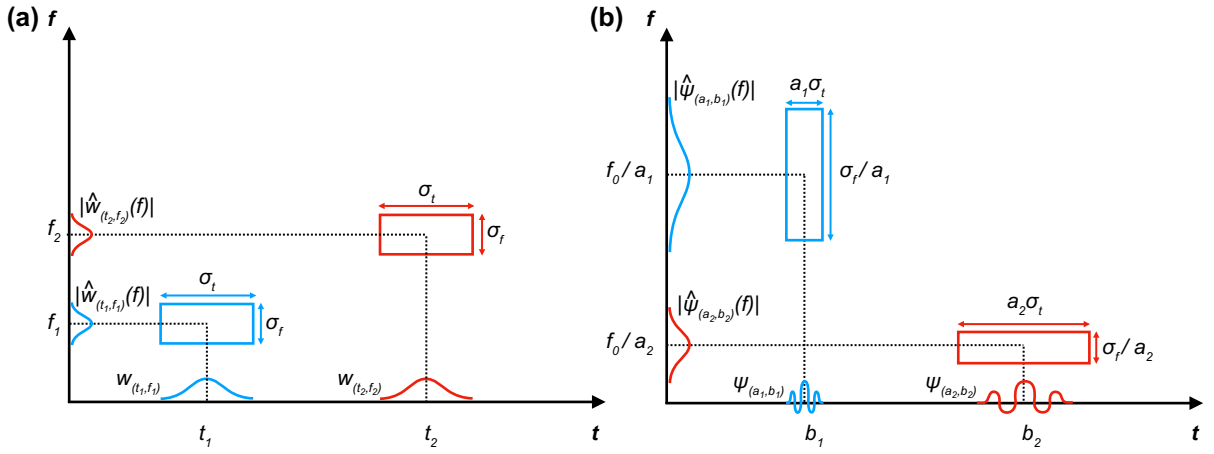

Figure 2.4: The time-frequency resolution of STFT and WT. (a) two Heisenberg rectangles of same window function in time-frequency plane. The two Heisenberg rectangles have the same resolution. (b) Heisenberg rectangles of two wavelets. Smaller scale (a_1) decreases the time spread but increases the frequency support, which is shifted toward higher frequencies.

The expression of complex Morlet Wavelet is:

$$\psi(t) = \frac{1}{\sqrt{\pi f_b}} e^{-(t^2/f_b)} e^{(2\pi j f_c t)}, \tag{2.24}$$

where f_c is the center frequency and f_b controls the decay in the time domain and the corresponding energy spread (bandwidth) in the frequency domain. Increasing f_b makes the wavelet energy more concentrated around the center frequency and results in slower decay of the wavelet in the time domain. Decreasing f_b results in a faster decay of the wavelet in the time domain and more energy spread in the frequency domain. The value of f_b does not affect the center frequency. When converting from scale to frequency, only the center frequency affects the frequency values. The energy spread or bandwidth parameter affects how localized the wavelet in the frequency domain [Teolis and Benedetto, 1998].

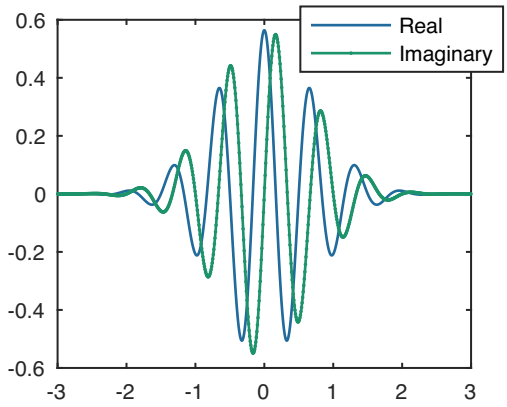

Figure 2.5: The real and imaginary parts of a complex Morlet wavelet.

The real and imaginary parts of a complex Morlet wavelet are shown in Figure 2.5. The CWT needs to be discretized for computation purposes, therefore, we have used a discrete version of CWT on Matlab thanks to its 'Wavelet toolbox' to compute the wavelet scalogram of the digital AE signals.

Wavelet scalogram A wavelet scalogram is a visual representation of the CWT of a signal, similar to a spectrogram created using a short-time Fourier transform (STFT). Similar to STFT, wavelet coefficients are also a complex-valued variables. The wavelet scalogram is defined as the squared modulus of the wavelet coefficients (see Equation 2.19), with the expression as [Rioul and Flandrin, 1992]:

$$\text{Scalogram} = |\text{CWT}_x(a,b)|^2\,, \tag{2.25}$$

while the scalogram represents the energy distribution of the signal $x(t)$ in the time-frequency plane.

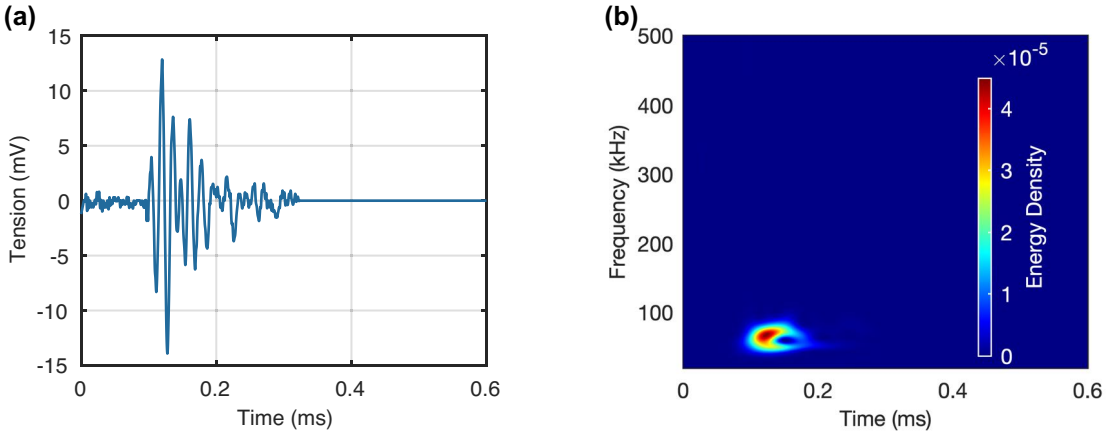

Figure 2.6: (a) Waveform of an AE signal and its (b) wavelet scalogram.

For an AE signal illustrated in Figure 2.6(a), its wavelet scalogram is displayed in Figure 2.6(b). This time-frequency distribution based on wavelet scalogram is clearly realized in different frequency components and time variations. Brightness and color can be used to indicate the energy distribution level of the AE signal, which has high energy distribution at 50 kHz with a duration of about 100 μs. In this case, the characteristics of the AE signal in time and/or frequency domain can be directly expressed by a two-dimensional representation as a wavelet scalogram. This time-frequency representation can also be considered as an image. This observation reminds us to use the wavelet scalogram to analyze AE data and in AE signal classification. A novel classification approach is proposed and discussed in section 2.6.

2.2.4 Discrete wavelet transform and decomposition analysis

The Discrete wavelet transforms (DWT) are defined by discretizing the variables a and b. Equation (2.26) presents the expression of DWT which is the projection of the signal $x(t)$ on a discrete wavelet basis.

$$DWT_x(j,k) = \int_{-\infty}^{\infty} x(t)\psi^*_{j,k}(t)dt, \tag{2.26}$$

and

$$\psi_{j,k}(t) = a_0^{-j/2}\psi(a_0^{-j}t - kb_0), j \in \mathbb{Z}, k \in \mathbb{Z}, \tag{2.27}$$

with j represents the scale and k represents the shift in time, $x(t)$ is the analyzed signal and $\psi(t)$ is the analyzing mother wavelet. Commonly, $a_0 = 2$ and $b_0 = 1$.

The main application of DWT in the AE domain is the wavelet decomposition of AE signals and Wavelet packet decomposition of AE signals. The signal passes through two filters and two signals are obtained, corresponding to the approximation (A) and the detail (D) coefficients of the first level [Sikorski, 2012]. The approximations are the high scale, low-frequency components of the signal. The details are the low scale, high-frequency components. Then, there are two methods:

– Wavelet decomposition: At the next decomposition level, the two filters are just applied to the resulting approximation coefficients and so on [Mallat, 1999].

– Wavelet packet decomposition [Antonini and Orlandi, 2001]: At the next decomposition level, approximation and detail signals resulting from the previous level are decomposed again that can be represented in the form of a tree [Maillet et al., 2014].

Figure 2.7 shows the two methods of decomposition performed on 3 levels. In the next subsection, some classical time-frequency features which depend on CWT and decomposition of signals by DWT presented in literature will be described.

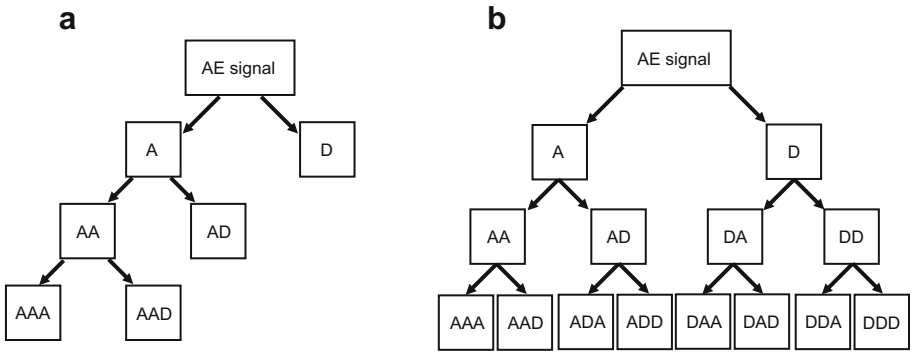

Figure 2.7: The decomposition tree on 3 levels: (a) Wavelet decomposition and (b) Wavelet packet decomposition.

2.2.5 Classical time-frequency features

In [Marec et al., 2008], Marec et al. proposed several scale-frequency features by using the CWT and DWT which were used in the classification of AE signals on glass fiber/polyester cross-ply composites and sheet molding compound (SMC). Morizet et al. [Morizet et al., 2016] used the wavelet packet decomposition to analysis the AE signals on corrosion. Here, a short review is shown of these existing time-frequency features.

– Feature 1 : The sum of the square modulus of CWT as

$$f_d(a, I_b) = \sum_b \left|\mathrm{CWT}_x(a, b)\right|^2, b \in I_b. \tag{2.28}$$

– Feature 2 : The maximum of the square modulus of CWT as

$$f_f(a, I_b) = \max \left|\mathrm{CWT}_x(a, b)\right|^2, b \in I_b. \tag{2.29}$$

Both two features are calculated for each scale (a) on a limited time duration I_b. This time duration is set from a new threshold which corresponds to a percentage of (10%) of

the maximum amplitude of the wavelet coefficient. Then the features corresponding to the most energetic scale are selected as new features.

– Feature 3 : By using the DWT, signal can be decomposed by different level of details and approximations. The maximum of the square detail coefficients for each level of decomposition as

$$f_3(j) = \max(\mathrm{DWT}_x(j,k)^2), \tag{2.30}$$

where $\mathrm{DWT}_x(j,k)$ are the detail coefficients of each level of decomposition j. Features f_d, f_f and f_3 are described in literature [Marec et al., 2008].

– Feature 4 : The wavelet packet energy which is the energy percentage of the terminal nodes of the wavelet packet tree is computed. In some literature leading to $2^3 = 8$ wavelet packet energy features [Maillet et al., 2014].

However, in this thesis, for AE data analysis, we use the wavelet scalogram to replace these conventional features. In fact, in a T-F representation, the wavelet scalogram has all the T-F information of a time-series signal. Various studies have already presented the potentiality of the wavelet scalogram in many domains [Jing and Hao, 2009, Van Drongelen, 2018, Lim et al., 2015]. For this purpose, we propose a method that combines the wavelet scalogram and the convolutional neural network (CNN) to classify the AE signals. The detail of this classification approach will be presented in the section 2.6.

2.3 Acoustic emission preprocessing

In AE analysis, the detected AE data need a pretreatment. In this section, according to our needs, we will introduce three preprocessing steps:

– 1. AE signal denoising by Modified Soft Thresholding Technique (MSTT).

– 2. AE features selection based on the Laplace Score (LS) analysis.

– 3. AE features optimization by using the Principal Component Analysis (PCA).

The first technique is used for AE signals detected from nonlinear measurements (Chapter 4) to improve the feature extraction results of low-energy signals. The other two processing techniques are important steps to improve cluster analysis of acoustic emission data in an unsupervised pattern recognition.

2.3.1 Acoustic emission signal denoising

During the measurements, AE hits were recorded by the AE system by using a fixed acquisition threshold. This threshold was set between 35 dB and 50 dB, depending on experiments and materials. This limitation is mainly due to the noisy experimental conditions, which makes signals obtained during the recording of AE hits usually mixed with noise. However, when we use a lower acquisition threshold, some low-amplitude AE signals can be recorded, which is related to the very weak energy emitted in materials. In Chapter 4, during the slow dynamics measurements, as the detected AE activity is low amplitude, the acquisition threshold needs to be very low to detect them. For this reason, we use the CWT denoising method which removes noise in the AE waveform while

retaining as much as possible the AE features. This denoising method called Modified Soft Thresholding Technique (MSTT) was proposed by Satour et al. [Satour et al., 2014].

The first step of the MSTT algorithm is gathering a set of real noise signals with a lower threshold (for example 20 dB). Different wavelet coefficients modulus taken from the collected real noise signals are calculated by using the CWT. Then these wavelet coefficients modulus of the noise signals are used to calculate an estimators as a coefficients matrix. The suppression of noise was carried out by means of MSTT on the basis of the wavelet coefficients calculated for the considered AE signal. Finally, denoised signals were obtained by the reconstruction process with the help of the inverse CWT. This MSTT algorithm is considered as the original AE signal $x(t)$ has the continuous wavelet transform $CWT_x(a,b)$ and this signal after denoising obtains a modified continuous wavelet transform $MCWT_x(a,b)$. The inverse CWT of $MCWT_x(a,b)$ give the denoised AE signal $x_d(t)$. The algorithm to compute the modified transform $MCWT_x(a,b)$ is considers as follows:

$$\begin{aligned}
&\textbf{if} \quad \{|CWT_x(a,b)| > T(a,b)\}, \textbf{then} \\
&\qquad MCWT_x(a,b) = (|CWT_x(a,b)| - T(a,b))e^{i\arg(CWT_x(a,b))} \\
&\textbf{else}, \\
&\qquad MCWT_x(a,b) = 0; \\
&\textbf{end}
\end{aligned} \tag{2.31}$$

In Equation (2.31), $T(a,b)$ is a noise threshold value associated with the wavelet coefficient located by parameters a and b in the time-scale plane. This threshold value is estimated using information extracted from CWT applied to several noise signal $n(t)$. If we denote $M_n(a,b)$ the modulus of the CWT of the noise signal $n(t)$, the $T(a,b)$ is given by expression:

$$T(a,b) = \alpha F([M_n(a,b)]), \tag{2.32}$$

where the function F is an estimator (average of $M_n(a,b)$) of the assumed random variable $M_n(a,b)$ obtained from numerous noise signal. Parameter α allows tuning the amount of noise to be removed through the denoising procedure.

In order to separate AE signals from noise signals, we need a coefficient which is denoted 'Spectral Flatness' [Johnston, 1988]. From the power spectral density of the digital signal $x(n)$, the spectral flatness is computed as the geometric mean (G_x) of the Fourier coefficients divided by its arithmetic mean (A_x).

$$\text{Flatness} = \frac{G_x}{A_x} = \frac{\sqrt[1/N]{\prod_{k=0}^{N-1} |X(k)|^2}}{\frac{1}{N}\sum_{k=0}^{N-1} |X(k)|^2} = \frac{\exp\left(\frac{1}{N}\sum_{k=0}^{N-1} \ln |X(k)|^2\right)}{\frac{1}{N}\sum_{k=0}^{N-1} |X(k)|^2}. \tag{2.33}$$

where $X(k)$ is computed with a FFT applied to the signal $x(n)$. A high value of spectral flatness means the energy is equally distributed along the spectrum of the signal (approaching 1.0 for white noise). The low values are obtained when the energy is concentrated in a small number of components of the spectrum [Painter and Spanias, 2000]. Since AE signals originate from the impulsive energy, the spectral flatness after denoising should be smaller.

2.3.2 Acoustic emission features selection

Feature selection is the process of extracting features that are beneficial to classification. 'Good features' means that objects of the same class have similar feature values while objects of different classes have different values. The goal of feature selection is to find a subset of parameters and eliminate irrelevant and redundant features while preserving relevant features, to improve clustering efficiency and quality. The existence of irrelevant features in data sets may reduce clustering quality and consume more memory and computation time. In addition, different subsets of related features may produce different clusters, which may help to discover different hidden information in AE data [Alelyani et al., 2018].

For unsupervised feature selection, there exist the following methods: maximum variance, Laplacian Score, spectral feature selection method, and multi-cluster feature selection method [Zhao and Liu, 2007]. Laplace Score (LS) is an advanced variance analysis that not only prefers those features with larger variances which have more representative power, but it also tends to select features with stronger locality preserving ability [He et al., 2006]. The basic idea of LS is to evaluate the features according to their locality preserving power [Benabdeslem and Hindawi, 2011]. A key assumption in LS is that data from the same class are close to each other. LS is fundamentally based on Laplacian Eigenmaps [Belkin and Niyogi, 2002] and Locality Preserving Projection [He and Niyogi, 2004].

Laplacian Score For AE analysis, d features collected from n AE signals are considered as a data group (or matrix) $\mathbf{X}_{(d\times n)}$, where $\mathbf{X} = [\mathbf{x}_1, \mathbf{x}_2, ...\mathbf{x}_n]$. In the Laplacian Score algorithm, n is the sample number, d is the dimension of features and $\mathbf{x}_i$ is the ith sample point. Therefore, the Laplacian Score can be computed by the following steps [He et al., 2006, Li et al., 2017]:

1. Constructing a nearest neighbor graph G: We collect between sample points $\mathbf{x}_i$ and $\mathbf{x}_j$ if $\mathbf{x}_i$ and $\mathbf{x}_j$ are 'close', i.e. $\mathbf{x}_i$ is among k nearest neighbors of $\mathbf{x}_j$ or $\mathbf{x}_j$ is among k nearest neighbors of $\mathbf{x}_i$ (normally $k = 5$).

2. Choosing the weights of $\mathbf{x}_i$ and $\mathbf{x}_j$: If sample points $\mathbf{x}_i$ and $\mathbf{x}_j$ are connected, the weight S_{ij} between $\mathbf{x}_i$ and $\mathbf{x}_j$ has the expression as:

$$S_{ij} = e^{-\frac{\left\|\mathbf{x}_i - \mathbf{x}_j\right\|^2}{t}}, \tag{2.34}$$

where t is a suitable constant (normally $t = 1$). Otherwise, we set $S_{ij} = 0$. The weight matrix $\mathbf{S}$ of the graph shows the local structure of the data space.

3. For the rth feature, we define $\mathbf{f}_r$ as:

$$\mathbf{f}_r = [f_{r1}, f_{r2}, \cdots, f_{rn}]^{\mathrm{T}}, \tag{2.35}$$

where f_{ri} is the rth feature in ith sample. And we define $\widetilde{\mathbf{f}}_r$ as:

$$\widetilde{\mathbf{f}}_r = \mathbf{f}_r - \frac{\mathbf{f}_r^{\mathrm{T}}\mathbf{D}\mathbf{1}}{\mathbf{1}^{\mathrm{T}}\mathbf{D}\mathbf{1}}\mathbf{1}, \tag{2.36}$$

where $\mathbf{D}$ is a diagonal matrix with $D_{ii} = \sum_j S_{ij}$ and $\mathbf{1} = [1, 1, \cdots, 1]^{\mathrm{T}}$.

Thus, the estimated variance of the rth feature $\mathbf{f}_r$ is computed as:

$$\mathrm{Var}\left(\mathbf{f}_r\right) = \sum_i \widetilde{\mathbf{f}}_{ri}^2 D_{ii} = \widetilde{\mathbf{f}}_r^{\mathrm{T}} \mathbf{D} \widetilde{\mathbf{f}}_r \tag{2.37}$$

4. Computing the Laplacian Score: makes $\mathbf{L} = \mathbf{D} - \mathbf{S}$, where the matrix $\mathbf{L}$ is called graph Laplacian. Then the Laplacian Score of the rth feature is:

$$L_r = \frac{\sum_{i,j} \left(f_{ri} - f_{rj}\right)^2 S_{ij}}{\sum_i \left(f_{ri} - \frac{1}{n}\sum_i f_{ri}\right)^2 D_{ii}} = \frac{\tilde{\mathbf{f}}_r^{\mathrm{T}} \mathrm{L} \tilde{\mathbf{f}}_r}{\tilde{\mathbf{f}}_r^{\mathrm{T}} \mathrm{D} \widetilde{\mathbf{f}}_r} \tag{2.38}$$

As shown in the references [Li et al., 2015, Carvelli et al., 2017], for AEanalysis, if the Laplace score of an AE feature is greater than 0.9, it can be considered as a 'good feature' and has the ability to cluster the AE signal. In most cases, the selected AE features may have still a large dimension and the dimension need to be reduced by feature optimization.

2.3.3 Acoustic emission features optimization

The features used for the cluster analysis should be relevant and limited in number. There are two main reasons for keeping the number of features as small as possible: measurement cost and classification accuracy [Momon et al., 2012]. The principal component analysis (PCA) algorithm is important before clustering. It is a mathematical method of data analysis that can reduce multidimensional data into lower dimensions which project them into a reduced space [Wold et al., 1987, Oja, 1989] and also improves the results, which is useful to visualize the data [Oskouei et al., 2012].

Principal component analysis In AE analysis, m features collected from n AE signals are the components of the n input vectors $\mathbf{x}_i$ $(i = 1, 2, ..., n)$. Each component includes AE signals information which represents this signal. The matrix population $\mathbf{X}$ $(n \times m)$ is composed of the n inputs $\mathbf{x}_i$ as:

$$\mathbf{X} = \begin{bmatrix} \mathbf{x}_1^{\mathrm{T}} \\ \mathbf{x}_2^{\mathrm{T}} \\ \vdots \\ \mathbf{x}_n^{\mathrm{T}} \end{bmatrix} = \begin{bmatrix} x_{1,1} & x_{1,2} & \cdots & x_{1,m} \\ x_{2,1} & x_{2,2} & \cdots & x_{2,m} \\ \vdots & \vdots & \ddots & \vdots \\ x_{n,1} & x_{n,2} & \cdots & x_{n,m} \end{bmatrix} = \left[\mathbf{X}_1, \mathbf{X}_2, ..., \mathbf{X}_m\right]. \tag{2.39}$$

The element $x_{i,j}$ represents the jth feature in the ith AE signal, symbol T represents the transpose of the vector and column vector $\mathbf{X}_j$ $(j = 1, 2, ..., m)$ includes all the variables of the jth feature [MacGregor and Kourti, 1995].

Based on the matrix $\mathbf{X}$, the algorithm of PCA will be presented in five steps:

1. Standardization: The data are first centered and reduced (the mean is null and the standard deviation is equal to unity for each column) by using expression as:

$$z_{i,j} = \frac{x_{i,j} - \overline{\mathbf{X}}_j}{\sigma_{\mathbf{X}_j}} \quad (i = 1, 2, ..., n; j = 1, 2, ..., m), \tag{2.40}$$

where $\overline{\mathbf{X}}_j$ is the mean of $\mathbf{X}_j$ and $\sigma_{\mathbf{X}_j}$ is the standard deviation of $\mathbf{X}_j$. The matrix $\mathbf{X}$ can be rewritten as a new matrix $\mathbf{Z} = (z_{i,j})_{n\times m}$. Once the standardization is done, all the variables will be transformed to the same scale.

2. Covariance matrix computation: In the base of matrix $\mathbf{Z}$, the covariance matrix $\mathbf{C}$ is calculated as [Shlens, 2014]:

$$\mathbf{C} = \frac{1}{n-1} E[\mathbf{Z}\mathbf{Z}^{\mathrm{T}}], \tag{2.41}$$

where the symbol T represents the transpose of matrix and $E[\,]$ is the expected value. The components of $\mathbf{C}$, denoted by $c_{kl}(k = 1, 2, ..., m$ and $l = 1, 2, ..., m)$ represents the covariances between the column vectors $\mathbf{Z}_k$ and $\mathbf{Z}_l$:

$$\mathbf{Z}_k = \begin{bmatrix} z_{1,k} \\ z_{2,k} \\ \vdots \\ z_{n,k} \end{bmatrix}, \quad \mathbf{Z}_l = \begin{bmatrix} z_{1,l} \\ z_{2,l} \\ \vdots \\ z_{n,l} \end{bmatrix}. \tag{2.42}$$

3. Eigenvectors and eigenvalues of the covariance matrix calculation : As the covariance matrix is a symmetric matrix, an orthogonal basis can be calculated by finding its eigenvalues and eigenvectors. Using the expression:

$$|\mathbf{C} - \lambda I| = 0, \tag{2.43}$$

the eigenvalues of matrix $\mathbf{C}$ are calculated as λ_k $(k = 1, 2, ..., m)$. The eigenvalues are sorted from big to small as $\lambda_1 \geq \lambda_2 \geq .. \geq \lambda_m$ and the eigenvectors $\mathbf{u}_k(m \times 1)$ are the solutions of the equation:

$$\mathbf{C}\mathbf{u}_k = \lambda_k \mathbf{u}_k, \quad k = 1, 2, ..., m. \tag{2.44}$$

4. Variance estimation: For each component $(k = 1, 2, ..., m)$, it is possible to calculate the variances in percentages α_k of component k and cumulative percentages β_k as:

$$\alpha_k[\%] = \frac{\lambda_k}{\sum_{i=1}^{m} \lambda_i} \times 100, \tag{2.45}$$

$$\beta_k[\%] = \frac{\sum_{i=1}^{k} \lambda_i}{\sum_{i=1}^{m} \lambda_i} \times 100. \tag{2.46}$$

5. An ordered orthogonal basis can be created with the first eigenvectors having the direction of the largest variances of the data [Jolliffe, 2011]. Thus, directions in which the data set has the most significant amounts of energy can be found. Instead of using all the eigenvectors of the covariance matrix, we may represent the data in terms of only first several most representative eigenvectors. If $\mathbf{A}_k$ $(m \times k)$ has the first k eigenvectors (normally $\beta_k \geq 90\%$), by transforming the standardization data matrix $\mathbf{Z}$, we obtain:

$$\mathbf{Y} = \mathbf{Z}\mathbf{A}_k, \tag{2.47}$$

where matrix $\mathbf{Y}$ $(n \times k)$ represents n AE signals in k-principal components base and it contains more than 90 % of the standard deviation of the original data $\mathbf{X}$. It means that the remaining principal components could be neglected without losing information (less than 10%) by reducing the dimension of data. It is an effective and useful multivariate

analysis method which is usually used to reduce dimension of a large data set to enable better analysis.

As an example, several AE signals are selected with three features (amplitude, duration and rise time) that have been computed. Figure 2.8(a) shows the AE data representation in 3D, each point presents one AE signal. Figure 2.8(b) shows the PCA visualization of the two uncorrelated features (PC1 and PC2) of these AE signals. As can be seen, the two principal components contain 91.8% ($\beta_k = 91.8\%$) of the standard derivation of the original data, meaning the losing information is acceptable. This PCA projection shows that the distribution of the data does not overlap. Thus, the clustering of the AE signals is based on the two uncorrelated features. This unsupervised clustering approach will be detailed in the next section.

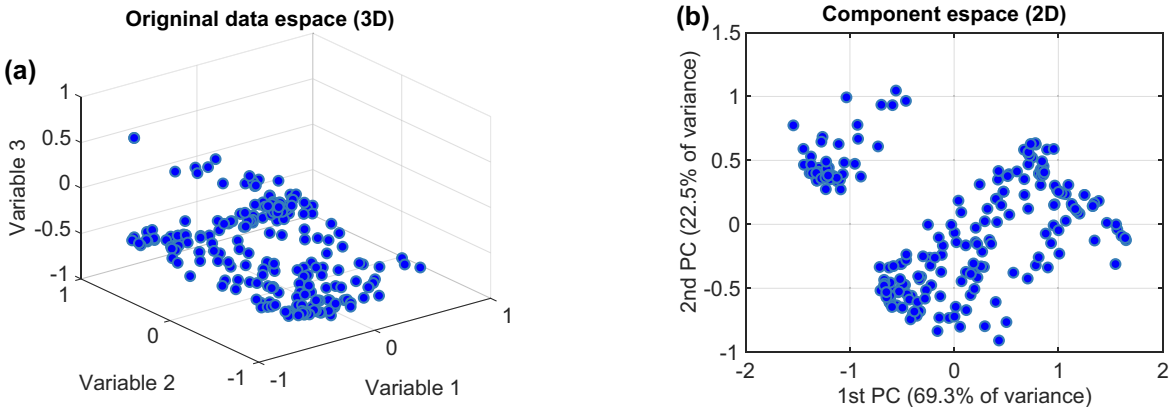

Figure 2.8: (a) Original AE data representation. (b) 2D PCA visualization of the AE data.

In this thesis, the PCA is used as a feature optimization procedure in Chapter 3 and Chapter 4. The AE features is applied by PCA and several principal components (based on $\beta_k \geq 90\%$) as new uncorrelated features will be used as input of cluster analysis.

2.4 Cluster analysis of acoustic emission data

In AE analysis, the main challenge is to find the relationship between AE events and corresponding damage mechanisms. This means discovering the grouping of AE signals in the clusters. The signals in each cluster, having certain similarities, can be corresponded to the same damage mechanisms. When detected AE signals are not labeled, the unsupervised clustering algorithm needs to be used. As we know, the most used methods are k-means [Pashmforoush et al., 2012, Assarar et al., 2015, Li et al., 2016], Self-Organized Map [Huguet et al., 2002, Godin et al., 2004] and fuzzy-C means [Marec et al., 2008]. In this study, we choose k-means as the clustering algorithm. In this section, the algorithm of k-means will be introduced in subsection 2.4.1. In addition, the determination of the relevant number of clusters requires the cluster validity indices, which will also be discussed in subsection 2.4.2.

2.4.1 k-means clustering algorithm

The k-means algorithm was first proposed at the 1950s and is still one of the most widely used algorithms for unsupervised clustering in data analysis. Ease of implementation, simplicity, efficiency, and empirical success are the main reasons for its popularity [Jain, 2010]. The aim of the k-means method is to minimize the sum of squared distances between all the input vectors of a cluster and its centre [Likas et al., 2003]. This method assumes the cluster number k to build known and specified in advance. The k-means algorithm is introduced by using a simple example.

k-means algorithm To cluster a set of n input vectors $\mathbf{x}_j$ $(j = 1, 2, ..., n)$ into k clusters $(C_1, C_2, ..., C_k)$ that $\mathbf{c}_i$ $(i = 1, 2, ..., k)$ is the mean of cluster C_i, algorithm has four steps which are:

1. Initialize the clusters centers $\mathbf{c}_i$ in a random way.

2. Compute the distance between the centers $\mathbf{c}_i$ and every input vector $\mathbf{x}_j$ and attribute each input vector to the closest cluster.

3. Recompute the location of the clusters centers basing on mean of the input vector in each cluster, so that error function (Equation (2.48)) is minimized.

$$E = \sum_{i=1}^{k} \sum_{x_j \in C_i} \|\mathbf{x}_j - \mathbf{c}_i\|^2. \tag{2.48}$$

4. Repeat steps 2 and 3 until Equation (2.48) converge and the centers location do not change.

In Equation (2.48), $\|\cdot\|$ is the Euclidean distance. Figure 2.9 shows an illustration of the k-means algorithm on a 2D data with two clusters.

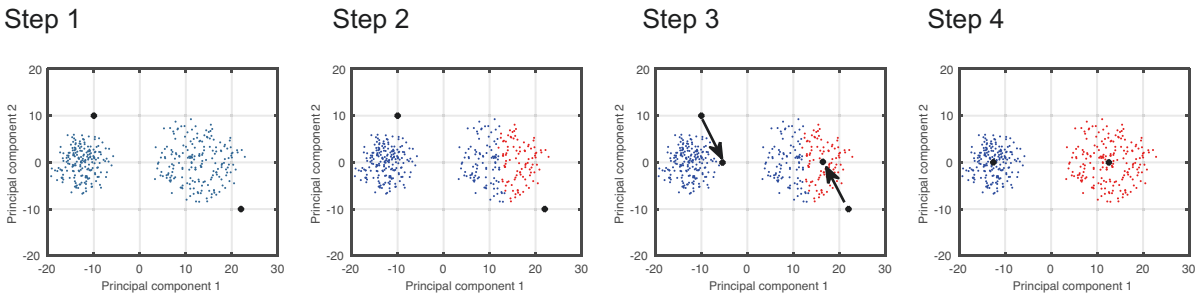

Figure 2.9: Illustration of k-means algorithm.

2.4.2 Cluster validity indices

The number of clusters chosen depends on some cluster validity indices. The most used in the AE literature are Davies-Bouldin (DB) index and the Silhouette coefficient (SC). The optimal cluster number has the lower Davies-Bouldin index and the higher Silhouette coefficient [Sause et al., 2012a, Sibil et al., 2012].

Davies-Bouldin index The Davies-Bouldin (DB) index [Davies and Bouldin, 1979] is a function of the ratio of the sum of within-cluster scatter to between-cluster separation which is defined as:

$$DB = \frac{1}{k}\sum_{i=1}^{k}\max_{j\neq i}\left\{\frac{d_i + d_j}{D_{ij}}\right\} \tag{2.49}$$

where k is the number of clusters, d_i and d_j are the average within-cluster distances of clusters i and j respectively, D_{ij} denotes the distance between the centers of the ith and jth cluster. To understand Equation (2.49), variable d_i is defined as:

$$d_i = \sqrt{\frac{1}{M_i}\sum_{j=1}^{M_i}|\mathbf{x}_j - \mathbf{c}_i|^2} \tag{2.50}$$

where $\mathbf{c}_i$ is the center of cluster C_i, $\mathbf{x}_j$ is the input vector assigned to cluster C_i and M_i is the size of the cluster C_i (number of input vectors in the cluster C_i). The variable d_j has the same expression. The variable D_{ij} is the Euclidean distance between two centers $\mathbf{c}_i$ and $\mathbf{c}_j$. The lower is the DB index, the better is the compactness and the separability.

Silhouette Coefficient The Silhouette Coefficient (SC) [Rousseeuw, 1987] has a value between 0 and 1, the higher score relates the clusters are dense and well separated which is used as the second measure of clustering quality. For k clusters, if $\mathbf{x}_i$ is in the cluster C_a ($a \in [1, 2, ..., k]$), $A(i)$ is the average distance between $\mathbf{x}_i$ and all other data vectors in the same cluster with expression as:

$$A(i) = \frac{1}{M_a - 1}\sum_{j\in C_a, j\neq i}\|\mathbf{x}_i - \mathbf{x}_j\| \tag{2.51}$$

where M_a is the number of vectors in cluster C_a. It is possible to interpret $A(i)$ as a measure of how well $\mathbf{x}_i$ is assigned to its cluster (the smaller the value, the better the assignment). The variable $B(i)$ is the smallest average distance between the vector $\mathbf{x}_i$ and vectors in another cluster C_b which has expression as:

$$B(i) = \min_{a\neq b}\frac{1}{M_b}\sum_{j\in C_b}\|\mathbf{x}_i - \mathbf{x}_j\| \tag{2.52}$$

where M_b is the number of vectors in cluster C_b. For one vector $\mathbf{x}_i$, its silhouette value is defined as:

$$S(i) = \frac{B(i) - A(i)}{\max\{A(i), B(i)\}} \tag{2.53}$$

The solution quality can be represented either by the average silhouette value for each cluster or by the average silhouette value of the entire clustering solution composed of k clusters, denoted SC and calculated as follows for a data set of n vectors:

$$SC = \frac{1}{n}\sum_{i=1}^{n}S(i). \tag{2.54}$$

The number k is chosen for each test and its average silhouette SC is computed. A SC value greater than 0.6 generally assures that the clustering is of sufficient quality [Gutkin et al., 2011].

With the lower Davies-Bouldin index and higher Silhouette coefficient, the optimal cluster number can be confirmed. In AE analysis, the chosen features are normalized and the PCA is used to reduce the dimension. The relevant number of principal components are used as the input vectors of the k-means algorithm so that AE signals are grouped into confirmed number of clusters.

We continue the mentioned example shown in subsection 2.3.3, AE data are represented by two principal components as inputs of the k-means algorithm, which is shown in Figure 2.10(a). Figure 2.10(b) shows the Davies-Bouldin (DB) index and the Silhouette Coefficient (SC) with different numbers of clusters.

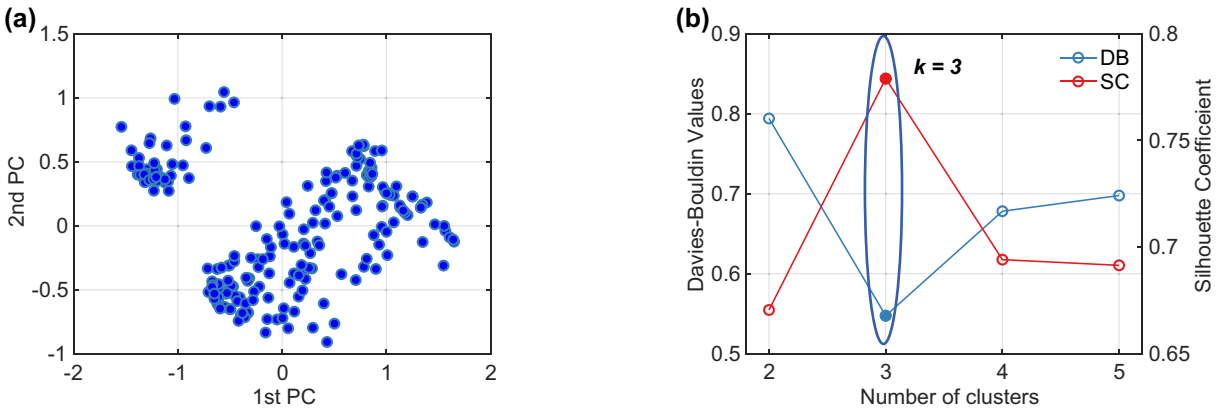

Figure 2.10: (a) 2D presentation of AE data as input of k-means algorithm. (b) Davies and Bouldin index and the Silhouette Coefficient of AE data for k-means algorithm.

The optimal clustering is obtained with ($k = 3$) according to the minimum values of the DB index and the maximum of SC. The k-means clustering algorithm is therefore applied to AE data with three clusters. Figure 2.11 depicts the projection of the two clusters of AE signals to the two-dimensional plot by two principal components. These

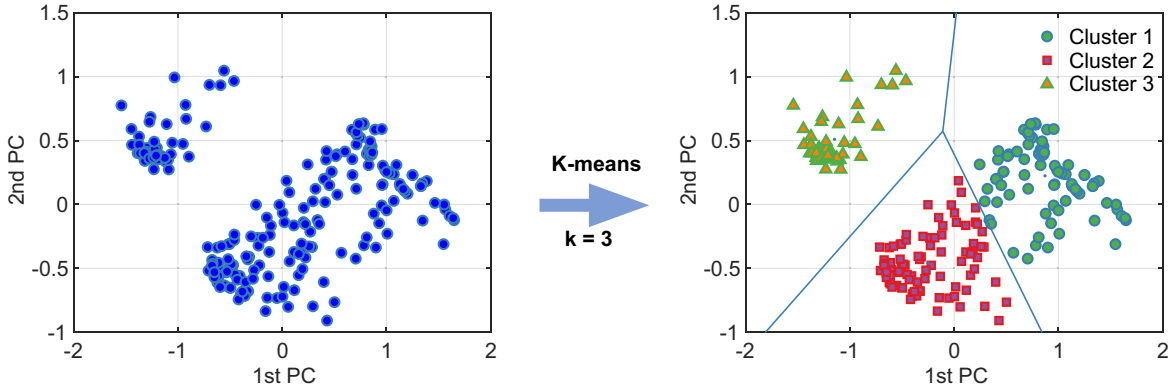

Figure 2.11: Illustration of 2D AE data applied by k-means clustering algorithm with three clusters.

results clearly show that the PCA-based k-means clustering algorithm has good ability of unsupervised clustering. However, the data between clusters 1 and 2 need to be carefully treated because of the cluster analysis groups the data in a mathematical way. Therefore, the clustering results include uncertainty and need observation validation.

2.5 Unsupervised pattern recognition methodology

In this thesis, in order to associate AE signals with damage mechanisms, we use unsupervised pattern recognition to cluster AE signals. The goal of the unsupervised pattern recognition method is to create an automatic technique to select promising feature combinations for unsupervised clustering of detected AE signals. The visualization of the complete method is shown as a flow diagram in Figure 2.12. This method comprises four steps:

AE feature extraction AE signals are represented by the time domain features and the frequency domain features as an AE dataset (15 features as shown in Table 2.1).

Data preprocessing First, the AE dataset is normalized between 0 and 1, giving the same weight to all features. Then the appropriate features are selected by using the Laplacian Score (LS) and the AE dataset transformed into the selected feature dataset. The selected feature dataset may still have a large dimension which is subjected to the principal component analysis (PCA) algorithm to reduce the dimension. In addition, the computed principal components are uncorrelated as features that may improve the clustering results.

Unsupervised cluster analysis Finally, the principal component dataset is used as input of the k-means algorithm. The number of clusters is chosen by two cluster validity indices: the Davies-Bouldin (DB) index and the Silhouette coefficient (SC). The optimal cluster number (k) is confirmed by the lowest DB index and the highest SC value. Then applied by the k-means algorithm, the dataset is clustered into k clusters.

Cluster identification In addition, the validation of clustering results and damage mechanism identification needs to be further confirmed. This work is focused on comparing the AE features and/or wavelet scalogram of AE signals from different clusters which are shown in Chapters 3 and 4.

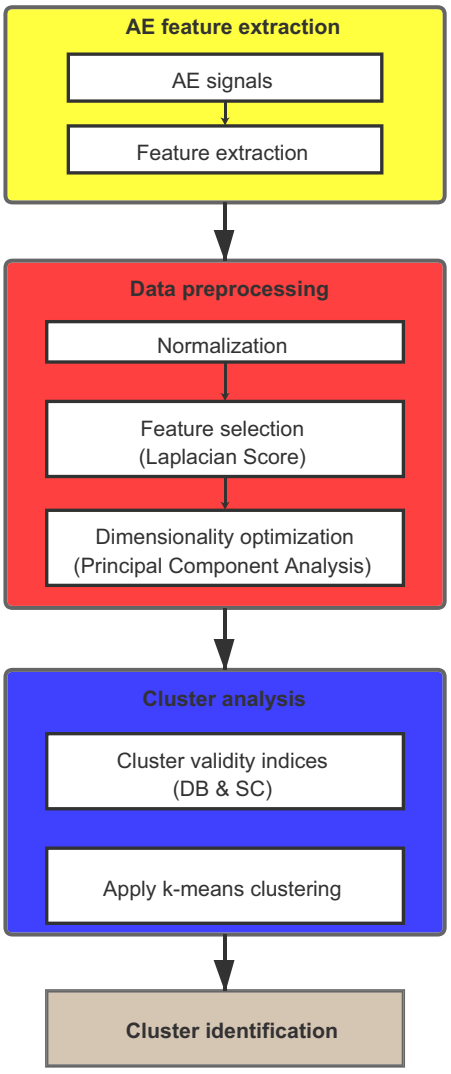

Figure 2.12: Flowchart of the unsupervised pattern recognition process.

2.6 Image-based acoustic emission data classification

2.6.1 Introduction

In this section, we introduce an acoustic emission (AE) data classification algorithm combining continuous wavelet transform (CWT) and convolution neural network (CNN). The CWT has the ability to create a time-frequency representation of AE signals, which contains detailed information of the signals and effectively captures relevant frequency components. Moreover, this time-frequency representation can be treated as an image (AE image). Meanwhile, artificial intelligence (AI) and machine learning (ML) technology are developing rapidly, especially the application of deep learning (DL) in computer vision, which has made giant progress in recent years.

Convolutional neural network (CNN) [Krizhevsky et al., 2012, Zeiler and Fergus, 2014] is the core of the recent noticeable progress in deep learning which is most commonly applied to analyze visual imagery. For this reason, we can use CNN to extract deep features from these AE images and classify the corresponding AE signals. In the field of biology, in order to classify human electrocardiogram (ECG) signals, some similar algorithms have been proposed and a CNN architecture has been designed [Acharya et al., 2017]. Qian et al. [Qian et al., 2016] used sounds' spectrogram and DL for multi-feature classification of the excitation location of snoring sounds in the upper airway which is helpful for the diagnosis of obstructive sleep apnea (OSA). To correct the identification of the fundamental heart sounds, Meintjes et al. [Meintjes et al., 2018] used the CWT and CNN. In some acoustic studies, such as [Gwardys and Grzywczak, 2014], Gwardys and Grzywczak used frequency spectrograms of music track as images and to train their CNN model. In [Valenti et al., 2017], a novel application of CNN for the task of acoustic scene classification (ASC) was presented which was based on the STFT and a deep CNN. Guan et al. proposed an intelligent acoustic signal processing system based on deep neural networks that integrate four working modes (perform acoustic scene classification, audio tagging, and rare sound event detection) together [Guan et al., 2018]. In addition, Chen et al. [Chen et al., 2018] proposed an approach to learn audio scene patterns from wavelet scalogram.

To sum the above up, many similar methods have been done, which give us some enlightenment. In this study, continuous wavelet analysis (CWT) and convolutional neural network (CNN) are integrated together for AE data classification. This section includes five main parts: I. AE image representation; II. Introduction of CNN; III. AlexNet architecture; IV. Transfer learning algorithm; V. CWT and CNN-based AE signal classification.

2.6.2 Acoustic emission image representation

In this study, we seek to extract the time-frequency information which is hidden in AE signals by using continuous wavelet transform (CWT). The classical time-frequency representation is the wavelet scalogram, which is the squared modulus of the continuous wavelet transform (CWT). Wavelet scalogram represents the local energy density of a signal by using different colors. However, for two different signals, their wavelet scalogram is incomparable because the same color shows different magnitudes in different wavelet scalogram (see Figures 2.13(a) and (c)). In order to compare different acoustic emission

signals, each wavelet scalogram uses the same color scale bar. For this reason, each color presents the same magnitudes in different wavelet scalogram. Each detected AE signal has different intensity, signals have tension levels from 1 mv to 10 V. To cover this huge range ($\sim 1 \times 10^4$), the traditional resolution of the color scale bar is not enough. Hence, a novel representation is used in this study. The methodology consists in transforming the magnitude of wavelet coefficients modulus in dB and using the same color scale bar of intensity values between 20 dB (smallest sensitivity of the AE system) and 100 dB for each AE signal.

Figure 2.13 shows two AE signals and their wavelet scalogram, which are based on complex Morlet Wavelet and their AE image representations. In Figures 2.13(a) and 2.13(c), each wavelet scalogram have its own color scale bar. However, in the AE image, each signal has the same range of color scale bar which makes two images comparable. Figure 2.13(b) shows that AE signal $s_1(t)$ has a high energy distribution around 50kHz with a duration around 100 μs which show the information of scalogram. In Figure 2.13(d), the AE image shows two high energy distributions around 350 kHz and 100 kHz, which have different durations. Comparing two AE images, different brightness and colors can be used to indicate the energy level of each signal. In summary, the visualization in AE image representation is very useful to analyze the AE signals. This type of representation (AE image) will be used in our work.

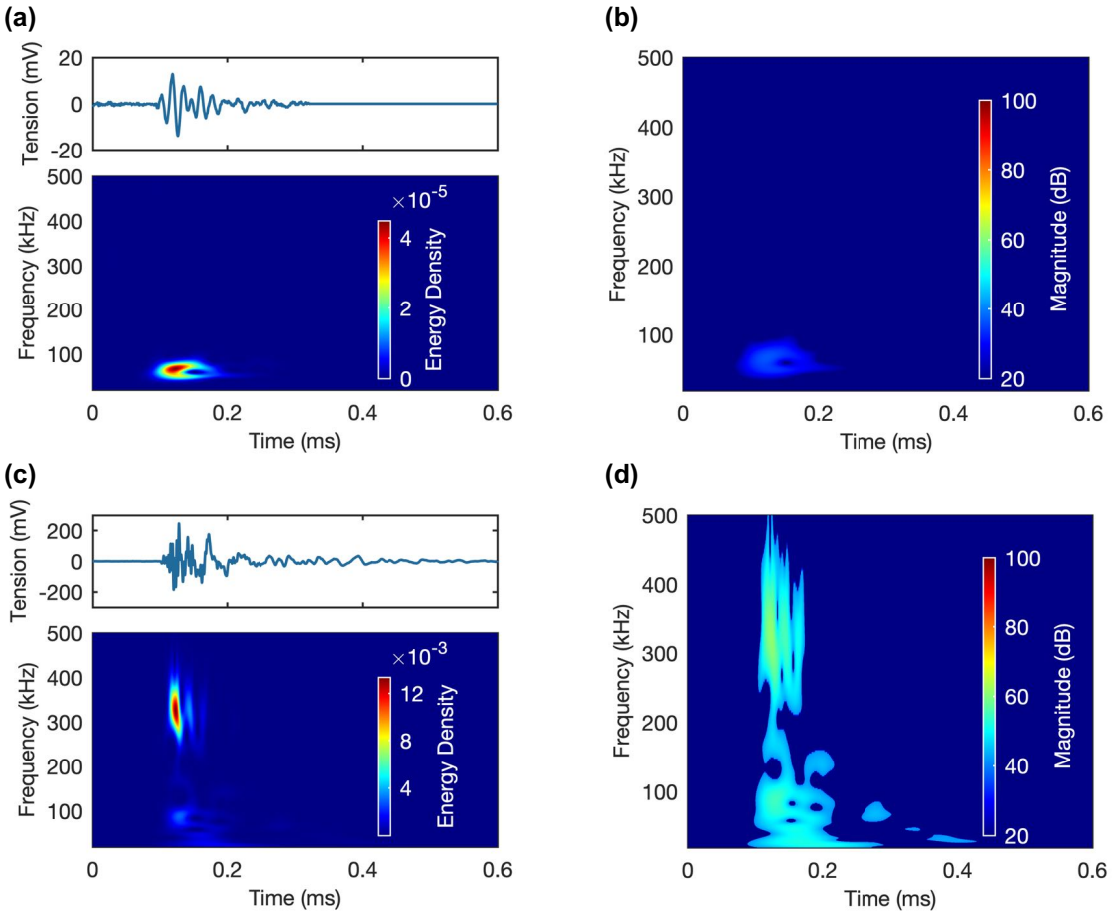

Figure 2.13: (a) AE signal $s_1(t)$ with its wavelet scalogram and (b) its AE image representation. (c) AE signal $s_2(t)$ with its wavelet scalogram and (d) its AE image representation.

2.6.3 Deep convolutional neural network

In this subsection, some theoretical background and developments of artificial neural network (ANN) and convolutional neural network (CNN) will be presented. The CNN is one of the most commonly used types of ANN for image classification [Goodfellow et al., 2016]. As a supervised deep neural network, CNN has multiple hidden layers and needs to be trained in a robust manner [Géron, 2019]. Generally, CNN architectures consist of convolutional layers, pooling layers, either one or more fully connected layers, as in a standard feedforward neural network [LeCun et al., 2015].

Figure 2.14 illustrates typical CNN architecture for an image classification task. An image is an input to the network, and this is followed by several stages of convolution and pooling. Thereafter, representations from these operations feed one or more fully connected layers. Finally, the last fully connected layer outputs the corresponding class label.

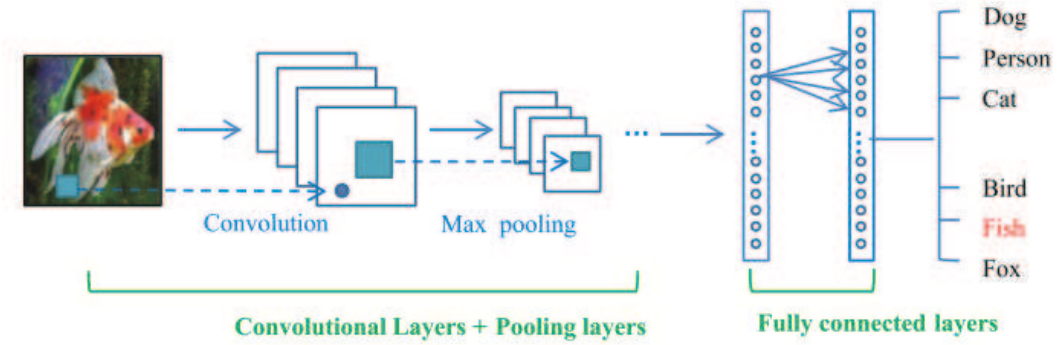

Figure 2.14: The pipeline of the general CNN architecture.[Guo et al., 2016]

Different kinds of layers play different roles. Here, we take the famous LeNet-5 as an example to introduce the main layers in the CNN architecture, because the basic components of numerous variants of CNN architectures are very similar [Nielsen, 2015].

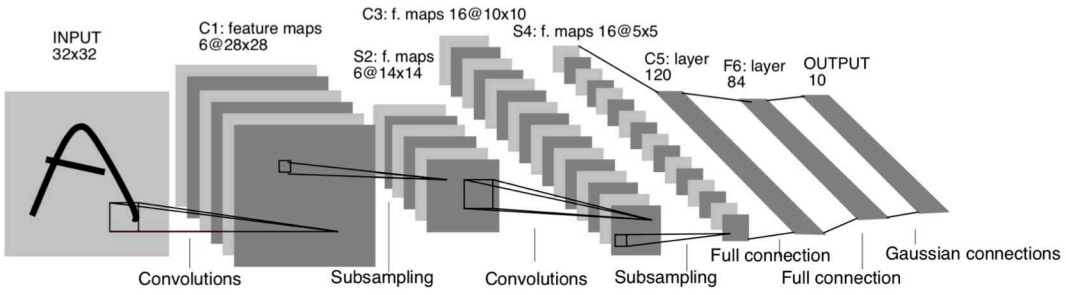

Figure 2.15: The architecture of the LeNet-5 network, which works well on digit classification task. [LeCun et al., 1998]

Convolutional layer The convolutional layers aim to serve as features extractor, they can feature the representations of the input images [Nielsen, 2015, Schmidhuber, 2015]. Normally, a convolution layer is composed of several convolution kernels (likes filters), which are used to compute different feature maps (see Figure 2.16(a)). For the LeNet-5,

the input image (32×32 pixel) has the dimension of 32×32×1 (Height×Breadth×Number of channels, eg. RGB). It means that the input layer has as a 32×32×1 square of neurons, the first hidden layer $C1$ is a convolution layer with 6 different kernels, each kernel has 25 neurons which are called 'local receptive field' with the dimension of 5×5×1. The kernel resembles a little window on the input pixels. The kernel is fielded across the entire input image, which begins on the top-left corner. Stride (S) controls how does the kernel field. When the stride is 1, then the kernel is moved by one pixel at a time to the right and up to down (i.e., by one input neuron). The dimension of the feature map can be calculated with the expression as follows:

$$D = \frac{W - K + 2P}{S} + 1, \tag{2.55}$$

where W is the input volume size, K is the kernel size and P is the number of zero paddings used on the border. For LeNet-5 (see Figure 2.15), $W = 32$, $K = 5$ and $P = 0$, if $S = 1$, the dimension of the feature map is 28. In some cases, setting zero padding to be $P = (K - 1)/2$ when the stride $S = 1$ ensures that the input volume and feature map will have the same size spatially. The complete feature maps are obtained by using several different kernels. Mathematically, the feature value at location (i, j) in the kth feature map ,$z_{i,j,k}$ is calculated by:

$$z_{i,j,k} = \sigma({\mathbf{w}_k}^T \mathbf{x}_{i,j} + b_k). \tag{2.56}$$

Here, σ is the neural activation function (as sigmoid, tanh and ReLU...), $\mathbf{w}_k$ and b_k are the weight vector and bias terms of the kth kernel and $\mathbf{x}_{i,j}$ is the inputs path center at location (i, j). For one feature map, we use the same bias to save time. The aim of the activation function (σ) is to introduce nonlinearities to CNN, which are desirable for multi-layer networks to detect nonlinear features.

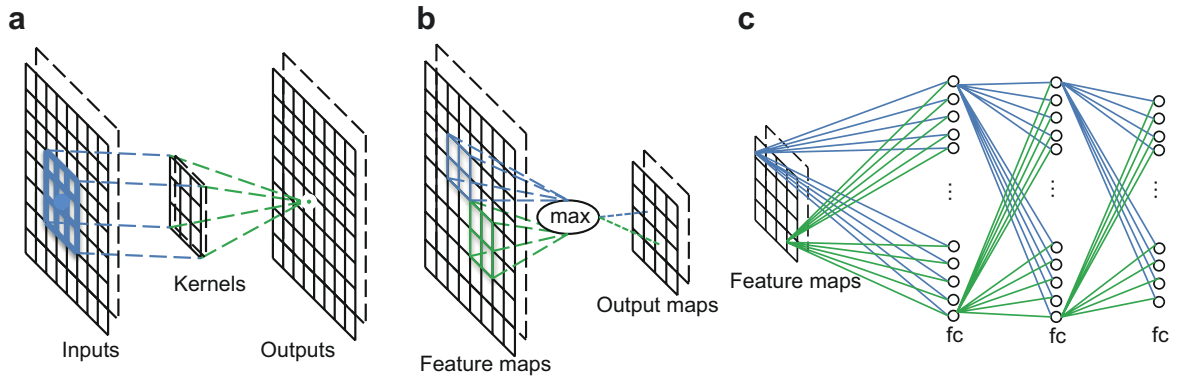

Figure 2.16: (a) The operation of a convolutional layer, the kernel has a local receptive field of 3 × 3. (b) The operation of the max pooling layer. (c) Features maps connect with three fully-connected layers. [Guo et al., 2016]

Pooling layer Generally, a pooling layer follows a convolutional layer and can be used to reduce the dimensions of feature maps and network parameters, which will simplify the information in the output from the convolutional layer (Sub-sampling layer in Figure 2.15). In detail, a pooling layer takes each feature map output from the convolutional layer and prepares a condensed feature map. For instance, each unit in the pooling layer may

summarize a region of 2×2 neurons in the previous layer. The pooling technique can include the max pooling, the average pooling and the L2 pooling (square root of the sum of the squares of the activation). Figure 2.16(b) gives an example of a max-pooling process. In max-pooling, a pooling unit simply outputs the maximum activation in the 2×2 input region. For LeNet-5, the features maps of $C1$ were reduced to 14×14 dimensions with a max-pooling operator which has size 2×2 and stride 2.

Fully-connected layers Generally, following the last pooling layer in the network, there are several fully-connected layers converting the 2D feature maps into a 1D feature vector, for further feature representation (see Figure 2.16(c)). Fully-connected layers perform like a traditional neural network and contain about 90% of the parameters in this CNN architecture. It enables us to feed forward the neural network into a vector with a predefined length. For LeNet-5, $F6$ is a real fully-connected layer, which has 84 neurons and each neuron is connected with 120 neurons of layer $C5$. With the tanh activation function (see Figure 2.18(b)), the output of this layer is connected with the output layer with 10 neurons. This output layer is a fully-connected layer, its 10 neurons are labeled '0' to '9'. For LeNet-5, its output layer is composed of Euclidean Radials Basis Function units (RBF). The output of each RBF unit y_i is computed as follows:

$$y_i = \sum_j (x_i - w_{ij})^2, \tag{2.57}$$

where x_i is the input vector and w_{ij} is the parameter vector, meaning that each output BRF unit computes the Euclidean distance between its input vector and its parameter vector.

Supervised learning In general, the network needs to be trained by a large number of labeled datasets in a supervised manner. The training network has two stages: the forward stage and the backward stage [Gu et al., 2018]. First, the main goal of the forward stage is to represent the input image with the current parameters (weights and bias) in each layer then get the predicted output. The difference between the predicted output and target (truth labels) can be computed by the 'cost function'. Secondly, based on the cost function, the gradient of each parameter is calculated by chain rules in the backward stage. All the parameters are updated based on the gradients and are prepared for the next forward computation. After sufficient iterations of the forward and backward stages, network learning can be stopped when the cost function is minimized.

To understand this training process, we first introduce the backpropagation (BP) algorithm [Werbos, 1974, Rumelhart et al., 1986, Nielsen, 2015, Géron, 2019]. This algorithm is used to calculate a gradient that is needed in the calculation of the weights to be used for classification in the network. In order to train the network, training set $\{(\mathbf{x}_1, \mathbf{t}_1), \ldots, (\mathbf{x}_N, \mathbf{t}_N)\}$ is given. For a set of input vectors $\mathbf{x}_n$, where $n = 1, \ldots, N$, we denote a corresponding set of target vectors $\mathbf{t}_n$. However, when the input vectors $\mathbf{x}_n$ from the training set is presented to this network, it produces a predicted output $\mathbf{y}_n$ different in general from the target $\mathbf{t}_n$. To solve this problem, the quadratic cost function $J(\mathbf{y}_n, \mathbf{t}_n)$ is proposed with the following expression:

$$J(\mathbf{y}_n, \mathbf{t}_n) = \frac{1}{2} \sum_{n=1}^{N} \|\mathbf{y}_n - \mathbf{t}_n\|^2 . \tag{2.58}$$

The purpose of training is to minimize the cost function J using the training dataset and the gradient descent algorithm to update the parameters. This algorithm is introduced in Appendix A with a simple example.

With the help of LeNet-5, the main layers and supervised learning of CNN have been presented. Altogether the LeNet 5 laid the basic foundation for CNN. One of the main drawbacks is that there was not much computational power available on those days like GPUs till recently and the CPUs were not faster enough. Furthermore, the introduction of GPUs to general-purpose computing and CPUs becoming more and more powerful made deep learning problems solving feasible and efficient with reasonable time cost. In the next part, we will present another CNN, which can be considered as the first modern successful CNN architecture named 'AlexNet'.

2.6.4 AlexNet architecture

AlexNet is a CNN, which was designed by Alex Krizhevsky et al. [Krizhevsky et al., 2012] that achieved top results on the ILSVRC-2010 and ILSVRC-2012 image classification tasks. AlexNet is a large network structure with 60 million parameters and more than 650,000 neurons. Since AlexNet is deeper than the LeNet, the concept of going deeper with network model came into the play after this. Some of the researchers started building deeper networks, the most famous are GoogLeNet [Szegedy et al., 2015], VGGNet [Simonyan and Zisserman, 2014], ResNet [He et al., 2016], etc. Theoretically, the deeper the number of networks is, the better detection and recognition effect are obtained, but the higher the time cost complexity is. In this thesis, as a new attempt to connect the AE wavelet scalogram and CNN, we choosed the AlexNet.

Figure 2.17 shows the illustration of the architecture of the original AlexNet. AlexNet

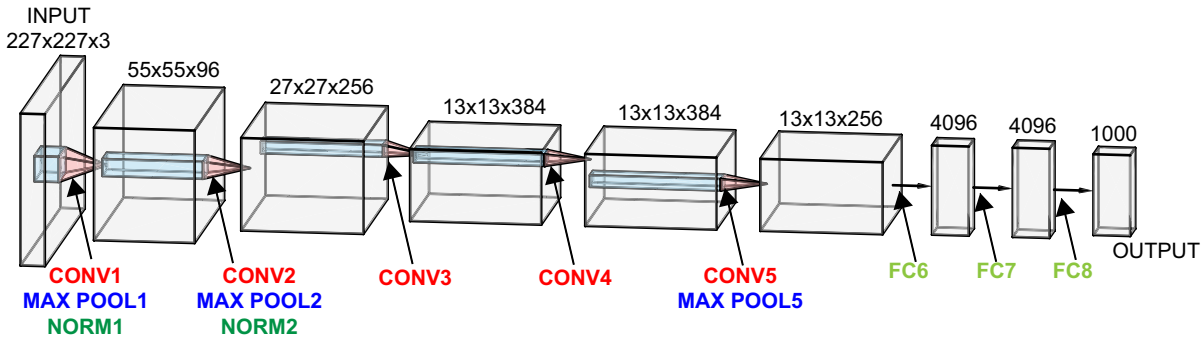

Figure 2.17: Sectific illustration of the architecture of AlexNet with 8 main layers, each layer with its output dimension.

contains eight main layers; the first five are convolutional layers, some of them are followed by max-pooling layers and the last three are fully connected layers. The output of the last fully-connected layer (FC8) is fed to a 1000-way softmax layer which produces a distribution over the 1000 class labels. The detailed statistics can be found in Table 2.2. We consider this network with 25 layers; detailed information of this network will be introduced below.

1	'Data'	Image input	227×227×3 images with 'zero-center' normalization
2	'Conv1'	Convolution	96 11×11×3 convolutions with stride [4 4] and padding [0 0 0 0]
3	'Relu1'	ReLU	ReLU
4	'Norm1'	Local Response Normalization	Local Response Normalization with 5 channels per element
5	'Pool1'	Max Pooling	3×3 max pooling with stride [2 2] and padding [0 0 0 0]
6	'Conv2'	Convolution	256 5×5×48 convolutions with stride [1 1] and padding [2 2 2 2]
7	'Relu2'	ReLU	ReLU
8	'Norm2'	Local Response Normalization	Local Response Normalization with 5 channels per element
9	'Pool2'	Max Pooling	3×3 max pooling with stride [2 2] and padding [0 0 0 0]]
10	'Conv3'	Convolution	384 3×3×256 convolutions with stride [1 1] and padding [1 1 1 1]
11	'Relu3'	ReLU	ReLU
12	'Conv4'	Convolution	384 3×3×192 convolutions with stride [1 1] and padding [1 1 1 1]
13	'Relu4'	ReLU	ReLU
14	'Conv5'	Convolution	256 3×3×192 convolutions with stride [1 1] and padding [1 1 1 1]
15	'Relu5'	ReLU	ReLU
16	'Pool5'	Max Pooling	3×3 max pooling with stride [2 2] and padding [0 0 0 0]
17	'Fc6'	Fully Connected	4096 fully connected layer
18	'Relu6'	ReLU	ReLU
19	'Drop6'	Dropout	50 % dropout
20	'Fc7'	Fully Connected	4096 fully connected layer
21	'Relu7'	ReLU	ReLU
22	'Drop7'	Dropout	50 % dropout
23	'Fc8'	Fully Connected	1000 fully connected layer
24	'Prob'	Softmax	Softmax
25	'Output'	Classification Output	cross entropy function with 1000 classes

Table 2.2: Parameters in AlexNet.

Rectified Linear Unit (ReLU) The AlexNet first used the non-saturating ReLU activation function in CNNs. The activation function ReLU has the expression as:

$$f(x) = \max(0, x), \tag{2.59}$$

while the gradient of ReLU is always 1 if the input is not less than 0. Before AlexNet, the standard way to model a neuron's output used activation function f of its input x is with tanh (eq: $f(x) = \tanh(x)$) or sigmoid (eq: $f(x) = (1 + e^{-x})^{-1}$), etc. But in such so deep models, these functions tend to run into gradient vanishing problem, because the gradient is a large value only when the input is around a small range of 0. To overcome this problem, a new non-saturating activation function was used: Rectified Linear Unit (ReLU), which follows the [Nair and Hinton, 2010]. -Figure 2.18 presents these three activation functions (sigmoid, tanh and ReLU).

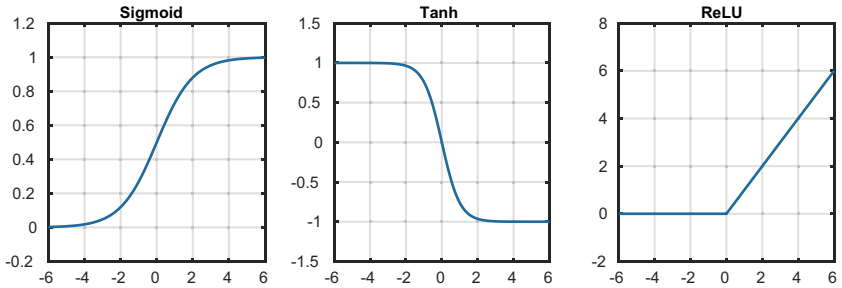

Figure 2.18: The example of 3 activation functions: sigmoid, tanh and ReLU.

It has been proven that deep networks with ReLU as activation function converge faster than tanh and sigmoid functions (see Figure 2.19). This acceleration greatly contributed to the training.

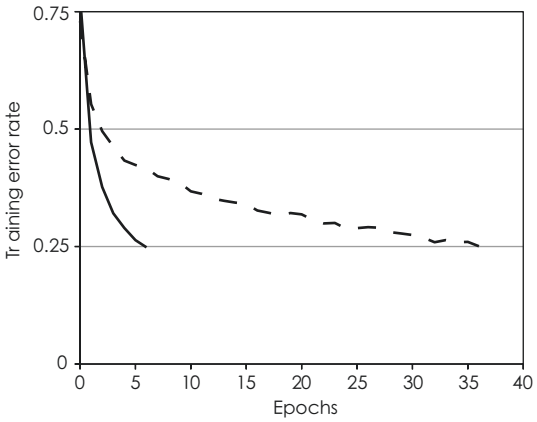

Figure 2.19: Training times of ReLU versus tanh activations: solid line and dotted line represent the ReLU and tanh activation function of training time, respectively. [Krizhevsky et al., 2012]

Local Response Normalization (LRN) Local Response Normalization (LRN) was first proposed in AlexNet architecture to normalize the results obtained by ReLU. LRN is a non-trainable layer that square-normalizes the pixel values in a feature map within a local neighborhood. The response-normalized activity $b^i_{(x,y)}$ has the expression as:

$$b^i_{(x,y)} = \frac{a^i_{(x,y)}}{(k + \alpha \sum_{j=\max(0,i-n/2)}^{\min(N-1,i+n/2)} (a^j_{(x,y)})^2)^\beta}. \tag{2.60}$$

We denote by $a^i_{(x,y)}$ the activity of a neuron computed by applying kernel i at position (x,y) and applying the ReLU nonlinearity. The sum runs over n 'adjacent' kernel maps at the same spatial position, and N is the total number of kernels in the layer. The constants k, n, α and β are hyper-parameters. In [Krizhevsky et al., 2012], authors determined them by using a validation set: $k = 2$, $n = 5$, $\alpha = 10^{-4}$ and $\beta = 0.75$. And this normalization was used to apply the ReLU nonlinearity in first and second convolution layers of the AlexNet architecture as shown in Figure 2.17.

Dropout AlexNet uses Dropout technique to overcome overfitting. Overfitting happens when a model learned the noise in the training data. To some extent, it has a negative

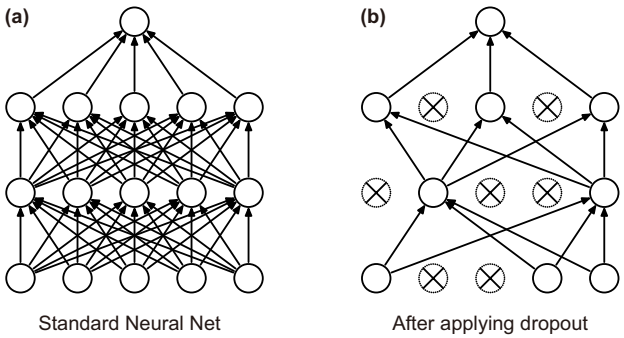

Figure 2.20: Dropout Neural Net Model. [Srivastava et al., 2014] (a) A standard neural net with 2 hidden layers. (b) An example of a thinned net produced by applying dropout to the network on the subplot (a).

impact on the performance of the model on new data. Dropout randomly freezes (drops) neurons (along with their connections) from the neural network with a dropout probability P_D. During training phase, those dropped out neurons are not engaged in both forward and backward pass. During the test phase, all neurons are used but without outputs multiplied by P_D. Figures 2.20(a) and (b) show a plain neural network and the corresponding dropout neural network where the crossed neurons have been dropped.

Softmax layer The softmax layer is widely used in the last fully connected layer of CNNs, owing to its simplicity and probabilistic interpretation. In Table 2.2, a softmax layer (layer 24) is connected to layer 'Fc8'. However the softmax function P is defined as:

$$P\left(x_i\right) = \frac{e^{x_i}}{\sum_{i=1}^{k} e^{x_i}}, \tag{2.61}$$

where x_i is the output of the class i, i represents the class index, k represents the total number of class and $P\left(x_i\right)$ is the probability value. Employing softmax function, the network gives a probability for each class [Bridle, 1990]. To classify an input value, we choose the class with the highest probability as the predicted result,x which is the function of layer 25 in Table 2.2.

Based on these novel techniques, on the benchmark data set at that time, AlexNet's classification accuracy was about 10 % better than other methods, which was a great improvement. In this PhD work, we used this architecture for 2D image-based AE signals classification.

2.6.5 Transfer learning

AlexNet has shown its good classification ability, but to train this deep architecture, it requires a large amount of labeled data. For personal computers without a powerful GPU, training is very time-consuming. In real applications, useful data sometimes are very expensive and in most of the cases, only a few data can be collected. To overcome this drawback, a technique known as transfer learning has been proposed and applied in many studies. Transfer learning has been proven to be a highly effective technique, particularly when faced with domains with limited data [Pan and Yang, 2009, Hertel et al., 2015, Litjens et al., 2017] and with a small number of training images, the transfer learned features can be completed quickly [Donahue et al., 2014].

In the CNN, parameters in shallower layers extract low-level features, such as color, texture, and edges, while deeper layers attempt to capture more complicated and abstract high-level features [Zeiler and Fergus, 2014]. For this reason, the shallower layers of the architecture are frozen and deeper layers are replaced by new layers and retrained by a new task. The transfer learning algorithm has been applied to various studies [Shin et al., 2016, Lu et al., 2019]. Tajbakhsh et al. have demonstrated that transfer learning is useful in limited training data for medical image analysis [Tajbakhsh et al., 2016]. An AI system has been developed for the diagnosis of eye diseases and pediatric pneumonia which have performance comparable to that of doctors experts [Kermany et al., 2018]. These examples show that AE images classification with CNN may be achievable.

In this study, we sought to develop an effective transfer learning algorithm in the pre-trained AlexNet to process the 'AE image' to provide an AE signal classification

system. The pre-trained AlexNet is already trained on 1.2 million labeled images dataset of ImageNet that have already been learned to extract powerful and informative features from natural images and use it as a starting point to learn a new task – 'AE Images'.

The pre-trained AlexNet includes five Convolutional layers (Conv1—Conv5) pursued by three completely associated fully-connected layers (Fc6—Fc8). In the proposed transfer learning algorithm, we freeze and extract layers 1–22 meanwhile last three layers are fine-tuned for the new classification task (AE Images). Layers 23–25 of the pre-trained AlexNet (in Table 2.2) is replaced with a new fully-connected layer with k neurons (k is the number of AE class), a softmax layer and a new output classification layer with k classes. Figure 2.21 presents the diagram of transfer learning for AlexNet.

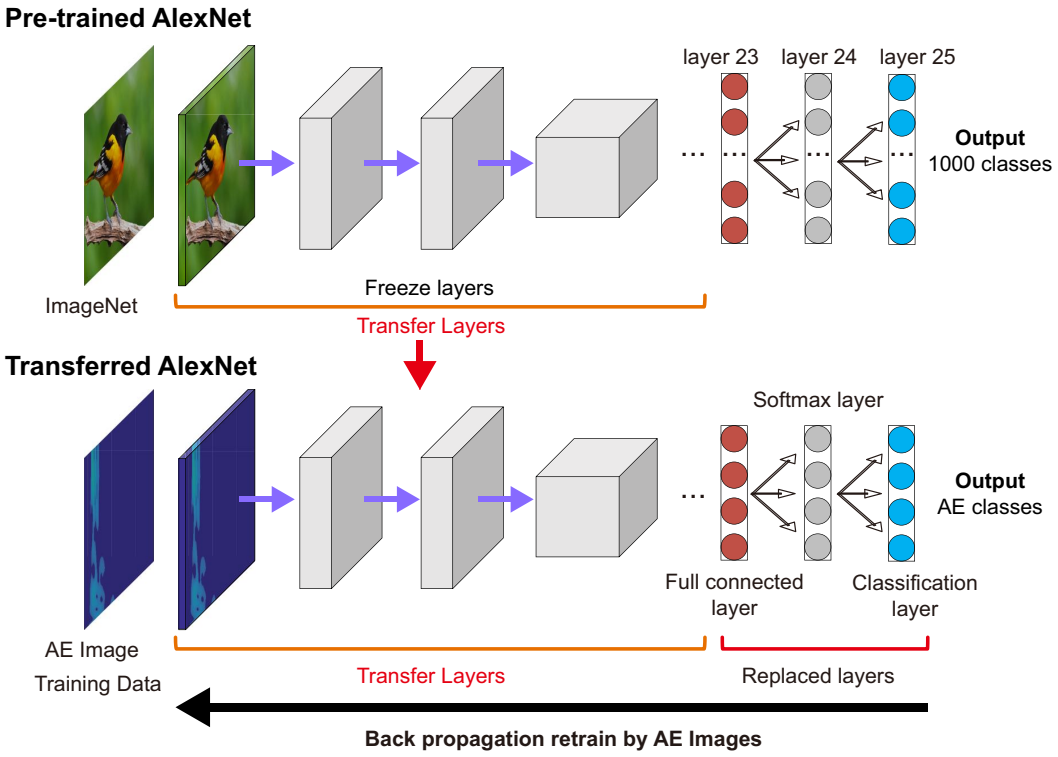

Figure 2.21: The pipeline of proposed methodology: transfer learning by AlexNet and AE image training.

The entire architecture is divided into two parts: the transfer layers and the replaced layers. The parameters in the transfer layers were already trained, and the extracted features have been proven effective for classification [Chen et al., 2015, Yosinski et al., 2014]. These parameters may just need marginal adjustment to adapt to the new task (AE images). While the parameters in the replaced layers are suitable for training on a small dataset. The replaced layers learn the class-specific features to categorize the AE images into specific classes. In this study, the proposed algorithm is implemented on Matlab R2018a with a computer (CPU: Intel i7-4710H, Memory: 16 GB RAM, Graphics Card: NVIDIA GeForce GTX 960M 4G memory).

2.6.6 Image-based acoustic emission data classification methodology

Combining the advantages of continuous wavelet transform (CWT) and convolutional neural network (CNN), we propose an acoustic emission signals classification algorithm which consists of three steps:

– 1. AE signal can be transformed into a wavelet scalogram through time-frequency (T-F) representation by the CWT. Then wavelet scalogram is represented in dB to recalculate different intensity of signals in the same range between 20 dB and 100 dB. This novel T-F representation is denoted 'AE image'. These AE images, corresponding to different damage mechanisms, may be different, as the characteristic frequencies and intensity of the damages are different.

– 2. Pre-trained AlexNet is therefore applied to these AE images, making the architecture to learn the underlying features of AE images by transfer learning.

– 3. Then, unknown AE signals can be converted into images using the CWT and classified by the retrained AlexNet, forming an effective AE-based damage mechanism classification system.

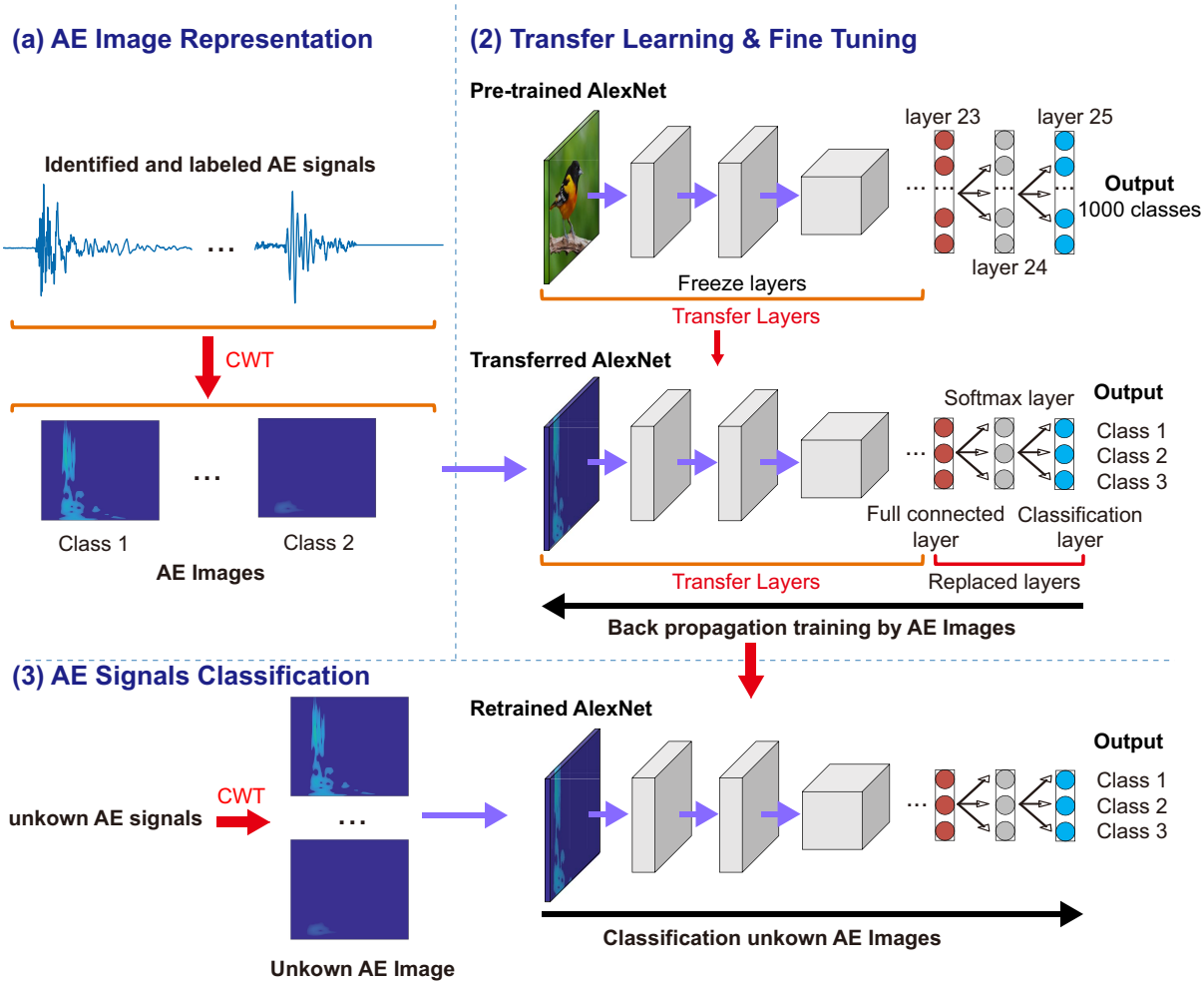

Figure 2.22: Flowchart of the proposed classification Methodology.

The flowchart shown in Figure 2.22 illustrates the steps involved in the process of the

proposed Methodology. Evaluation metrics for the classification performance are based on the notion of true and false positives (TP and FP), and true and false negatives (TN and FN). TP (TN) refers to a positive (negative) instance that is correctly classified as positive (negative). FP (FN) means a negative (positive) instance that is incorrectly classified as positive (negative). Classification results widely use performance metrics defined as follows:

$$\text{Accuracy (ACC)} = \frac{\text{TP} + \text{TN}}{\text{TP} + \text{TN} + \text{FP} + \text{FN}} \tag{2.62}$$

$$\text{Sensitivity (SN)} = \frac{\text{TP}}{\text{TP} + \text{FN}} \tag{2.63}$$

$$\text{Specificity (SP)} = \frac{\text{TN}}{\text{TN} + \text{FP}} \tag{2.64}$$

In this section, we proposed a novel approach for AE signal classification based on pre-trained CNN (AlexNet) and CWT. In the next Chapter, we present mechanical tests performed on specific polymer concrete (PC) samples, some damages mechanisms and the corresponding AE signals that could be identified. The AE images are computed based on the wavelet scalogram. They can be used as label datasets for transfer learning to retrain the pre-trained AlexNet. Then, the classification system can be applied to the unlabeled AE signals collected from new PC samples. Results and discussion will be shown in the next Chapter.

2.7 Conclusion

In this chapter, we introduced several signal processing methods for investigating the characteristics of AE signals. All AE waveforms can be represented by AE features as input data, then performed on the proposed unsupervised pattern recognition analysis, signals are classified in different classes. We also proposed an 'image-based AE signal classification' approach, which consists on the continuous wavelet transform (CWT) and convolutional neural network (CNN). These above-mentioned methods will be applied to analyze the AE signals obtained during quasi-static three-point bending tests and nonlinear relaxation tests of concrete samples in Chapter 3 and Chapter 4.

Chapter 3

Acoustic emission characterization of micro-cracked concrete

The aim of this chapter is to present quasi-static three-point bending tests performed on concrete samples. In particular, we will focus the study on the monitoring of damage mechanisms using acoustic emission (AE) technique and associated signal processing methods, which have been presented in Chapter 2. Indeed, total and partial damage stages of samples are characterized using a parametric approach and an unsupervised pattern recognition. Furthermore, we propose the use of an 'image classification' approach based on continuous wavelet transform (CWT) and convolutional neural network (CNN). The relevance of this approach will be evaluated by comparing to the results obtained from unsupervised pattern recognition.

3.1 Civil engineering concrete

3.1.1 Materials and specimens

The considered civil engineering concrete is made in laboratory conditions (see Table 3.1). The cement was first mixed with water (w/c ratio of 0.5:1 by mass). After several minutes of mixing, the fine aggregates (sand) and coarse aggregates (crushed granite) were mixed together. Before the casting of the concrete into metallic molds, inner surfaces of molds were lubricated with oil for easier demolding. The mold was then subjected to vibration for more than one hour in order to ensure good compaction and reduce the air bubbles within concrete samples. After the hardening of the samples, they were demolded after 24 hours and then put into water for curing for 28 days before being submitted to mechanical tests.

Specimen size(mm)	$200 \times 40 \times 40$
Fine aggregates size (mm)	2
Coarse aggregate size (mm)	15
Water to cement (by mass)	0.5:1
Fine aggregate to cement (by mass)	2:1
Coarse aggregates to cement (by mass)	3:1

Table 3.1: Concrete specimen and the mixture characteristics.

Finally, note that the same ingredient (water, cement, sand) were used to prepare mortar samples, which have the same dimensions as concrete samples.

3.1.2 Experimental setup and procedure

In this study, the cracking of the samples is obtained through the three-point bending tests. An Instron universal testing machine with a 10 kN capacity was used with a fixed crosshead velocity of 1 mm/min during each test up to the final rupture of samples. Simultaneously, the AE activity within samples is monitored using the PCI-2 AE system where AE sensors are glued on the lateral surface of samples. Figure 3.1(a) shows the experimental setup.

To investigate the mechanical behavior of these quasi-brittle specimens, bending tests were used according to ASTM C293 [Hashemi and Jamshidi, 2015, Shokrieh et al., 2017]. The flexural strength (σ in MPa) of samples can be written as:

$$\sigma_f = \frac{3FL}{2bd^2}, \tag{3.1}$$

where b (mm) and d (mm) are the width and height of the specimen, L (mm) is the distance between two supports and F (N) is the maximum force applied at the center of the sample.

Consequently, the flexural strain (ϵ_f in mm/mm) at the center of the sample is:

$$\epsilon_f = \frac{6Dd}{L^2}, \tag{3.2}$$

where D (mm) is the deflection due to the applied load at the center of the specimen. These above-mentioned parameters are illustrated in the Figure 3.1(b).

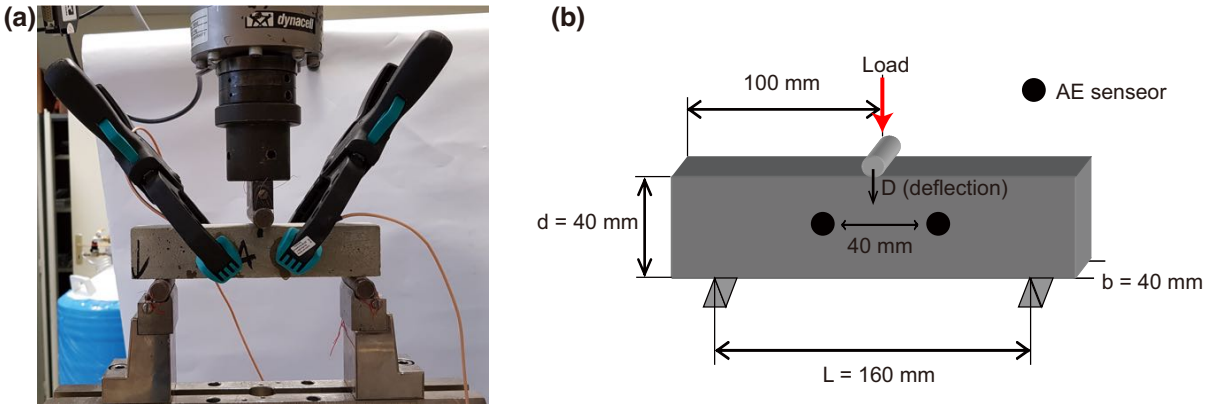

Figure 3.1: (a) Experimental setup of the three-point bending of a concrete specimen monitored by AE with two AE sensors. (b) Geometry of specimens and localization of AE sensors.

A two-channel Physical Acoustic (Mistras Group, Inc.) PCI-2 AE acquisition system was employed to monitor the AE activity during mechanical tests. Two WSα wideband AE sensors (Mistras Group) with a frequency bandwidth of 100 kHz - 1 MHz were glued on samples by phenyl salicylate (salol) where two clamps were used to secure the fixing. AE signals were detected by the sensors and enhanced by the pre-amplifiers set on a fixed gain (40 dB) over the sensor's frequency bandwidth. The acquisition parameters are presented in Table 3.2. In addition, the pencil-lead break tests were used to check the sensitivity of each sensor and to verify that the coupling of all sensors is consistent. Only the AE signals detected by both sensors are taken into account for the analysis. AE hits are collected at 5 MHz sampling rate and 5120 data points. AE signals are then processed in order to extract their 15 main features based on Table 2.1.

AE data acquisition setup	
Threshold	40 dB
Sample rate	5 MHz
Pre-trigger	100 µs
Length	5120 points
Pre-ampli gain	40 dB
Analog filter	100 kHz–1 MHz
Digital filter	100 kHz–1 MHz
Peak-Definition-Time (PDT)	50 µs
Hit-Definition-Time (HDT)	100 µs
Hit-Lockout-Time (HLT)	400 µs

Table 3.2: Experimental AE system setup

3.1.3 Acoustic emission based fracture process analysis

The fracture process in concrete can be studied through the AE event amplitude distribution, which is known as AE-based b-value analysis [Sagar et al., 2012]. The analysis

is performed by analogy to observations made in seismology, where events with large magnitudes occur less frequently than events with small magnitudes. In this fact, the b-value is defined as the negative gradient of the log-linear graph between earthquake frequency and magnitude [Colombo et al., 2003]. These parameters are grouped together in the empirical formula proposed by Gutenberg and Richter [Richter, 1958]:

$$\log N = a - bM \tag{3.3}$$

where N is the number of earthquakes of magnitude greater than M, b is an empirical constant and M is the Richter magnitude of earthquakes.

In the case of AE analysis, Equation (3.3) can be rewritten as:

$$\log N = a - b\left(\frac{A_{dB}}{20}\right), \tag{3.4}$$

where N is the number of AE events with amplitude greater than the threshold value used, A_{dB} is the amplitude value of those events in decibels (dB) and b is an empirical constant which is called 'AE-based b-value'. The b-value varies systematically with different stages of the fracture growth, so it can be used to estimate the development of the fracture process [Rao and Lakshmi, 2005]. By using the b-value analysis, it is possible to identify the development of micro-cracks and macro-cracks within materials under test, where high b-value corresponds to micro-cracking and low b-value corresponds to macro-cracking [Carpinteri et al., 2009]. Figure 3.2 shows an example of AE based b-value calculation.

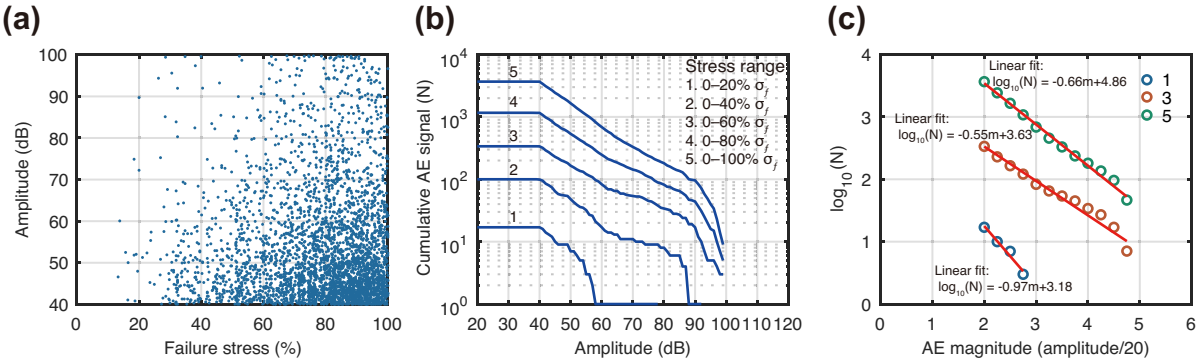

Figure 3.2: Example of AE based b-value calculation. (a) Evolution of amplitude of AE events versus percentage of failure stress. (b) Cumulative AE events versus amplitude distribution for different stress ranges. (c) The log(N)-AE magnitude chart and its relative curve fitting for b-value calculation performed for the stress range 1,3 and 5 of subplot(b).

3.1.4 Parametric approach of crack mode classification

According to relevant recommendation [Committee et al., 2010], the shape of AE waveforms is considered to be characteristic of the crack mode in concrete structures. Two AE parameters are used for estimating crack modes: average frequency (AF) and RA value, which are defined as:

$$\text{RA } [\mu\text{s/V}] = \frac{\text{Rise time (RT)}}{\text{Amplitude (A)}}, \tag{3.5}$$

and

$$\text{AF [kHz]} = \frac{\text{Counts (CNTS)}}{\text{Duration (DU)}}. \tag{3.6}$$

Previous studies [Aggelis, 2011, Aggelis et al., 2013a] have shown that for tensile cracks, AE rise time would be shorter. Therefore, a tensile-type crack is referred to as an AE signal with high AF and low RA value. In addition, shear-type crack is identified by low AF and high RA value as shown in Figure 3.3).

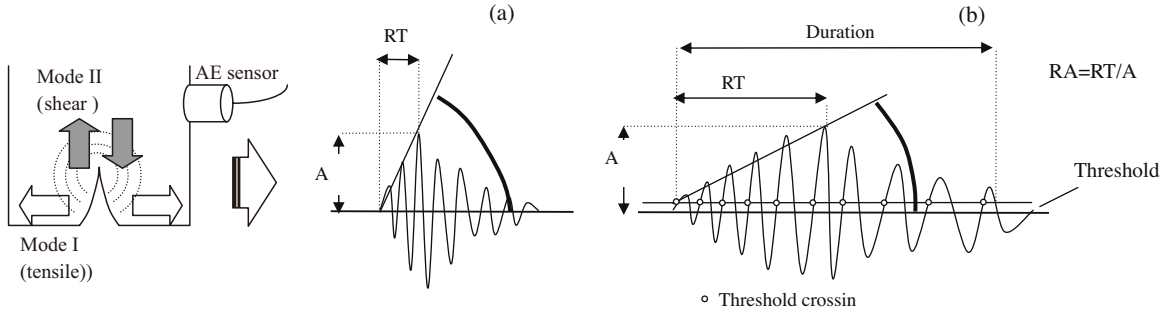

Figure 3.3: Crack mode in concrete materials. Typical waveforms of (a) tensile and (b) shear event. [Soulioti et al., 2009]

Therefore, variations in RA and AF values during the concrete damage process is likely to identify the changes in the prevalent damage mode within the specimen. The results in the literature reveal that the detected AE signals during the early stages of damage are mainly due to tensile crack and have therefore higher AF and lower RA. As the material approaches to the final failure, the average value of AF increases and RA decreases, meaning that more shear cracks are formed at this stage. This observation has been confirmed by many studies and regarded as a relevant indicator in the field of concrete engineering [Aldahdooh and Bunnori, 2013, Behnia et al., 2014].

3.1.5 Unsupervised pattern recognition

In the present thesis, we have proposed an unsupervised pattern recognition in order to cluster the huge number of unlabeled AE signals by using several relevant independent features. The detail of this approach was introduced in section 2.5.

The inherent characteristic of each AE signal is represented by 15 features (see Table 2.1). After feature normalization, by using the Laplacian Score (LS) selection approach, the selected feature dataset consists of the more appropriate features (LS>0.9). Then we use the principal component analysis (PCA) algorithm to reduce the dimension of the dataset. Finally, a new dataset containing uncorrelated principal components with a smaller dimension is used as input of the k-means algorithm. The optimal cluster number (k) is confirmed by the lowest Davies-Bouldin (DB) index and the highest Silhouette coefficient (SC) value. After application of the k-means algorithm, the AE signals are separated into k clusters. The identification consists in correlate each cluster to its corresponding damage mechanism. In fact, clustering does not lead to a unique solution, and there is no indisputable standard to determine, which classification result is

more appropriate and more representative of the studied damage mechanism. The main purpose of this unsupervised pattern recognition is to achieve the well-separated clusters and assume that each cluster consists of one unique damage mechanism.

In this chapter, some specimens are manufactured by different formulations in order to isolate damage mechanisms. For civil engineering concrete materials, we use the mortar specimens and plain concrete specimens to investigate the micro damages mechanisms. For polymer concrete materials, we used some specific specimens to simplify and validate the clustering results.

3.2 Damage characterization of mortar

3.2.1 Global observation

Three-point bending tests were performed on the mortar specimen. The test was monitored with AE. Figure 3.4(a) depicts the simultaneous evolution of AE hits amplitude and the applied force as a function of loading time. In addition, according to Equations (3.1) and (3.2), the flexural stress versus flexion strain curve is determined and shown in Figure 3.4(b). Note that, the flexural strength of this mortar specimen is $\simeq 9.4\,\mathrm{MPa}$.

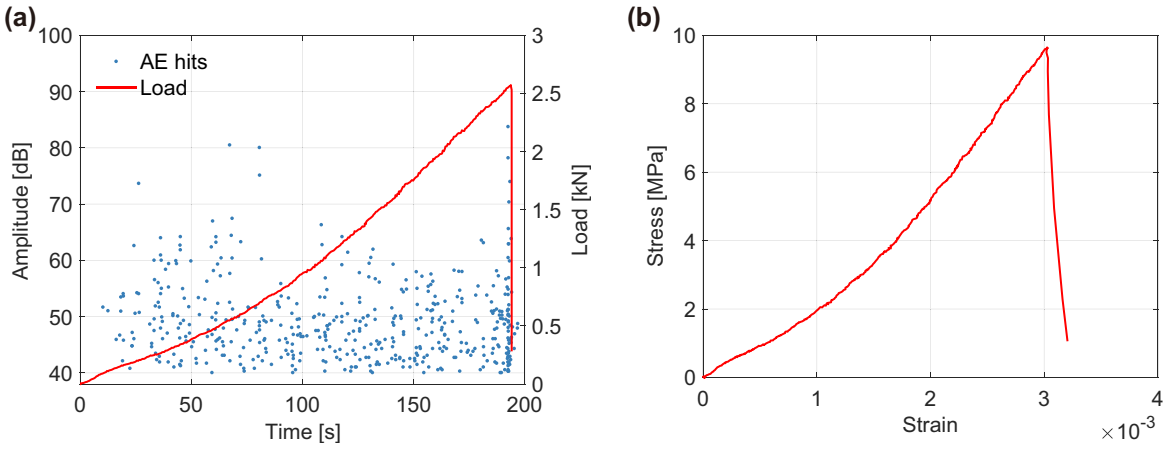

Figure 3.4: Three-point bending test performed on a mortar specimen: (a) Evolution of amplitude of AE signals and applied force versus loading time. (b) Flexural stress-strain behavior.

Firstly, the cumulative AE hits are used to investigate the evolution of damage process as a function of the applied force and loading time (see Figure 3.5(a)). From the first AE signal detected to the main crack formation, the mechanical test can be divided into two stages separated by following times: $t_0 = 11\,\mathrm{s}$, $t_1 = 180\,\mathrm{s}$ and $t_2 = 190\,\mathrm{s}$. In accordance, the AE based b-values are computed as shown in Figure 3.5(b) for these two stages.

– Stage I (t_0 to t_1): the rate of AE activity is approximately constant. In this stage, some micro-cracks begin to emit discontinuous AE events whose count evolves linearly. The AE activity can be attributed to the local effects, such as pore closing and/or the micro-crack initiation and formation [Elaqra et al., 2007]. Computed AE-based b-value during this stage is $\simeq 1.48$, meaning that micro-cracks are the predominant AE sources during this stage [Sagar et al., 2012].

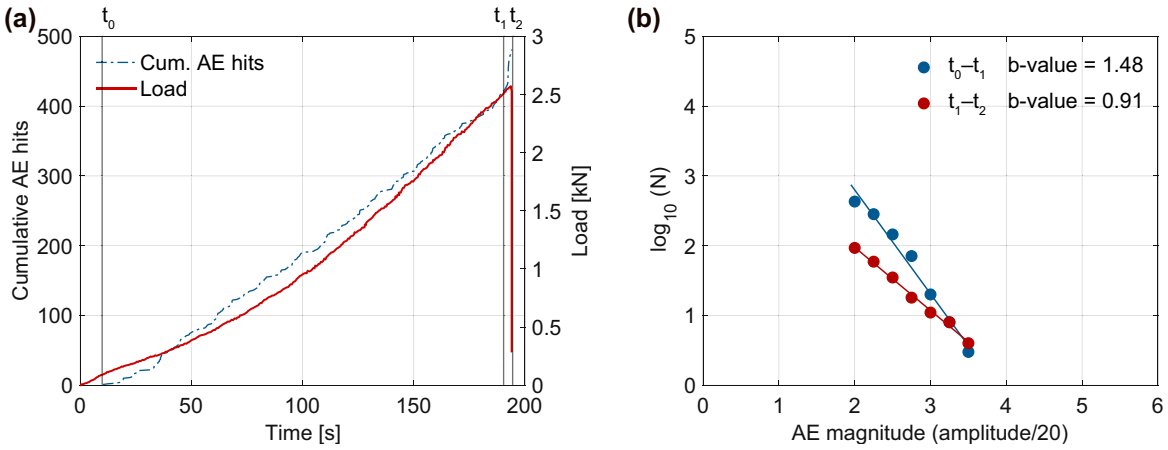

Figure 3.5: (a) Evolution of cumulative AE hits and applied force versus loading time. (b) Relation between the RA value and the average frequency (AF) during the first stage (t_0, t_1) of the bending test.

– Stage II (t_1 to t_2): a rapid increase of AE hits occurs during this very short period. This sudden increase in AE activity can be interpreted as a precursor of the final rupture of specimens, which is mainly attributed to the interconnection of micro-cracks and/or sand to cement interfaces cracking, leading to the final main crack that emits higher amplitude AE hits. The involved AE-based b-value is $\simeq 0.91$ in accordance with the results of the literature [Colombo et al., 2003].

Indeed, mechanical tests performed on mortar specimens as presented in numerous references [Wu et al., 2000, Aggelis et al., 2013a, Sagar et al., 2013, Stavrakas et al., 2016] have shown the possibility to go beyond the b-value description by using the shape of AE waveforms recorded during the different stages. Therefore, a crack mode description becomes possible with the help of the relationship between the previously defined RA value and the average frequency (AF) [Aggelis, 2011]. In the following, results of the RA-AF classification are presented and discussed.

3.2.2 Parametric crack mode classification

Figure 3.6(a) is a 3-D plot presenting the evolution of AE hits' characteristics, namely RA value and Average Frequency (AF) as a function of loading time. It is clear that at the initial stages of loading, AE hits have high AF values up to 300 kHz and low RA value. As a function of the loading time, the detected AE hits have lower AF value and high RA value AE hits are also recorded at the end of the measurement. The evolution of the AF and RA are computed by a moving average of 60 hits as in Figure 3.6(b). It makes this observation easier, where the mean value of AF increases during the test and RA value decreases. It is, however, important to note that these experimental results can be used to detect the shift of the cracking mode from tensile to shear.

Indeed, an AE-based classification of cracking modes in cementitious materials can be performed by comparing the evolution of both parameters RA and AF as shown in Figure 3.7. The aim of the analysis is to get the relevant RA/AF proportion which is predefined using a diagonal line to define the type of cracks classification. Above the diagonal line, signals with high AF and low RA are associated with the tensile cracks,

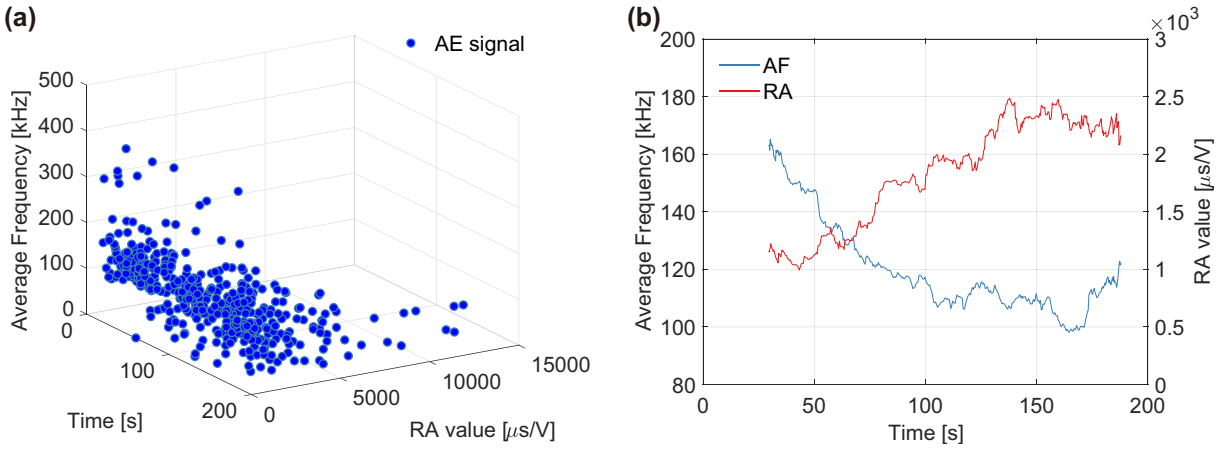

Figure 3.6: (a) Evolution of AE signals on RA value and Average Frequency (AF) in a function of loading time. (b) Moving average of RA and AF versus loading time.

and inversely, shear cracks are characterized by low AF and high RA values.

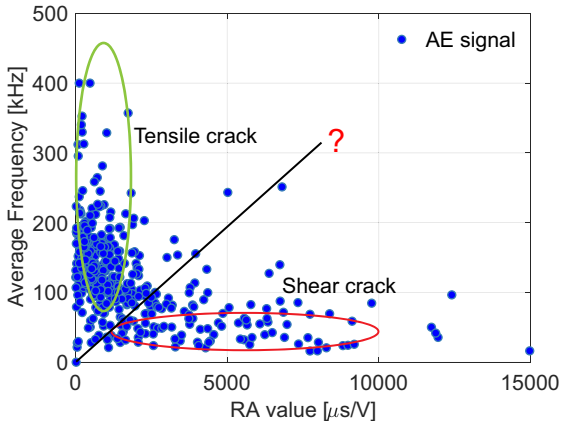

Figure 3.7: Illustration of the RA-AF analysis.

The determination of the line's slop separating signals originating from shear or tensile cracks is not straightforward. Indeed, based on the moment tensor analysis (MTA), the crack locations, crack types and orientation can be quantitatively determined [Shigeishi and Ohtsu, 2001, Kawasaki et al., 2010, Ohno et al., 2014]. Tensile, shear and mixed-mode crack classification was then possible with the help of the Simplified Green's Function (SiGMA) analysis in laboratory conditions when at least six AE sensors were used for the cracks monitoring [Ohno and Ohtsu, 2010]. When the crack location is not known a priori, the random distribution of AE sensors in the studied structure makes the distance between neighboring sensors not convenient to detect a signal cracking with the necessary number of sensor [Aggelis et al., 2013c]. In order to overcome the problems related to the lack of sensors, long series of fracture tests were performed in [Aggelis, 2011]. Flexural, tensile and shear tests were used in order to link the AE activity (trends of AF and RA, etc.) with the micro-cracking stage before, during and after the main fracture [Carpinteri et al., 2013, Aggelis et al., 2013b, Shahidan et al., 2013, Aggelis et al., 2013a].

The present thesis does not consider an important number of tests nor an important number of AE sensors. In such conditions, we propose a first approach to determine the

diagonal line. This is performed by considering the three-point bending test in different steps. Figure 3.8 shows that the first stage of damage is mainly dominated by AE hits with high AF and low RA. This situation is in accordance with the fact that at the initial

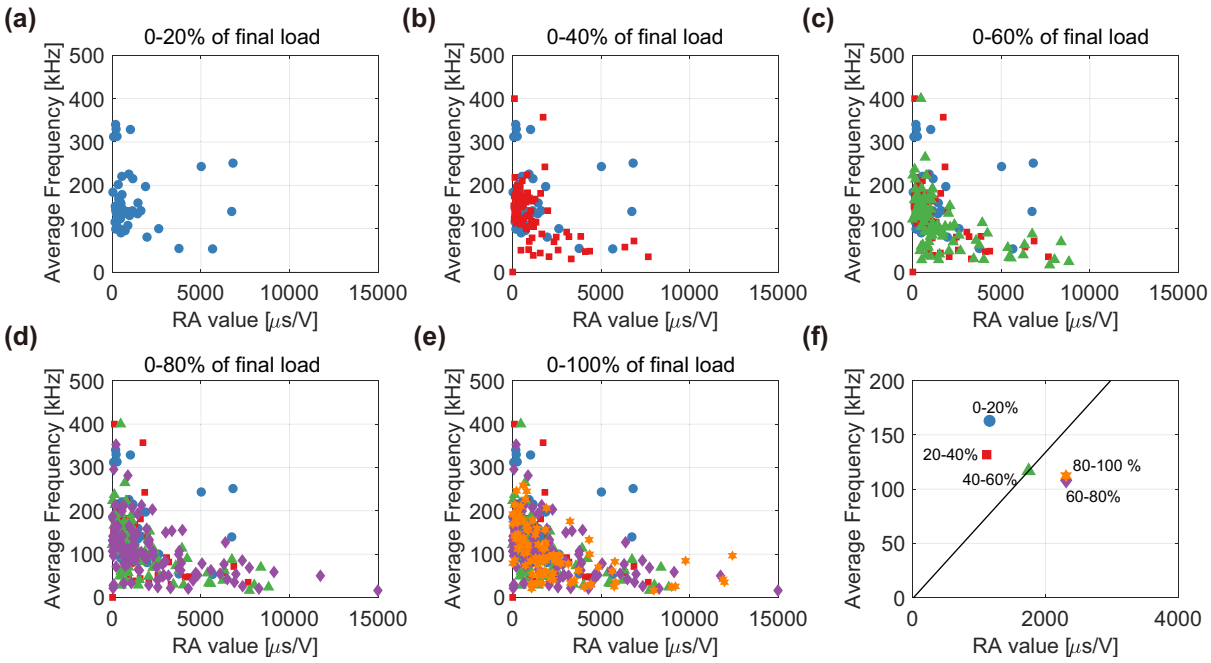

Figure 3.8: The RA-AF relation of detected AE events by different percentage of loading: (a) $0-20\%$ of final load; (b) $0-40\%$ of final load; (c) $0-60\%$ of final load; (d) $0-80\%$ of final load; (e) 0−failure. The blue dot, red square, green triangle, purple prism, orange star symbols correspond to the AE events detected in five damage stages (0 to 20%, 20 to 40%,..., 80 to 100% of final load), respectively. (f) Average value on RA-AF analysis for each damage step.

stage of loading, tensile cracks dominate the detected signals. The number of shear cracks evolves according to the evolution of the mechanical test and becomes more significant at the final stages. By considering the average value of RA and AF for the five damage stages, Figure 3.8(f) depicts that the first two stages ($0-20\%$ and $20-40\%$ of final load) have higher AF and relatively low RA, which the last two stages ($60-80\%$ and $80-100\%$ of final load) are characterized by higher RA values. This makes the stage ($40-60\%$ of final load) reasonably on the border between the proportion between tensile and shear cracks in approximately RA/AF $\simeq$ 3000/200 (1/0.067).

Note that the RA/AF proportion is strongly dependent on the material used as well as the experimental configuration. Aggelis [Aggelis, 2011] proposed a proportion of 1/0.03 in the case of steel fiber reinforced concrete characterized by two AE sensors (Pico, PAC). In [Ohno and Ohtsu, 2010], the proportion was 1/0.2 using eight AE sensors of 150 kHz resonance (R15, PAC). However, it should be pointed out that the proportion we proposed (1/0.067) gives $\simeq$ 33.6% shear cracks AE signals and $\simeq$ 66.4% tensile cracks AE signals. These values are in accordance with those given by Ohno and Ohtsu [Ohno and Ohtsu, 2010] where shear and tensile cracks proportion were 37.3% and 62.7%, respectively.

The AE signals separated into two classes are shown in Figure 3.9(a), where the separation line is presented according to the RA/AF proportion 1/0.067. From the latter,

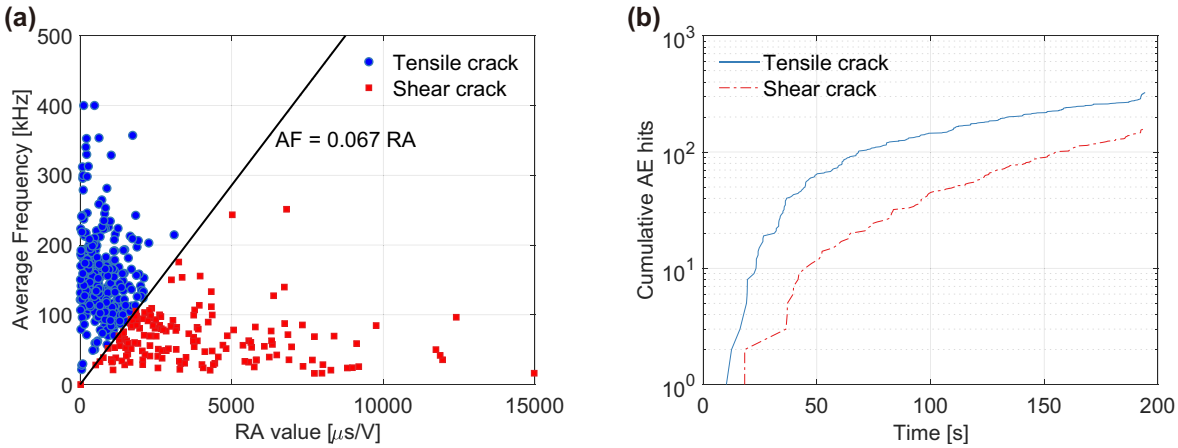

Figure 3.9: (a) The RA-AF representation of AE data classification. (b) Evolution of two crack modes generation versus loading time.

the evolution of the cumulative number of AE signals of the two classes of cracks are illustrated in Figure 3.9(b) as a function of loading time. We can see that the tensile crack is more dominant than shear crack during the test and that beyond 100 s, the evolution of shear cracks becomes faster until the main crack is formed.

Table 3.3 presents the average value of six AE features related to the studied crack modes. Results show that AE waveforms with shorter rise time and higher frequency content (FC and AF) are mainly related to tensile cracks. Whereas, shear cracks in cementitious materials have AE waveforms with longer rise time and lower frequency. These results confirm that RA and AF values can be considered as two effective parameters in crack mode classification. However, even if the separation of crack modes seems to be obvious under laboratory conditions, it still needs to be impressed by taking into accounts new parameters other than RA and AF. This will be developed in the next subsection.

Crack mode	Amplitude [dB]	Rise time [µs]	FC [kHz]	Counts	AF [kHz]	RA value [µs/V]
Tensile crack	50.5	27.7	395.9	48	150.7	677
Shear crack	45.7	90.2	319.8	30	65.4	4062

Table 3.3: Average value of six features calculated from AE signals related to the two crack modes.

3.2.3 Unsupervised pattern recognition

Many previous works have shown that before the main crack creation, all the detected AE signals are due to micro-cracks created within the matrix of cementitious specimens [Soulioti et al., 2009, Aggelis, 2011, Aggelis et al., 2013b]. In this study, the unsupervised pattern recognition was performed to cluster the AE data. The purpose of the clustering analysis is to separate and identify the micro-damage mechanisms in specimens during the three-point bending tests before the final crack. The relevant features are selected from 15 AE features and based on the Laplacian Score (LS), which is more than 0.9 as described in Chapter 2. Six high score features (counts, energy, frequency centroid, PP1, PP3, PP4) were therefore selected for mortar specimens. The selected features were subjected to the PCA to get more independent parameters to be used as

the input of k-means analysis. Figure 3.10(a) shows the variance and cumulative variance in percent of each principal component of the mortar specimen. The number of principal

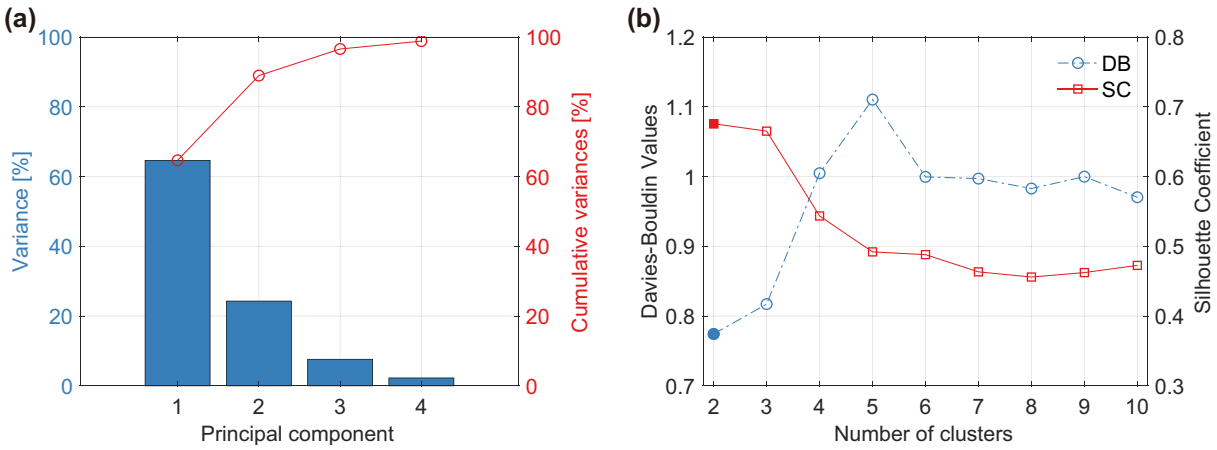

Figure 3.10: (a) The variance (blue bars) of first 4 principal components of concrete specimen. The y axis on the right side shows the cumulative variances (red line). (b) The number of clusters evaluated by Davies-Bouldin value and Silhouette Coefficient (y axis on the right).

components for the k-means algorithm was chosen to be three, which is based on the cumulative variance of $\simeq 95\%$. Optimal clustering is obtained with two clusters according to the minimum value of the Davies and Bouldin (DB) index and the maximum value of the Silhouette coefficient (SC) which is shown in Figure 3.10(b). Finally, for the tested mortar specimen, the k-means algorithm was therefore applied to AE data with three principal components as features and with two clusters ($k = 2$).

The clustering results of AE data is illustrated in Figure 3.11, where 64.4 % of total AE events are classified into cluster CL1 and 35.6 % are classified into cluster CL2. These two AE clusters are then presented in Figure 3.11(a). This result shows that, in the

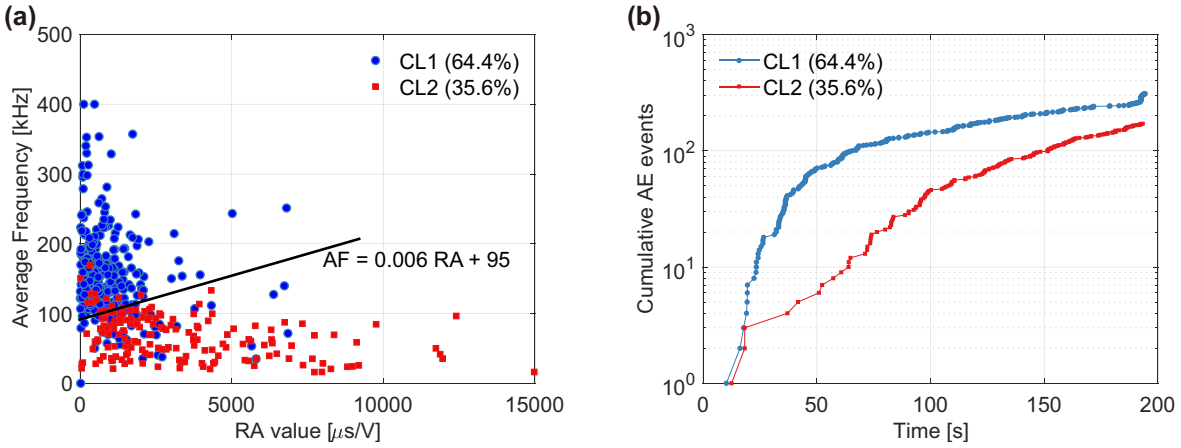

Figure 3.11: (a) Illustration of the clustering results of AE data in RA value versus average frequency plane. (b) Evolution of AE events in two clusters versus loading time.

absence of the RA and AF as input features, k-means algorithm distributed AE data into two clusters: CL1 with high AF and low RA values and CL2 with low AF and high RA. In light of the results obtained, we can reasonably propose a line (AF = 0.006 RA+95)

to separate the two AE clusters. In [Farhidzadeh et al., 2014], a similar line has been proposed, where AF = 0.005 RA+94.5. In their paper, the three-point bending tests were performed on mortar specimens where the AE monitoring is performed using broadband AE sensors (Pco, PAC) and the distance between the center of the specimen and the sensors was 15 mm. With these similar experimental configurations and similar results, the unsupervised pattern recognition reveal to be reliable in view of the lack of AE sensors and samples to be tested. Finally, note that the evolution of the cumulative number of two AE clusters shown in Figure 3.11(b) allows us to draw the same conclusions discussed in the previous subsection.

Table 3.4 presents the average values and the coefficient of variance of the six features related to AE data divided into two clusters (CL1/CL2) for mortar. Note that, the coefficient of variance (COV) is determined as a standard deviation over average. AE events in cluster CL1 have low rise time and high frequency and AE events in cluster CL2 have high rise time and low frequency.

Cluster		Amplitude [dB]	Rise time [µs]	FC [kHz]	Counts	AF [kHz]	RA value [µs/V]
CL1	Average	50.2	34.1	412.1	45	156.4	882
	COV	14.5%	133.5%	9.4%	100.9%	40.6%	122.2%
CL2	Average	47.3	72.1	303.7	38	66.8	3310
	COV	11.2%	98.6%	7.8%	86.3%	46.1%	85.99%

Table 3.4: Average results of six features calculated from AE signals related to the two clusters (CL1 and CL2).

Based on these results, the cluster CL1 is associated with tensile matrix cracking and the cluster CL2 corresponds to shear matrix cracking. Finally, the occurrence of sand/matrix interface debonding cannot be separated from matrix cracking by these AE features and unsupervised pattern recognition analysis. Aggelis et al. [Aggelis et al., 2013a] have studied mortar specimens submitted to three-point bending tests and monitored with broadband AE sensors (Pico, PAC). They have reported that 'tensile' waveform has an amplitude much higher than 'shear' waveform and also characterized by shorter rise time (30 μs instead of 60 μs). Similar experimental configurations (sensor to specimen's center distance 20 mm versus 15 mm, broadband AE sensors, etc.) present average values similar to the ones of Table 3.4 which confirms the existing agreement between the unsupervised pattern recognition analysis with moment tensor analysis (MTA) and parametric analysis [Soulioti et al., 2009, Ohno and Ohtsu, 2010, Carpinteri et al., 2013, Shahidan et al., 2013]. On the strength of this observation, the next section will present the results relating the civil engineering concrete.

3.3 Damage characterization of civil engineering concrete

In this section, the three-point bending tests were performed on civil engineering concrete specimens where the same AE monitoring was used.

3.3.1 Global observation

Figure 3.12(a) depicts the evolution of AE hits amplitude as a function of applied force and loading time. Here again, only the AE hits detected by both two sensors are taken into account. In addition, according to Equations (3.1) and (3.2), the flexural stress versus strain is determined and shown in Figure 3.12(b). Finally, note that the flexural strength of the concrete specimen is $\simeq 9.5\,\mathrm{MPa}$.

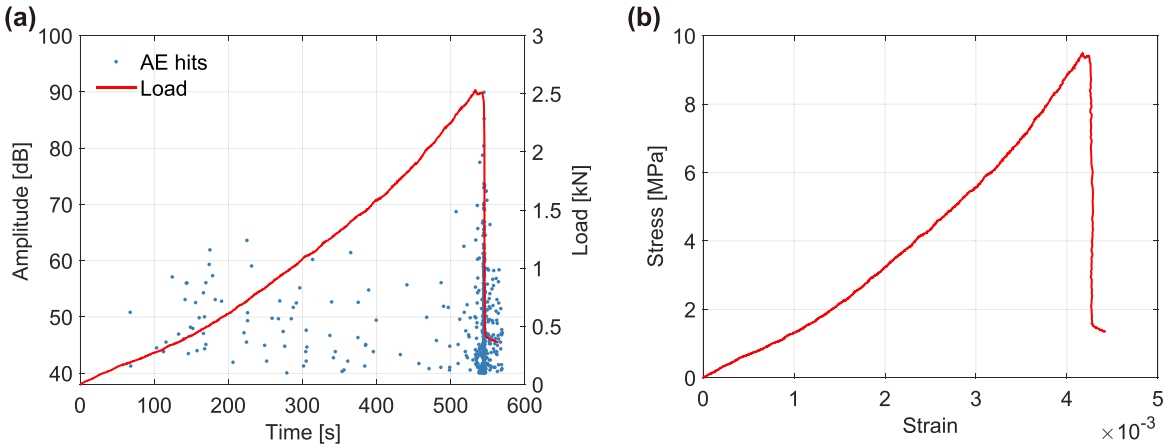

Figure 3.12: Three-point bending test results corresponding to concrete specimen: (a) Evolution of amplitude of AE signals and applied force versus loading time. (b) Flexural stress-strain behavior during the test.

To better understand the evolution of damage, AE signals rate is plotted as a function of applied force and loading time in Figure 3.13(a). The AE signal rate is computed

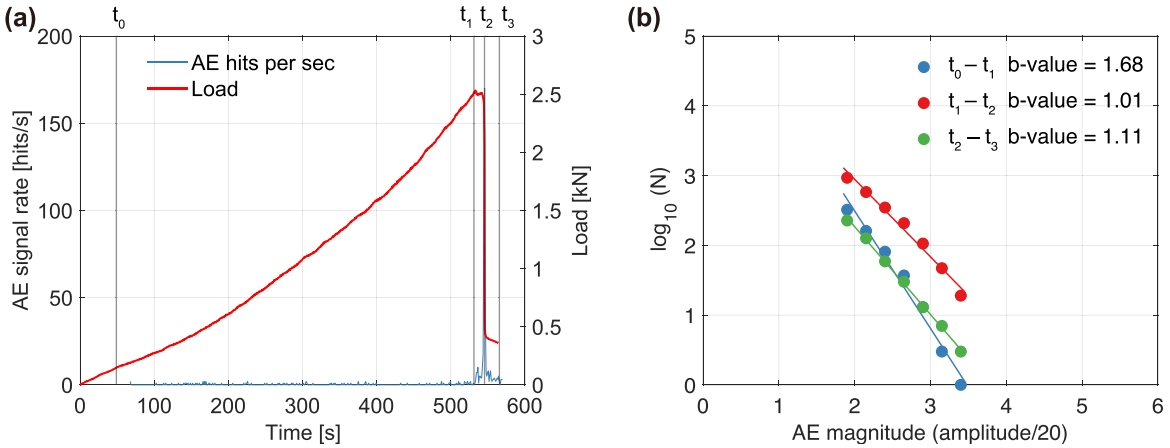

Figure 3.13: Three-point bending test results for concrete specimen: (a) Evolution of AE signal rate (AE hits per second) and applied force versus loading time. (b) AE based b-values during the loading time from three stage. The four plotted times are $t_0 = 51\,\mathrm{s}$, $t_1 = 536\,\mathrm{s}$, $t_2 = 545\,\mathrm{s}$ and $t_3 = 560\,\mathrm{s}$, respectively.

by recording AE hits per unit time taken as 1 s. It can be seen that highest AE signal rate appears when the main crack is formed. The experimental results show that fracture processes of specimens are characterized by three stages determined by the following times $t_0 = 51\,\mathrm{s}$, $t_1 = 536\,\mathrm{s}$, $t_2 = 545\,\mathrm{s}$ and $t_3 = 560\,\mathrm{s}$. In accordance with Equation (3.4), AE based b-values are computed and shown in Figure 3.13(b).

In the first stage (t_0 to t_1), the AE signal rate evolves regularly with time. Some micro-cracks begin to develop emitting discontinuous AE hits, whose amplitudes are in the range of 40 to 70 dB representing micro-crack initiation and formation with the matrix. This observation has been mentioned in many references on concrete [Carpinteri et al., 2009, Ohno and Ohtsu, 2010] and reinforced concrete [Aggelis, 2011, Carpinteri et al., 2016]. Computed AE-based b-value during this stage is $\simeq$ 1.68, which is the relevant value corresponding to the micro-cracking generation stage [Carpinteri et al., 2009].

The second stage (t_1 to t_2) has a very short time period and characterized by an abrupt increase of the AE signal rate (from 20 to 400 hits per second). The abrupt increase of AE activity can be used as the failure precursor of concrete, which corresponds to $\simeq$ 95% of maximum peak load. During this stage, initiation, coalescence, and propagation of micro-matrix cracking are the main sources of AE events, leading to eventual failure [Soulioti et al., 2009]. Additionally, the formation of the visible crack of the specimen appears in the center at the bottom of the specimen which is caused by some much stronger cracking events (more than 80 dB in Figure 3.12). In this stage, AE-based value is $\simeq$ 1.01, corresponding to the increase of macro-crack formation [Colombo et al., 2003].

During the third stage (t_2 to t_3), AE events can be attributed to crack propagation (macro crack growth and crack opening). As the main crack is formed, it propagates from the bottom of the specimen to the top as a function of the continuous descent of the crosshead [Carpinteri et al., 2009]. During this stage, the AE-based value is $\simeq$ 1.11.

Right after the main crack is formed, the mechanical test is stopped. This main crack was visually localized just before the final failure near the mid-span of the tested specimen as illustrated in Figure 3.14. In the following, the micro-cracks are defined as cracks formed before the main crack (between t_0 and t_2). In the following, the crack mode

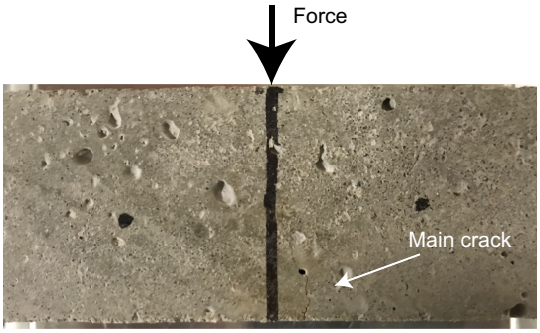

Figure 3.14: Typical main crack of concrete specimen with illustration of applied force.

classification will be first based on the shape of the AE signal waveform with the help of the parametric approach used for mortar specimens.

3.3.2 Parametric crack mode classification

For the civil concrete specimen, Figure 3.15(a) depicts the cumulative AE hits and applied force versus loading time until the main crack formation. As mentioned above, the fracture process was separated in time by $t_0 = 51$ s, $t_1 = 536$ s and $t_2 = 545$ s before the main crack is formed.

During the first stage (t_0 to t_1), AE data are plotted in the RA-AF plan as shown

in Figure 3.15(b). We note that most of the signals have low RA and high AF values, meaning that tensile crack is the dominant AE source during this stage.

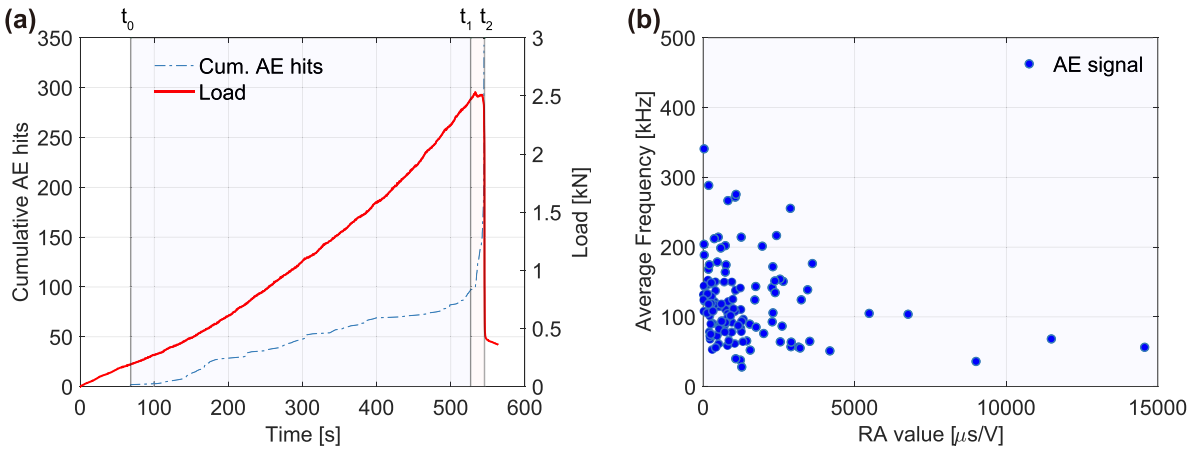

Figure 3.15: (a) Evolution of cumulative AE hits and applied force versus loading time up to the main crack formation. (2) Relation between RA and AF values of the detected AE signals during the first stage (t_0 to t_1) of the tests.

In the second stage (t_1 to t_2), several hundreds of AE hits were detected within short duration (see Figure 3.15(a)). To better indicate the evolution of the crack characteristics, the AE hits is plotted as a function of RA and AF as shown in Figure 3.16(a). Then,

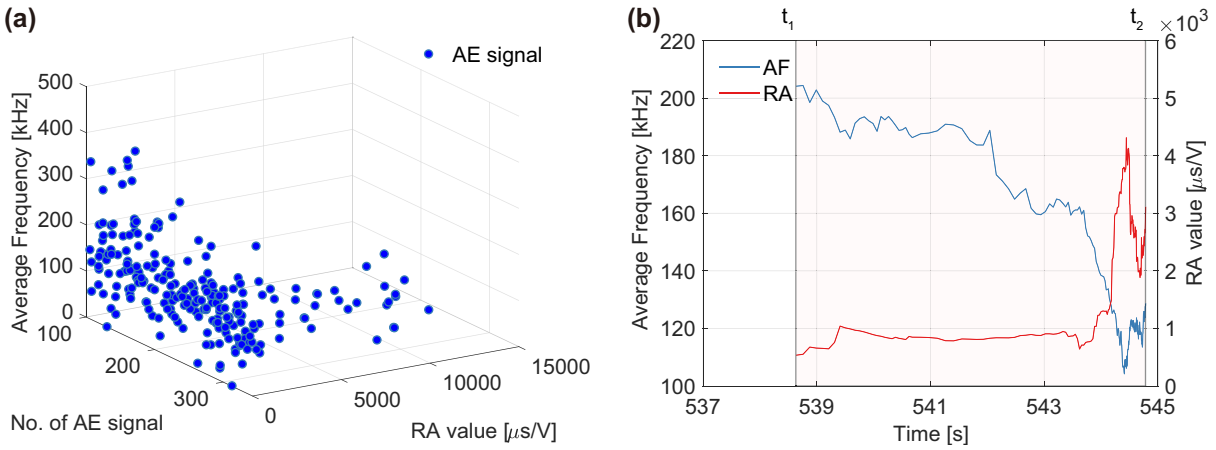

Figure 3.16: (a) Projection of AE data in 3D representation: number of AE hits vs. RA vs. AF. (b) Evolution of RA and AF by moving average of AE hits during the second stage ($t_1 - t_2$) of the test.

the evolution of AF and RA are computed by a moving average of 60 recent hits during this stage as shown in Figure 3.16(b), where the increase (or decrease) of both parameters indicates the shift of the main cracking modes from tensile to shear. As discussed earlier, unsupervised pattern recognition has shown a very good capacity to analyze damage mechanisms. Therefore, it will be used to analyze and separate AE data in concrete samples.

3.3.3 Unsupervised pattern recognition

The clustering of AE data of concrete is based on the previously defined six AE features, which were initially processed thanks the PCA algorithm. Figure 3.17(a) shows the percent variance and cumulative variance of each principal component of the concrete specimen. The number of principal components for the k-means algorithm was set to three, based on the cumulative variance of $\simeq 97\%$. Optimal clustering is obtained with two clusters according to the minimum value of the Davies and Bouldin (DB) index and the maximum value of the Silhouette coefficient (SC) as shown in 3.17(b). Finally, the k-means algorithm was therefore applied to AE data with three principal components and two clusters ($k = 2$).

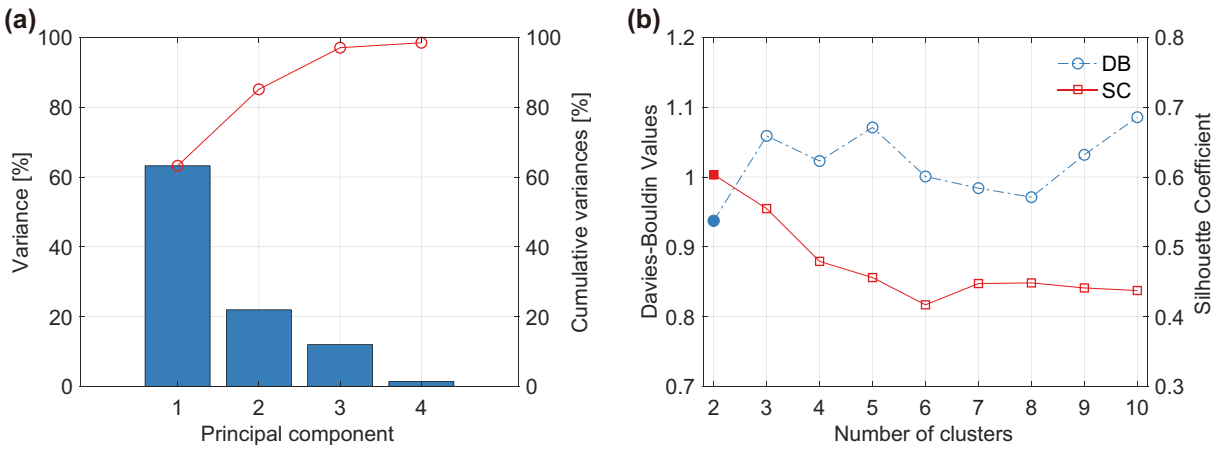

Figure 3.17: (a) The variance (bars) of first 4 principal components of concrete specimen. The y axis on the right side shows the cumulative variances (line). (b) The number of clusters evaluated by Davies-Bouldin value and Silhouette Coefficient (y axis on the right).

The clustering results of AE data are illustrated in Figure 3.18(a). Here, $\simeq 62.1\%$ of total AE events are classified into cluster CL1 and $\simeq 37.9\%$ into cluster CL2. Compared

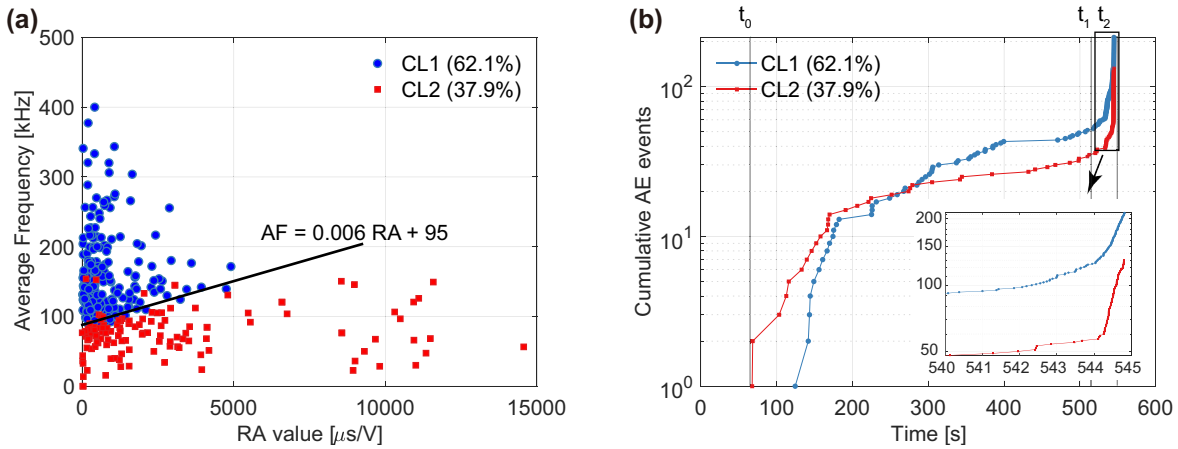

Figure 3.18: (a) Illustration of the clustering results of AE data in RA value versus AF plan. (b) The cumulative number of AE data in two clusters versus loading time.

with the results of the mortar specimen, the proportions of clusters are similar, which allowed us to draw a separation line having the same slope (AF = 0.006 RA+95) between

the two clusters. Figure 3.18(b) shows the evolution of CL1 and CL2 during the test. The evolution of the two clusters are approximately equivalent before 300 s, then more tensile cracks occurred up to the end of the first stage. The experimental results show that in the first stage, more shear cracks are formed in the concrete specimen than in the mortar specimen (see Figure 3.11(b)). In the second stage (t_1 to t_2), as it can be seen from the slope in the insert, cluster CL2 has a higher evolution speed than cluster CL1.

Table 3.5 presents average value and the coefficient of variation (COV) of the six features of the two clusters. Indeed, it can be observed that AE events in cluster CL1 have lower rise time and higher frequency (AF and CF) and AE events in cluster CL2 have higher rise time and lower frequency, which correspond to the relevant RA value and AF. These results are similar to the clustering results in mortar specimen as presented in Table 3.4.

Cluster		Amplitude [dB]	Rise time [µs]	FC [kHz]	Counts	AF [kHz]	RA value [µs/V]
CL1	Average	50.7	31.3	449.7	53	165.6	758
	COV	17.4%	100.9%	11.1%	90.3%	53.1%	113.3%
CL2	Average	47.5	114.6	297.4	39	74.9	3853
	COV	12.9%	148.8%	15.7%	95.5%	42.6%	143.1%

Table 3.5: Average results of 6 features calculated from AE data related to the two clusters (CL1 and CL2) in concrete specimen.

Numerous researchers studied the link between AE waveforms and crack modes in connection with the elastic waves generated by the different modes of crack tips [Aggelis, 2011, Aggelis et al., 2012, Aldahdooh and Bunnori, 2013]. When a tensile event occurs, due to the opposite displacement of the sides vertical to the crack plane, a transient volumetric change occurs in the location of the crack tip. Therefore, most of the energy is released in the form of a longitudinal wave (P-wave). Note that in such a case, only a small amount is released in the form of transverse wave (S-wave), whose velocity is relatively low. Thus, the major part of energy arrives quite early within the waveform which favors a short rise time (RT) and small RA value. On the other hand, under shear cracking the sides of the crack move in opposite directions but in parallel to the crack plane, which introduces a change of shape deformation instead of volume deformation. Most of the emitted energy is in the form of S-wave and only a small amount is emitted in the form of P-wave. Therefore, the major part of energy (maximum amplitude) arrives late, leading to longer RT and consecutively high RA value.

Typical AE waveforms of CL1 and CL2 and their time-frequency representation (TFR) are presented in Figure 3.19. The TFR is the scalogram (squared modulus of the continuous wavelet transform) of two AE signals computed by continuous wavelet transform. In general, the AE waveform with a shorter rise time and lower duration usually indicate a tensile crack (see Figure 3.19(a)) and its TFR depicts high energy area, which is located in the frequency range of $\simeq$ 500 - 600 kHz with a short duration (see Figure 3.19(b)). In contrast, the waveform of the shear crack has a longer rise time as in Figure 3.19(c), and its high energy area is locally distributed in the frequency range of $\simeq$ 200 - 300 kHz with a longer duration which is illustrated in Figure 3.19(d).

Finally, we note that in the mortar and civil engineering concrete, when submitted to quasi-static bending tests, many studies have described the detected AE hits as originating from small events related to the matrix cracking [Carpinteri and Massabo, 1997, Soulioti et al., 2009, Aggelis, 2011, Farnam et al., 2015, Carpinteri et al., 2016]. For in-

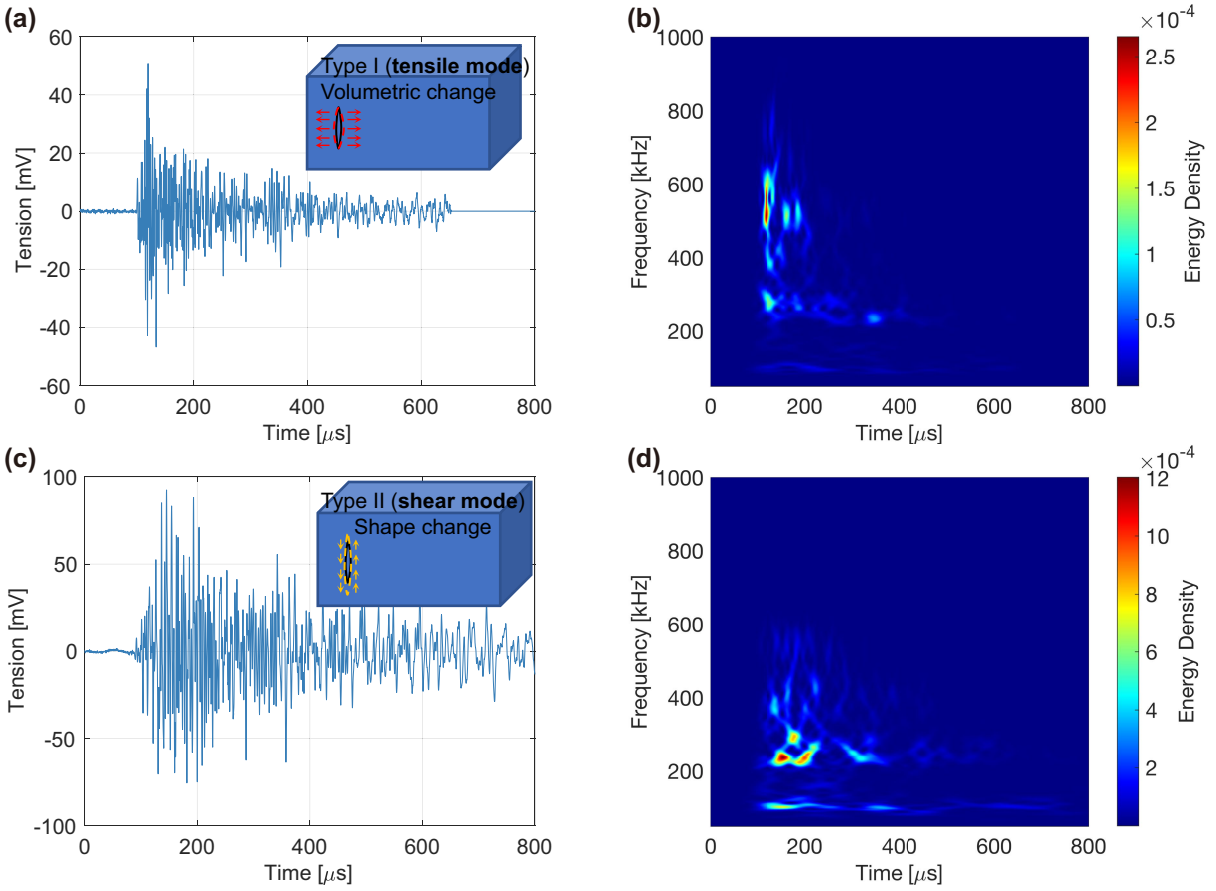

Figure 3.19: The classical AE waveform associated with two damage mechanisms and their TFRs. Plots (a) and (b) for tensile matrix cracking (CL1); plots (c) and (d) for shear matrix cracking (CL2).

stance, in [Farnam et al., 2015], it has been reported that for concrete with w/c = 0.5, the captured AE events during the splitting test belong mostly to crack formations within the matrix due to its relatively lower strength, see also [Shah et al., 1995]. This is the reason for which mortar and concrete specimens have almost the same peak load in three-point bending tests: the stress concentration mainly occurs in the matrix, which becomes large enough to initiate micro-crack coalescence. With the applied load increasing, matrix cracking continues to coalesce until the creation of a localized main crack. In this configuration, nearly all the micro-cracks belong to the matrix and the interface between matrix and aggregates may not be damaged before the main crack formation [Mehta and Monteiro, 2006].

On the other hand, unsupervised pattern recognition results show that even in the absence of AF and RA as input features, AE data were still clustered into two clusters. The visualization of clusters in the RA-AF plan added valuable information related to the presence and evolution of shear and tensile cracks.

At this stage, the manufactured concrete samples and the unsupervised pattern recognition have only allowed obtaining two clusters of the recorded AE hits, representing two cracking modes. In order to go beyond this observation, we propose in the following to study a new material 'polymer concrete' and will try to characterize damage mechanism in conjunction with the involved constituents of the polymer concrete samples.

3.4 Polymer Concrete

3.4.1 Introduction

Polymer concrete (PC) is a kind of composite material which consists of mineral fillers (gravel, sand, ...) and a polymer binder. In comparison with conventional cement concrete, it is made by replacing the cement hydrate binders with resin. Its properties such as mechanical strength, adhesion, watertightness, chemical resistance, freeze-thaw durability and abrasion resistance are generally improved to a great extent by polymer replacement [Toufigh et al., 2016]. On the other hand, disadvantages of polymer concrete include high costs, odor thereof especially in the production process, toxicity and flammability of polymer materials and their poor resistance to high temperatures [Bedi et al., 2013]. To this end, research and development of polymer concrete have been initiated from the 1950s.

3.4.2 Specimens and mechanical tests

The considered polymer concrete in this study is made in the laboratory following the same protocol described for the civil engineering concrete. The epoxy is used as polymer, where the liquid resin mixture consists of two parts: the liquid resin (Sicomin SR-1500) and the hardener (Sicomin SD 2505) with resin/hardener mix ratio of 100:33 (100:37 in volume). Aggregates are the most important part of polymer concrete as they constitute the major part of its total volume and vastly influence its behavior. According to [Marec, 2008] and [Berbaoui, 2010], two kinds of aggregates (fine sand and coarse gravel) can be used to prepare polymer concrete specimens. The aggregates were dried to ensure a good bonding quality between the polymer and the mineral filler (see Table 3.6).

Specimen size(mm)	$200 \times 40 \times 40$
Epoxy resin	Sicomin SR 1500
Hardener	Sicomin SD 2505
Fine aggregates size (mm)	0.5
Coarse gravel size (mm)	4

Table 3.6: Constituents of polymer concrete samples.

In order to identify the different damage mechanisms of this heterogeneous material (matrix cracking, interfacial debonding, etc.), we manufactured different samples with different formulations in terms of matrix and reinforcement (see Table 3.7). Mechanical

	Resin (%)	Gravel (%)	Fine sand (%)
Type-I	40 %	60 %	0 %
Type-II	40 %	0 %	60 %
Polymer concrete	40 %	30 %	30 %

Table 3.7: Volume fraction of constituents of specimens.

testing of these specific samples enables us to more easily correlate the detected AE signals

with the damage mechanisms. By using these specific specimens (Type-I and Type-II), the number of damage mechanisms and their frequency of occurrence were controlled in the experiments. The results of these specific specimens were also used to verify the identification conducted on polymer concrete samples.

All the specimens were loaded under the same conditions as for civil engineering concretes using three-point bending tests with a distance between external supports equal to 160 mm and under displacement control conditions with a constant crosshead speed of 2 mm/min. Flexural strength and flexion stress were computed and for each type of specimen, where three specimens were tested each time to determine the flexural strength. During the mechanical tests, the acoustic activity was monitored using the previously described AE system with two sensors (see section 3.1.2 for detail).

Acoustic emission monitoring of mechanical tests was performed using the acquisition setup presented in Table 3.2. Figure 3.20 illustrates the Laplacian score (LS) of the initially considered 15 AE features.

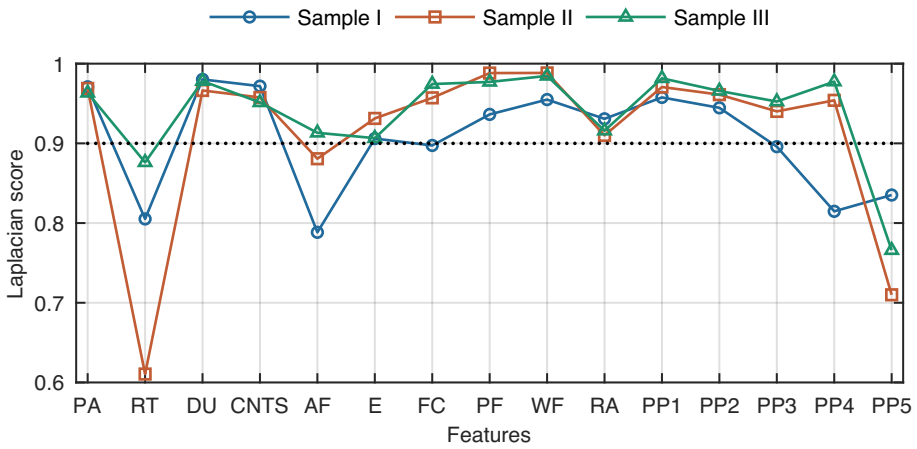

Figure 3.20: Feature selection by using Laplacian score for all tested specimens Sample Type-I, Sample Type-II and polymer concrete (Sample Type-III). The AE features with Laplacian score bigger than 0.9 will be used in this study.

Then the same feature selection for all PC samples was performed on a Laplacian Score higher than 0.9. We recall that a larger score indicates a higher clustering ability of the investigated feature. Based on this criterion, 11 features are chosen for clustering analysis namely: peak amplitude, duration, counts, energy, frequency centroid, peak frequency, weighted frequency, RA value, PP1, PP2, and PP3, as presented in Table 3.8.

No.	Features	Dimension	No.	Features	Dimension
1	Peak Amplitude (PA or A)	dB	7	Weighted Frequency (WF)	kHz
2	Duration (DU)	µs	8	RA value (RA)	µs/V
3	Counts (CNTS)		9	Partial Power 1	
4	AE Energy (E)	aJ	10	Partial Power 2	
5	Frequency Centroid (FC)	kHz	11	Partial Power 3	
6	Peak Frequency (PF)	kHz			

Table 3.8: Selected features for AE clustering analysis based on Laplacian Score (LS>0.9).

3.5 Damage characterization of 'Type-I' specimen

Three-point bending tests were performed on 'Type-I' specimens which are composed of 60% gravels and 40% epoxy resin in volume fraction (see Table 3.7).

3.5.1 Global Observation

Figure 3.21(a) depicts the evolution of AE signal amplitudes as a function of the applied load and loading time. Here again, only the AE hits detected by both sensors are taken into account. In addition, according to Equations 3.1 and 3.2, the flexural stress–strain curve is shown in Figure 3.21(b).

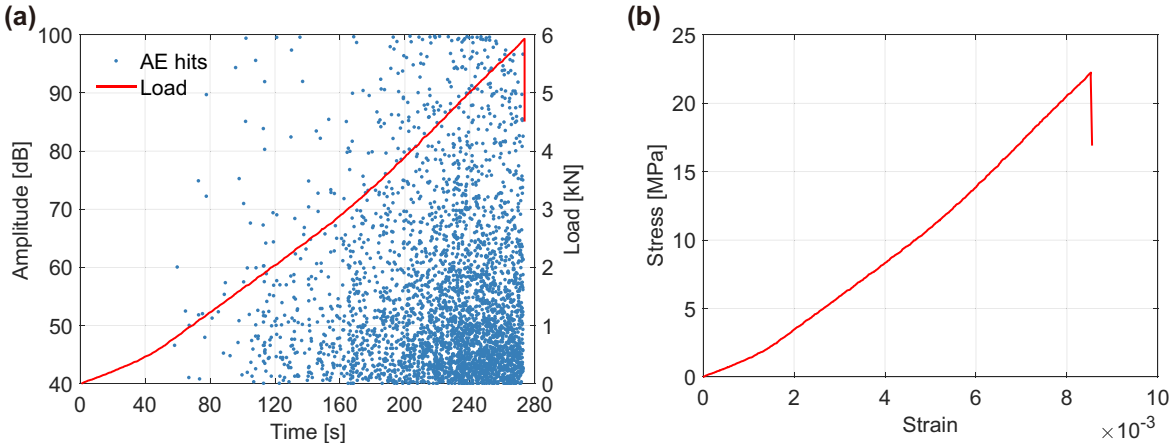

Figure 3.21: Three-point bending test results for Type-I specimen: (a) Evolution of amplitude of AE signals and applied force versus loading time. (b) Flexural stress–strain behavior during the test.

Figure 3.22(a) shows the cumulative AE energy and the AE signal rate as a function of loading time. The AE signal rate is computed by recording AE hits per unit time,

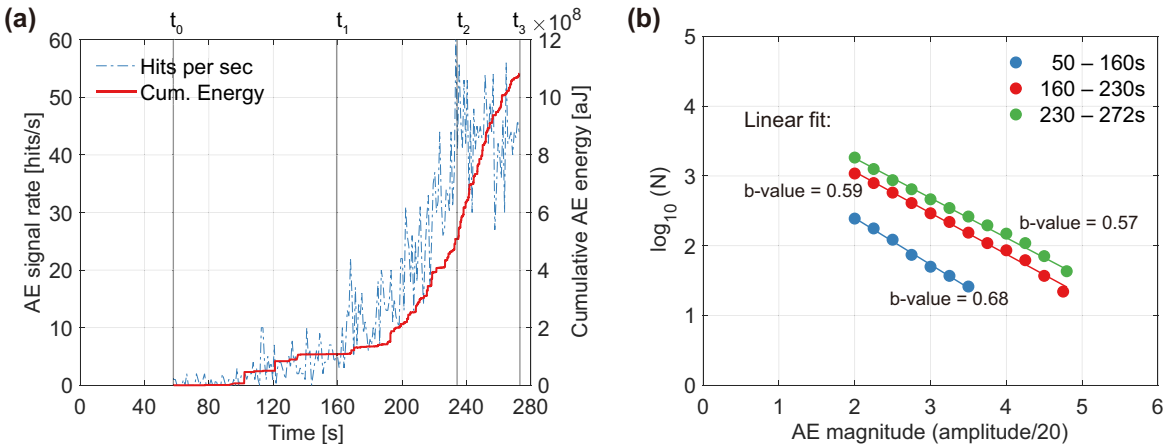

Figure 3.22: (a) Evolution of AE signal rate and cumulative AE energy versus loading time. (b) Representation of log-(N) versus amplitude-magnitude chart and calculated AE based b-value.

taken as '1 s'. The evolution of AE signals can be divided into three stages determined by

the following times $t_0 = 50\,\text{s}$, $t_1 = 160\,\text{s}$, $t_2 = 230\,\text{s}$ and $t_3 = 272\,\text{s}$. The AE-based b-value is computed for these three stages as illustrated in Figure 3.22(b):

– Stage 1 (from t_0 to t_1): the AE activity is weak (AE signal rate < 10 hits/s) and the detected AE signals have small energy. By linearly fitting the data, AE based b-value during this stage is $\simeq 0.68$.

– Stage 2 (from t_1 to t_2): the AE activity evolves linearly, increasing thus the cumulative AE energy. The AE based b-value in this stage is $\simeq 0.59$.

– Stage 3 (from t_2 to $t3$): more than 50 AE hits are recorded per second, showing the intense AE activity as the final rupture of the specimen approaches. At $\simeq 272\,\text{s}$, the specimen is split into two parts and the bending test stops. The AE based b-value during this stage is $\simeq 0.57$.

The decrease of b-values from 0.68 to 0.57 during the mechanical test shows that the fracture level increases in loading time (or applied force). Note that this value is much smaller than those measured in cementitious concrete specimens [Sagar et al., 2012, Carpinteri et al., 2009]. If we consider the acoustic activity from stage 2 (i.e. neglect the weak AE activity), the average frequency (AF) and the RA values can be computed by averaging their respective values of every 100 recent hits to investigate the evolution of tensile crack and shear crack during the test as shown in Figure 3.23. Indeed, the two parameters

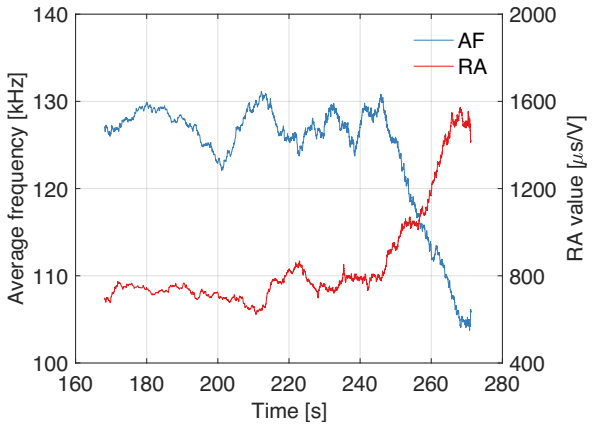

Figure 3.23: Moving average of RA value and average frequency (AF) versus loading time.

AF and RA seem to evolve according to each other, where the decrease of AF and the increase of RA always appear simultaneously. In particular, an abrupt variation was noted during the last 20 second before the fracture of the specimen, where a large increase of RA and a huge decrease of AF can be observed. This situation coincides with the highest AE signal rate ($\simeq 50$ hits/s) shown in Figure 3.22(a). This result also mentioned on some cementitious concrete [Soulioti et al., 2009, Ohno and Ohtsu, 2010, Carpinteri et al., 2016], which was interpreted by the fact that it corresponds to the appearance of a large number of shear cracks before the final fracture within a short time.

3.5.2 Unsupervised pattern recognition

Here, AE signals were clustered using an unsupervised pattern recognition analysis, which is based on the principal component analysis (PCA) and k-means algorithm. The selected

features are processed using the PCA algorithm which provides the variance percentage and cumulative variance of each principal component of 'Type-I' specimen. Figure 3.24(a) shows that the first three principal components produce $\simeq 90.8\,\%$ of the total variance, meaning that these three principal components are sufficient for the k-means algorithm. Then, optimal clustering is obtained with two clusters according to the minimum values

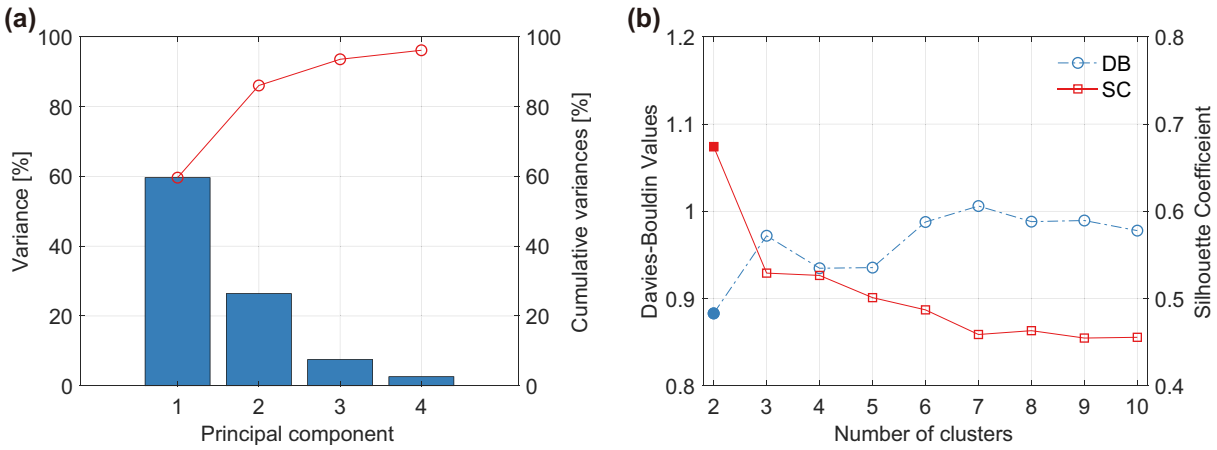

Figure 3.24: (a) The variance (bars) of first 4 principal components of sample Type-I. The y axis on the right side shows the cumulative variances (line). (b) The number of clusters evaluated by Davies-Bouldin value and Silhouette Coefficient (y axis on the right).

of the Davies and Bouldin (DB) index and the maximum of Silhouette Coefficient (SC) as shown in Figure 3.24(b). Indeed, the cluster number is two with SC $\simeq 0.87$ and DB $\simeq 0.62$, which verifies that the quality of clustering is acceptable [Gutkin et al., 2011]. The k-means clustering algorithm can therefore be applied to AE data with three principal components as input features and two clusters ($k = 2$).

Figure 3.25 presents the projection of the two clusters (CL1 and CL2) of AE data in the 'Type-I' specimen. We can see that AE signals of both clusters can be easily sepa-

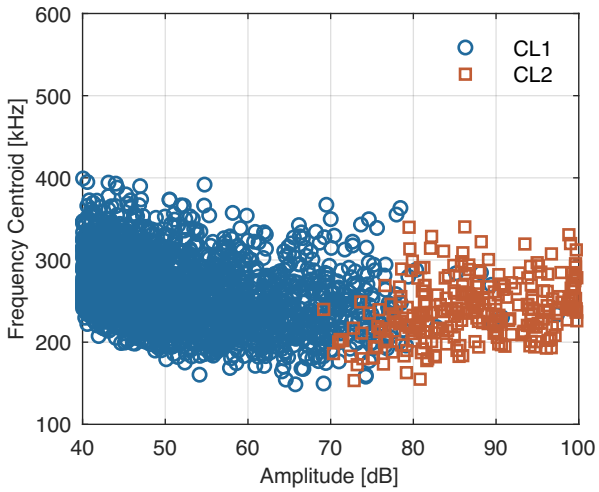

Figure 3.25: Illustration of the AE data in the two-dimensional plane: Amplitude (dB) versus Frequency Centroid (kHz) with clustering results of Type-I specimen.

rated in Amplitude. Note that within this sample, three main damage mechanisms can

be created, namely: matrix cracking, gravel-resin debonding and gravel breakage. Based on the post mortem observations and other authors' observations as well [Marec, 2008, Berbaoui, 2010], CL1 is the AE cluster with amplitude between $\sim$ 40 dB and 70 dB corresponds to matrix cracking which is in accordance with tests performed in epoxy resin samples. On the other hand, CL2, which is more energetic ($\sim$ 70 dB to 100 dB), corresponds to gravel-resin debonding and gravel breakage.

Figure 3.26 depicts the evolution of the moving average of RA and AF in time for the two clusters. For cluster CL1, the moving average of RA and AF are approximately

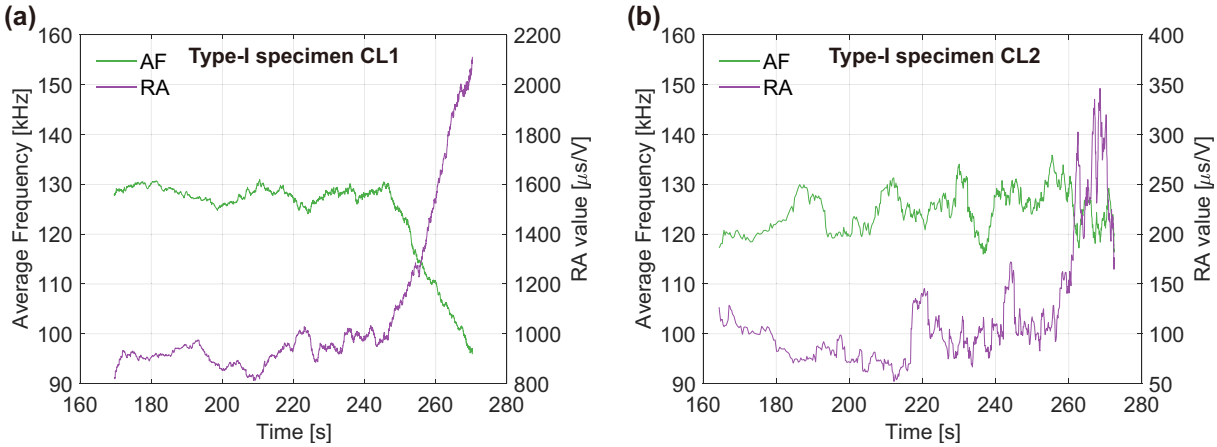

Figure 3.26: Illustration by moving average of RA value and average frequency in 2 clusters (a) CL1 and (b) CL2 versus time during the mechanical test.

constant up to $\simeq$ 250 s then the increase of RA and the decrease of AF are significant. However, the evolution of AF and RA for CL2 presents fluctuations during all the test until the moment where RA increase from $\simeq$ 100 μs/V to $\simeq$ 350 μs/V. The contrast between CL1 and CL2 can be explained by the fact that the main crack is developed within the matrix where a large number of shear cracks appear in the epoxy resin before the final rupture. However, the tensile/shear transition doesn't seem to appear clearly at the interface. Finally, note that the initial stable average AF value is $\simeq$ 130 kHz for both clusters. The average RA value is $\simeq$ 900 μs/V and $\simeq$ 70 μs/V for cluster CL1 and CL2, respectively. This remarkable difference is reasonable since signals in CL2 have a high amplitude (typically 30 dB higher) and rise time in the range of $\simeq$ 10–500 μs, which corresponds to low RA values.

3.6 Damage characterization of 'Type-II' specimen

In this section, three-point bending tests are performed on 'Type-II' specimens composed of 60% sand and 40% epoxy resin in volume fraction (see Table 3.7).

3.6.1 Global Observation

Figure 3.27(a) shows the evolution of AE hits amplitude and applied load versus loading time during the bending test. In addition, the flexural stress-strain curve is shown in Figure 3.27(b). When the flexural strength of the material is reached ($\simeq$ 34.2 MPa),

a macroscopic main crack is formed and propagates through the cross-section of the material. At that moment, the specimen is split into two pieces and the sudden decrease of the load line also depicts this occurrence.

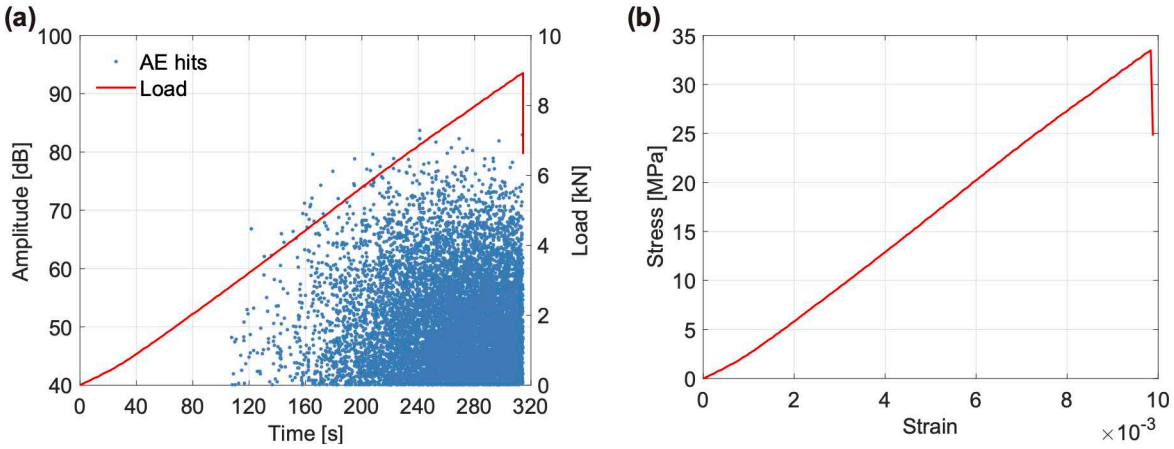

Figure 3.27: Three-point bending test results for one Type-II specimen: (a) Evolution of amplitude of AE signals and applied force versus loading time. (b) Flexural stress–strain behavior during the mechanical test.

Type-II specimens exhibit a rich AE activity and withstand more charge than Type-I specimens, which means that the fine sand provides more flexural strength to specimens than gravels. In this resin-sand specimen, all of the AE signals are between $\simeq$ 40 dB and $\simeq$ 80 dB and the involved amplitudes remain lower than the ones observed in resin-gravel samples. Therefore, the gravel-resin debonding seems to generate AE events more energetic than matrix cracking and sand-resin debonding. Here, we assume that fine sand cannot be damaged under the three-point bending tests. These observations are in accordance with the results mentioned in the reference [Marec, 2008].

For the damaging of Type-II specimens, the AE signal rate is computed by recording AE hits per unit time, taken '1 s'. As illustrated in Figure 3.28(a), the cumulative AE energy and the AE signal rate are presented as a function of loading time. Experimental

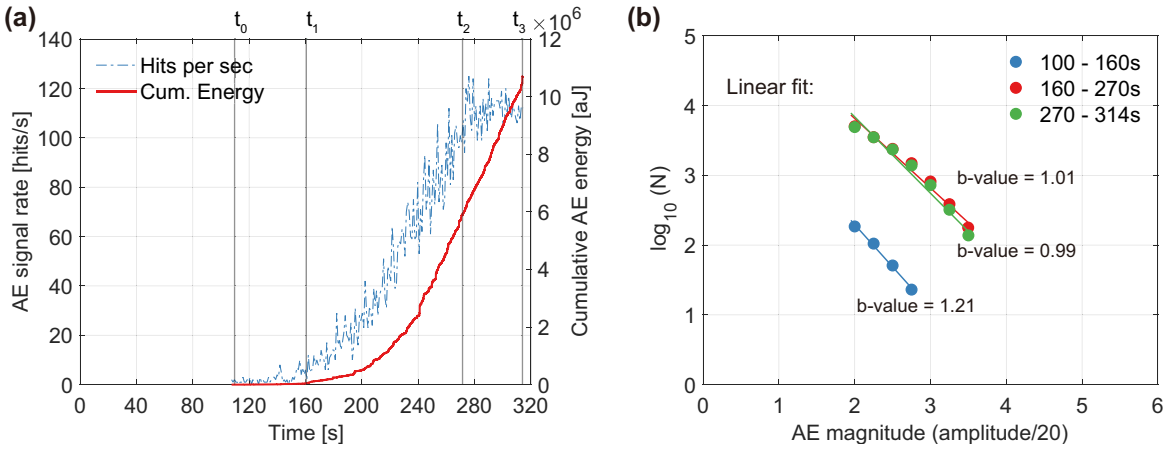

Figure 3.28: (a) Evolution of AE signal rate and cumulative AE energy versus loading time (b) Representation of log-frequency versus amplitude-magnitude chart and calculated AE based b-value.

results show that the evolution of AE signals can a priori be divided into three stages

determined by the following times $t_0 = 100\,\text{s}$, $t_1 = 160\,\text{s}$, $t_2 = 270\,\text{s}$ and $t_3 = 314\,\text{s}$. Then, AE-based b-values are computed for each stage as shown in Figure 3.28(b):

– Stage 1: $[t_0, t_1]$ The AE activity is weak (AE signal rate $< 10\,\text{hits/s}$) and the detected AE signals have small energy. By linearly fitting the data, AE based b-value in this stage is $\simeq 1.21$.

– Stage 2: $[t_1, t_2]$ The evolution of the AE signal rate evolves linearly and so does the cumulative AE energy. During this stage, AE based b-value is $\simeq 1.01$.

– Stage 3: from t_2 to the failure of the specimen. More than 110 AE hits are recorded per second as we get close to the final fracture of this specimen. At $\simeq 314\,\text{s}$, the specimen is split into two parts and bending test stops. The AE based b-value during this stage is $\simeq 0.99$.

For this specimen, the b-values decrease as a function of the applied force from 1.21 to $\simeq 1$, where the fracture process is approximately the same in stages 2 and 3. These b-values, compared to the ones in Type-I specimens, are higher which shows that the proportion of micro cracks such as sand-resin debonding is higher than the debonding in Type-I specimen. Lower b-value in Type-I specimen refers more likely to macro cracks related to gravel-resin debonding and/or matrix cracking. During the Type-II specimen testing, the sand-resin debonding occur more frequently and generate more AE events than gravel-resin debonding, but with lower energy.

Figure 3.29 depicts the evolution of RA and AF versus loading time (from 160 s to the fracture of the specimen) for Type-II specimen. Each point of the curves corresponds to the moving average for 100 consecutive AE signals. The results show that as the loading force increases, RA value is almost stable and increase at the end of the test, whereas AF is gradually decreasing until the end of the experiment, where it shows a sudden decrease especially during the last 20 s. Note that equivalent behavior has been found in Type-I specimen, meaning that during the final stage before the specimen fracture, we create more shear cracks.

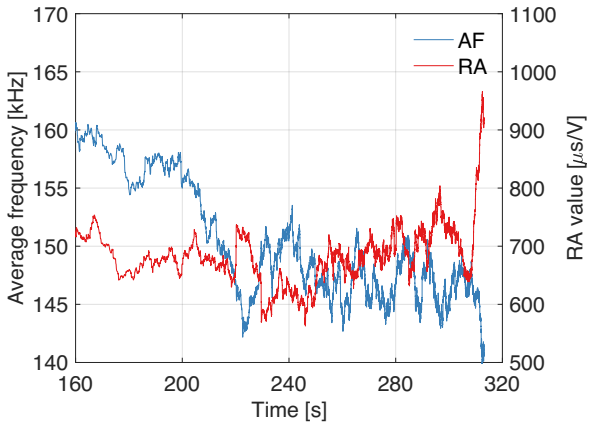

Figure 3.29: Moving average of RA value and average frequency (AF) versus loading time.

However, we think that the multiplication and dispersion of the contact surfaces between the matrix and the reinforcements (fine sand) is the origin of the significant fluctuation that we observe in the evolution of RA and AF as a function of loading time. This point will also be verified during the application of unsupervised pattern recognition, which will be described in the following.

3.6.2 Unsupervised pattern recognition

The selected features are processed using the PCA algorithm. Figure 3.30(a) shows that on the basis of the variance and cumulative variance, we can reasonably choose three principal components for the k-means algorithm, where the cumulative variance exceeds $\simeq 93\%$. Optimal clustering is obtained with two clusters according to the minimum values of Davies and Bouldin (DB) index $\simeq 0.55$ and maximum of Silhouette Coefficient (SC) $\simeq 0.81$ which are shown in Figure 3.30(b).

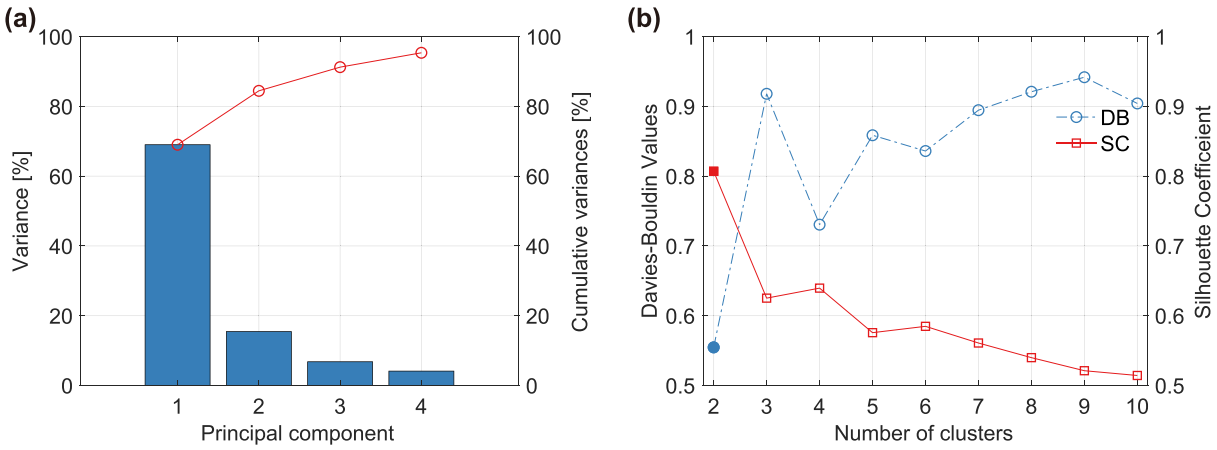

Figure 3.30: (a) The variance (bars) of first 4 principal components of Type-II specimen. The y axis on the right side shows the cumulative variances (line). (b) The number of clusters evaluated by Davies-Bouldin value and Silhouette Coefficient (y axis on the right).

Figure 3.31 shows the projection of the clustering results of AE data in Type-I and Type-II specimens where two clusters have been separated. Comparison between the two specimens shows that the unsupervised clustering approach has the ability to separate AE signals based on the chosen features. As mentioned earlier, CL1 and CL2 are the two AE clusters found in Type-I specimens. The use of new constituents in Type-II specimens reasonably suggests that CL3 corresponds to a new damage mechanism, which is the sand-resin debonding. These results confirm that high amplitude signals which appear in

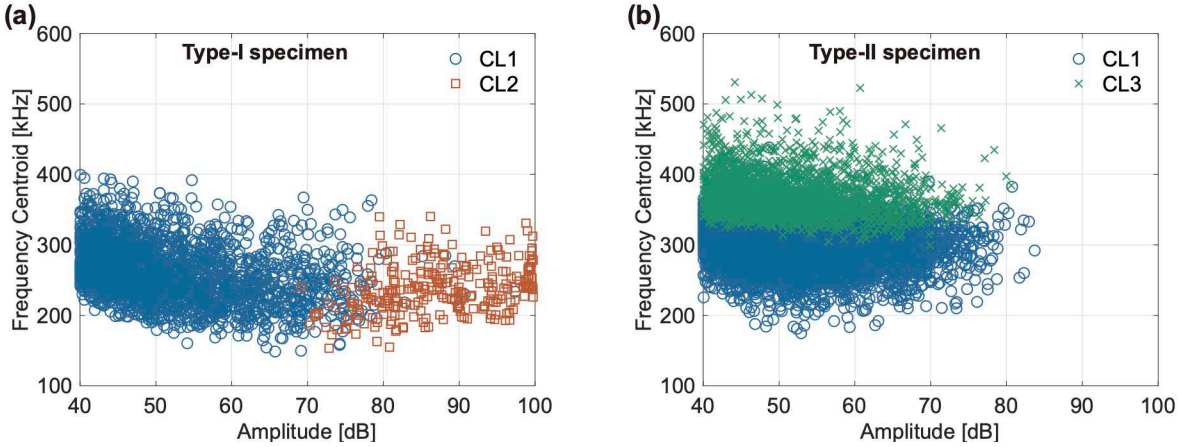

Figure 3.31: Illustration of the AE data in the two-dimensional plane: Amplitude [dB] versus Frequency Centroid [kHz] with clustering results of (a) Type-I specimen and (b) Type-II specimen

Type-I specimen correspond to the gravel-resin debonding. The frequency and amplitude characteristic of the three clusters can be therefore presented as shown in Table 3.9.

AE cluster name	Amplitude [dB]	Frequency Centroid (FC) [kHz]
CL1 (matrix cracking)	40–75 dB	200–300 kHz
CL2 (gravel-resin debonding)	70–100 dB	100–350 kHz
CL3 (sand-resin debonding)	40–70 dB	300–500 kHz

Table 3.9: Amplitude and frequency characteristic of three AE clusters.

Figure 3.32 shows the evolution of RA and AF as a function of loading time for two clusters CL1 and CL3. The global trend for the two characteristics is in accordance with the observation made earlier regarding the evolution of the crack mode from tensile to shear. Here again, the multiplication and dispersion of the tiny contact surfaces between the resin and sand, generates fluctuation in RA and AF for both clusters. We also note that CL3 signals have high AF value, meaning that signals are impulsive (short rise time and short duration). The work carried out made it possible to study the damage mechanisms separately, where the mixing was only carried out between one constituent (sand or gravel) and the matrix (resin). This sample definition allowed identifying three main classes of damage, their evolution during the mechanical test was detailed. The following study concerns the characterization of damage of polymer concrete samples using the analysis methods presented above.

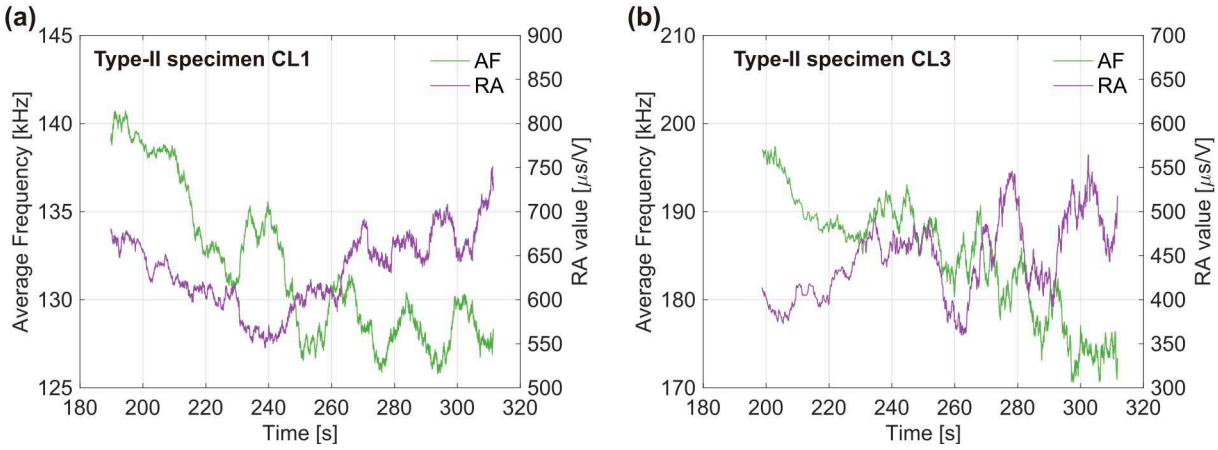

Figure 3.32: Illustration by moving average of RA value and average frequency in two clusters (a) CL1 and (b) CL3 versus time during the bending test of specimen Type-II.

3.7 Damage characterization of polymer concrete specimen

In this section, three-point bending tests are performed on PC specimens composed of 30% sand, 30% gravel and 40% epoxy resin in volume fraction (see Table 3.7).

3.7.1 Global Observation

Figure 3.33(a) shows experimental results corresponding to a PC sample where the distribution of AE signals and the applied load are plotted versus loading time during a three-point bending test. In addition, the relation of flexural stress-strain curve is illustrated in Figure 3.33(b) where the flexural strength is $\simeq 22.1\,\text{MPa}$. All bending tests showed a sudden decrease of the applied load around the failure of specimens. This experimental observation was also mentioned in [Shokrieh et al., 2011, Heidari-Rarani et al., 2014, Hashemi and Jamshidi, 2015] showing the brittle behavior of resin-based composites when submitted in the flexural tests.

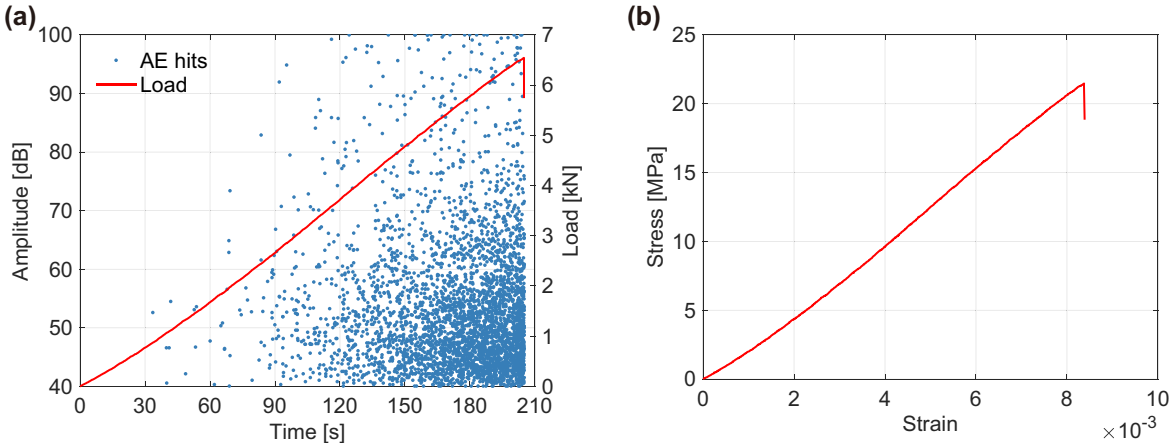

Figure 3.33: Three-point bending test results for one polymer concrete specimen: (a) Evolution of amplitude of AE signals and applied force versus loading time; (b) Flexural stress-strain behavior during the test.

Figure 3.34(a) presents the cumulative AE energy and the AE signal rate versus loading time; the evolution of the AE activity has three stages. The results show that the evolution of AE signals can a priori be divided into three stages determined by the following times $t_0 = 60\,\text{s}$, $t_1 = 120\,\text{s}$, $t_2 = 190\,\text{s}$ and $t_3 = 208\,\text{s}$. For each stage, the AE-based b-value is computed as illustrated in Figure 3.34(b):

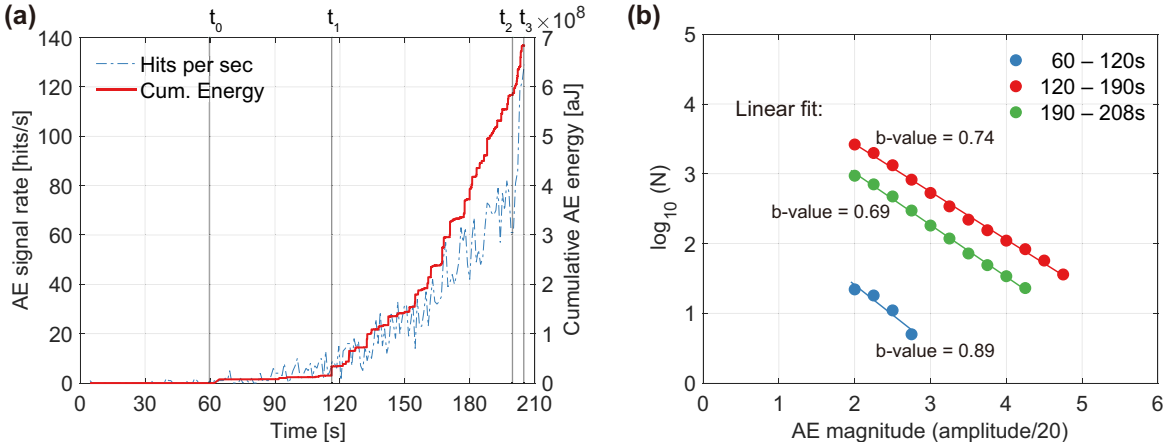

Figure 3.34: (a) Variation of RA value and AF versus loading time. (b) Representation of log-(N) versus amplitude-magnitude chart and calculated AE based b-value during three stages.

– Stage 1: $[t_0, t_1]$ The rate of AE activity is low (<10 hits per second) and the detected AE signals have small energy. By linear fitting the data, AE based b-value in this stage is $\simeq 0.89$.

– Stage 2: $[t_1, t_2]$ The evolution of the AE signal rate has a linear growth which increased the cumulative AE energy. During this stage, the AE based b-value in this stage is $\simeq 0.74$.

– Stage 3: $[t_2, t_3]$ The number of failure mechanisms is very high and the AE signal rate has increased up to more than $\simeq$ 120 hits per second. This intense AE activity indicates the imminent arrival of the final break of the specimen. During this stage, the AE based b-value during this stage is $\simeq 0.69$.

The PC specimens have b-values between 0.9 and 0.7, which is between the minimum value of the Type-II specimen and the maximum value of the Type-I. The AE-based b-value can, therefore, be used as an index of damage level, due to the influence of damage mechanisms on the increase and/or decrease of b-value. Figure 3.35 depicts the variation of RA value and Average Frequency (AF) versus loading time (from $\simeq$ 120 s until the fracture of the specimen) for PC specimen. Each point of the curves corresponds to the moving average for 100 consecutive AE signals. It can be seen from the plot that in general, the RA value is increasing and AF is decreasing as a function of loading time. This observation shows that tensile crack mode is predominant in the early stages of damage before the appearance of a large number of shear cracks as we approach the break of the PC specimen. Compared with the other two specimens, the variation of RA and AF is more similar to Type-II specimen with a significant decrease in fluctuations, which is certainly linked to the presence of reinforcements. The AF decreased from $\simeq$ 155 kHz to $\simeq$ 140 kHz and RA increased up to $\simeq$ 1100 μs/V. In order to go beyond this

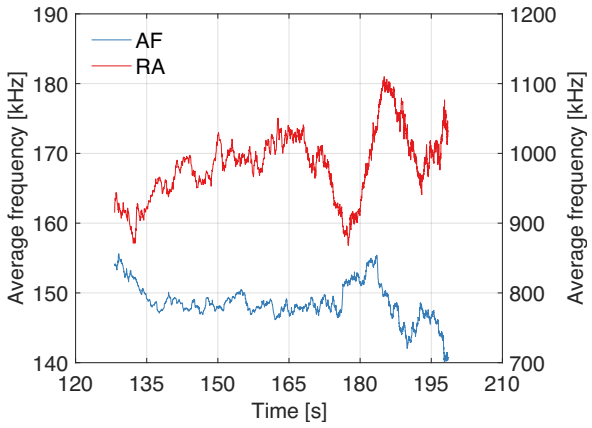

Figure 3.35: Moving average of RA value and average frequency (AF) versus loading time.

global observation, the damage process of PC specimens will be analyzed using the same unsupervised pattern recognition method, as it will be presented in the following.

3.7.2 Unsupervised pattern recognition

Figure 3.36(a) shows the variance and cumulative variance corresponding to the damaging of PC sample. The number of principal components for the k-means algorithm is chosen as three which is based on a cumulative variance is $\simeq$ 94%. Moreover, optimal clustering

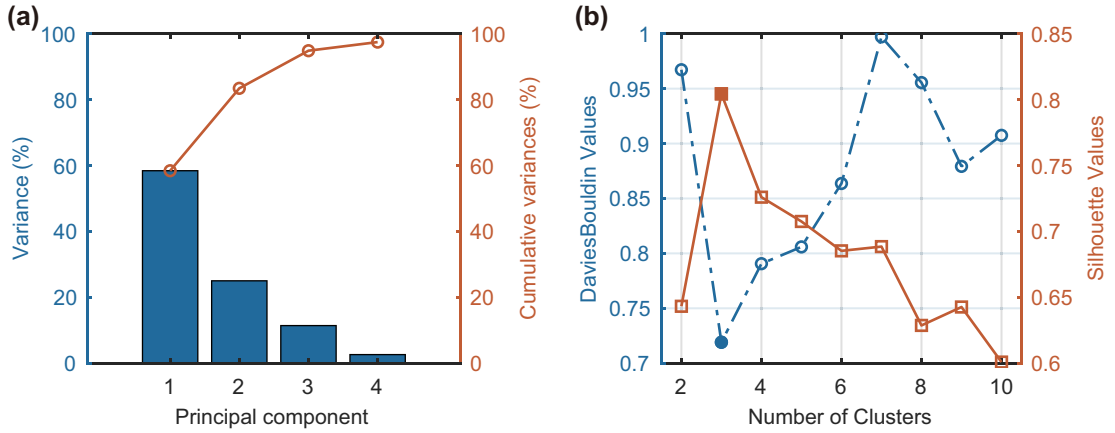

Figure 3.36: (a) The variance (bars) of first 4 principal components of PC specimen. The y axis on the right side shows the cumulative variances (line). (b) The number of clusters evaluated by Davies-Bouldin value and Silhouette Coefficient (y axis on the right).

is obtained with three clusters according to the minimum values of Davies and Bouldin (DB) index and maximum of Silhouette Coefficient (SC) as shown in in 3.36(b).

Figure 3.37 presents results of clustering of AE data and the evolution of RA and AF for each AE cluster as a function of loading time. Figure 3.37(a) shows that three clusters

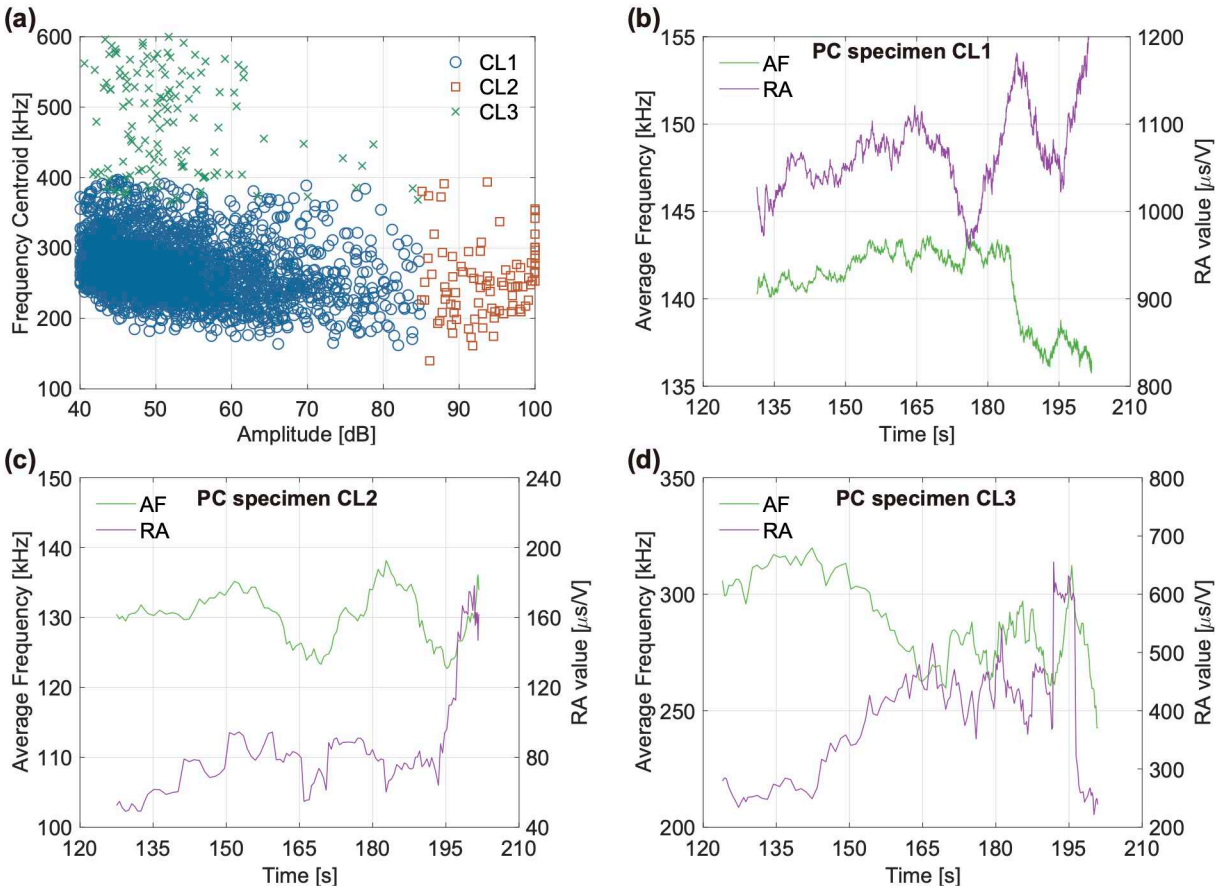

Figure 3.37: (a) Illustration of clustering results of PC specimen. Illustration by moving average of RA value and average frequency for cluster (b) CL1, (c) CL2 and (d) CL3.

can be clearly separated according to the differences between their different characteristics.

In particular, signals in cluster CL1 have small amplitude and low frequency. Cluster CL2 is mainly characterized by AE signals with high amplitude, whereas AE signals in cluster CL3 stand out for their high frequency centroid (FC) which can reach the value of 600 kHz. Note that, these results also confirm the clustering analysis performed on Type-I and Type-II specimens (see Figure 3.31). For the three clusters, we monitored the variation of RA and AF as a function of loading time as presented in Figures 3.37(b), (c) and (d). Recall that, each point of the curves corresponds to the moving average for 50 consecutive AE signals. In general, we can observe that the evolution of RA and AF is in accordance with the evolution of the cracking mode from tensile to shear. The fluctuations mentioned earlier concern the three clusters showing once again the influences of the existing contact surfaces (dispersion) in the evolution of RA and AF.

The identification of the three AE clusters shown previously on different kind of specimens was obtained by means of an unsupervised pattern recognition algorithm. Therefore, in order to confirm whether the cluster 'CL1' in a given specimen is the same as the cluster 'CL1' in another specimen, the average attribute and statistical distribution of all clusters for each specimen are compared with the box-and-whisker plots. The insert in Figure 3.38

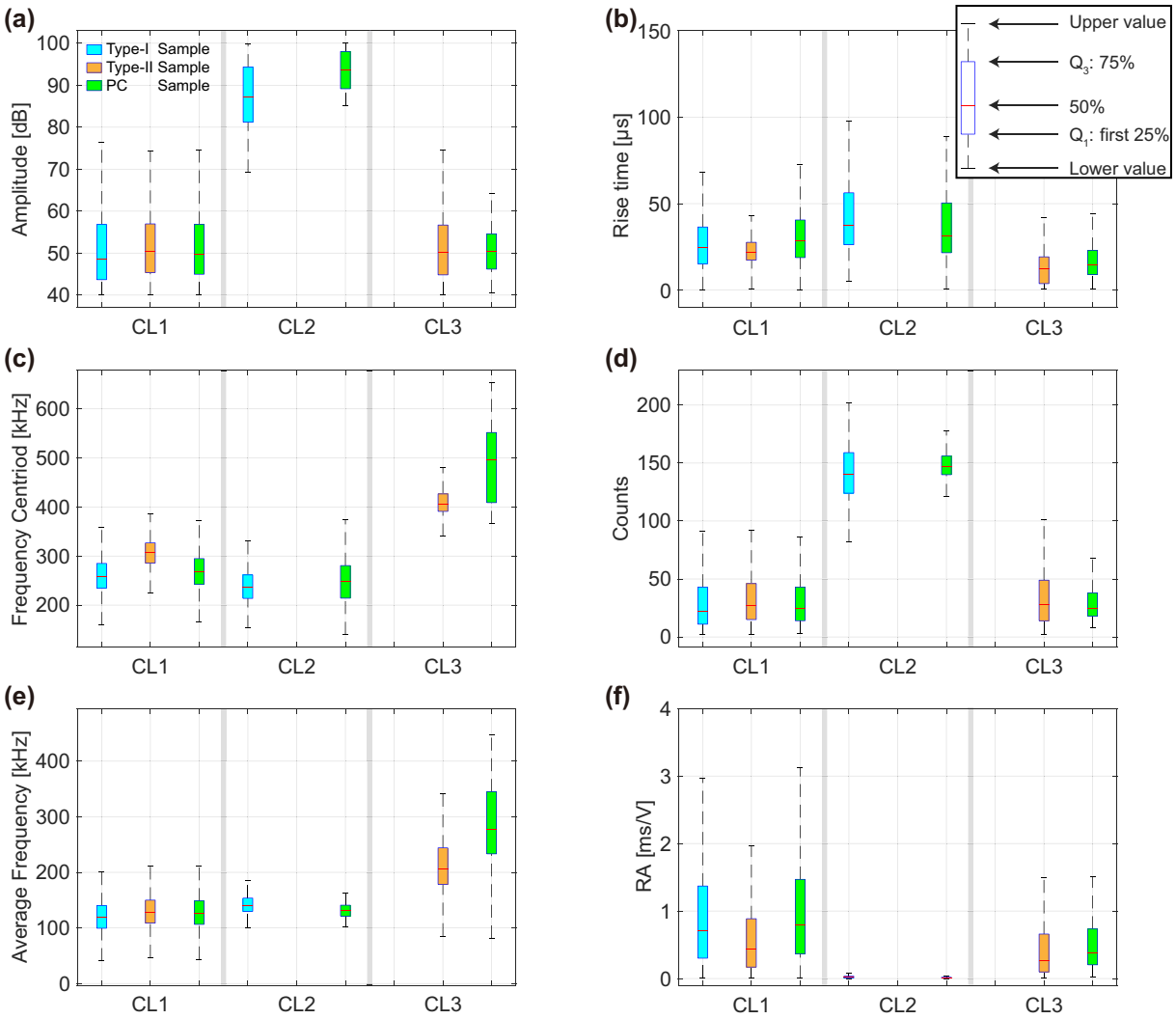

Figure 3.38: Statistical dispersion of the six AE features versus the three damage mechanisms for three specimens (Type-I,Type-II and PC). (a) Amplitude, (b) Rise time, (c) Frequency centroid, (d) Counts, (e) Average frequency and (f) RA value (in ms/V).

presents a box-and-whisker plot, where the bottom and top edges of the box indicate the first quartile Q_1 (the first 25%) and the third quartile Q_3 (75%), respectively. The median value (50%) is represented by the line cutting through the box. The whiskers indicate the lower and upper values located in the interval $[Q_1 - 1.5(Q_3 - Q_1), Q_3 + 1.5(Q_3 - Q_1)]$.

Figure 3.38 shows box and whiskers plots of the three AE clusters determined for Type-I, Type-II and PC specimens, according to the same AE features and same unsupervised clustering analysis. Through the evolution of the six considered features, we can see that cluster CL1 presents quite similar characteristics for the three types of specimens. Equivalent observations can be made for the evolution of clusters CL2 and CL3 with the presence of effects between the mean values of certain AE features such as the rise time of CL2 or the frequency centroid of CL3. Nevertheless, the existing offsets remain acceptable and the overlap between the whiskers in clearly visible despite the huge difference of the AE activity between the different inhomogeneous specimens and the complex propagation of elastic waves in such materials.

The performed study and data analysis confirm that a correspondence between the clusters of AE events and damage mechanisms is possible. Based on the unsupervised pattern recognition approach and the different experiments, we propose the following correspondences: CL1 - matrix cracking; CL2 - gravel-resin debonding; CL3 - sand-resin debonding. Figure 3.39 shows a comparison between the average values of the selected AE features corresponding to the above mentioned three clusters. Indeed, the star diagram

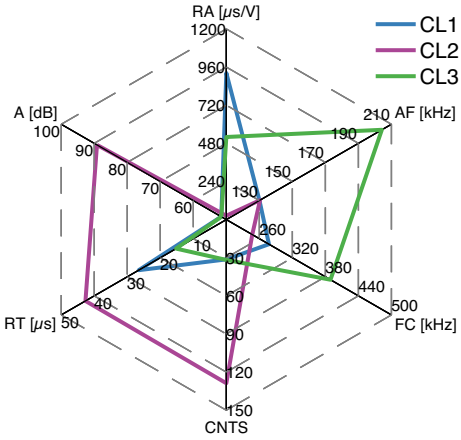

Figure 3.39: Average properties of the three AE clusters on the six features as Amplitude, Duration, Counts, Frequency Centroid, Average Frequency and RA value.

allows to appreciate the relevance of the selected features and their capacity to assign each AE signal to one of the three clusters in the configuration space. From the above, we can propose a quantitative presentation of the six AE features according to thee types of damage mechanisms, as it can be seen in Table 3.10.

Damage mechanism	Amplitude	Rise time	Frequency centroid	Counts	Average frequency	RA value
Matrix cracking	40–75 dB	20–40 μs	100–350 kHz	30–50	50–200 kHz	0–4000 μs/V
Gravel-resin debonding	70–100 dB	30–60 μs	100–250 kHz	100–200	100–200 kHz	0–100 μs/V
Sand-resin debonding	40–70 dB	10–30 μs	>350 kHz	10–50	>100 kHz	0–1000 μs/V

Table 3.10: Synthesis of 6 features calculated on AE signals related to the type of damage corresponding to a polymer concrete.

3.8 Image-based classification of AE signals.

3.8.1 Time-frequency representation of AE signals

Another way to appreciate the existing differences between AE signals is to investigate their time-frequency characteristics. Figure 3.40(a)-(f) presents three typical AE signals waveforms and their corresponding wavelet scalograms for the three clusters.

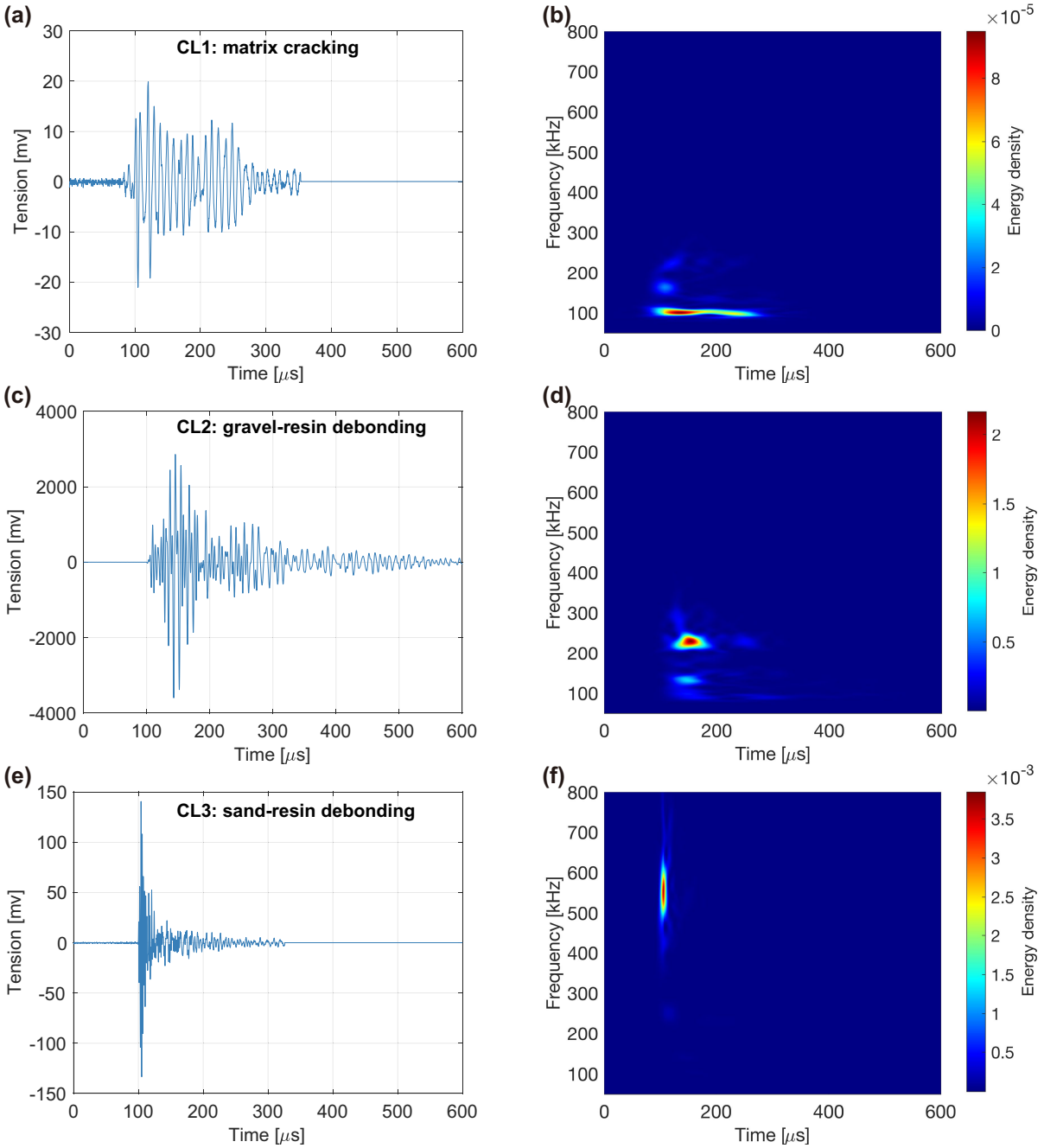

Figure 3.40: The typical AE waveform associated with three damage mechanisms and their T-F representation. Plots (a) and (b) for micro-matrix cracking; plots (c) and (d) for gravel-resin depending; plots (e) and (f) for sand-resin debonding.

The wavelet scalogram is obtained by calculating the square of the modulus of wavelet

coefficients in continuous wavelet transform (CWT) and the time-frequency representation (TFR) computed by using Morlet wavelet. Through the energy density distribution in the TFR, it can be seen that the signal in cluster CL1 has a low amplitude and a middle duration, the frequency distribution of energy is below 250 kHz, which corresponds to the matrix cracking. The AE signal corresponding to the gravel-resin debonding has a high amplitude and its energy distribution is mainly located between 200 kHz and 300 kHz. Finally, the AE signal corresponding to the sand-resin debonding has a short rise time and is, therefore, more impulsive. Correspondingly, its energy distribution is essentially between 500 kHz and 600 kHz. The continuous wavelet transform (CWT) analysis clearly shows that it is possible to classify AE signals according to their time-frequency characteristics. Indeed, the latter can be considered as an image which can serve as a basis for a learning process with a view to an automated classification. This will be developed in the case of polymer concrete in the following.

3.8.2 Image-based classification methodology

The proposed AE signal classification approach consists in the association of the continuous wavelet transform (CWT) with the convolutional neural network (CNN) algorithm. This supervised classification algorithm is applied using the following three steps:

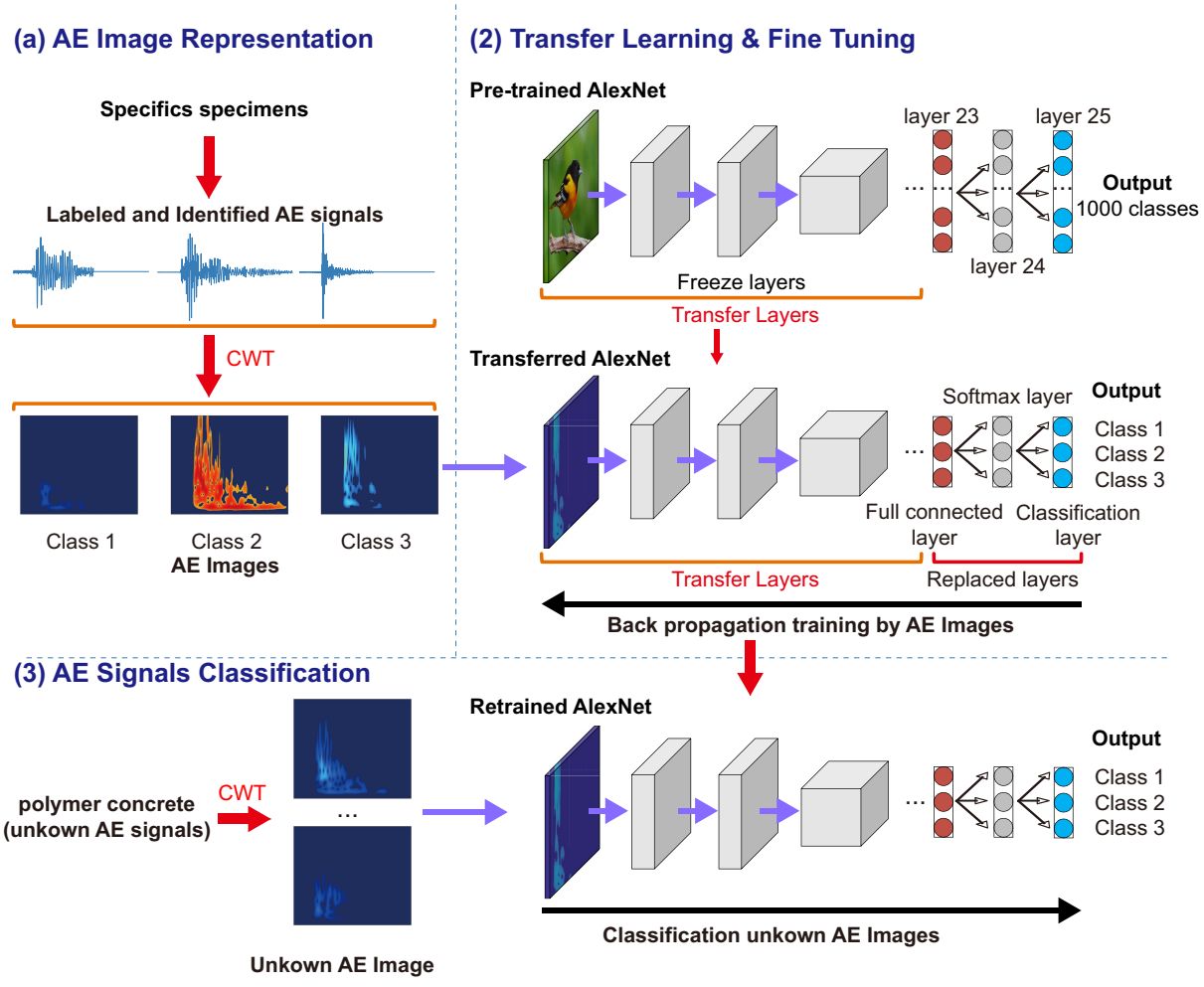

Figure 3.41: Flowchart of analysis processing.

1. Select AE signals taken from the three-point bending tests of Type-I and Type-II specimens in order to build the training dataset (i.e. AE images) with the help of the CWT.

2. Transfer learning and retrain the AlexNet network with the training dataset (i.e. AE images).

3. Classify the AE signals corresponding to the damaging of the polymer concrete (PC) specimens by using the retrained the AlexNet.

The flowchart shown in Figure 3.41 illustrates the steps involved in the process of this proposed methodology. In order to build the training dataset, 300 AE signals (100 signals for each damage mechanism) are selected from the mechanical tests applied on Type-I and Type-II specimens. In the following, we will present the application of each step on the selected AE images and will compare with the proposed new classification method and the classical method in the case of PC specimens.

3.8.3 Acoustic emission (AE) image processing

Each AE signal is first converted to AE image using the continuous Morlet wavelet transform (detail is shown in subsection 2.6.2), where 300 AE images are generated, 100 for each damage mechanism. For each damage mechanism, 80 images are used to retrain the AlexNet architecture and parameters and the rest are used for testing.

Figure 3.42 illustrates 3 typical AE image representations corresponding to the three main damage mechanisms, namely, matrix cracking, gravel-resin debonding and sand-resin debonding. The limit of frequency axis was fixed at 800 kHz and timescale was taken up to 500 μs, which is long enough to show the main part of the AE signals. Each image is 224 $\times$ 224 $\times$ 3 pixels to suit the input of AlexNet algorithm. These three types of AE images are used as input data for the training of transferred AlexNet algorithm.

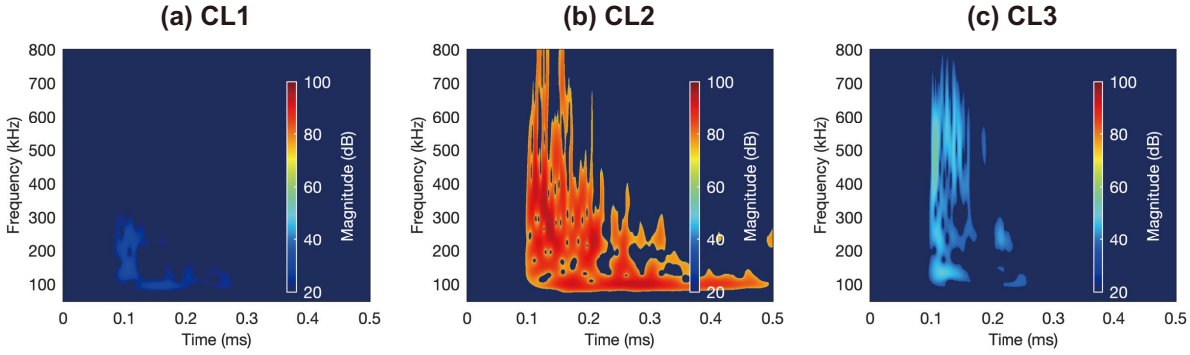

Figure 3.42: Three typical AE image representations for the corresponding damage mechanisms: (a) matrix cracking, (b) gravel-resin debonding and (c) sand-resin debonding.

3.8.4 Transfer learning and training

In order to achieve the transfer learning, the last fully connected layer with the softmax and the output layer (layer 23-25 in Table 2.2) of the pre-trained AlexNet are replaced

with a new fully-connected layer (with 3 nodes, 3 is the number of AE classes), a new softmax layer and an output classification layer.

This transferred AlexNet network was first trained with labeled AE images. The stochastic gradient descent method was used to train the network with a learning rate of 10^{-4}, where the batch size was taken as 10. The training was performed for 10 epochs, meaning the network examined every image 10 times (i.e. 10 cycles of forward and backward propagations) [Goodfellow et al., 2016]. The time taken to train the network was approximately $\simeq 102\,\mathrm{s}$ thanks to the transfer learning approach and power of GPU (Nvidia GeForce GTX 960M). Figures 3.43(a) and (b) illustrate the evolution of the accuracy and training error of the network. Both figures show that the trining stops when the accuracy is maximum and the training error approaches 0%.

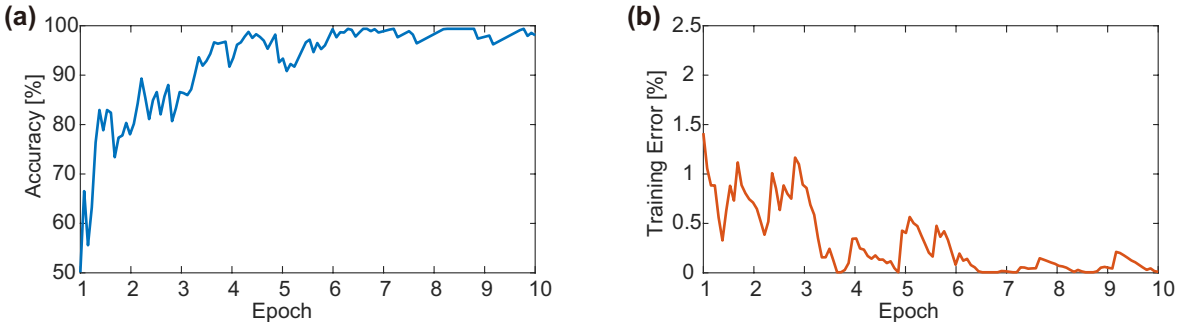

Figure 3.43: (a) Accuracy of training data and (b) the variation in training error as a function of epoch number.

As mentioned earlier, test data were 60 images (20 images for each damage mechanism), which has not been used for the training process. From this consideration, the confusion matrix presented in Figures 3.44(a) shows that for the 60 test AE images, the network was able to classify data with an accuracy of 98.3 %. In particular, results show that only one CL3 signal was 'misclassified' as CL1 class. Figure 3.44(b) illustrates the

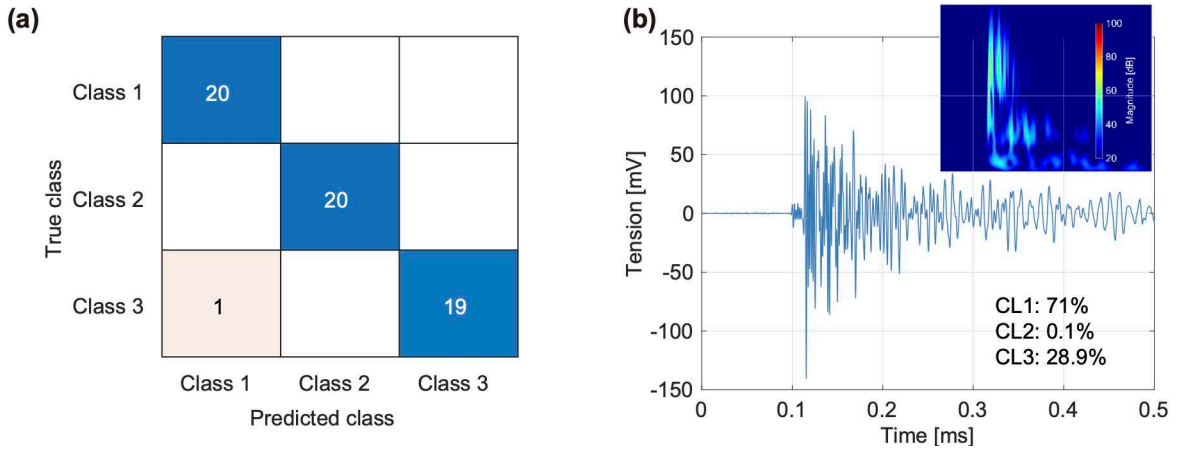

Figure 3.44: (a) Confusion matrix of the test data. (b) The misclassified AE signal and its corresponding AE image.

waveform and the time-frequency characteristics (AE image) of the 'misclassified' signal. Through the latter, we can see that the signal has a short rise time and a high frequency. It can, therefore, correspond to the damage mechanism of the sand-resin debonding. However, the time-frequency representation (TFR) shows that this signal seems to blend the

characteristics of two damage mechanisms: matrix cracking and sand-resin debonding. In addition, for this signal, the probabilities belonging to one of the three classes CL1, CL2 and CL3 are 71%, 0.1% and 28.9%, respectively. This result illustrates the fact that the classification, which we believe to be wrong or misleading, is not necessarily incorrect and that the presence of signals originating from a mixture of modes in complex materials is not necessarily an isolated event. In fact, such a mixture is often the product of a main (or pure) mechanism that occurs in the vicinity of an interface mechanism, such as the above-described signal. On the strength of these observations, we retain the fact that the classification carried up till now is obtained with good accuracy. In the following, the retrained AlexNet network will be used for the classification AE data collected during the damaging of PC samples.

3.8.5 Classification of AE data of polymer concrete

AE data obtained during the quasi-static bending on PC specimens were processed using the retrained AlexNet network, following the approach described in subsection 3.8.2. For each AE signal, AlexNet network computes the probability of belonging to one of the three main damage mechanisms. Therefore, a given AE signal will have a maximum of three non-zero probability of belonging.

Firstly, we only considered the highest probability for all signals and have compared the results with those obtained earlier on the same data with the help of the unsupervised pattern recognition, as it can be seen in Figure 3.45. The latter shows that the results

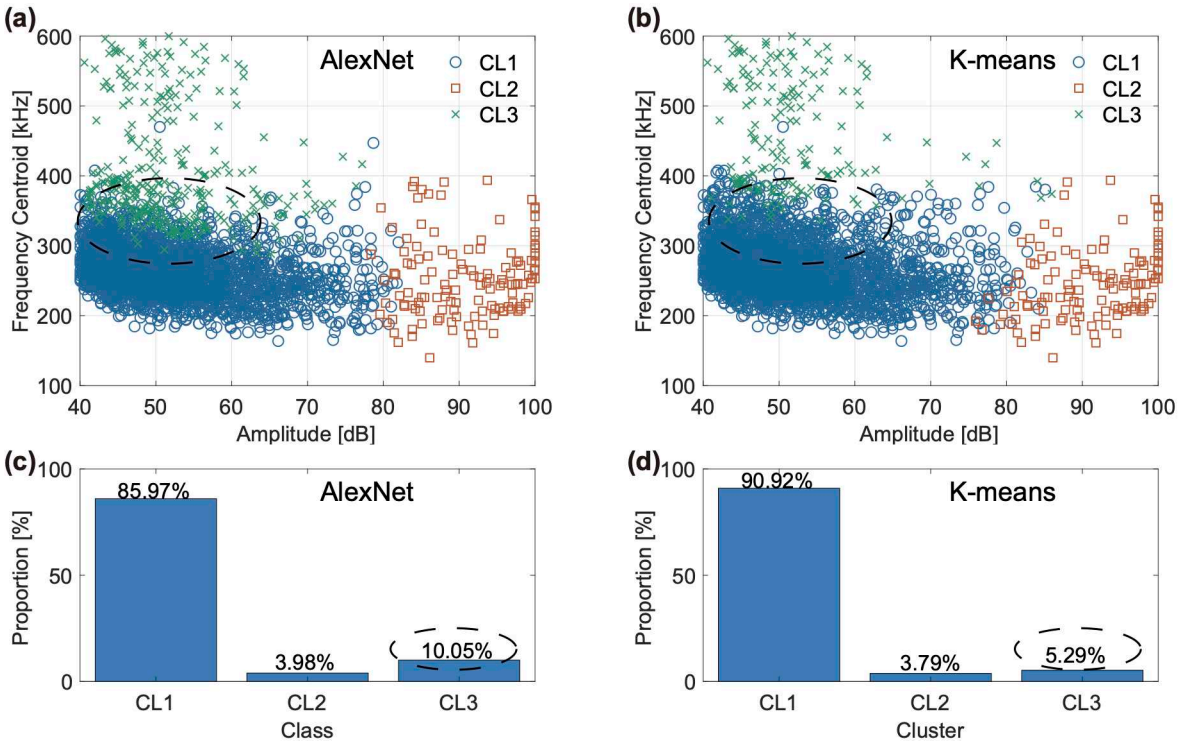

Figure 3.45: Illustration of (a) the classification results and (b) clustering results of AE data in Amplitude versus Frequency centroid plan. Proportion of AE events for each class (clusters) by (c) AlexNet and (d) unsupervised pattern recognition algorithms.

of the two algorithms coincide with signals of class CL2. For signals in class CL1 and

CL3, we notice a slight difference in the classification results. Indeed, the main difference between the classification results in the two algorithms may be related to the fact that an AE signal is a mix of with two damage mechanisms. This result is also noticed in the confusion matrix of test data (see Figure 3.44(a)) and the confused data accounts for $\simeq 5\%$ of total signals analyzed.

In order to study if the difference between the two classification methods can be optimized, we carried out a probability threshold study. Indeed, instead of taking the maximum of the probability of belonging for each AE signal, we fixed threshold, namely 90%, 80% and 70%, above which the probability of belonging will be considered, and the AE signal will be therefore affected to one of the three classes. If the maximum of the probability belonging is smaller than the threshold, the AE signal will be put in a confusion class. This definition led to the results of Figure 3.46.

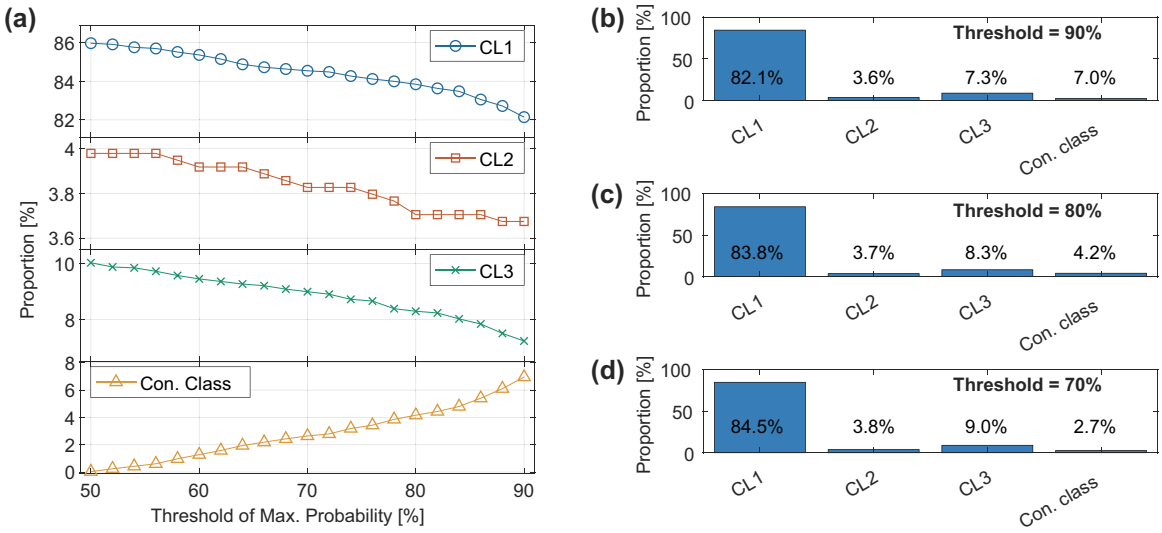

Figure 3.46: (a) Proportion of AE signals in different classes versus the threshold. Proportion of AE signals in each class in the case of (b) threshold = 90%, (c) threshold = 80% and (d) threshold = 70%.

Figure 3.46(a) shows that when the threshold is taken at 90%, the created confusion accounts for $\simeq$ 7% of the total AE signals analyzed ($\simeq$ 3600 signals). In that case, the results of the two classification methods become very close for three classes (see Figure 3.46(b)). Also, we want to show through this approach that the classification is not unique and that a change in threshold can modify the results obtained. However, the quality of a classification method should not be affected by the different threshold changes. Thus, the robustness of the method that we present can be noticed through the results of 80% and 70% threshold, where the variation obtained for each class doesn't exceed 3% (see Figures 3.46(c) and (d)). Finally, we note that whatever the threshold, the proportion of AE signal within the confusion class is always under $\simeq$ 7%, which is consistent with the different classification methods, despite the complexity of the material studied.

3.9 Conclusion

In this chapter, damage mechanisms of two types of concrete samples submitted to quasi-static three-point bending tests are studied by using the acoustic emission (AE) technique and different signal processing methods. Researches are mainly focused on the fracture process analysis (b-value) of concrete specimens, parametric approach (RA value and average frequency) of crack mode classification and multi-parametric unsupervised pattern recognition of AE data.

For civil engineering concrete, micro-cracks of specimens are separated into two main modes: shear and tensile cracks by using the recorded AE signals. Results show the existing agreement between the unsupervised pattern recognition with parametric approach analysis. For polymer concrete (PC), as a novel kind of composite material, with the help of the unsupervised pattern recognition approach and different experiments, three damage mechanisms are identified: CL1 - matrix cracking; CL2 - gravel-resin debonding; CL3 - sand-resin debonding. AE date in the PC specimen is also analyzed by using a proposed 'image-based AE classification' approach based on continuous wavelet transform (CWT) and convolutional neural network (CNN). Results show that according to the time-frequency characteristics of AE data and transfer learning technique, retrained AlexNet algorithm has high classification accuracy.

In the next chapter, in order to explore the correlation between the damage mechanism and the non-classical (hysteretic) nonlinear behavior of complex materials, we propose an original protocol to monitor the evolution of the nonlinear relaxation of micro-cracked concrete samples using AE. In addition, the obtained AE signals will be studied by similar signal processing methods as the ones used in Chapter 2.

Chapter 4

Nonlinear dynamic experiments with acoustic emission

The aim of this chapter is to probe the hysteretic nonlinear dynamic behavior in polymer concrete (PC) and civil engineering concrete samples. The nonlinear experiments are performed on intact and damaged samples, and results will initially concern the behavior of the materials during fast and slow dynamic experiments. Once the nonlinear parameters are known and the nonlinear behavior well described, the same experiments are reproduced in order to study the capacity of acoustic emission (AE) to monitor the evolution of the nonlinear behavior. To this end, we will discuss the advantages and limits of this original approach.

4.1 Nonlinear dynamic experiments

4.1.1 Introduction of the experimental setup

The nonlinear dynamic experiments are conducted on the intact and micro-damaged samples by exciting materials at resonance around one of their bending modes. The applied standing wave dynamic method is also denoted as 'Nonlinear Resonant Ultrasound Spectroscopy' in some references [Renaud et al., 2013, Johnson and Rasolofosaon, 1996, Van Den Abeele et al., 2001, TenCate, 2011].

Figure 4.1 depicts the experimental setup for the nonlinear dynamic experiments. A Stanford Research Systems SR785 analyzer is used to generate the excitation signal (linear sweep), which is amplified by a power amplifier (B&K type-2719) at a constant gain. Then, the excitation is conducted with a shaker (B&K type-4809), which is fixed on a passive damped optical table to avoid external interferences. The sample is firmly linked to the vibrating pot using a rigid clamping device and a piezoelectric sensor is glued by phenyl salicylate (salol) on the other edge of the tested sample to detect its response.

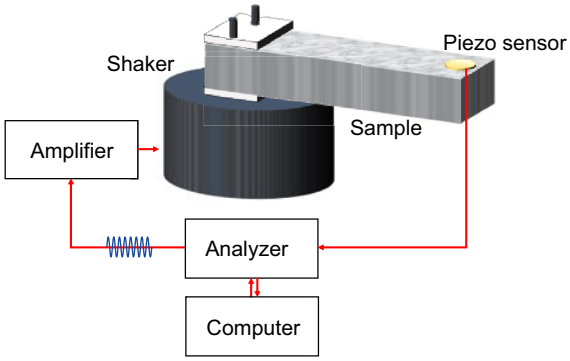

Figure 4.1: Schematic representation of the experimental setup used to perform the dynamic nonlinear measurements.

Vibration signals are first processed with the dynamic signal analyzer, which computed automatically amplitudes and phases for each frequency of the sweep source function around and away from bending modes. The system is controlled and data are transferred to the computer with the help of a GNU Octave software. This analyzer is very stable for long-term measurements and its swept-sine excitation (duration and signal-to-noise-ratio) is ideal for the proposed resonance experiments as it has been shown in different contributions [Novak et al., 2012, Idriss et al., 2015, Hammami et al., 2016, Toumi et al., 2017].

4.1.2 Linearity of the experimental setup

The quality of nonlinear acoustic measurements depends strongly on the experimental setup. Therefore, we must ensure that the operation of the experimental device is linear at the frequencies and amplitudes of applied excitation. As non-classical (hysteretic) behavior is strain-dependent, the imposed samples displacement needs to be measured to estimate the dynamic strain amplitude. Our measurements were thus carried out using a

double head laser Doppler vibrometer (Polytec OFV-5000 controller and OFV 552 Fiber-Optic Sensor Head) to measure the displacement of the sample at the different levels of excitation (see Figure 4.2).

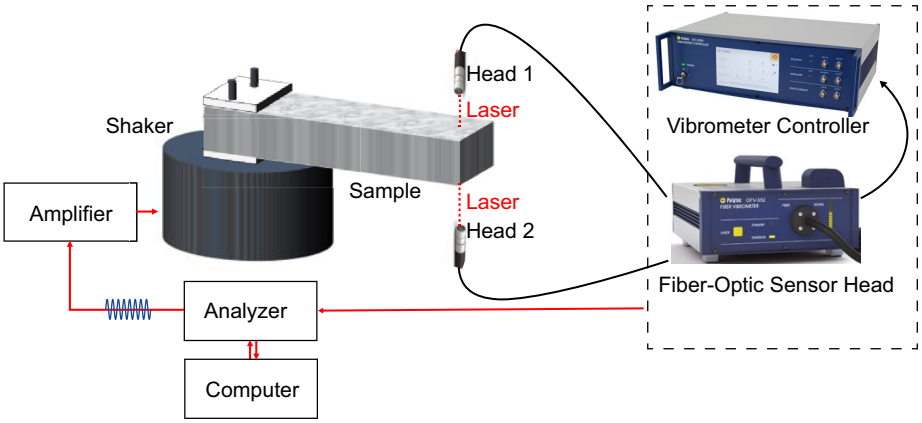

Figure 4.2: Schematic diagram of the experimental setup used to investigate the linearity of device.

Linearity measurements were conducted on a resin beam of size and shape similar to the concrete samples ($200 \times 40 \times 40$ mm^3), where the real displacement is equal to the difference of the displacements recorded at the opposite surfaces. Finally, we note that the displacement is evaluated using the laser conversion coefficient, where 100 nm corresponds to 1 V. The relative vertical displacement is measured at the edge of the tested sample with two laser beams positioned on the opposite upper and lower sides of the sample. The excited and detected signals are acquired, digitized by an analyzer and stored in a computer with the help of GNU Octave software.

The linearity of the experimental device, including the amplifier, the shaker and the holder with the sample, which is verified in the frequency range from 100 Hz up to 20 kHz. At each frequency, twelve amplitudes of excitation are gradually increased from 10 mV to 3.5 V, then pass the amplifier (at a constant gain) and conducted to the shaker. Figure 4.3 shows the evolution of the displacement at increasing amplitude around 5500 Hz. We can

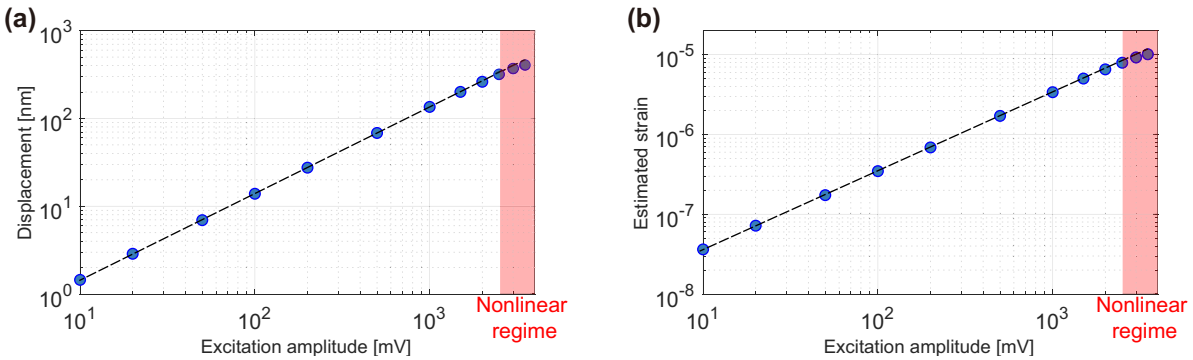

Figure 4.3: Linearity of the experimental device measurements. (a) The maximum displacement at the edge versus different excitation amplitudes at 5500 Hz. (b) The estimated strain as a function of different excitation amplitudes at 5500 Hz.

see through the latter that the experimental device behaves linearly up to 2.5 V, above which a deviation starts to appear. For the maximum linear excitation amplitude (2.5 V

before amplification), the displacement is $\sim$ 400 nm at resonance. As the thickness of the sample is 40 mm, the estimated strain amplitude is $\sim 10^{-5}$ at resonance. For the minimum excitation amplitude (10 mV), the strain amplitude is $\sim 10^{-8}$, which shows that the excitation strain amplitude used to determine the linearity of the experimental device covers three orders of magnitude.

In the following, the excitation amplitudes are selected up to 2 V (maximum voltage before amplification) for polymer concrete samples and 1.6 V (maximum voltage before amplification) for civil engineering concrete samples. Maximum amplitudes used in the experiment allow us to work in the nonlinear regime of the tested samples, but still well within the limits of linearity of the setup.

4.2 Nonlinear dynamics of polymer concrete samples

4.2.1 Materials and experiments

In this section, we will mainly focus on the nonlinear characterization of polymer concrete (PC) samples. The damaged PC sample was tested at a stress level corresponding to $\sim$ 70% of its maximum strength using the same three-point bending tests presented in the previous chapter. Nonlinear acoustic measurements are performed by exciting PC samples at intact and damaged states in fast dynamic (FD) and slow dynamic (SD) regimes. The results of both nonlinear dynamic excitations will be presented in the following.

4.2.2 Fast dynamics of polymer concrete samples

Fast dynamics (FD) experiments were conducted on PC samples taken at intact and damaged states having the same dimensions 200 $\times$ 40 $\times$ 40 mm^3. Both samples were excited in the frequency range around the third bending resonance (between 5300 Hz and 5450 Hz) using the linear sweeps. In the following, we denote A_{source} as the source amplitude of the linear sweep, f_0 as the linear resonance frequency (the same as the one obtained at the very low excitation) and Q_0 as the linear quality factor. The amplitude of the excitation signal was gradually increased from 20 mV up to 2 V (before amplification) to excite the samples in the linear and nonlinear regimes following the protocol shown in Figure 4.4. Note that the maximum excitation amplitude, i.e. $A_{source} = 2$ V, corresponds to a strain amplitude of $\sim 6 \times 10^{-6}$ at resonance.

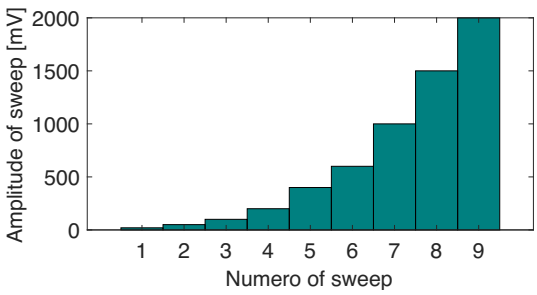

Figure 4.4: Input excitation amplitude during the fast dynamics (FD) analysis. For each amplitude, a linear sweep is performed around the third bending resonance.

The experimental results of the PC sample in the intact and damaged states are shown in Figure 4.5. The latter depicts the amplitudes and phases at resonance as a function of the normalized frequency (frequency is normalized with respect to the linear resonance frequency f_0) for increasing excitation level. At each excitation level, the resonance frequency (f) is determined by considering the phase shift, which coincides with the frequency at which the phase is zero (see the red circles in Figure 4.5(d)). The quality factor (Q) at each excitation can also be calculated as the ratio of the resonance frequency to its half-power bandwidth ($A_{max}-3\,\mathrm{dB}$) from the resonance curves in Figures 4.5(a) and (b).

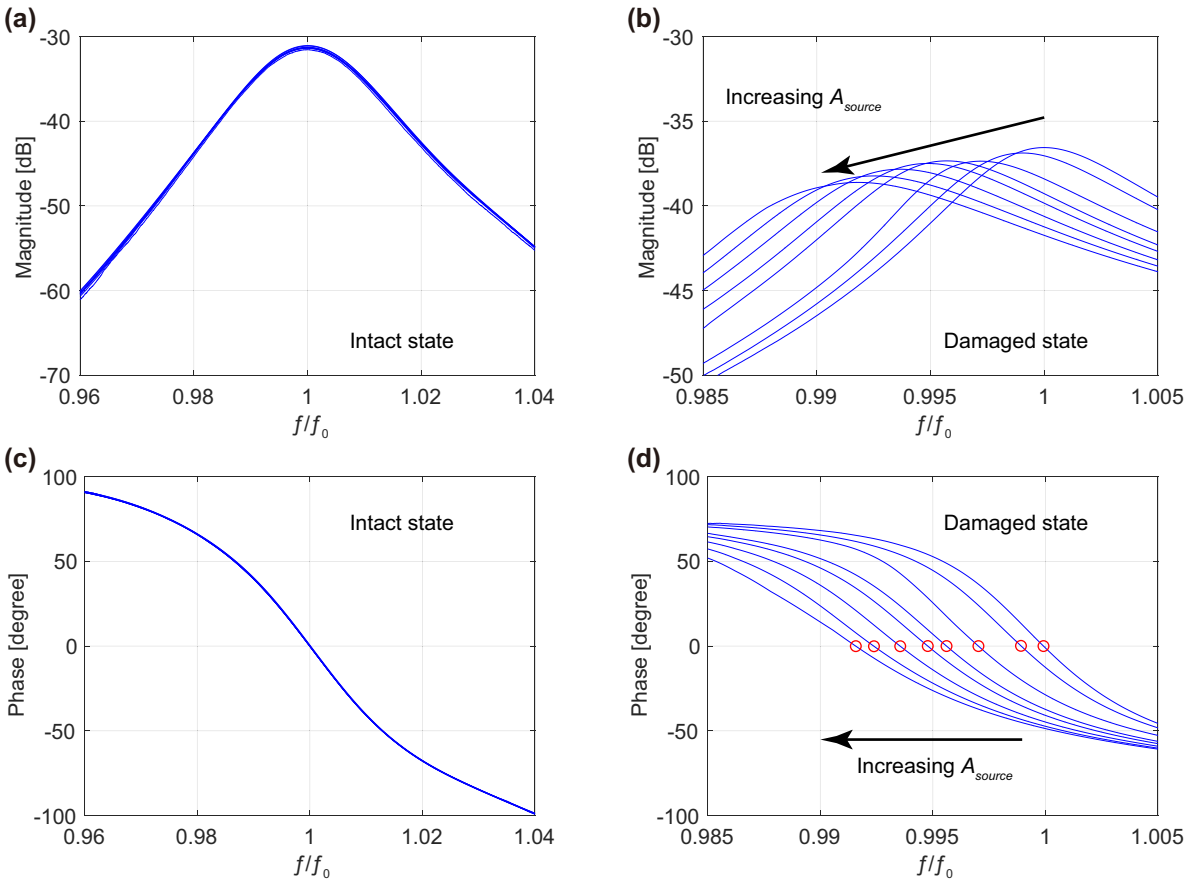

Figure 4.5: Fast dynamics (FD) of a PC sample taken at intact ((a) and (b)) and damaged ((b) and (d)) states: phases and amplitudes (normalized to input amplitude) versus frequency (normalized to linear resonance frequency f_0) of the detected signals at increasing input excitation A_{source}. Red circles in the phase subplot(d) indicate the zero phase crossing, from which the resonance frequency could be derived at each amplitude of excitation.

For an intact PC sample, results are plotted, for the different excitation levels, in Figures 4.5(a) and (c), where all the normalized curves are superimposed. Meanwhile, in the intact state, no strain amplitude-dependent phenomenon can be observed. This observation indicates that both resonance frequency and Q factor are not strain-dependent and the increase of the excitation does not influence the elastic properties of the material, within the limits of the linear functioning of the experimental devices. However, from the results of the damaged state shown in Figures 4.5(b) and (d), the resonance frequency and Q factor are considerably influenced by the increasing excitation amplitude A_{source}.

Figure 4.6(a) illustrates the relative variation of resonance frequency $(f - f_0)/f_0$ as a function of excitation amplitude for one PC sample taken at intact and damaged states, respectively. In addition, Figure 4.6(b) shows the relative variation of inverse quality factor $(1/Q - 1/Q_0)/(1/Q_0)$, which is proportional to damping, versus increasing excitation amplitude A_{source} for the same states. The hysteretic nonlinearity is known to be responsible for the downward shift of the resonance frequency (or equivalently in wave velocity or elastic modulus) in the presence of micro-cracks. In addition, the hysteretic nonlinearity also leads to the relative change of the damping, and consequently to an increase in the elastic wave attenuation.

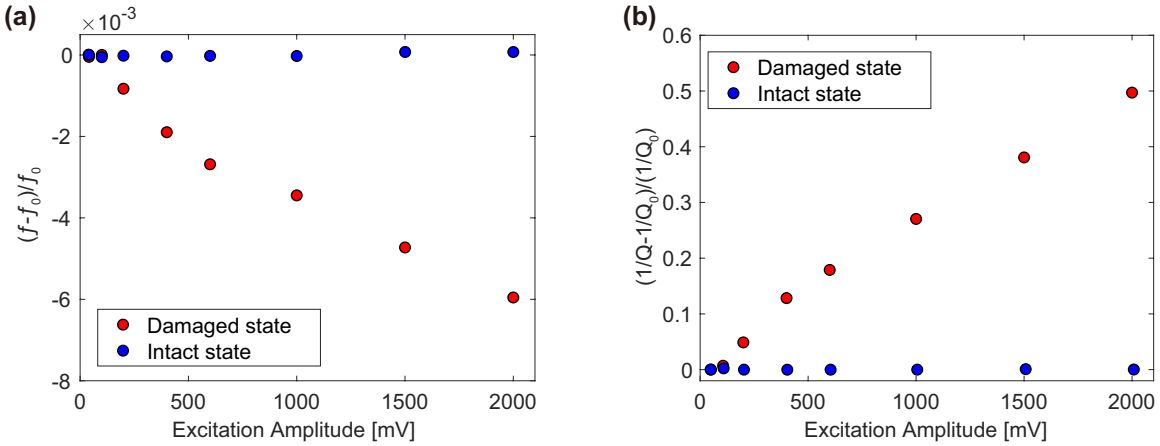

Figure 4.6: Relative variation of resonance frequency and damping as a function of the source amplitude a PC sample at intact and damaged states.

The resonance frequency and quality factor decrease with increasing excitation amplitude is a result of the change in the viscoelastic properties, which is only observed in our case when the PC sample is micro-cracked. This observation has been described in many references where the fast dynamics method has been used as an NDT tool to highlight the sensitivity of nonlinear effects to the presence of damage [Payan et al., 2007, Chen et al., 2010, Eiras et al., 2014].

4.2.3 Slow dynamics of polymer concrete samples

Slow dynamics (SD) experiments were performed on the same set of polymer concrete (PC) samples (intact and damaged). The experimental setup is identical to the FD, where the involved amplitudes belong to the linear operating range (see Figure 4.1). The protocol of the SD experiment was considered in three steps, as shown in Figure 4.7(a):

1 – Preconditioning: the PC sample (intact or damaged) is repeatedly excited with a very low excitation amplitude around its third bending resonance mode. During this stage, we verify that the resonance curves (both in amplitude and phase) are perfectly superimposed, indicating that we have an initial linear equilibrium state, which is considered as a reference.

2 – Conditioning: then, the sample is conditioned with a high amplitude excitation around the same resonance mode. Note that the excitation amplitude remains constant during all the conditioning stage. After the first sudden (or instantaneous) variation of the resonance frequency and damping, the transition of the sample from the linear to a

non-equilibrium state is observed. When the conditioning time is increased which can be performed by repeating the high amplitude excitation around resonance, the damping increases (i.e. the quality factor of the curve decreases) and elastic modulus decreases (the resonance frequency shifts towards lower values).

3 – Relaxation: after being conditioned by the application of a large dynamic strain (higher than $\sim 10^{-6}$), the high drive amplitude is removed. Then a low excitation amplitude is applied (the same as the one used at the preconditioning stage). Under these conditions, the material properties recover slowly to their initial values until the original linear equilibrium state (of the preconditioning) is reached. Measurements showed that the effects of conditioning and relaxation are fully reversible. In general, the relaxation behavior is followed by tracking the evolution of resonance frequency and quality factor Q. Over time, the system relaxes back to its preconditioning state as the logarithm of time over minutes, hours, or days depending on the conditioning characteristics [TenCate, 2011].

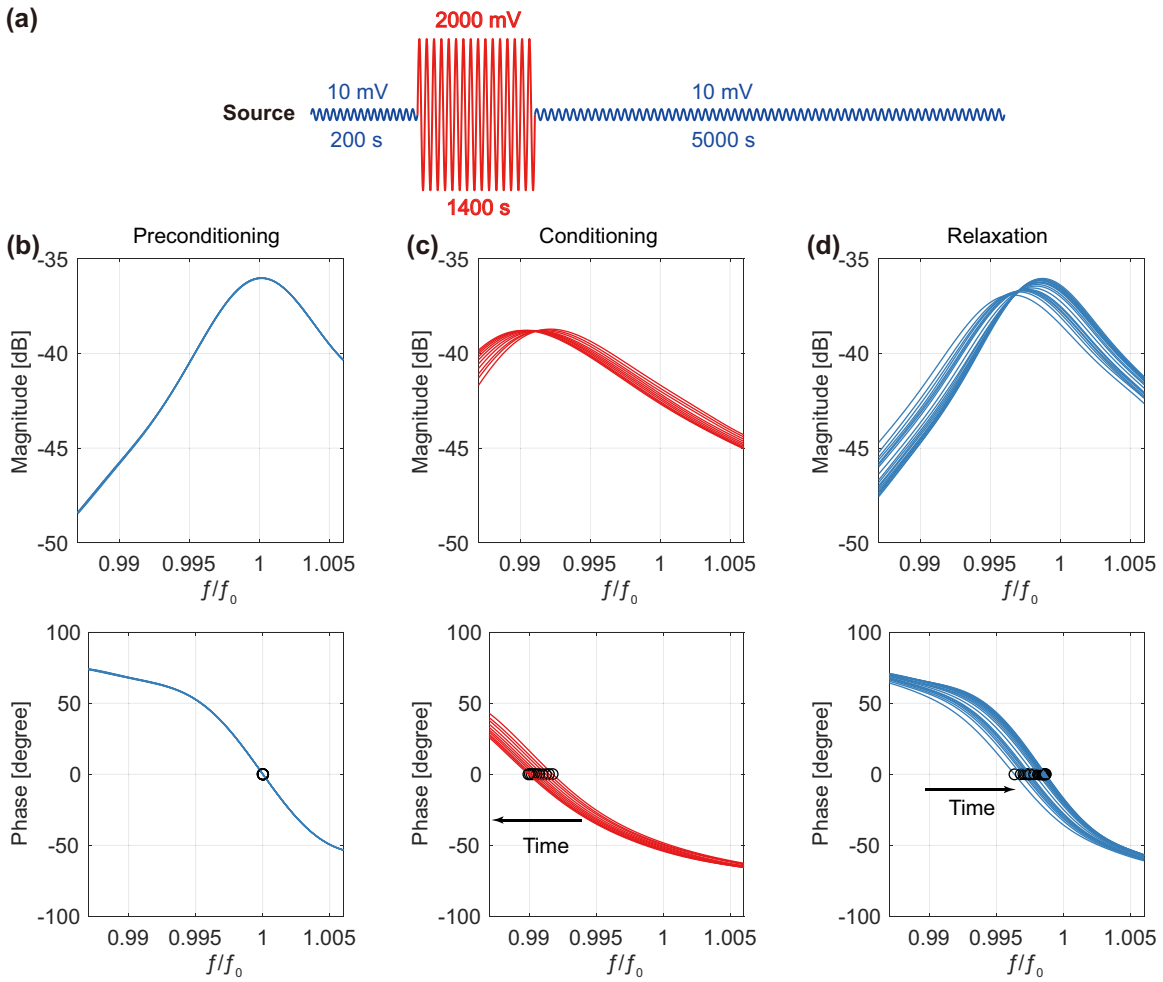

Figure 4.7: (a) Protocol of excitation in slow dynamics experiment. Three experimental steps conducted during slow dynamic experiments and typical results on damaged polymer concrete samples: preconditioning (b), conditioning (c) and relaxation (d).

In the preconditioning and relaxation stages, the weak excitation amplitude is 10 mV (before amplification). This excitation level is calibrated using the differential Fiber-Optic Sensor Head as presented in Figure 4.2 during fast dynamics experiments on intact samples, where the involved strain rates ($\sim 10^{-8}$) were found to be well below the threshold

corresponding to the nonlinear behavior of the tested materials. For the conditioning, the high-level of excitation has an amplitude of 2 V. The sweep signals are then amplified, and the maximum dynamic strain of the samples during these experiments was $\sim 3 \times 10^{-6}$. The full conditioning was obtained after more than 1000 s (35 sweep cycles) of high dynamic strain conditioning. Then, the nonlinear slow recovery of the elastic properties was probed by repeating the same resonance sweep at 10 mV until the full relaxation is reached. Figures 4.7(b), (c), and (d) illustrate the results on the damaged PC sample for each of the three steps (note that the frequency is normalized with respect to the linear resonance frequency f_0). The upper row in each column represents the amplitude of the resonance curve and the lower row depicts the phase of the resonance curve, recorded at the same frequency. Finally, we note that the resonance frequency of each curve is selected by zero phases (see the black circles in the lower subplots).

Based on the relaxation process in the damaged PC samples, the resonance curves illustrated in Figure 4.7(d) allows us to compute the evolution of the resonance frequency (elastic modulus) and the quality factor (damping) as a function of time. The relaxation time as shown in Figure 4.8 is determined when the preconditioning parameters are recovered. As mentioned earlier, the sweep duration is $\sim$ 38 s. The experimental data in blue dots within the same figure show the times at which the resonance frequencies and the quality factors were measured. Indeed, the first dot indicates that the relaxation time recording starts at $\sim$ 22 s.

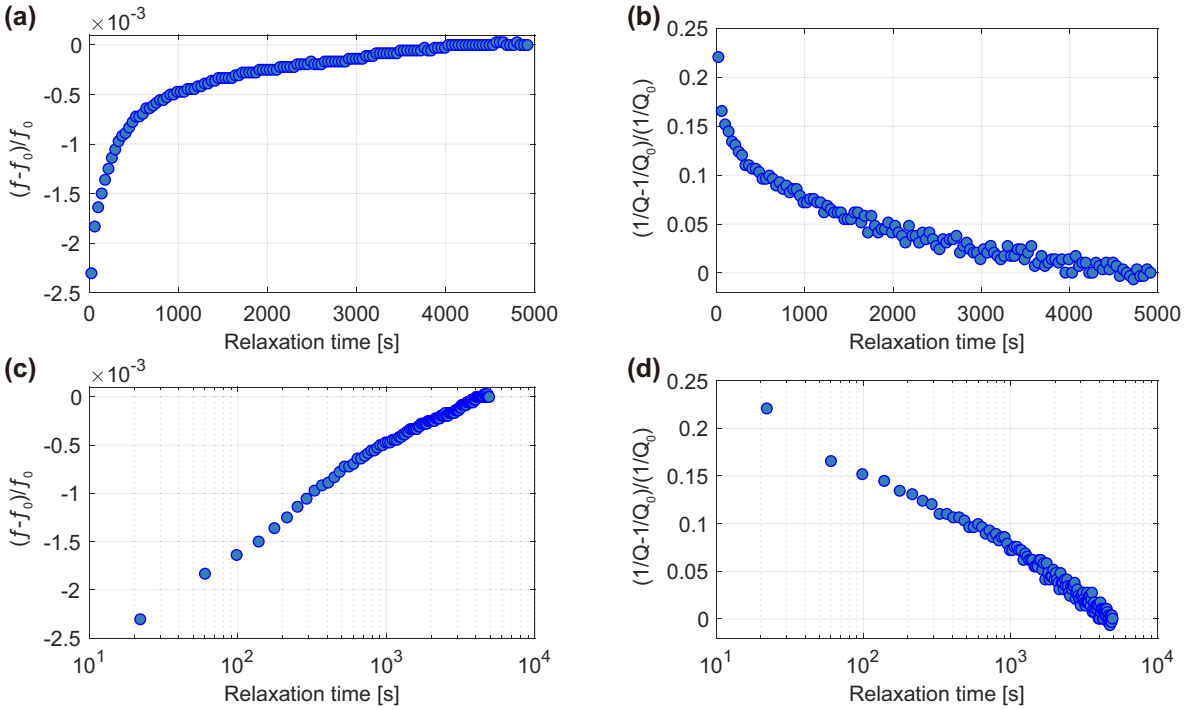

Figure 4.8: Relative variation of resonance frequency (elastic modulus) and inverse Q factor (damping) as a function of time during the nonlinear relaxation of a polymer concrete sample taken at intact (a) and damaged (b) states. (c) and (d) represent the same plots when the relaxation time is in the logarithmic scale.

Figures 4.8(a) and (b) clearly shows the slow recovery of the elastic properties as a function of time in the case of the damaged PC sample, where the relaxation time is $\sim$ 4200 s (monitoring during 5000 s). Date obtained by repeating the same resonance sweep,

show that the tested sample has almost recovered its initial properties, where the variation of both resonance frequency and damping is less than 0.1%.

The log-time evolution of the resonance frequency and damping are presented in Figures 4.8(c) and (d). During the first moments of relaxation, when the sample is probed using a low source amplitude, the tested sample is in a 'metastable state', which is similar to the observations performed in references [Mechri et al., 2019, Bentahar et al., 2020]. Indeed, in the middle time range, experimental results show that the recovery of elastic modulus and damping is linearly related to logarithmic relaxation time, in accordance with results of the literature [TenCate et al., 2000b, Bentahar et al., 2006, Scalerandi et al., 2010, Scalerandi et al., 2019]. This behavior has been observed for different media (consolidated and unconsolidated granular, damaged composites or metals, etc.), which is due to the hysteretic nonlinear relationship existing between stress and strain where different microstructural features can be involved (sliding or frictional interfaces, clapping micro-cracks, etc.). Finally, we mention that the intact PC sample was not subject to relaxation, which makes the presence of recovery, in this case, a reliable acoustic signature of the presence and evolution of damage.

Indeed, in literature [Bentahar and El Guerjouma, 2009], Bentahar and El Guerjouma have demonstrated that the nonlinear relaxation behavior of progressively damaged polymer composites can be quantified and related to the cumulative AE energy recorded at each damage stage. However, the AE data were not recorded simultaneously with the nonlinear hysteretic data, namely the relaxation time. In order to better understand the physical origin of the nonlinear slow dynamics of micro-cracked materials. The present thesis aims to use acoustic emission (AE) as a passive monitoring tool to investigate the relaxation of damaged samples by replacing the weak excitation probing. Results related to the characterization of intact and damaged samples will be presented in the following.

4.3 Passive monitoring of nonlinear relaxation

4.3.1 Materials and experiments

As mentioned earlier, the nonlinear dynamic experiments around resonance showed that intact PC samples show no relaxation. This was not the case of the partially damaged polymer concrete (PC). Indeed, compared with the intact PC, the presence of micro-cracks created during the quasi-static loading, as described in Chapter 3, seems to be at the origin of the hysteretic nonlinear behavior. To investigate the relationship between the existing micro-cracks and the nonlinear behavior of the tested materials, the acoustic emission (AE) was used on the intact and damaged PC samples to detect the existence of acoustic signatures and thus to monitor the nonlinear relaxation during slow dynamics experiments.

The experimental setup in this study is illustrated in Figure 4.9. By keeping the same equipments used for the previously presented classical nonlinear measurements, samples (intact and damaged) were subjected to standing bending waves around their third resonance mode. In order to probe the relaxation so as to get rid of the weak amplitude probe wave, an AE sensor (WSα) was glued by phenyl salicylate (salol) around the center of the sample (near the damage zone). Detected AE signals are then filtered

and amplified by the USB AE Node, which is a preamplifier (40 dB) and are collected thanks to a computer via the AE win Mistras software. The experimental equipments are

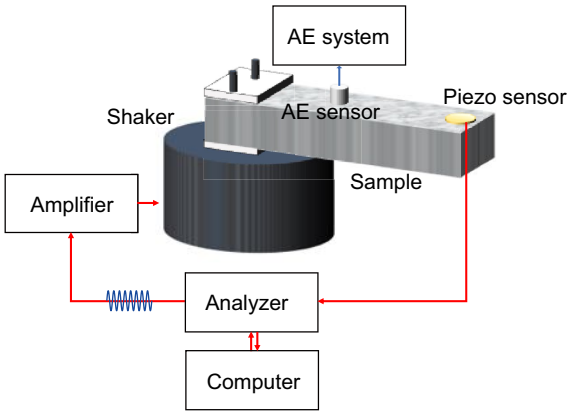

Figure 4.9: Schematic representation of the experimental setup used to perform the nonlinear measurements monitored with the acoustic emission (AE) system.

summarized in Table 4.1 and the proposed excitation to passively probe the relaxation with AE sensors is shown in Figure 4.10.

Name	Brand and model
Dynamic signal analyzer	Stanford research system model SR785
Power amplifier	B&K type 2719
Shaker	B&K type 4809
AE sensor	Mistras WSα (100-1000 kHz)
AE system	Mistras USB AE Node (40 dB preamplifier)

Table 4.1: Equipments for the proposed passive monitoring experiments.

Note that during the passive monitoring experiments, the room temperature was controlled and fixed at 23 °C. According to the proposed protocol, the AE activity was first monitored on the PC samples during 1 hour in the absence of any dynamic excitation in order to verify the existence of any acoustic activity due to the environmental conditions (temperature, humidity, etc.). Then the PC samples were subjected to a weak (linear) excitation at 10 mV during 1 hour around resonance. During this stage, we have noticed that all resonance curves were superimposed, indicating the samples were at an initial equilibrium state. On the other hand, we have also noticed the absence of AE activity

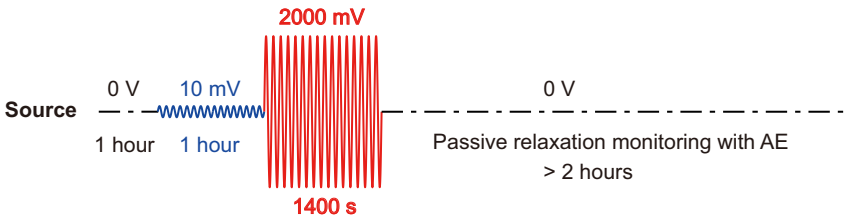

Figure 4.10: Passive relaxation monitoring experiments excitation protocol for polymer concrete samples.

during this weak excitation stage. Then, the samples were repeatedly excited at the same

high amplitude excitation signal (35 passes of linear sweeps around resonance frequency at 2 V before amplification) to reach the full conditioning state of the material under test. The excitation amplitude was then set back to zero to let the samples recover naturally their initial properties without any interference with a possible probe wave. The Probing of the relaxation of PC samples was performed passively using the AE system, where the detection threshold was set at 30 dB (0 dB refers to 1 μV). The acquisition parameters were set as follows: Peak-Definition-Time (PDT) 50 µs, Hit-Definition-Time (HDT) 100 µs, Hit-Lockout-Time (HLT) 400 µs. The AE signals were sampled at 5 MHz over 5120 points.

4.3.2 Passive relaxation monitoring

The long-time conditioning didn't have any effect on the intact PC sample. Indeed, passive monitoring didn't show the existence of any AE activity when the high voltage excitation is removed. This is due to the absence of the slow dynamics phenomenon, which can be also confirmed by the above-mentioned fast dynamic experiments, showing that on intact PC samples the normalized resonance curves remain unchanged for increasing excitation amplitude.

In the case of the partially damaged PC samples, we also noticed the absence of AE activity during the early times of relaxation after the full conditioning ($\sim$ 600 s depending on the considered PC samples). Following this period of 'silence', we started to detect AE hits whose number was gradually increasing as a function of the relaxation time. The AE energy of each detected AE hit versus relaxation time is plotted in Figure 4.11(a). In the

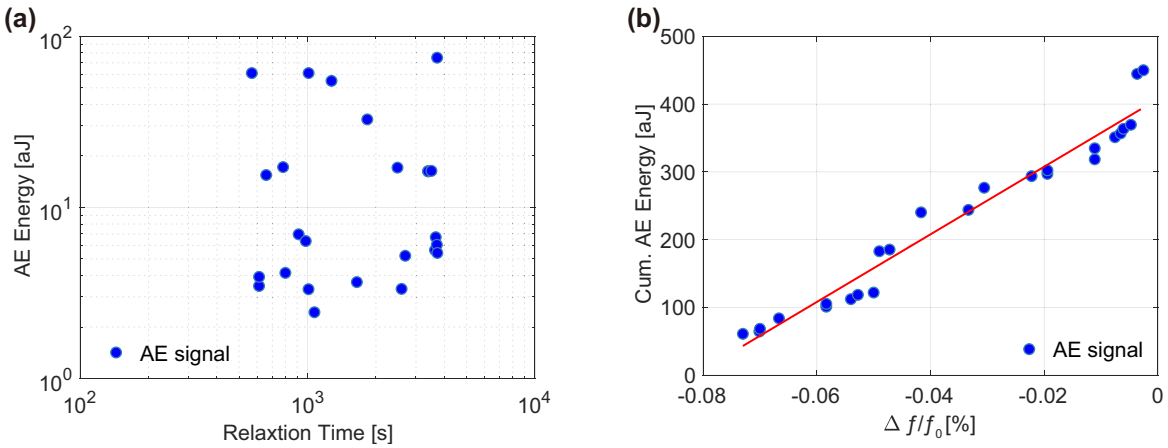

Figure 4.11: (a) AE Energy of the AE signals detected during the relaxation (in log-time) of the damaged PC sample. (b) Proportionality between cumulative energy of AE signals and resonance frequency determined during passive and active relaxation monitoring, respectively.

latter, each dot corresponds to an AE hit with a weak amplitude (between 30 and 34 dB) where the 'silence period' which seems to be a characteristic of the passive relaxation was around $\sim$ 550 s for the presented data. The most likely hypothesis regarding the period of silence would be that the increase in damping due to conditioning will prevent AE hits from reaching the surface of the sample with a measurable amplitude. Indeed, with the help of the results presented in Figure 4.8(b), we can see that the silence period (which

lasts $\sim 550\,\mathrm{s}$) corresponds to a decrease or recovery of the relative damping from $\sim 22\%$ to $\sim 10\%$ with a potential link with the first stage in Figures 4.8(c) and (d) as a 'metastable state', which is also described in references [Mechri et al., 2019, Bentahar et al., 2020].

4.3.3 About the origin of the silence period

During the conditioning experiments, an AE system (PCI-2 Mistras Group, Inc.) was continuously recording the response of the material under test. Figure 4.12(a) shows the evolution of the sweeps that excited the damaged PC sample repeatedly around the third bending resonance. As mentioned earlier, the excitation signal was generated at a constant amplitude within the linear operating region. The conditioning phase was performed using 35 sweep cycles. The evolution of the resonance frequency and damping related to the third bending resonance are presented in Figure 4.12(b). We can see through the latter that conditioning increases the damping and decreases the frequency of monitored resonance mode in accordance with the literature.

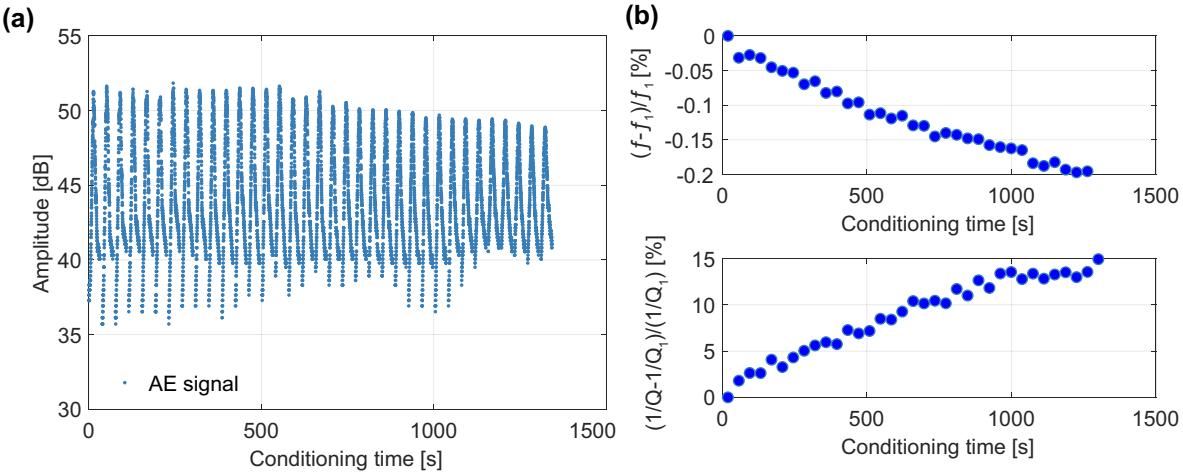

Figure 4.12: (a) AE Monitoring of the damaged PC response during conditioning; (b) Evolution of the relative frequency and damping during conditioning; f_1 and Q_1 correspond to resonance frequency and quality factor collected from the first cycle, respectively.

Furthermore, it is important to remember that during the conditioning, the AE system recorded cycle consists of ~ 300 signals generated around the above-mentioned resonant frequency using time window $1000\,\mu\mathrm{s}$ for each signal. Figure 4.13(a) shows a resonance curve (the second sweep cycle), where it is easy to notice that the isolated signal is already affected by the nonlinear behavior of the PC sample. Figure 4.13(b) shows the evolution of the frequency components related to the isolated signal. Indeed, we note that the fundamental as well as the higher harmonics are all affected by the conditioning where the softening of the elastic modulus during the conditioning seems to be continuous up to a limit value.

When we consider the evolution of the energy of the signals detected with the help of the AE system during the conditioning, as presented on Figure 4.14(a), we notice that it fluctuates during the entire conditioning period around an average value, where the relative evolution doesn't exceed $\sim 3\%$.

We recall that the detected AE signals during the passive relaxation have frequency

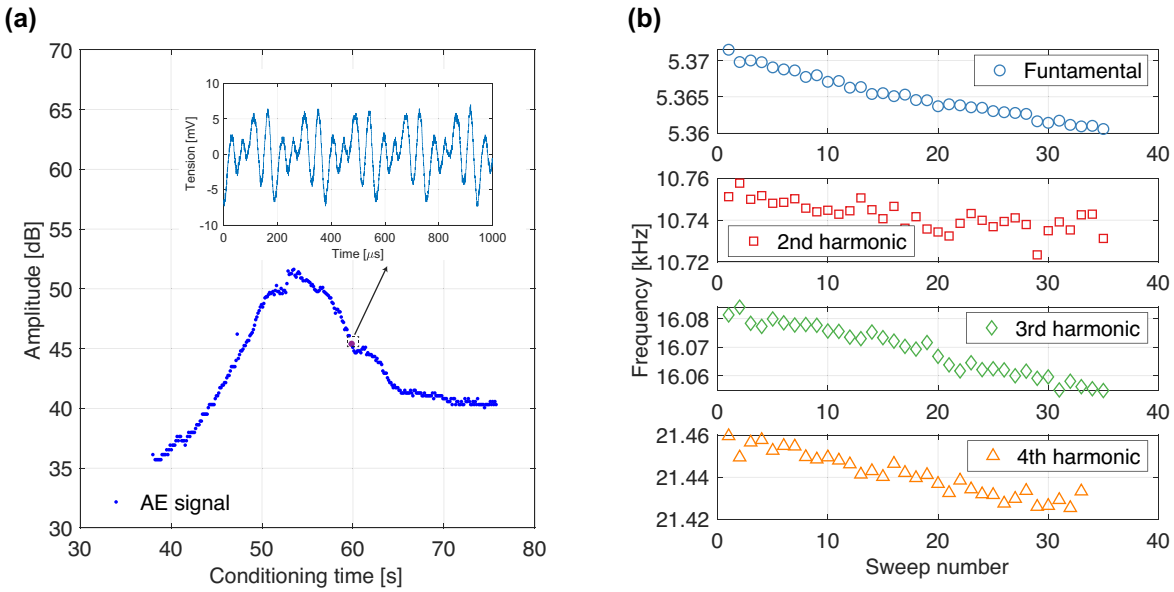

Figure 4.13: (a) Representation of the second excitation cycle recorded during the conditioning. The insert represents one of the $\sim$ 300 signals that make up a resonance curve. (b) Evolution of the fundamental frequency and harmonics of the isolated signal during the 35 sweeps used to condition the damaged PC sample.

components well above the ones involved during the conditioning experiments, where the smallest frequency is around $\sim$ 100 kHz. In order to investigate the influence of the ultrasonic wave attenuation due to conditioning, the recorded signals presented in Figure 4.14(a) are Butterworth high-pass filter processed (we used the order 5) where the cutoff frequency was fixed at 80 kHz. With the help of Figure 4.14(b), it becomes possible to notice the monotonous decrease of the high frequency component. Indeed, the total energy per sweep undergoes a reduction of approximately $\sim$ 35% of its initial value as a function of the conditioning time until the full conditioning of the tested damaged PC is reached.

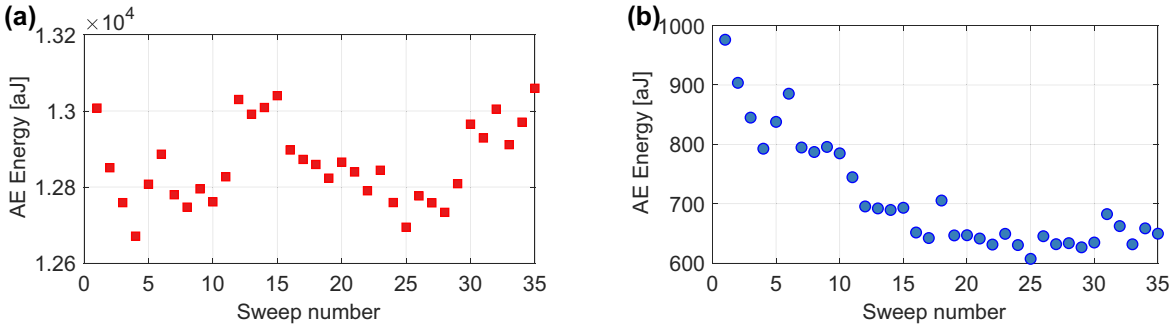

Figure 4.14: Evolution of total AE energy per sweep of original signals (a) and of filtered signals (b) during the 35 sweeps.

We believe that this observation is at the origin of the 'silence period' highlighted in Figure 4.11, where the conditioning effect increases the damping of the material even in the ultrasonic domain. This behavior makes the AE hits emitted at the beginning of relaxation attenuate considerably before they reach the surface of the sample.

Following the 'silence period', we notice that, globally, the more the time advances

and the more the energy of the detected AE signals decreases. This observation confirms that the elastic energy released by the material during its relaxation is decreasing as the material reaches back its initial state. This effect is in accordance with the evolution of the resonance frequency and damping since the nonlinear relaxation tends to bring them closer to their initial limit values. For this reason and for geometric reasons related to the fact that the different ultrasonic paths are equivalent (the damage i.e. micro-cracks is localized at the center of the sample), we did not perform an attenuation compensation for the detected AE signals during relaxation in this work. Experimental results showed that the cumulative energy of the detected AE signals changes as the logarithm of relaxation time. Therefore, by applying the same conditioning on the damaged PC sample and by following the relaxation with a weak amplitude signal first and then with acoustic emission (passive probing), we found an interesting proportionality between the cumulative AE energy and the relative change of the resonance frequency (see Figure 4.11(b)). Indeed, the latter shows the linear relationship between the cumulative elastic energy released by the material and the elastic properties recovery of material during relaxation. Finally, note that the relaxation experiments were repeated on the intact and damaged samples at successive days. The trends presented here were reproducible with the range of $\pm 15\,\%$ in terms of silence period, signals energy, cumulative energy, etc.

In the active method (monitoring of resonance frequency and damping with a weak amplitude), the relaxation time is determined once the full recovery of the initial properties is reached. In the proposed passive method, the relaxation 'stops' at the time when no AE activity is detected, even if the monitoring time (more than 2 h) is much longer than the relaxation time measured by the above-mentioned active method (i.e. ~ 4200 s). Figure 4.15 compares the relaxation times based on both passive and active methods. The figure shows that both ways of monitoring do not perfectly overlap. However, we note that at the time when the passive relaxation 'stops', the relative resonance frequency change is 0.005% which means that the material has reached $\sim 97\%$ of its preconditioning frequency f_0. This suggests that the difference in relaxation time between both methods could be due to the application of the weak (i.e. linear) probe excitation.

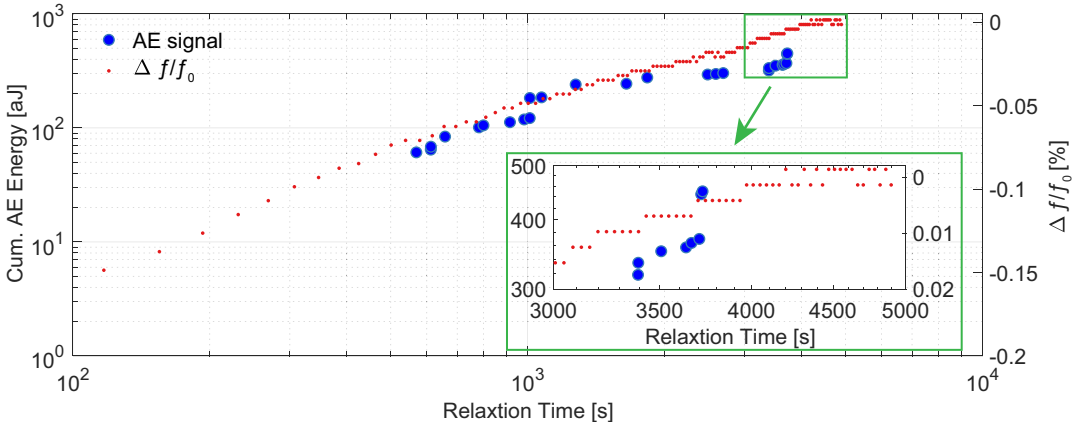

Figure 4.15: Comparison between the active (resonance frequency) and passive (acoustic emission) relaxation monitoring methods.

4.3.4 Nonlinear relaxation and damage mechanisms

The performed AE experiments show that the amplitudes (or energy) of the detected AE hits during the passive relaxation ($\sim 5\,\mathrm{mV}$) are significantly lower than those detected during the quasi-static bending tests (up to 10 V). The application of the classical AE features extraction method is not straightforward in this situation because the weak-amplitude AE signals are mixed with noise. For this case, we used a denoising method, named 'modified soft thresholding technique (MSTT)' whose application allows computing the AE features for further analysis.

An AE signal recorded during the nonlinear relaxation and the same signal after denoising are shown in Figures 4.16(a) and (b), respectively. The background noise was significantly reduced thanks to the application of MSTT, which can be seen on the temporal signals.

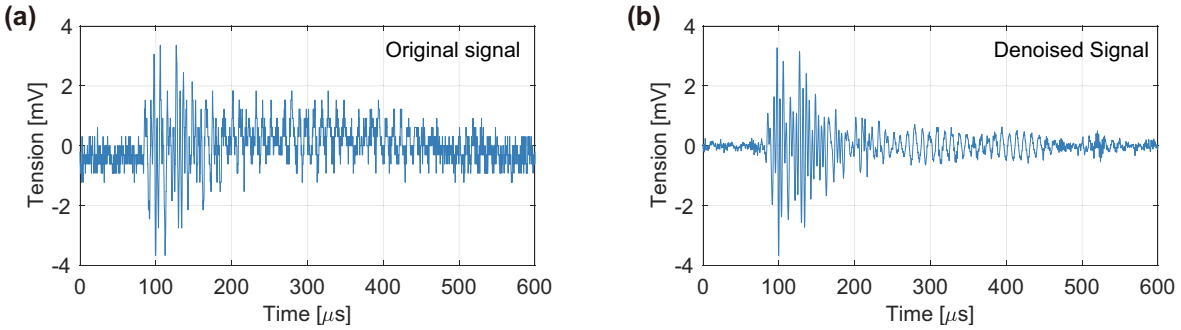

Figure 4.16: Modified soft thresholding technique (MSTT) analysis results: (a) Original (untreated) AE signal. (b) Denoised signal.

Denoised and original signals are firstly compared, as shown in Figure 4.17(a), where the main waveform features remain similar (amplitude, rise time, etc). In addition, the difference between the original and denoised is also computed by comparing their wavelet scalograms (squared modulus of continuous wavelet transform) as illustrated in Figure 4.17(b). Indeed, the time-frequency representation shows the existence of a blue

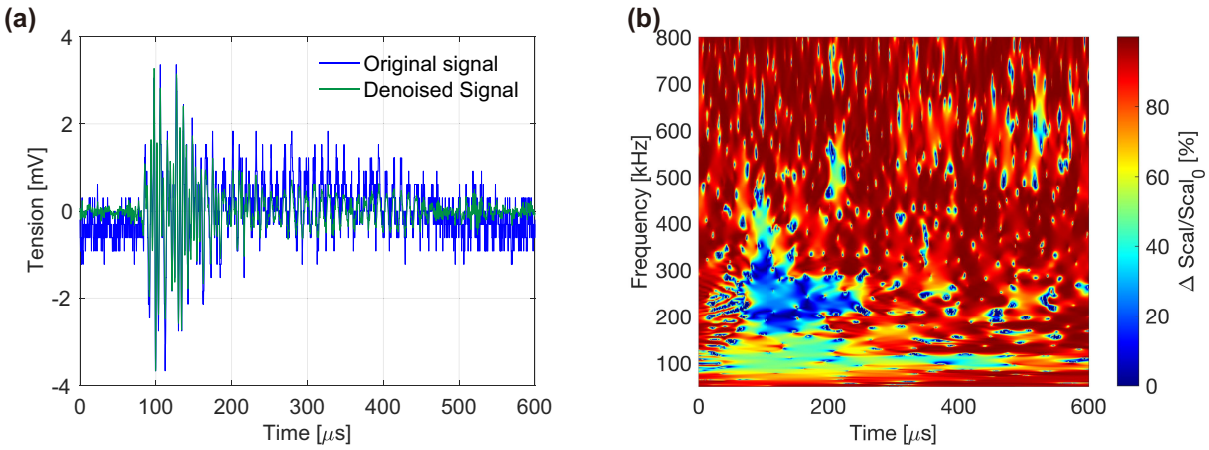

Figure 4.17: (a) Comparison of AE signal before denoising and after MSTT denoising. (b) Difference between the two signals in time-frequency representation.

area, which corresponds to the lowest differences between signals. This means that the

MSTT method removes efficiently the background noise (more than 90% of the energy reduction in most area) while the useful information of the AE signals is saved. The blue area, which represents the most energetic part of the AE signal is distributed in the frequency range of 180 to 300 kHz (see Figure 4.20(c)).

Once the AE signals are denoised, the application of the multi-parameter unsupervised pattern recognition analysis allowed to separate the detected signals into two classes (CLA and CLB). In the beginning, both classes of signals are detected right after the 'silence period'. However, CLA signals were the only ones to be detected until the end of the PC relaxation. This can be confirmed by Figure 4.18(a) which presents the evolution of energy of the detected signals for the two classes versus relaxation time. On the other

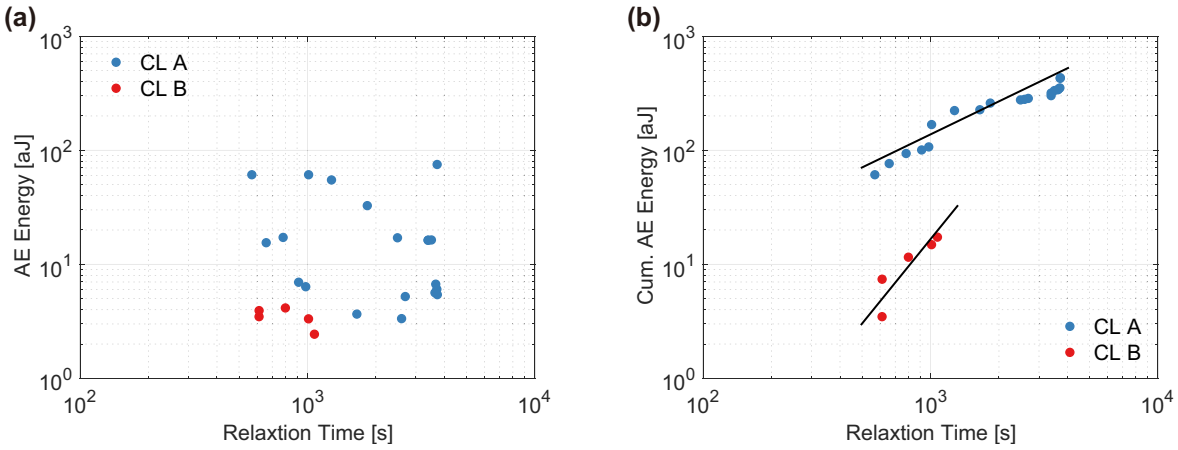

Figure 4.18: (a) Evolution of energy of the detected AE signals as a function of relaxation time. (b) Cumulative AE energy of the detected AE signals in two classes versus relaxation time.

hand, Figure 4.18(b) presents the dynamic evolution of both types of signals as a function of time. We can clearly see that the kinematics of relaxation corresponding to the CLA and CLB signals is different, where CLB signals relax faster even if their energy contribution during relaxation is not the most important. Signals in class CLA and CLB are clearly different which can be also distinguished by other AE features as shown in Table 4.2.

Class	Amplitude	Energy	Rise time	Duration	Counts	PF	FC	WF
CLA	30-40 dB	5-80 aJ	30-50 μs	200-400 μs	30-60	100-120 kHz	100-150 kHz	100-120 kHz
CLB	30-33 dB	5-20 aJ	5-20 μs	100-200 μs	10-30	200-300 kHz	200-300 kHz	180-220 kHz

Table 4.2: Characteristics (AE features) of AE signals (CL A and CL B) detected during the passive relaxation of damaged PC samples.

Furthermore, the properties of AE signals obtained during the passive relaxation measurements and those corresponding to damage mechanisms created during the quasi-static tests appeared to be similar. Figure 4.19 presents typical waveforms and time-frequency representations (TFR) of AE signals corresponding to class CLA and matrix cracking type. In addition, the comparison between the signals corresponding to class CLB and the gravel/matrix debonding signals is shown in Figure 4.20.

Here, the energy density in each wavelet scalogram is normalized to the most energetic magnitude in the time-frequency plan (maximum value in the time-frequency matrix) to

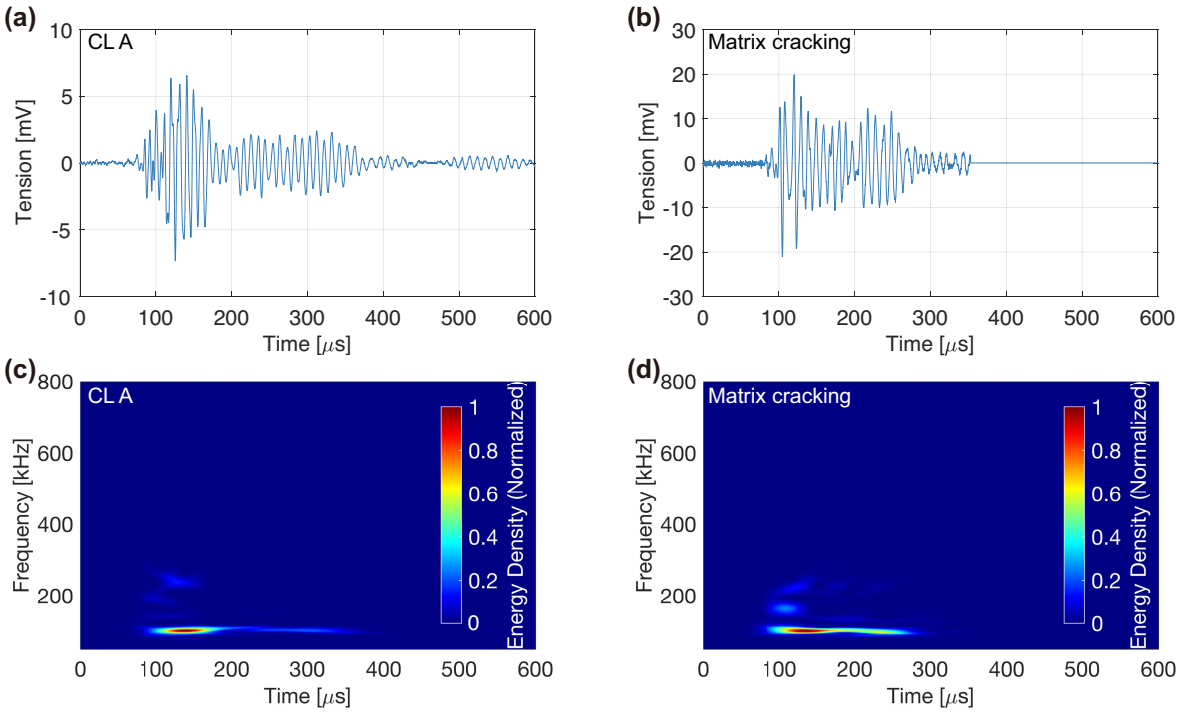

Figure 4.19: Time-amplitude and time-frequency representations of AE hits detected during the nonlinear relaxation (CLA) ((a) and (c)) and during the quasi-static tests (matrix cracking) ((b) and (d)).

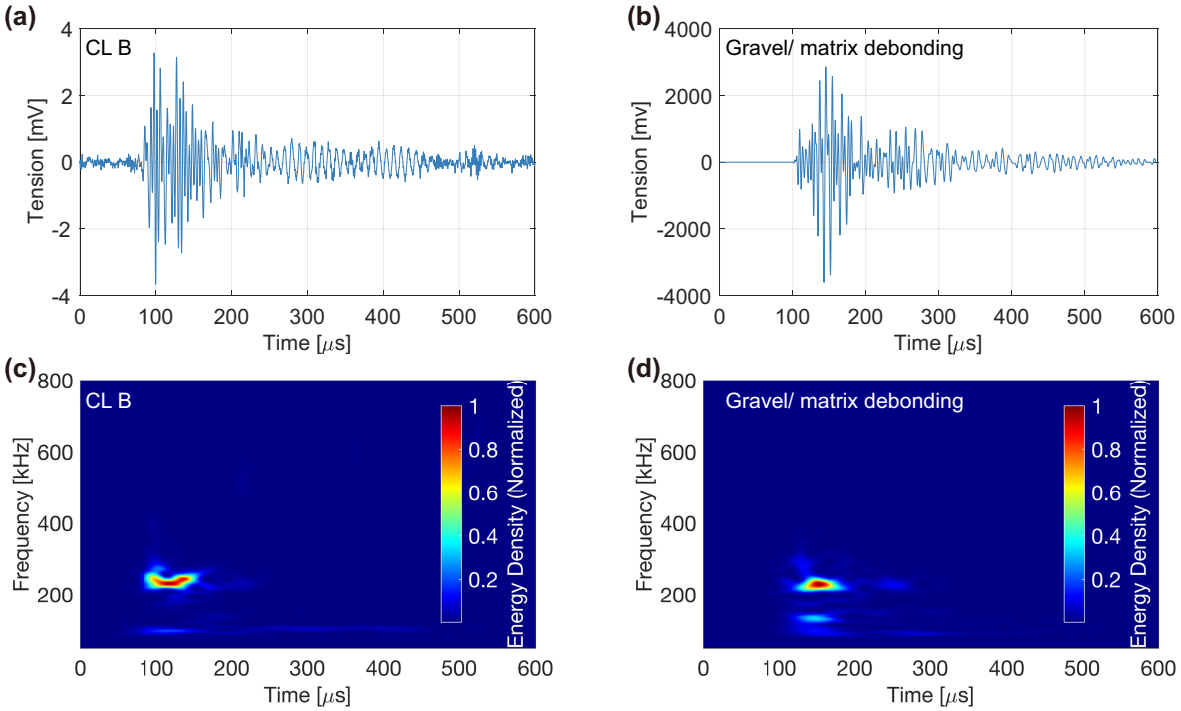

Figure 4.20: Time-amplitude and time-frequency representations of AE hits detected during the nonlinear relaxation (CLB) ((a) and (c)) and during the quasi-static tests (gravel/matrix debonding) ((b) and (d)).

make the energy distribution of both types of signals comparable. By comparing the normalized wavelet scalograms of these two signals, we can see that CLA signals share

the same energy domain as matrix cracking mechanism in the time-frequency representation. In this case we note that the highest energy distribution is around $\sim 100\,\text{kHz}$ with a duration of $\sim 200\,\mu\text{s}$. In addition, as shown in Figures 4.20, waveforms and the energy distribution in the time-frequency representation of the two types of signals are similar even if their amplitude is significantly different. Their high energy areas are all located within the frequency range of 180-300 kHz as shown in the wavelet scalogram representation in the same figure.

Within the limits of the sensitivity of our passive detection system and the environmental conditions, we have first verified the absence of any AE signals during the nonlinear relaxation of the intact PC samples. Once these samples are damaged, the application of the same nonlinear relaxation experiments revealed the existence of AE signals. These experimental observations show that the created micro-cracks within the PC samples are at the origin of the detected AE signals detected during the nonlinear relaxation. Then, we have compared the obtained waveforms and wavelet scalograms (energy distribution) of AE signals recorded during the three-point bending quasi-static tests and the nonlinear relaxation experiments. Measurements, which were performed on the same samples, revealed the existence of a striking resemblance between AE signals, which are actually detected under very different experimental conditions. Indeed, the signals referred to as CLA and CLB strongly resemble the matrix cracking and gravel/matrix debonding signals. At the same time, we note that all mechanisms are not necessarily detected during the passive monitoring of the nonlinear relaxation. Indeed, the sand-resin debonding (presented in Chapter 3) was not detected but that doesn't mean it doesn't exist. This is probably related to the effect of the attenuation on this type of signal which, in addition to its low amplitude, has frequency components clearly higher than those of the two mechanisms mentioned above ($\sim 600\,\text{kHz}$). We nevertheless retain that from the energy point of view, the matrix cracking type AE signals are the ones that contribute the most to the nonlinear relaxation of micro-cracked PC samples. The work thus carried out shows that the use of AE as a tool to monitor slow dynamics helps to detect the most emissive (or energetic) events spontaneously operated within materials (in relation to the micro-mechanisms involved) and brings experimental evidence for the follow-up of stress variation along the existing cracks for a better understanding of slow dynamics in complex media.

In the following, the passive monitoring of the nonlinear relaxation will be applied to a more common material, the civil engineering concrete, before and after being damaged.

4.4 Nonlinear dynamics of civil engineering concrete samples

4.4.1 Materials and experiments

The civil engineering concrete samples are manufactured in the laboratory by mixing fine aggregates (sand), coarse aggregates (crushed granite) with cement and water following the procedure described in Chapter 3. Then, the civil engineering concrete sample is micro damaged using a three-point bending test, where the maximum load was around $\sim 2\,\text{kN}$, which corresponds to $\sim 75\%$ of its rupture force. Note that the created cracks

were not visible at the material's surface. The intact and micro-cracked samples are then submitted, in the same way as the polymer concrete samples, to fast and slow dynamic experiments. Finally, passive monitoring of the nonlinear relaxation is performed on the concrete samples with the help of acoustic emission (AE). Results related to these experiments will be detailed and discussed in the following.

4.4.2 Fast dynamics of civil engineering concrete samples

The fast dynamic (FD) experiments are conducted on the intact and previously described damaged concrete sample with the help of the experimental setup illustrated in Figure 4.1. The tested concrete samples (intact/ damaged) were excited around their third bending resonance mode following a linear sweep. The sweeping time of each excitation signal is $\sim 35\,\mathrm{s}$. The source amplitude, which is denoted A_{source}, is gradually increased from 20 mV to 1600 mV (before amplification) in order to excite the sample in the linear and nonlinear regimes. The response of the sample is measured using a piezoelectric sensor that was glued by phenyl salicylate (salol).

Figure 4.21(a) shows the evolution of resonance curves as a function of frequency for increasing excitation level of damaged concrete. Results show that at low excitation level ($A_{source} = 20\,\mathrm{mV}$ or 50 mV), the resonance curves remain unchanged and overlap, meaning the sample is excited in the linear regime. When A_{source} increases beyond 100 mV and up to 1600 mV, the change in the resonance curves becomes easily observable.

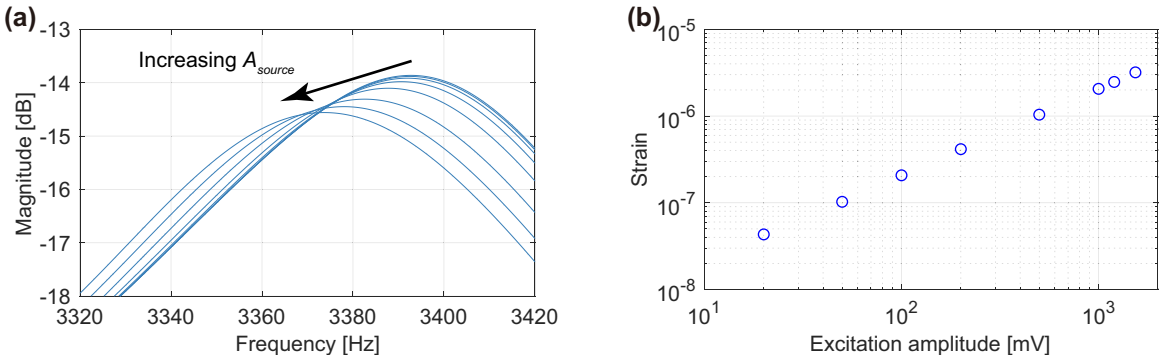

Figure 4.21: Fast dynamic (FD) of the damaged civil engineering concrete sample: (a) resonance curves (normalized to input amplitude) versus frequency of the detected signals at increasing input excitation A_{source}. (b) Maximum dynamic strain at the edge of the tested sample at resonance with different input excitation A_{source}.

In order to explore the involved dynamic strain within the sample during the bending resonance, a double head laser Doppler vibrometer (Plytec OFV-5000 controller and OFV 552 Fiber-Optic Senior Head) was used to probe its dynamic response. One laser head was fixed at the upper side and the other was fixed at the opposite side in order to detect the vertical displacement of the sample. The dynamic strain amplitude of the sample at resonance is determined and results are illustrated in Figure 4.21(b) for different excitations. This figure shows the linear correspondence between the excitation amplitude and the generated dynamic strain. When the strain amplitude is $\sim 4 \times 10^{-8}$, i.e. input excitation $A_{source} = 20\,\mathrm{mV}$, the tested sample is in the linear regime. This excitation level will then be used to probe the nonlinear relaxation of this sample in the slow dynamic (SD) experiments. As the excitation amplitude increases to reach 1600 mV, the strain

amplitude during resonance reaches $\sim 4 \times 10^{-6}$. This value will therefore be used for the conditioning during SD experiments.

Figure 4.22(a) illustrates the variation of the relative resonance frequency $(f - f_0)/f_0$ versus the excitation amplitude for a concrete sample taken at intact and damaged states, respectively. Results show the downward shift of the resonance frequency (or equivalently in wave velocity or elastic modulus) when the strain amplitude is increasing for a concrete sample taken at intact and damaged states. In addition and for the same states, Figure 4.22(b) depicts the change of the relative inverse quality factor $(1/Q - 1/Q_0)/(1/Q_0)$, which is proportional to damping, as a function of the excitation amplitude. Results show that for both states, resonance frequency and nonlinear damping evolve linearly when the excitation amplitude increases. Finally, we note that for the damaged state, when the excitation amplitude increases up to 1600 mV, the relative variation of resonance frequency and damping is $\sim 0.6\%$ and $\sim 5.5\%$, respectively. In addition, the presence of the fast dynamic effect within the intact concrete sample is due to the fact that cementitious materials contain naturally diffused micro-cracks within the cement matrix and at the matrix/aggregates interface. Meanwhile, for the maximum excitation amplitude (i.e. strain amplitude $\sim 4 \times 10^{-6}$), the relative variation of resonance frequency and damping is $\sim 0.25\%$ and $\sim 2\%$, respectively, which are all smaller than the ones observed when the concrete sample is damaged.

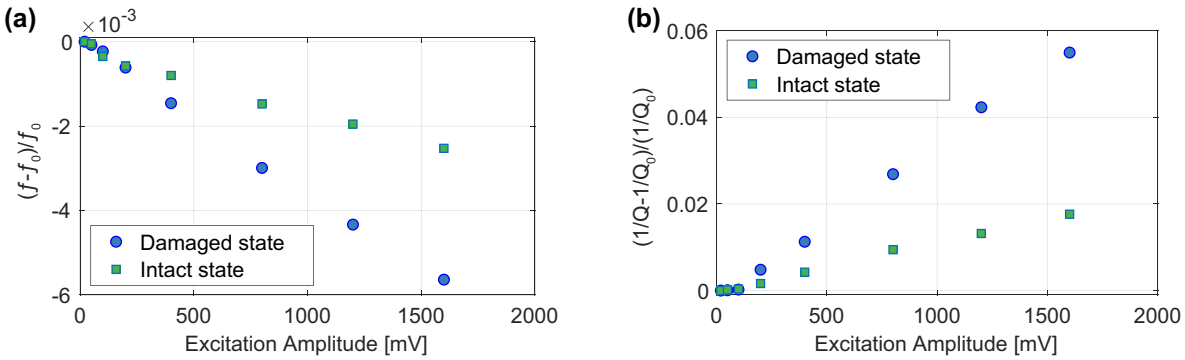

Figure 4.22: Relative resonance frequency variation (a) and relative inverse quality factor variation (b) as a function of the source amplitude for the intact and damaged concrete samples, respectively.

4.4.3 Slow dynamics of civil engineering concrete samples

Slow dynamics (SD) experiments were performed on the above-mentioned intact and micro-damaged civil engineering concrete samples. The experimental setup is similar to that of the FD experiments (see Figure 4.1). The excitation protocol of the SD experiments consists of the following three phases: Preconditioning - Conditioning - Relaxation, as already described for the slow dynamics experiments performed on the PC samples.

The excitation signals are linear sweeps where the frequency evolves around the third bending resonance mode of the tested sample. The sweeping time of each excitation is $\sim$ 35 s. In the preconditioning phase, 20 resonance sweeps at 20 mV were used to excite the sample around its resonance mode. The recorded resonance curves were superimposed, which means that the sample was vibrating in a linear regime at resonance. During the conditioning phase, the sample was repeatedly pumped by the amplified high amplitude

sweep around the same resonance mode at 1600 mV (strain amplitude $\sim 4\times10^{-6}$). The full conditioning was obtained after more than 10 minutes of high dynamic strain conditioning. Then, the nonlinear slow recovery of the elastic properties was probed by repeating the same resonance sweep at 20 mV until the full relaxation is reached.

For the intact and damaged states, the relative variation of the resonance frequency and the inverse quality factor (damping) as a function of relaxation time are shown in Figures 4.23(a) and (b). Results show that after removing the high dynamic strain, the

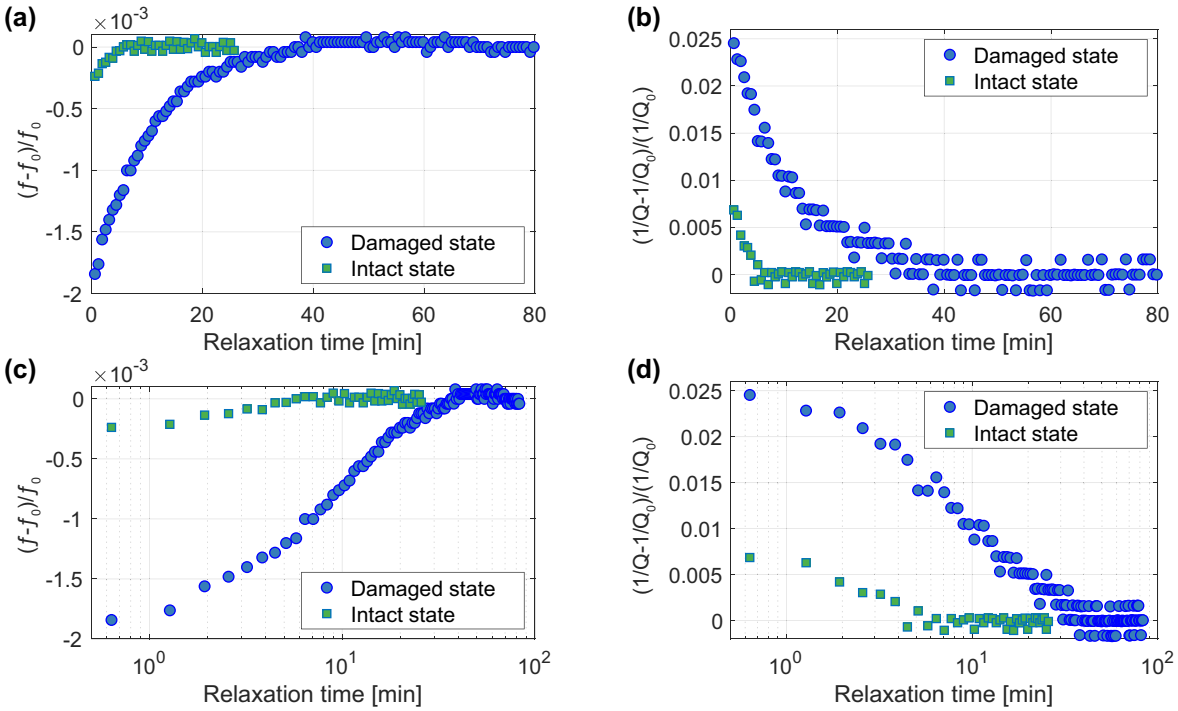

Figure 4.23: Evolution of resonance frequency and damping as a function of time during the nonlinear relaxation of a concrete sample taken at intact (a) and damaged (b) states. (c) and (d) represent the same plots when the relaxation time is in the logarithmic scale.

changes in resonance frequency and the inverse quality factor are not instantaneous. In addition, for both damaged and intact states, the elastic modulus (resonance frequency) increases and the damping (inverse quality factor) decreases versus the relaxation time until recovering their initial linear equilibrium states. At the damaged state, the complete recovery is observed after $\sim$ 40 minutes of relaxation (monitoring during 80 minutes). Recorded data between 40 minutes and 80 minutes, by repeating the same resonance sweep, show that the sample has almost recovered its initial properties, where the variation of both resonance frequency and damping is less than 0.1%. For the intact state, we measured a shorter relaxation time of $\sim$ 8 minutes for a monitoring of $\sim$ 25 minutes. This observation shows that the relaxation time evolves as a function of damage, in accordance with other results found in literature [Bentahar and El Guerjouma, 2009].

To better investigate the evolution of relaxation, a semi-log representation is used, as shown in Figures 4.23(c) and (d). As expected, during the first moments of relaxation, when the sample is probed using a low source amplitude, the concrete sample is in a 'metastable state'. This is true at the damage state, but also, at the intact state. In the middle time range, the logarithmic time behavior describes well the relaxation, in accordance with the results of the literature [Bentahar et al., 2020]. Indeed, the

recovery behavior of elastic modulus and damping is proportional to the logarithm of time [TenCate et al., 2000b]. We also note that at the very late (near equilibrium) stages of relaxation, deviations from the expected log-time behavior are observed. Similar observations were performed in references [Mechri et al., 2019, Bentahar et al., 2020], where the same sample was tested using compression resonance modes. Therefore, the behavior in the process of relaxation should thus be described by a kinetic law more complex than a simple logarithmic function, such as the one proposed in [Snieder et al., 2016] or multi-scale relaxation model [Shokouhi et al., 2017] or others [Ostrovsky et al., 2019].

4.5 Passive monitoring of nonlinear relaxation

4.5.1 Materials and experiments

As for the PC samples, we used AE sensors to study the nonlinear relaxation of intact and micro-damaged civil engineering concrete samples during slow dynamic experiments. In the light of the results obtained for the PC samples, we therefore expect to detect weak energy amounts which can be emitted by the material during the recovery process. The experimental setup is illustrated in Figure 4.9 and detailed information are given. The experimental protocol is shown in Figure 4.24, which presents the following four steps:

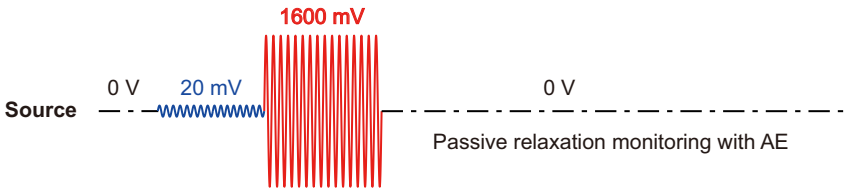

Figure 4.24: Passive relaxation monitoring experiments protocol for civil engineering concrete samples.

1 – AE monitoring in the absence of excitation: During this phase, after samples were installed on the shaker, the experimental setup was placed at room temperature fixed at 23 °C and isolated from outside, because concrete is known to be sensitive to the environmental conditions (temperature, humidity, etc.). Then, samples are monitored with AE to verify the absence or presence of any acoustic activity that may be created by any undesirable external source. The acquisition parameters were set the same as PC samples.

2 – Preconditioning: The sample was repeatedly excited with a low excitation amplitude (20 mV, strain $\sim 10^{-8}$), where the frequency is linearly swept between 3300 Hz and 3450 Hz to encompass the third bending resonance mode. We verify that resonance curves (amplitude and phase) are superimposed with the help of gain-phase analyzer.

3 – Conditioning: The sample is repeatedly excited around the same frequency range while the excitation amplitude is set at 1600 mV (strain $>10^{-6}$). After more than 10 minutes of high dynamic strain conditioning, we notice a softening within the viscoelastic properties of the concrete sample. In order to have results that could reasonably be compared with those of the classical slow nonlinear experiments, the conditioning time was not changed (20 cycles of sweep excitation), i.e. sufficiently long to reach the full conditioning state.

4 – Passive relaxation monitoring with AE: The excitation amplitude was then set back to zero to let the samples recover naturally. The relaxation of concrete samples is passively probed with AE, where the detection threshold is 30 dB.

4.5.2 Passive relaxation and conditioning

4.5.2.1 Intact concrete

For the civil engineering concrete sample taken at the initial intact state, results of slow dynamic experiments presented in Figure 4.23, show the presence of a relaxation time of $\sim$ 8 minutes when using the classical probing method. However, during the passive relaxation

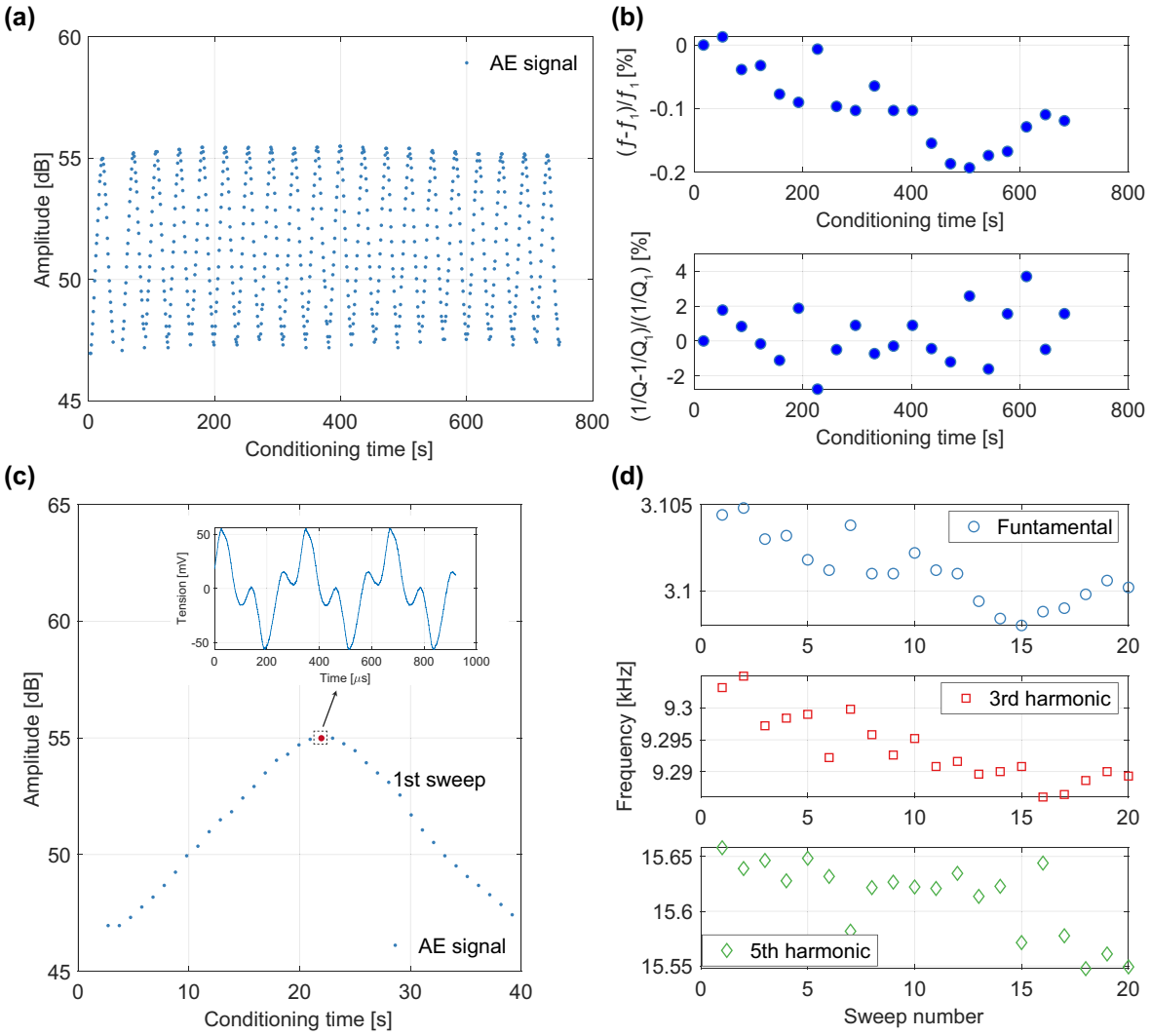

Figure 4.25: (a) AE Monitoring of a intact concrete sample response during conditioning. (b) Evolution the relative frequency and damping during conditioning; f_1 and Q_1 correspond to resonance frequency and quality factor collected from the first cycle, respectively. (c) The first excitation cycle recorded during the conditioning. The insert represents one of the $\sim$ 35 signals that make up the resonance curve. (d) Evolution of the fundamental frequency and harmonics of the isolated signal during the 20 sweeps used to condition the intact concrete sample.

experiments, the AE monitoring didn't show the existence of any acoustic activity within the same sample, even for a longer monitoring (more than 1 hour). Unlike the intact PC sample, which has no relaxation, the intact concrete sample has a weak recovery behavior which is due to the existing micro-cracks. In order to understand the absence of AE during the relaxation of intact concrete samples, we analyzed the conditioning data collected using AE sensors (connected to the Mistras USB AE Node acquisition system). During this phase, the AE sensor positioned at the center of the sample continuously recorded the material's response as shown in Figure 4.25(a). The analysis of the data recorded by the AE system shows that the frequency at resonance drops slightly whereas the damping doesn't have a clear evolution (see Figure 4.25(b)). The frequency drop (even if it's weak) was also verified on the harmonics generated during the conditioning (see Figures 4.25(c) and (d)), however no conclusion could be drawn for the damping related to the different harmonics.

In order to highlight the damping effect on the high frequency components, signals were high-pass filtered with a cutoff frequency of 80 kHz. Results corresponding to the evolution of the energy per sweep before and after filtering is plotted in Figure 4.26. The latter shows that the high-frequency components are decreasing as a function of the conditioning time until the sample reaches the full conditioning state. Therefore, the high frequency components are much more affected by the conditioning (and therefore by post-conditioning) than the low frequencies. Furthermore, we believe that the micro-cracks distribution (the randomly distributed micro-cracks are non-localized in the case of intact concrete samples) will not necessarily help emitting elastic waves in the direction of the AE sensor which is located at the center of the sample. This makes the amplitude of the detected waves weak enough to be ifnored by the AE sensor.

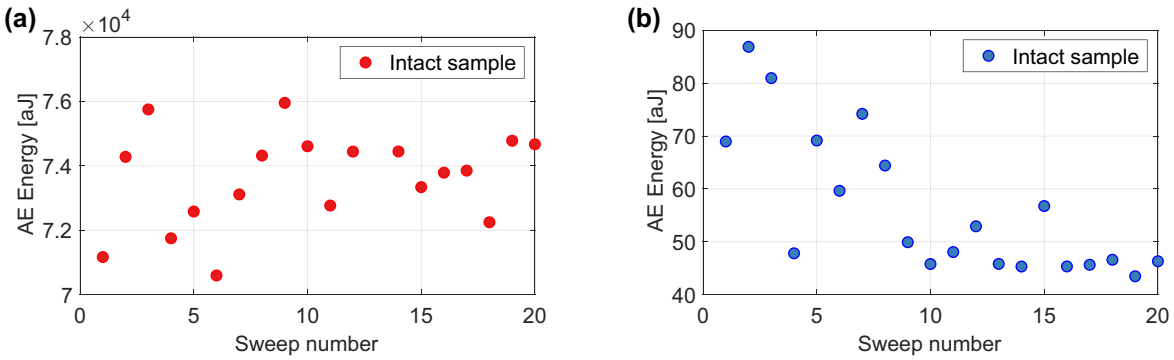

Figure 4.26: Total AE energy of recorded signals (a) and of high-pass filtered signals (b) for each sweep.

4.5.2.2 Damaged concrete

The effect of conditioning on the partially damaged concrete samples is presented in Figure 4.27. During this phase, the AE sensor positioned at the center of the sample continuously recorded the material's response along the applied cycles. The analysis of the data recorded by the AE system shows an increase in the resonance frequency drop and a clear evolution of the damping in comparison with the intact state (see Figures 4.27(a) and (b)). Furthermore, the frequency analysis of a single sweep revealed the existence of odd harmonics whose frequencies also drop during the conditioning (see Figures 4.27(c) and (d)).

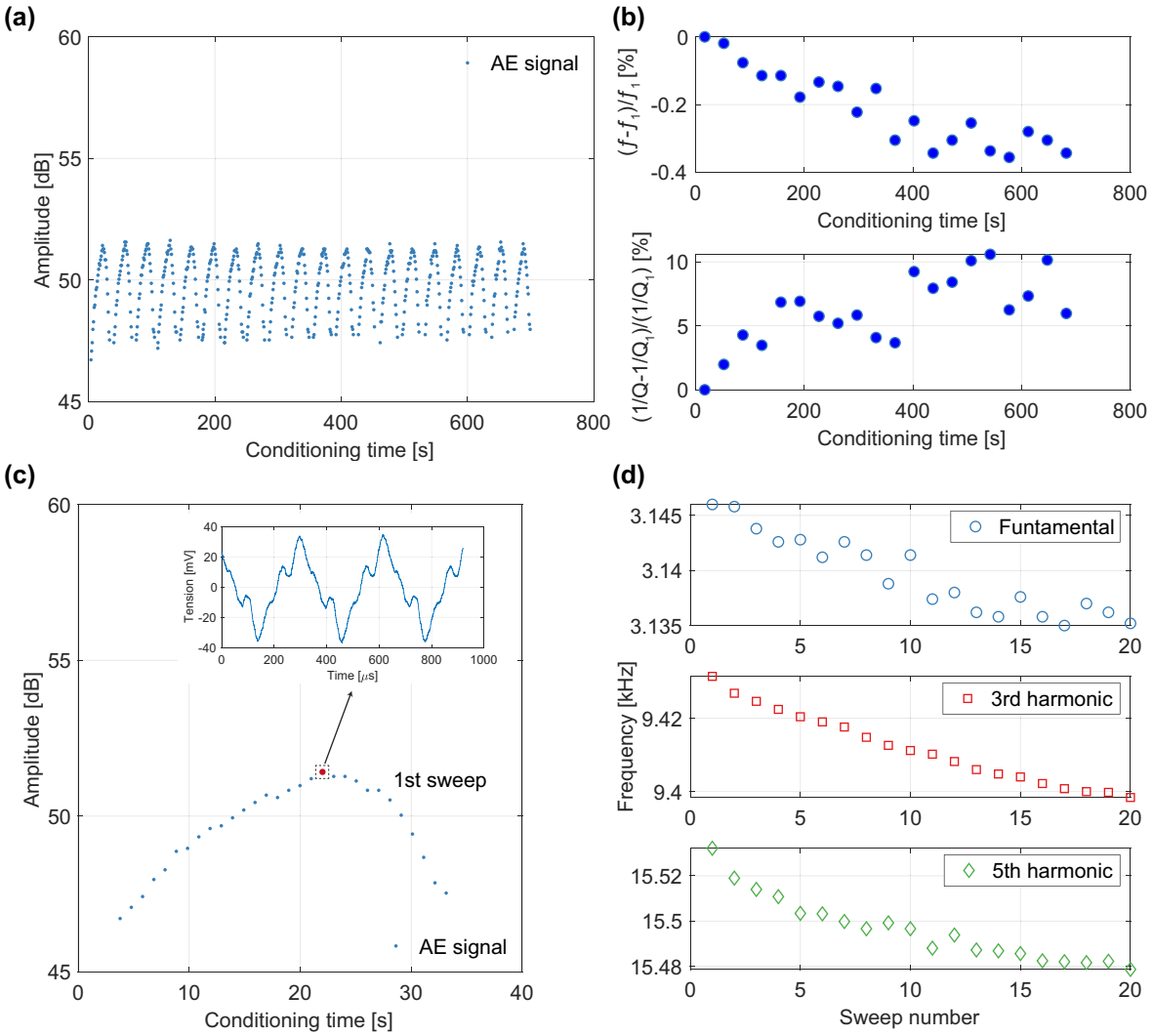

Figure 4.27: (a) AE Monitoring of the above-mentioned concrete sample (at the partially damaged state) response during conditioning. (b) Evolution the relative frequency and damping during conditioning; f_1 and Q_1 correspond to resonance frequency and quality factor collected from the first cycle, respectively. (c) The first excitation cycle recorded during the conditioning. The insert represents one of the $\sim$ 35 signals that make up the resonance curve. (d) Evolution of the fundamental frequency and harmonics of the isolated signal during the 20 sweeps used to condition the concrete sample at the damaged state.

On the other hand, the damping effect was also observed on the energy of time-signals recorded during the conditioning before and after being high-pass filtered with a cutoff frequency at 80 kHz. Figure 4.28(a) shows that in the absence of filtering the recorded energy per sweep is just fluctuating during the 20 cycles of excitation. Whereas, the high-frequency components of the energy are decreasing as a function of the conditioning time until the sample reaches the full conditioning state. Note also that the amount of high frequency energy components has decreased from $\sim$ 90 aJ to $\sim$ 40 aJ between the intact and damaged states, and that evolution imposed by the conditioning is smaller in the case of the damaged state (8 aJ in the damaged state and 50 aJ in the intact state). The effect of the increase in damping can also be visible in the unfiltered energy values, which have decreased between the intact ($\sim 7.4 \times 10^4$ aJ) and damaged states ($\sim 3.9 \times 10^4$ aJ).

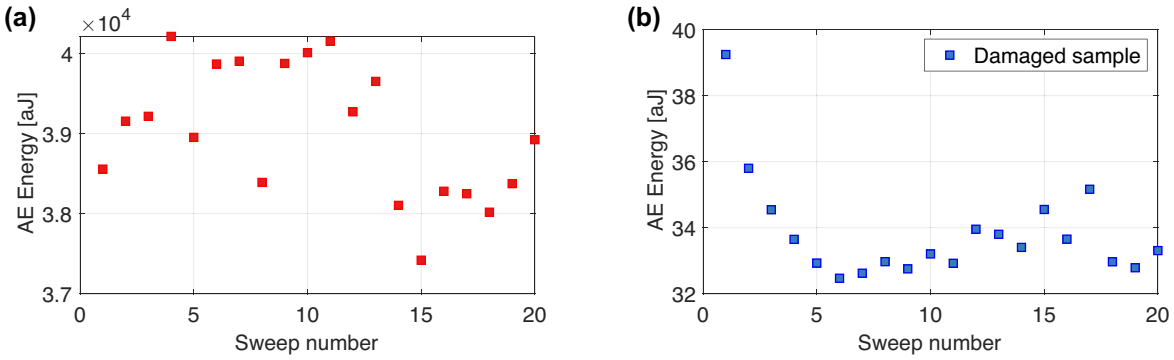

Figure 4.28: Total AE energy of recorded signals (a) and of high-pass filtered signals (b) for each sweep.

Right after the full conditioning, we noticed the absence of AE activity. Indeed, Figure 4.29 shows the existence of a 'silence period' which lasts $\sim 100\,\mathrm{s}$ and whose duration is approximately ~ 5 times shorter than the ones observed during the relaxation of damaged PC samples. With the help of the results presented in Figure 4.23(b), we notice that the silence period (which lasts $\sim 100\,\mathrm{s}$) corresponds to a decrease or recovery of the relative damping from $\sim 2.5\%$ to $\sim 2\%$ with a potential link with the previously described 'metastable state'.

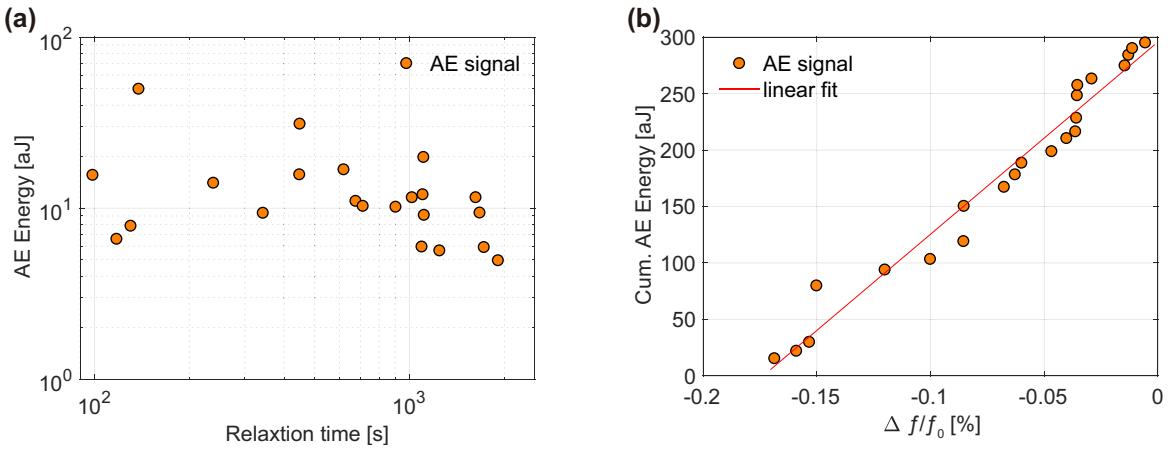

Figure 4.29: (a) Energy of the AE signals detected during the relaxation (in log-Time) of the damaged civil engineering concrete sample. (b) Proportionality between cumulative energy of AE signals and resonance frequency determined during passive and active relaxation monitoring, respectively.

Following this silence period, AE hits start to be detected and their number was gradually increasing as a function of the relaxation time. The AE energy of the detected AE hits versus relaxation time is shown in Figure 4.29(a), where each point represents an AE signal and the involved amplitudes are between 30 dB and 35 dB. By applying the same conditioning on the damaged concrete sample and by following the relaxation with a weak amplitude signal first and then with acoustic emission (passive probing), we found an interesting proportionality between the cumulative AE energy and the relative change of the resonance frequency (see Figure 4.29(b)). Indeed, the latter shows a linear relationship between the cumulative elastic energy released by the material and the elastic properties recovery of material during relaxation.

We recall that in the active probing method, the relaxation time is determined once the full recovery to the initial properties is reached. In the proposed passive method, the relaxation 'stops' at the time when no AE activity is detected, even if the monitoring time ($\sim 1\,\mathrm{h}$) is longer than the relaxation time measured by the above-mentioned active method ($\sim 2400\,\mathrm{s}$). Figure 4.30 compares the relaxation times based on both passive and active monitoring methods in the case of a damaged concrete sample. We note that the relaxation times $t_p \sim 2000\,\mathrm{s}$ and $t_a \sim 2400\,\mathrm{s}$ are a priori different. However, when the passive relaxation 'stops' (i.e. t_p) the relative resonance frequency change is 0.015%, which means that the material has reached $\sim 95\%$ of its preconditioning frequency recovery. Finally, we note that active and passive relaxation experiments were repeated on the same samples at successive days. The trends presented here were reproducible with the range of $\pm 15\%$ in terms of relaxation time, signals' energy, cumulative energy, etc.

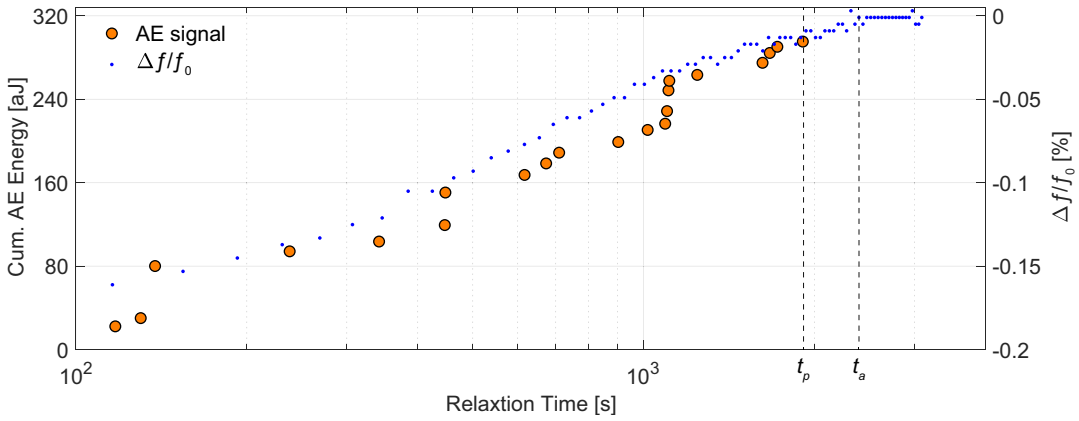

Figure 4.30: Comparison between the active (resonance frequency) and passive (acoustic emission) relaxation monitoring methods. t_a and t_p correspond to relaxation time based on both active and passive methods, respectively.

4.5.3 Nonlinear relaxation and damage mechanisms

As mentioned earlier, detected AE signals during the passive relaxation experiments have weak amplitudes, and are therefore mixed with noise. Before processing the AE signals in order to extract their features, we used the 'modified soft thresholding technique (MSTT)' to reduce the noise and perform further analyses. Figure 4.31(a) compares the waveforms of denoised and original signals, where the main waveform features remain similar (amplitude, rise time, etc). In addition, the difference between the original and denoised signals is also computed by comparing their wavelet scalograms as illustrated in Figure 4.31(b). Indeed, the time-frequency representation shows the existence of a blue area, which corresponds to the lowest differences between signals. This result means that the MSTT method removes efficiently the background noise, while the useful information of the AE signals is saved.

Once the AE signals are denoised and based on the classification results presented in chapter 3, the application of the unsupervised pattern recognition analysis allowed to separate the detected AE hits into two classes, namely CLC and CLD. The AE signals corresponding to class CLC were the ones to be detected during all the passive relaxation time whereas CLD signals were only detected during the second half of the relaxation time

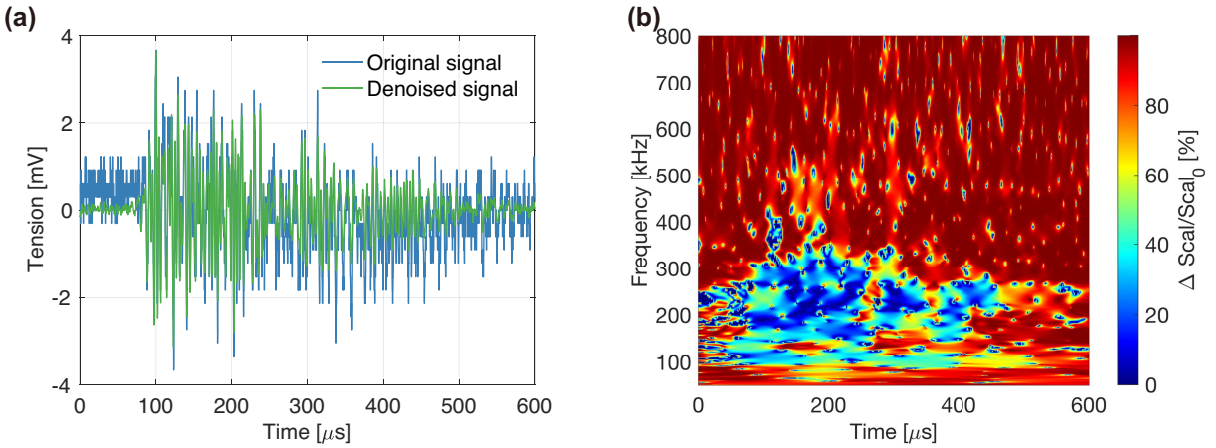

Figure 4.31: (a) Comparison of AE signal before denoising and after MSTT denoising. (b) Difference between two signal in time-frequency representation.

with a weak appearance. Figure 4.32(a) shows the evolution of AE energy corresponding to the two detected types of AE signals as a function of the relaxation time. CLD appears only in the middle of the relaxation process and represents approximately $\sim 20\%$ of the detected signals. Figure 4.32(b) allows to quantify the amount of the elastic energy freed by the concrete during the nonlinear relaxation. Indeed, the evolution of the cumulative AE energy of the two classes shows that CLC and CLD evolve with approximately the same slope. However, it remains possible to distinguish between both mechanisms using other AE features.

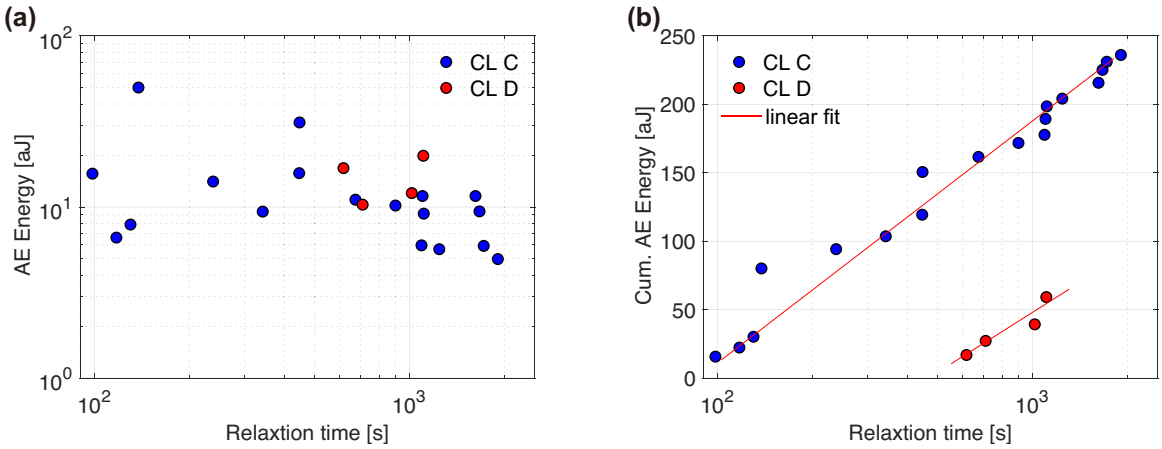

Figure 4.32: (a) Evolution of energy of the detected AE signals as a function of relaxation time. (b) Cumulative energy of the detected AE signals in two classes versus relaxation time.

In the literature related to AE monitoring of civil engineering concrete samples, the waveform of the AE signal is directly linked to the cracking mode [Aggelis, 2011, Aldahdooh and Bunnori, 2013]. For the tensile crack, rise time and duration of tensile AE signals are always shorter. However, shear AE signals have inverse characteristics. In that sense, two AE parameters, namely RA value and average frequency (AF) have been introduced when studying the crack mode classification.

Figures 4.33(a) and (b) depict a 2D projection of the identified AE classes within the feature plan (Rise time vs. Duration and RA value vs. AF). Results show that the

AE signals belonging to the CLC class have higher rise time and shorter duration, and are clearly separated from the ones of the CLD. Additionally, the RA-AF representation shows that CLC class signals have higher AF and lower RA value compared to CLD class signals. These results suggest that two classes of AE signals detected during the passive nonlinear relaxation experiments can be associated with the dynamics of the two kind of cracking modes whose movement is at the origin of the slow recovery of the concrete samples. The formation of a tensile crack corresponds to a transient volumetric change occurring in the location of the crack tip. However, in the case of a shear cracking, the sides of the crack move in opposite directions but in parallel to the crack plane, which mainly leads to shape deformation.

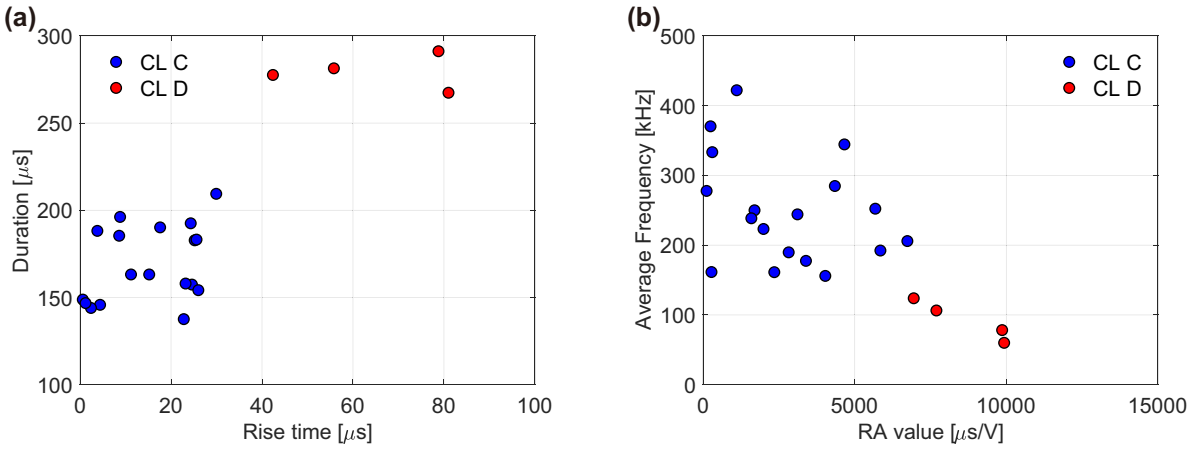

Figure 4.33: Illustration of the AE data with clustering results in the two-dimensional planes of AE features. (a) The projection of AE data into the plane of Rise time versus Duration. (b) The projection of AE data into the plane of RA value versus Average frequency (AF).

Furthermore, the properties of AE signals obtained during the passive relaxation measurements and those corresponding to damage mechanisms created during the quasi-static tests appeared to be similar. Figure 4.34 shows typical waveforms and wavelet scalogram of CLC signals and tensile cracking signals. In order to compare the energy distribution of dynamic and quasi-static AE signals, the energy density within each wavelet scalogram is normalized to the highest energy in the Time-Frequency (T-F) plan (i.e. maximum value in the T-F matrix). The waveforms of both signals show that CLC AE hits have a short rise time in accordance with those of the tensile cracking. From the wavelet scalogram of both types of signals, the highest energy distribution is around 500 kHz. On the other hand, the comparison between CLD signals and those associated to shear cracking mechanism obtained during the quasi-static tests is presented in Figure 4.35. The latter shows that both waveforms have their energy distribution mainly located in between $\sim$ 200 kHz and $\sim$ 230 kHz with a quiet long duration ($\sim$ 250 μs). These last results represent an additional proof of the relevance of the use of acoustic emission to monitor and characterize complex phenomena such as nonlinear relaxation.

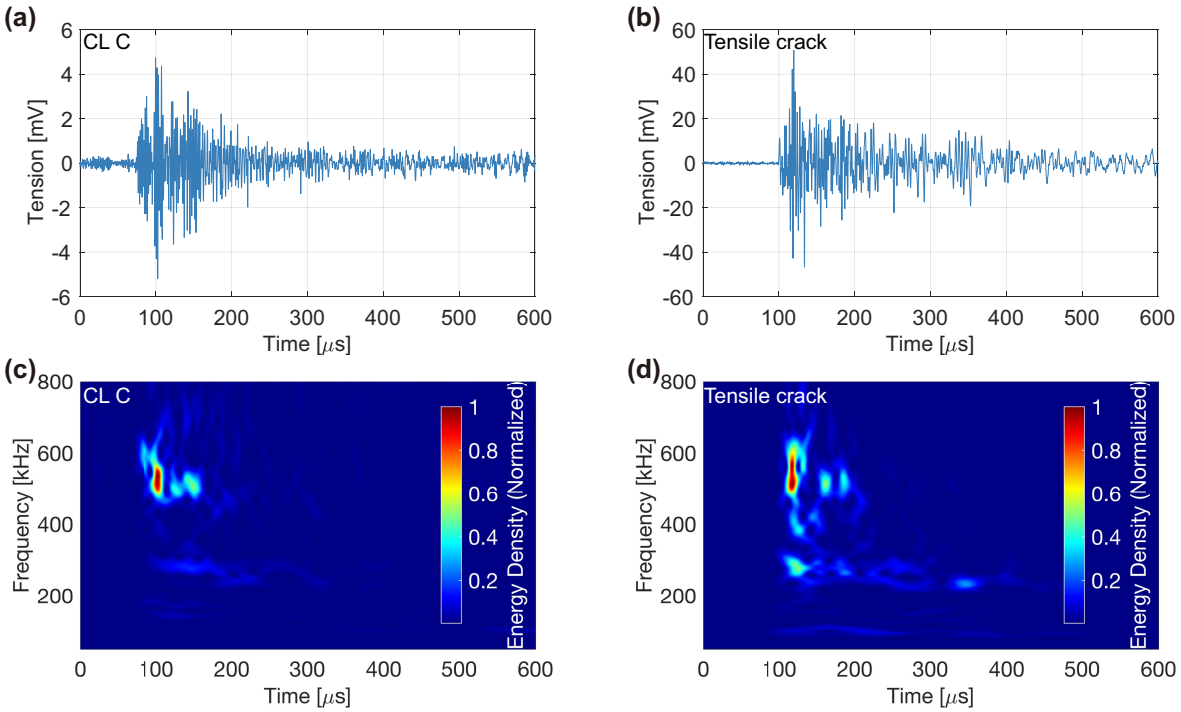

Figure 4.34: Time-amplitude and time-frequency representations of AE hits detected during the nonlinear relaxation (CLC) ((a) and (c)) and during the quasi-static tests (tensile crack) ((b) and (d)).

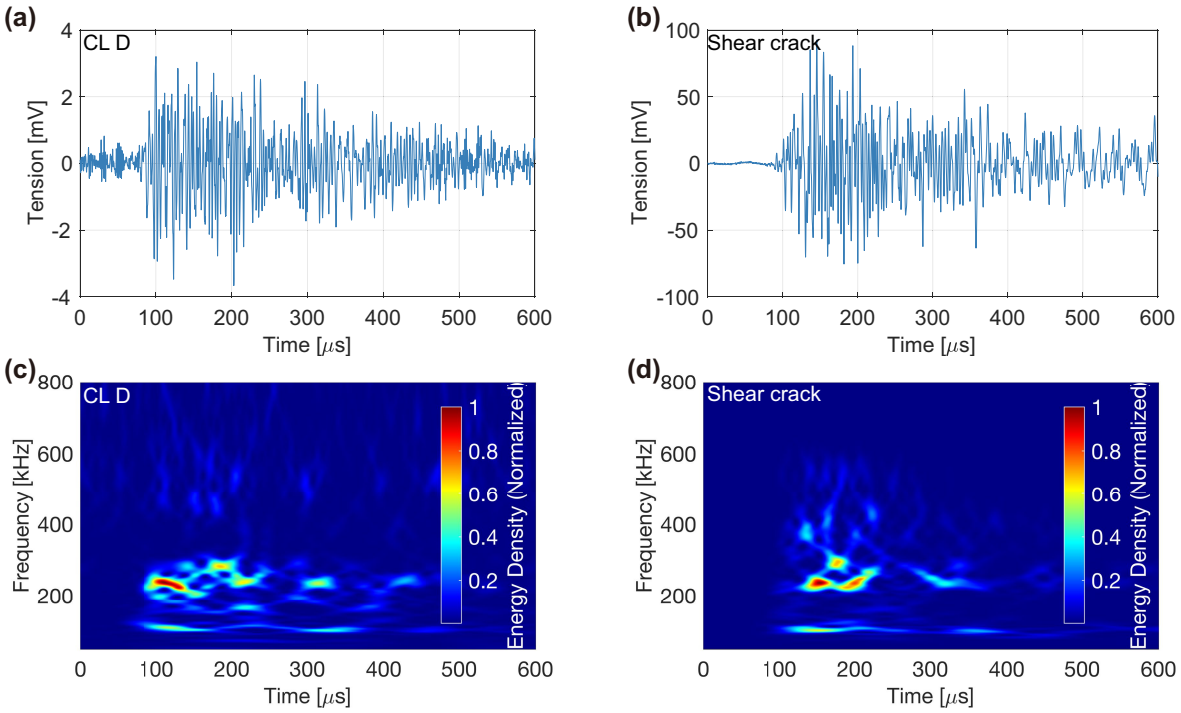

Figure 4.35: Time-amplitude and time-frequency representations of AE hits detected during the nonlinear relaxation (CLD) ((a) and (c)) and during the quasi-static tests (shear crack) ((b) and (d)).

4.6 Conclusion

In this chapter, we characterized the nonlinear behavior of intact and micro-cracked polymer concrete and civil engineering concrete samples. The use of a calibrated experimental setup allowed us to follow the evolution of their dynamic behavior around their bending resonances during fast and slow nonlinear dynamic experiments. In order to get rid of the low amplitude probe signal, commonly used in slow dynamic experiments (active method), we proposed an original passive relaxation monitoring protocol based on the use of AE sensors. Results showed a very good correlation between the active and passive approaches, which validates the use of the passive approach. Furthermore, the signal processing of the AE signals recorded during the passive relaxation showed a clear resemblance to those obtained during the quasi-static mechanical tests applied to the same concrete samples. The resemblance could be therefore related to the cracking at the interfaces or within the same phase. Finally, this work showed that the use of acoustic emission could even concern cracking mechanisms such as tensile or shear, which appear to have an important role during the relaxation of concrete.

General conclusion

The purpose of this thesis work was to study acoustic emission hits emitted by complex materials namely polymer concrete and civil engineering concrete. At first, AE hits were recorded during quasi-static mechanical tests in bending where it was possible to focus on the fracture process analysis by taking into account parameters such as the one inspired from observations made in seismology i.e. b-value. We have also used the RA and AF parameters, based on the shape of AE waveforms. For civil engineering concrete samples, results showed that micro-cracks of specimens can be separated into two main modes, namely shear and tensile cracks. This work has shown that a separation of AE signals originating from shear or tensile cracks is possible according to a specific procedure in which the RA/AF ratio should be argued and calculated. On the other hand, the development of an unsupervised pattern recognition method was performed to cluster the AE data. Indeed, the use of a Principal Components Analysis (PCA) followed by the k-means analysis allowed to separate AE hits into two classes, where the optimal clustering is obtained according to the minimum value of the Davies and Bouldin (DB) index and the maximum value of the Silhouette coefficient (SC). We also note that this result is valid for both mortar and civil engineering concrete samples and we believe that the resemblance is most probably due to the fact that crack formations is happening within the matrix due to its relatively lower strength.

Beyond the application of the abovementioned procedure to probe damage within polymer concrete samples, this work has also allowed to develop an image-based classification methodology through the analysis of the time-frequency representation of AE signals. Indeed, the association of the continuous wavelet transform and the use of a transfer learning procedure with the conventional neural network algorithm allowed to obtain the same three main damage mechanisms found when applying the unsupervised pattern recognition algorithm. Finally, this work has shown that despite the complexity of the material studied, the quality of the proposed classification method was not affected by the different threshold changes. Indeed, the proportion of AE signals within the confusion class was found to be always under $\sim 7\%$, independently from the chosen threshold.

This thesis has also showed that it is possible to apply acoustic emission as a technique to verify in situ the existence of micro-cracks within complex materials. Indeed, in literature AE is used to monitor the creation and propagation of microcracks when materials and/or structures are under load. Through the work developed, we showed that by exciting the complex materials around one of their resonance modes, the acoustic activity can change significantly depending on the microstructural state of the material. This is true as long as the material is excited in a nonlinear regime, which suggests at the same time that it is possible to link the acoustic activity to the micro-mechanisms that are activated during the nonlinear behavior of complex materials.

The results have shown interesting observations when it comes to characterizing conditioning. Our measurements showed that this was essentially linked to the fact that the sensitivity was not necessarily localized around the resonance frequencies (low frequencies) and that it was necessary to seek it in the high frequencies either for the resonance frequency (elastic modulus) or the quality factor (damping). Indeed, the AE probing during the conditioning of concrete samples is mainly dominated by the low frequency excitation signal (around bending resonance) and its harmonics. The probing during the conditioning showed that all of these frequencies are decreasing as a function of the conditioning time but the energy of the detected signals is almost constant. However, when we focus on frequencies above 80 kHz, we noticed that the total energy undergoes a monotonous decrease (of $\sim 35\%$) as a function of the conditioning time in the case of damaged concrete samples.

This thesis was also an opportunity to compare the classical nonlinear relaxation (based on the use of a probe wave) and the original passive relaxation probing. Results showed the existence of a 'silence period' at the first minutes of relaxation. The absence of AE during this period was naturally attributed to important increase in the attenuation during the conditioning phase. On the other hand, we have shown the existence of proportionality between cumulative energy of the detected AE signals during the passive relaxation and the resonance frequency recovery determined during the active relaxation monitoring. In this regard, we have found that the difference between relaxation times with the help of AE and the probe wave is very small (the difference starts around $\sim 97\%$ of the recovery but is always shorter for the AE probing). Nevertheless, we should keep in mind that the AE monitoring of the nonlinear relaxation is not a way to systematically replace the monitoring via a probe wave. Indeed, we have shown that in the case of intact concrete, the probe wave revealed the existence of a nonlinear relaxation while the AE is absent (may be due to an improper positioning of the AE sensors).

The application of the multi-parameter unsupervised pattern recognition analysis allowed to separate the AE signals detected during the nonlinear relaxation. Indeed, in the case of PC samples the properties of the latter signals and the ones corresponding to damage mechanisms (matrix cracking and gravel matrix debonding) created during the quasi-static tests appeared to be similar. Furthermore, the pattern recognition analysis showed that the kinematics of relaxation is class-dependent and that their energy contributions can be different by several orders of magnitude. On the other hand, in the case of civil engineering concrete samples, the existence of two main groups of AE hits was highlighted. Indeed, results suggest that the two classes of AE signals detected during the passive nonlinear relaxation experiments can be associated to tensile and/or shear cracking mechanisms based on the rise time, duration and the wavelet scalogram of AE signals.

Perspectives

Slow dynamics is a universal behavior that has been observed on a wide range of materials. Its universality hinders, very often, the identification of the physical mechanisms that are the origin of the experimental observations made during the nonlinear dynamic experiments such as conditioning and/or relaxation. By performing calibrated acoustic emission measurements, this PhD work made it possible to account for the links that exists between micro-mechanisms related to damage in concrete samples and slow dynamics. Also, this work has also opened up perspectives on possible improvements that can brought to the use of AE during slow dynamics experiments.

In the light of the results obtained we think that the orientation of the cracks as well as the type of resonances generated during conditioning could have an important effect on the detection of AE hits during slow dynamics. Indeed, on the PC sample damaged using a three-point bending test, we performed slow dynamic experiments with the help of a compressional wave around resonance. At the time when the evolution of attenuation and velocity showed a clear evolution due to conditioning, we noticed the absence of acoustic emission during the relaxation. This result differs from the one we obtained

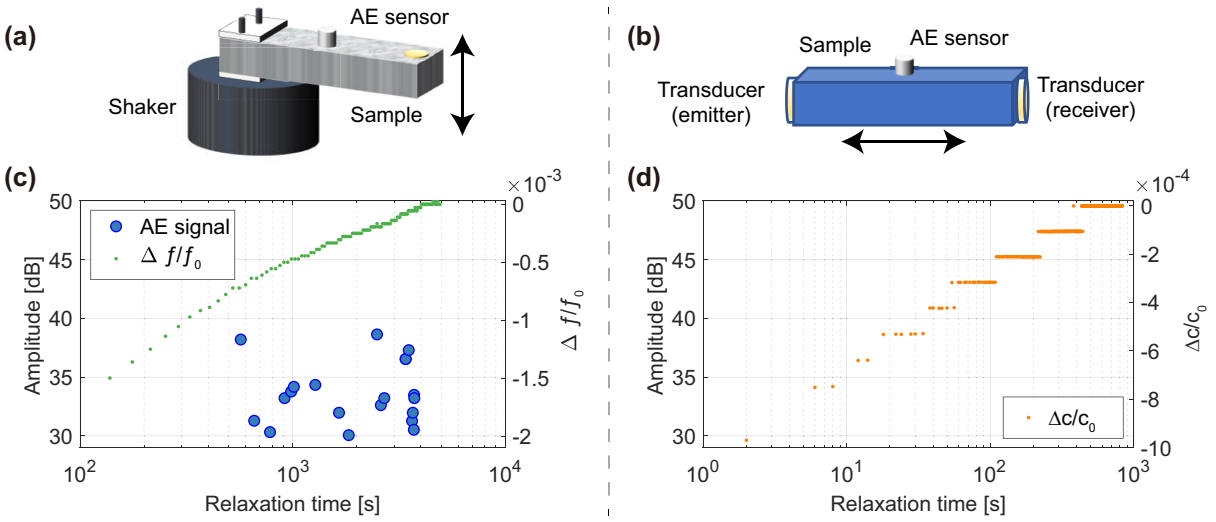

Figure 4.36: Experimental setup of the nonlinear measurements monitored with passive acoustic emission (AE) system in flexural mode (a) and longitudinal mode (b). Comparison between the active (resonance frequency or velocity) and passive (AE) relaxation monitoring methods of the same damaged polymer concrete excited around the bending (c) and the compressional (d) resonance.

on the same sample when the conditioning is applied around the bending resonance (see Figure 4.36). This result shows that the nonlinear response changes as a function of the way the nonlinear sources are excited and the consequences this could have on the emission of acoustic signals during the relaxation.

In general, it is difficult to specify the orientation of the cracks within complex materials. Therefore, a well-studied use of the AE sensors network would allow to better intercept the acoustic signatures of the nonlinear sources during slow dynamics. We believe that this step is necessary for the development of quantitative passive AE monitoring of slow dynamics which can be developed by taking into account simple thermodynamics-based [Li et al., 2018] or multi-scale relaxation models [Shokouhi et al., 2017] or others [Ostrovsky et al., 2019].

Moreover, the sensitivity of consolidated granular materials to environmental conditions requires particular attention with regard to temperature and humidity. Indeed, we believe that acoustic emission can play an important role in that sense like what we got when we highlighted the existence of the silence period. Indeed, Figure 4.37 shows an Environmental Scanning Electron Microscope (ESEM) image of a Portland cement sample. First, ESEM images show that the high moisture environment creates an adsorption of water within pores which prevents from seeing the texture. The texture of the undistributed hydration products in the pores can be observed again one second after the conditioning. After a recovery of ~ 67 seconds the moisture is returning again within the large pore [Bittner and Popovics, 2019]. With regard to civil engineering concrete samples, these observations show that there is a potential link between the 'silence period' and migration of water out of and back into the pore space.

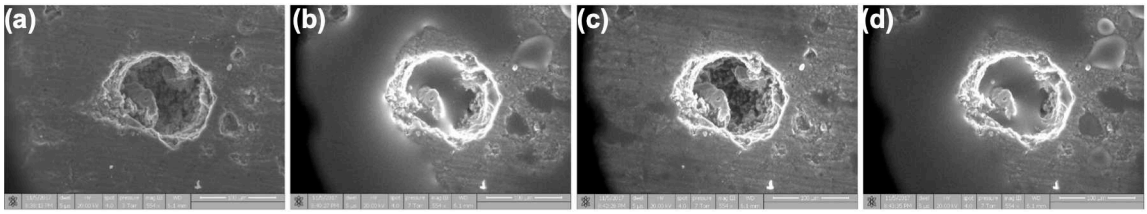

Figure 4.37: ESEM images from the center of the disc sample. The image on subplot(a) shows a measurement in the low moisture environment (RH 30% 10C) and subplot(b) in the high moisture environment (RH 97% 10C). The subplots(a) and (b) show the sample in the **Before** phase, prior to dynamic excitation being applied to the disc sample; subplot(c) in the **Recovery** phase 1 s after termination of dynamic excitation and subplot(d) in the **Recovery** phase 60 s after termination of dynamic excitation. [Bittner and Popovics, 2019]

Finally, we propose to deepen the conventional neural network (CNN) analysis by studying at first the influence of the representation used. This will concern the seeking of time-frequency transforms that propose other compromises than the time-scale (constant relative frequency resolution) such as the classic short-time Fourier transform (STFT). Besides, as an alternative to the transfer learning technique, we suggest testing the effectiveness of more recent approaches based on neural networks such as GAN (Generative Adversarial Network). This will allow us to obtain an explainable network in the context of the materials characterization and the nondestructive testing (NDT) and by the same to specify the properties of acoustic emission signals in connection with the damage mechanisms.

Bibliography

[Acharya et al., 2017] Acharya, U. R., Oh, S. L., Hagiwara, Y., Tan, J. H., Adam, M., Gertych, A., and San Tan, R. (2017). A deep convolutional neural network model to classify heartbeats. *Computers in biology and medicine*, 89:389–396. 51

[Aggelis et al., 2010] Aggelis, D., Barkoula, N., Matikas, T., and Paipetis, A. (2010). Acoustic emission monitoring of degradation of cross ply laminates. *The Journal of the Acoustical Society of America*, 127(6):EL246–EL251. 17

[Aggelis et al., 2013a] Aggelis, D., Mpalaskas, A., and Matikas, T. (2013a). Investigation of different fracture modes in cement-based materials by acoustic emission. *Cement and Concrete Research*, 48:1–8. 16, 67, 69, 70, 74

[Aggelis et al., 2012] Aggelis, D., Shiotani, T., Papacharalampopoulos, A., and Polyzos, D. (2012). The influence of propagation path on elastic waves as measured by acoustic emission parameters. *Structural health monitoring*, 11(3):359–366. 15, 78

[Aggelis et al., 2013b] Aggelis, D., Soulioti, D., Gatselou, E., Barkoula, N.-M., and Matikas, T. (2013b). Monitoring of the mechanical behavior of concrete with chemically treated steel fibers by acoustic emission. *Construction and Building Materials*, 48:1255–1260. 16, 70, 72

[Aggelis et al., 2013c] Aggelis, D., Verbruggen, S., Tsangouri, E., Tysmans, T., and Van Hemelrijck, D. (2013c). Characterization of mechanical performance of concrete beams with external reinforcement by acoustic emission and digital image correlation. *Construction and Building Materials*, 47:1037–1045. 70

[Aggelis, 2011] Aggelis, D. G. (2011). Classification of cracking mode in concrete by acoustic emission parameters. *Mechanics Research Communications*, 38(3):153–157. 16, 17, 31, 67, 69, 70, 71, 72, 75, 78, 79, 130

[Aggelis and Shiotani, 2007] Aggelis, D. G. and Shiotani, T. (2007). Experimental study of surface wave propagation in strongly heterogeneous media. *The Journal of the Acoustical Society of America*, 122(5):EL151–EL157. 15

[Aldahdooh and Bunnori, 2013] Aldahdooh, M. and Bunnori, N. M. (2013). Crack classification in reinforced concrete beams with varying thicknesses by mean of acoustic emission signal features. *Construction and Building Materials*, 45:282–288. 17, 67, 78, 130

[Alelyani et al., 2018] Alelyani, S., Tang, J., and Liu, H. (2018). Feature selection for clustering: A review. In *Data Clustering*, pages 29–60. Chapman and Hall/CRC. 43

[Antonaci et al., 2010] Antonaci, P., Bruno, C. L. E., Bocca, P. G., Scalerandi, M., and Gliozzi, A. (2010). Nonlinear ultrasonic evaluation of load effects on discontinuities in concrete. *Cement and Concrete Research*, 40(2):340–346. 23

[Antonini and Orlandi, 2001] Antonini, G. and Orlandi, A. (2001). Wavelet packet-based emi signal processing and source identification. *IEEE Transactions on Electromagnetic Compatibility*, 43(2):140–148. 40

[Assarar et al., 2015] Assarar, M., Bentahar, M., El Mahi, A., and El Guerjouma, R. (2015). Monitoring of damage mechanisms in sandwich composite materials using acoustic emission. *International Journal of Damage Mechanics*, 24(6):787–804. 46

[Auger and Flandrin, 1995] Auger, F. and Flandrin, P. (1995). Improving the readability of time-frequency and time-scale representations by the reassignment method. *IEEE Transactions on signal processing*, 43(5):1068–1089. 34

[Bedi et al., 2013] Bedi, R., Chandra, R., and Singh, S. (2013). Mechanical properties of polymer concrete. *Journal of Composites*, 2013. 80

[Behnia et al., 2014] Behnia, A., Chai, H. K., and Shiotani, T. (2014). Advanced structural health monitoring of concrete structures with the aid of acoustic emission. *Construction and Building Materials*, 65:282–302. 67

[Belkin and Niyogi, 2002] Belkin, M. and Niyogi, P. (2002). Laplacian eigenmaps and spectral techniques for embedding and clustering. In *Advances in neural information processing systems*, pages 585–591. 43

[Benabdeslem and Hindawi, 2011] Benabdeslem, K. and Hindawi, M. (2011). Constrained laplacian score for semi-supervised feature selection. In *Joint European Conference on Machine Learning and Knowledge Discovery in Databases*, pages 204–218. Springer. 43

[Bentahar et al., 2020] Bentahar, M., Bella, A. D., Mechri, C., Montresor, S., Scalerandi, M., and Yu, X. (2020). Exploiting slow dynamics effects for damage detection in concrete. *Frontiers in Built Environment*, 6. 111, 113, 123

[Bentahar et al., 2006] Bentahar, M., El Aqra, H., El Guerjouma, R., Griffa, M., and Scalerandi, M. (2006). Hysteretic elasticity in damaged concrete: Quantitative analysis of slow and fast dynamics. *Physical Review B*, 73(1):014116. 26, 111

[Bentahar and El Guerjouma, 2009] Bentahar, M. and El Guerjouma, R. (2009). Monitoring progressive damage in polymer-based composite using nonlinear dynamics and acoustic emission. *The Journal of the Acoustical Society of America*, 125(1):EL39–EL44. 2, 111, 123

[Berbaoui, 2010] Berbaoui, R. (2010). *Identification et analyse de l'endommagement par fatigue des matériaux granulaires à base polymère*. PhD thesis, LAUM. 81, 84

[Bergman and Shahbender, 1958] Bergman, R. and Shahbender, R. (1958). Effect of statically applied stresses on the velocity of propagation of ultrasonic waves. *Journal of Applied Physics*, 29(12):1736–1738. 8

[Bialasiewicz et al., 2012] Bialasiewicz, J. T., Gonzalez, D., Balcells, J., and Gago, J. (2012). Wavelet-based approach to evaluation of signal integrity. *IEEE Transactions on Industrial Electronics*, 60(10):4590–4598. 37

[Bittner and Popovics, 2019] Bittner, J. and Popovics, J. (2019). Direct imaging of moisture effects during slow dynamic nonlinearity. *Applied Physics Letters*, 114(2):021901. 24, 138

[Bohse, 2000] Bohse, J. (2000). Acoustic emission characteristics of micro-failure processes in polymer blends and composites. *Composites science and technology*, 60(8):1213–1226. 31

[Boulay, 2017] Boulay, N. (2017). *Modélisation des capteurs d'émission acoustique en vue de la simulation d'un contrôle*. PhD thesis, Paris Saclay. 18

[Bovik, 2010] Bovik, A. C. (2010). *Handbook of image and video processing*. Academic press. 36

[Bracewell, 1986] Bracewell, R. N. (1986). *The Fourier transform and its applications*, volume 31999. McGraw-Hill New York. 31

[Breckenridge et al., 1975] Breckenridge, F. R., Tschiegg, C. E., and Greenspan, M. (1975). Acoustic emission: some applications of lamb's problem. *The Journal of the Acoustical Society of America*, 57(3):626–631. 11

[Bridle, 1990] Bridle, J. S. (1990). Probabilistic interpretation of feedforward classification network outputs, with relationships to statistical pattern recognition. In *Neurocomputing*, pages 227–236. Springer. 59

[Bruno et al., 2009] Bruno, C., Gliozzi, A., Scalerandi, M., and Antonaci, P. (2009). Analysis of elastic nonlinearity using the scaling subtraction method. *Physical Review B*, 79(6):064108. 23

[Carpinteri et al., 2013] Carpinteri, A., Lacidogna, G., Accornero, F., Mpalaskas, A., Matikas, T., and Aggelis, D. (2013). Influence of damage in the acoustic emission parameters. *Cement and Concrete composites*, 44:9–16. 70, 74

[Carpinteri et al., 2016] Carpinteri, A., Lacidogna, G., Corrado, M., and Di Battista, E. (2016). Cracking and crackling in concrete-like materials: A dynamic energy balance. *Engineering Fracture Mechanics*, 155:130–144. 75, 79, 84

[Carpinteri et al., 2009] Carpinteri, A., Lacidogna, G., and Puzzi, S. (2009). From criticality to final collapse: Evolution of the "b-value" from 1.5 to 1.0. *Chaos, Solitons & Fractals*, 41(2):843–853. 66, 75, 76, 83

[Carpinteri and Massabo, 1997] Carpinteri, A. and Massabo, R. (1997). Continuous vs discontinuous bridged-crack model for fiber-reinforced materials in flexure. *International Journal of Solids and Structures*, 34(18):2321–2338. 79

[Carvelli et al., 2017] Carvelli, V., Dettorre, A., and Lomov, S. V. (2017). Acoustic emission and damage mode correlation in textile reinforced PPS composites. *Composite Structures*, 163:399–409. 44

[Chang et al., 2000] Chang, S. G., Yu, B., and Vetterli, M. (2000). Adaptive wavelet thresholding for image denoising and compression. *IEEE transactions on image processing*, 9(9):1532–1546. 36

[Chang and Lee, 2004] Chang, S.-H. and Lee, C.-I. (2004). Estimation of cracking and damage mechanisms in rock under triaxial compression by moment tensor analysis of acoustic emission. *International Journal of Rock Mechanics and Mining Sciences*, 41(7):1069–1086. 13

[Chen et al., 2015] Chen, H., Ni, D., Qin, J., Li, S., Yang, X., Wang, T., and Heng, P. A. (2015). Standard plane localization in fetal ultrasound via domain transferred deep neural networks. *IEEE journal of biomedical and health informatics*, 19(5):1627–1636. 60

[Chen et al., 2018] Chen, H., Zhang, P., Bai, H., Yuan, Q., Bao, X., and Yan, Y. (2018). Deep convolutional neural network with scalogram for audio scene modeling. In *Interspeech*, pages 3304–3308. 51

[Chen et al., 2010] Chen, J., Jayapalan, A. R., Kim, J.-Y., Kurtis, K. E., and Jacobs, L. J. (2010). Rapid evaluation of alkali–silica reactivity of aggregates using a nonlinear resonance spectroscopy technique. *Cement and Concrete Research*, 40(6):914–923. 108

[Chen et al., 2011] Chen, J., Kim, J.-Y., Kurtis, K. E., and Jacobs, L. J. (2011). Theoretical and experimental study of the nonlinear resonance vibration of cementitious materials with an application to damage characterization. *The Journal of the Acoustical Society of America*, 130(5):2728–2737. 24

[Cohen, 1989] Cohen, L. (1989). Time-frequency distributions-a review. *Proceedings of the IEEE*, 77(7):941–981. 35

[Cohen, 1995] Cohen, L. (1995). *Time-frequency analysis*, volume 778. Prentice hall. 35

[Colombo et al., 2003] Colombo, I. S., Main, I., and Forde, M. (2003). Assessing damage of reinforced concrete beam using "b-value" analysis of acoustic emission signals. *Journal of materials in civil engineering*, 15(3):280–286. 66, 69, 76

[Committee et al., 2010] Committee, R. T. et al. (2010). Recommendation of rilem tc 212-acd: acoustic emission and related nde techniques for crack detection and damage evaluation in concrete. *Materials and Structures*, 43(9):1183–1186. 66

[Crivelli et al., 2014] Crivelli, D., Guagliano, M., and Monici, A. (2014). Development of an artificial neural network processing technique for the analysis of damage evolution in pultruded composites with acoustic emission. *Composites Part B: Engineering*, 56:948–959. 17

[Curtis, 1975] Curtis, G. (1975). Acoustic emission energy relates to bond strength. *Non-Destructive Testing*, 8(5):249–257. 30

[Czochralski, 1916] Czochralski, J. (1916). Die metallographie des zinns und die theorie der formänderung bildsamer metalle. *Metall und Erz*, 22:381–393. 9

[Darling et al., 2006] Darling, T. W., TenCate, J. A., Vogel, S., Proffen, T., Page, K., Herrera, C., Covington, A. M., and Emmons, E. (2006). Localizing nonclassical nonlinearity in geological materials with neutron scattering experiments. In *AIP Conference Proceedings*, volume 838, pages 19–26. AIP. 22

[Daubechies, 1990] Daubechies, I. (1990). The wavelet transform, time-frequency localization and signal analysis. *IEEE transactions on information theory*, 36(5):961–1005. 34

[Davies and Bouldin, 1979] Davies, D. L. and Bouldin, D. W. (1979). A cluster separation measure. *IEEE transactions on pattern analysis and machine intelligence*, (2):224–227. 47

[De Groot et al., 1995] De Groot, P. J., Wijnen, P. A., and Janssen, R. B. (1995). Real-time frequency determination of acoustic emission for different fracture mechanisms in carbon/epoxy composites. *Composites Science and Technology*, 55(4):405–412. 33

[Delsanto and Scalerandi, 2003] Delsanto, P. P. and Scalerandi, M. (2003). Modeling nonclassical nonlinearity, conditioning, and slow dynamics effects in mesoscopic elastic materials. *Physical Review B*, 68(6):064107. 22, 25

[Doan et al., 2015] Doan, D. D., Ramasso, E., Placet, V., Zhang, S., Boubakar, L., and Zerhouni, N. (2015). An unsupervised pattern recognition approach for ae data originating from fatigue tests on polymer–composite materials. *Mechanical Systems and Signal Processing*, 64:465–478. 17

[Donahue et al., 2014] Donahue, J., Jia, Y., Vinyals, O., Hoffman, J., Zhang, N., Tzeng, E., and Darrell, T. (2014). Decaf: A deep convolutional activation feature for generic visual recognition. In *International conference on machine learning*, pages 647–655. 59

[Eiras et al., 2014] Eiras, J., Monzó, J., Payá, J., Kundu, T., and Popovics, J. S. (2014). Non-classical nonlinear feature extraction from standard resonance vibration data for damage detection. *The Journal of the Acoustical Society of America*, 135(2):EL82–EL87. 108

[Elaqra et al., 2007] Elaqra, H., Godin, N., Peix, G., R'Mili, M., and Fantozzi, G. (2007). Damage evolution analysis in mortar, during compressive loading using acoustic emission and x-ray tomography: Effects of the sand/cement ratio. *Cement and Concrete Research*, 37(5):703–713. 16, 68

[Farhidzadeh et al., 2014] Farhidzadeh, A., Mpalaskas, A. C., Matikas, T. E., Farhidzadeh, H., and Aggelis, D. G. (2014). Fracture mode identification in cementitious materials using supervised pattern recognition of acoustic emission features. *Construction and building materials*, 67:129–138. 31, 73

[Farnam et al., 2015] Farnam, Y., Geiker, M. R., Bentz, D., and Weiss, J. (2015). Acoustic emission waveform characterization of crack origin and mode in fractured and asr damaged concrete. *Cement and Concrete Composites*, 60:135–145. 79

[Ferreira et al., 2004] Ferreira, D., Da Silva, R., Rebello, J., and Siqueira, M. (2004). Failure mechanism characterisation in composite materials using spectral analysis and the wavelet transform of acoustic emission signals. *Insight-Non-Destructive Testing and Condition Monitoring*, 46(5):282–289. 33

[Géron, 2019] Géron, A. (2019). *Hands-On Machine Learning with Scikit-Learn, Keras, and TensorFlow: Concepts, Tools, and Techniques to Build Intelligent Systems*. O'Reilly Media. 53, 55, 157

[Gist, 1994] Gist, G. A. (1994). Fluid effects on velocity and attenuation in sandstones. *The Journal of the Acoustical Society of America*, 96(2):1158–1173. 22

[Giurgiutiu, 2007] Giurgiutiu, V. (2007). *Structural health monitoring: with piezoelectric wafer active sensors*. Elsevier. 9, 37

[Gliozzi et al., 2010] Gliozzi, A., Scalerandi, M., Antonaci, P., and Bruno, C. (2010). Conditioning-induced elastic nonlinearity ináhysteretic media. *Applied Physics A*, 100(2):421–424. 25

[Godin et al., 2004] Godin, N., Huguet, S., Gaertner, R., and Salmon, L. (2004). Clustering of acoustic emission signals collected during tensile tests on unidirectional glass/polyester composite using supervised and unsupervised classifiers. *Ndt & E International*, 37(4):253–264. 17, 46

[Godin et al., 2018a] Godin, N., Reynaud, P., and Fantozzi, G. (2018a). *Acoustic emission and durability of composite materials*. Wiley Online Library. 9

[Godin et al., 2018b] Godin, N., Reynaud, P., and Fantozzi, G. (2018b). Challenges and limitations in the identification of acoustic emission signature of damage mechanisms in composites materials. *Applied Sciences*, 8(8):1267. 10

[Goodfellow et al., 2016] Goodfellow, I., Bengio, Y., and Courville, A. (2016). *Deep learning*. MIT press. 53, 98, 157

[Goujon and Baboux, 2003] Goujon, L. and Baboux, J.-C. (2003). Behaviour of acoustic emission sensors using broadband calibration techniques. *Measurement Science and Technology*, 14(7):903. 17

[Grosse et al., 1997] Grosse, C., Reinhardt, H., and Dahm, T. (1997). Localization and classification of fracture types in concrete with quantitative acoustic emission measurement techniques. *Ndt & E International*, 30(4):223–230. 15

[Grosse and Ohtsu, 2008] Grosse, C. U. and Ohtsu, M. (2008). *Acoustic emission testing*. Springer Science & Business Media. 9, 30, 32

[Gu et al., 2018] Gu, J., Wang, Z., Kuen, J., Ma, L., Shahroudy, A., Shuai, B., Liu, T., Wang, X., Wang, G., Cai, J., et al. (2018). Recent advances in convolutional neural networks. *Pattern Recognition*, 77:354–377. 55

[Guan et al., 2018] Guan, S., He, W., Gu, W., Hou, Y., Chen, Y., and Zeng, X. (2018). Multi-mode study of deep learning applications in acoustic signal processing. In *2018 IEEE International Workshop on Signal Processing Systems (SiPS)*, pages 292–295. IEEE. 51

[Guo et al., 2016] Guo, Y., Liu, Y., Oerlemans, A., Lao, S., Wu, S., and Lew, M. S. (2016). Deep learning for visual understanding: A review. *Neurocomputing*, 187:27–48. 53, 54

[Gutkin et al., 2011] Gutkin, R., Green, C., Vangrattanachai, S., Pinho, S., Robinson, P., and Curtis, P. (2011). On acoustic emission for failure investigation in cfrp: Pattern recognition and peak frequency analyses. *Mechanical systems and signal processing*, 25(4):1393–1407. 33, 48, 84

[Guyer et al., 1995] Guyer, R., McCall, K., and Boitnott, G. (1995). Hysteresis, discrete memory, and nonlinear wave propagation in rock: A new paradigm. *Physical review letters*, 74(17):3491. 22

[Guyer et al., 1997] Guyer, R., McCall, K., Boitnott, G., Hilbert Jr, L., and Plona, T. (1997). Quantitative implementation of preisach-mayergoyz space to find static and dynamic elastic moduli in rock. *Journal of Geophysical Research: Solid Earth*, 102(B3):5281–5293. 22

[Guyer et al., 1999] Guyer, R., TenCate, J., and Johnson, P. (1999). Hysteresis and the dynamic elasticity of consolidated granular materials. *Physical review letters*, 82(16):3280. 22

[Guyer and Johnson, 1999] Guyer, R. A. and Johnson, P. A. (1999). Nonlinear mesoscopic elasticity: Evidence for a new class of materials. *Physics today*, 52:30–36. 22

[Guyer and Johnson, 2009] Guyer, R. A. and Johnson, P. A. (2009). *Nonlinear mesoscopic elasticity: the complex behavior of rocks, soil, concrete*. John Wiley & Sons. 22, 23

[Gwardys and Grzywczak, 2014] Gwardys, G. and Grzywczak, D. (2014). Deep image features in music information retrieval. *International Journal of Electronics and Telecommunications*, 60(4):321–326. 51

[Hammami et al., 2016] Hammami, M., El Mahi, A., Karra, C., and Haddar, M. (2016). Experimental analysis of the linear and nonlinear behaviour of composites with delaminations. *Applied Acoustics*, 108:31–39. 104

[Hamstad et al., 2002] Hamstad, M. A., O'Gallagher, A., and Gary, J. (2002). A wavelet transform applied to acoustic emission. *J. Acoust. Emiss*, 20:39–61. 33

[Han et al., 2015] Han, Q., Xu, J., Carpinteri, A., and Lacidogna, G. (2015). Localization of acoustic emission sources in structural health monitoring of masonry bridge. *Structural Control and Health Monitoring*, 22(2):314–329. 15

[Hashemi and Jamshidi, 2015] Hashemi, M. J. and Jamshidi, M. (2015). Flexural behavior of polyester polymer concrete subject to different chemicals. *IJE Trans. A*, 28(7):978–983. 64, 90

[Haupert et al., 2011] Haupert, S., Renaud, G., Riviere, J., Talmant, M., Johnson, P. A., and Laugier, P. (2011). High-accuracy acoustic detection of nonclassical component of material nonlinearity. *The Journal of the Acoustical Society of America*, 130(5):2654–2661. 24

[He et al., 2016] He, K., Zhang, X., Ren, S., and Sun, J. (2016). Deep residual learning for image recognition. In *Proceedings of the IEEE conference on computer vision and pattern recognition*, pages 770–778. 56

[He et al., 2006] He, X., Cai, D., and Niyogi, P. (2006). Laplacian score for feature selection. In *Advances in neural information processing systems*, pages 507–514. 43

[He and Niyogi, 2004] He, X. and Niyogi, P. (2004). Locality preserving projections. In *Advances in neural information processing systems*, pages 153–160. 43

[Heidari-Rarani et al., 2014] Heidari-Rarani, M., Aliha, M., Shokrieh, M., and Ayatollahi, M. (2014). Mechanical durability of an optimized polymer concrete under various thermal cyclic loadings–an experimental study. *Construction and Building Materials*, 64:308–315. 90

[Hertel et al., 2015] Hertel, L., Barth, E., Kaster, T., and Martinetz, T. (2015). Deep convolutional neural networks as generic feature extractors. In *2015 International Joint Conference on Neural Networks (IJCNN)*. IEEE. 59

[Huguet et al., 2002] Huguet, S., Godin, N., Gaertner, R., Salmon, L., and Villard, y. D. (2002). Use of acoustic emission to identify damage modes in glass fibre reinforced polyester. *Composites Science and Technology*, 62(10-11):1433–1444. 17, 46

[Idjimarene, 2013] Idjimarene, S. (2013). *Power laws behavior and nonlinearity mechanisms in mesoscopic elastic materials*. PhD thesis, Le Mans Université. 21

[Idriss et al., 2015] Idriss, M., El Mahi, A., and El Guerjouma, R. (2015). Characterization of sandwich beams with debonding by linear and nonlinear vibration method. *Composite Structures*, 120:200–207. 104

[Jain, 2010] Jain, A. K. (2010). Data clustering: 50 years beyond k-means. *Pattern recognition letters*, 31(8):651–666. 46

[Jing and Hao, 2009] Jing, G.-X. and Hao, Z.-Y. (2009). A new technique based on traditional wavelet transform used in nvh application of internal combustion engine. *Mechanical Systems and Signal Processing*, 23(3):979–985. 41

[Johnson and Rasolofosaon, 1996] Johnson, P. and Rasolofosaon, P. (1996). Manifestation of nonlinear elasticity in rock: convincing evidence over large frequency and strain intervals from laboratory studies. *Nonlinear processes in geophysics*, 3(2):77–88. 104

[Johnson and Sutin, 2005] Johnson, P. and Sutin, A. (2005). Slow dynamics and anomalous nonlinear fast dynamics in diverse solids. *The Journal of the Acoustical Society of America*, 117(1):124–130. 24, 26

[Johnson et al., 2004] Johnson, P. A., Zinszner, B., Rasolofosaon, P., Cohen-Tenoudji, F., and Van Den Abeele, K. (2004). Dynamic measurements of the nonlinear elastic parameter α in rock under varying conditions. *Journal of Geophysical Research: Solid Earth*, 109(B2). 24

[Johnston, 1988] Johnston, J. D. (1988). Transform coding of audio signals using perceptual noise criteria. *IEEE Journal on selected areas in communications*, 6(2):314–323. 42

[Jolliffe, 2011] Jolliffe, I. (2011). *Principal component analysis*. Springer. 45

[Kaiser, 1950] Kaiser, E. (1950). A study of acoustic phenomena in tensile test. *Dr.-Ing. Dissertation. Technical University of Munich.* 9

[Karal Jr and Keller, 1959] Karal Jr, F. C. and Keller, J. B. (1959). Elastic wave propagation in homogeneous and inhomogeneous media. *The Journal of the acoustical society of america*, 31(6):694–705. 7, 14

[Kawasaki et al., 2010] Kawasaki, Y., Tomoda, Y., and Ohtsu, M. (2010). Ae monitoring of corrosion process in cyclic wet–dry test. *Construction and Building Materials*, 24(12):2353–2357. 70

[Keprt and Benes, 2009] Keprt, J. and Benes, P. (2009). The determination of uncertainty in the calibration of acoustic emission sensors. *International Journal of Microstructure and Materials Properties*, 4(1):85. 17

[Kermany et al., 2018] Kermany, D. S., Goldbaum, M., Cai, W., Valentim, C. C., Liang, H., Baxter, S. L., McKeown, A., Yang, G., Wu, X., Yan, F., Dong, J., Prasadha, M. K., Pei, J., Ting, M. Y., Zhu, J., Li, C., Hewett, S., Dong, J., Ziyar, I., Shi, A., Zhang, R., Zheng, L., Hou, R., Shi, W., Fu, X., Duan, Y., Huu, V. A., Wen, C., Zhang, E. D., Zhang, C. L., Li, O., Wang, X., Singer, M. A., Sun, X., Xu, J., Tafreshi, A., Lewis, M. A., Xia, H., and Zhang, K. (2018). Identifying medical diagnoses and treatable diseases by image-based deep learning. *Cell*, 172(5):1122–1131.e9. 59

[Krizhevsky et al., 2012] Krizhevsky, A., Sutskever, I., and Hinton, G. E. (2012). Imagenet classification with deep convolutional neural networks. In *Advances in neural information processing systems*, pages 1097–1105. 51, 56, 58

[Landau et al., 1986] Landau, L. D., Kosevich, A., Pitaevskii, L. P., and Lifshitz, E. M. (1986). Theory of elasticity. 22

[Landis and Baillon, 2002] Landis, E. N. and Baillon, L. (2002). Experiments to relate acoustic emission energy to fracture energy of concrete. *Journal of engineering mechanics*, 128(6):698–702. 30

[Le Gall et al., 2018] Le Gall, T., Monnier, T., Fusco, C., Godin, N., and Hebaz, S.-E. (2018). Towards quantitative acoustic emission by finite element modelling: Contribution of modal analysis and identification of pertinent descriptors. *Applied Sciences*, 8(12):2557. 11, 13

[LeCun et al., 2015] LeCun, Y., Bengio, Y., and Hinton, G. (2015). Deep learning. *Nature*, 521(7553):436. 53

[LeCun et al., 1998] LeCun, Y., Bottou, L., Bengio, Y., Haffner, P., et al. (1998). Gradient-based learning applied to document recognition. *Proceedings of the IEEE*, 86(11):2278–2324. 53

[Li et al., 2017] Li, J., Cheng, K., Wang, S., Morstatter, F., Trevino, R. P., Tang, J., and Liu, H. (2017). Feature selection: A data perspective. *ACM Computing Surveys (CSUR)*, 50(6):1–45. 43

[Li et al., 2015] Li, L., Lomov, S. V., and Yan, X. (2015). Correlation of acoustic emission with optically observed damage in a glass/epoxy woven laminate under tensile loading. *Composite structures*, 123:45–53. 33, 44

[Li et al., 2014] Li, L., Lomov, S. V., Yan, X., and Carvelli, V. (2014). Cluster analysis of acoustic emission signals for 2d and 3d woven glass/epoxy composites. *Composite Structures*, 116:286–299. 33

[Li et al., 2016] Li, L., Swolfs, Y., Straumit, I., Yan, X., and Lomov, S. V. (2016). Cluster analysis of acoustic emission signals for 2d and 3d woven carbon fiber/epoxy composites. *Journal of Composite Materials*, 50(14):1921–1935. 46

[Li et al., 2018] Li, X., Sens-Schönfelder, C., and Snieder, R. (2018). Nonlinear elasticity in resonance experiments. *Physical Review B*, 97(14):144301. 138

[Likas et al., 2003] Likas, A., Vlassis, N., and Verbeek, J. J. (2003). The global k-means clustering algorithm. *Pattern recognition*, 36(2):451–461. 46

[Lim et al., 2015] Lim, A., Chong, V., Chew, W., Muniandy, S., Wong, C., and Ong, Z. (2015). Sound production in the tiger-tail seahorse hippocampus comes: insights into the sound producing mechanisms. *The Journal of the Acoustical Society of America*, 138(1):404–412. 41

[Lin and Qu, 2000] Lin, J. and Qu, L. (2000). Feature extraction based on morlet wavelet and its application for mechanical fault diagnosis. *Journal of sound and vibration*, 234(1):135–148. 37

[Litjens et al., 2017] Litjens, G., Kooi, T., Bejnordi, B. E., Setio, A. A. A., Ciompi, F., Ghafoorian, M., Van Der Laak, J. A., Van Ginneken, B., and Sánchez, C. I. (2017). A survey on deep learning in medical image analysis. *Medical image analysis*, 42:60–88. 59

[Liu et al., 2012] Liu, M., Tang, G., Jacobs, L. J., and Qu, J. (2012). Measuring acoustic nonlinearity parameter using collinear wave mixing. *Journal of applied physics*, 112(2):024908. 23

[Lu et al., 2019] Lu, S., Lu, Z., and Zhang, Y.-D. (2019). Pathological brain detection based on alexnet and transfer learning. *Journal of computational science*, 30:41–47. 59

[MacGregor and Kourti, 1995] MacGregor, J. F. and Kourti, T. (1995). Statistical process control of multivariate processes. *Control Engineering Practice*, 3(3):403–414. 44

[Maillet et al., 2014] Maillet, E., Godin, N., R'Mili, M., Reynaud, P., Fantozzi, G., and Lamon, J. (2014). Damage monitoring and identification in sic/sic minicomposites using combined acousto-ultrasonics and acoustic emission. *Composites Part A: Applied Science and Manufacturing*, 57:8–15. 40, 41

[Maillet and Morscher, 2015] Maillet, E. and Morscher, G. N. (2015). Waveform-based selection of acoustic emission events generated by damage in composite materials. *Mechanical Systems and Signal Processing*, 52:217–227. 33

[Mallat, 1999] Mallat, S. (1999). *A wavelet tour of signal processing*. Elsevier. 35, 36, 40

[Marec, 2008] Marec, A. (2008). *Contrôle de santé des matériaux hétérogènes par émission acoustique et acoustique non linéaire: discrimination des mécanismes d'endommagement et estimation de la durée de vie restante*. PhD thesis, Laboratoire d'Acoustique de L'université du Mans. 81, 84, 86

[Marec et al., 2008] Marec, A., Thomas, J.-H., and El Guerjouma, R. (2008). Damage characterization of polymer-based composite materials: Multivariable analysis and wavelet transform for clustering acoustic emission data. *Mechanical systems and signal processing*, 22(6):1441–1464. 33, 40, 41, 46

[Mayergoyz, 1985] Mayergoyz, I. (1985). Hysteresis models from the mathematical and control theory points of view. *Journal of Applied Physics*, 57(8):3803–3805. 22

[McCall and Guyer, 1994] McCall, K. and Guyer, R. (1994). Equation of state and wave propagation in hysteretic nonlinear elastic materials. *Journal of Geophysical Research: Solid Earth*, 99(B12):23887–23897. 22

[Mechri et al., 2017] Mechri, C., Scalerandi, M., and Bentahar, M. (2017). Enhancement of harmonics generation in hysteretic elastic media induced by conditioning. *Communications in Nonlinear Science and Numerical Simulation*, 45:117–128. 25

[Mechri et al., 2019] Mechri, C., Scalerandi, M., and Bentahar, M. (2019). Separation of damping and velocity strain dependencies using an ultrasonic monochromatic excitation. *Physical Review Applied*, 11(5):054050. 111, 113, 123

[Meegan Jr et al., 1993] Meegan Jr, G. D., Johnson, P. A., Guyer, R. A., and McCall, K. R. (1993). Observations of nonlinear elastic wave behavior in sandstone. *The Journal of the Acoustical Society of America*, 94(6):3387–3391. 21

[Mehta and Monteiro, 2006] Mehta, P. K. and Monteiro, P. J. (2006). *Concrete: microstructure, properties, and materials*. New York: McGraw-Hill. 79

[Meintjes et al., 2018] Meintjes, A., Lowe, A., and Legget, M. (2018). Fundamental heart sound classification using the continuous wavelet transform and convolutional neural networks. In *2018 40th Annual International Conference of the IEEE Engineering in Medicine and Biology Society (EMBC)*, pages 409–412. IEEE. 51

[Momon et al., 2012] Momon, S., Godin, N., Reynaud, P., R'Mili, M., and Fantozzi, G. (2012). Unsupervised and supervised classification of ae data collected during fatigue test on cmc at high temperature. *Composites Part A: Applied Science and Manufacturing*, 43(2):254–260. 44

[Morizet et al., 2016] Morizet, N., Godin, N., Tang, J., Maillet, E., Fregonese, M., and Normand, B. (2016). Classification of acoustic emission signals using wavelets and random forests: Application to localized corrosion. *Mechanical Systems and Signal Processing*, 70:1026–1037. 40

[Mostafapour et al., 2014] Mostafapour, A., Davoodi, S., and Ghareaghaji, M. (2014). Acoustic emission source location in plates using wavelet analysis and cross time frequency spectrum. *Ultrasonics*, 54(8):2055–2062. 36

[Muller et al., 2005] Muller, M., Sutin, A., Guyer, R., Talmant, M., Laugier, P., and Johnson, P. A. (2005). Nonlinear resonant ultrasound spectroscopy (nrus) applied to damage assessment in bone. *The Journal of the Acoustical Society of America*, 118(6):3946–3952. 22, 23

[Nair and Hinton, 2010] Nair, V. and Hinton, G. E. (2010). Rectified linear units improve restricted boltzmann machines. In *Proceedings of the 27th international conference on machine learning (ICML-10)*, pages 807–814. 57

[Ni and Iwamoto, 2002] Ni, Q.-Q. and Iwamoto, M. (2002). Wavelet transform of acoustic emission signals in failure of model composites. *Engineering Fracture Mechanics*, 69(6):717–728. 31, 36, 37

[Nielsen, 2015] Nielsen, M. A. (2015). *Neural networks and deep learning*. Determination press San Francisco, CA, USA:. 53, 55

[Novak et al., 2012] Novak, A., Bentahar, M., Tournat, V., El Guerjouma, R., and Simon, L. (2012). Nonlinear acoustic characterization of micro-damaged materials through higher harmonic resonance analysis. *Ndt & E International*, 45(1):1–8. 23, 104

[Ohno and Ohtsu, 2010] Ohno, K. and Ohtsu, M. (2010). Crack classification in concrete based on acoustic emission. *Construction and Building Materials*, 24(12):2339–2346. 13, 14, 16, 17, 70, 71, 74, 75, 84

[Ohno et al., 2014] Ohno, K., Uji, K., Ueno, A., and Ohtsu, M. (2014). Fracture process zone in notched concrete beam under three-point bending by acoustic emission. *Construction and building materials*, 67:139–145. 70

[Ohtsu, 1988] Ohtsu, M. (1988). Source inversion of acoustic emission waveform. *Doboku Gakkai Ronbunshu*, (398):71–79. 11

[Ohtsu, 1991] Ohtsu, M. (1991). Simplified moment tensor analysis and unified decomposition of acoustic emission source: application to in situ hydrofracturing test. *Journal of Geophysical Research: Solid Earth*, 96(B4):6211–6221. 11

[Ohtsu and Ono, 1986] Ohtsu, M. and Ono, K. (1986). The generalized theory and source representations of acoustic emission. *Journal of acoustic emission*, 5(4):124–133. 11, 12

[Ohtsu and Ono, 1988] Ohtsu, M. and Ono, K. (1988). Ae source location and orientation determination of tensile cracks from surface observation. *NDT international*, 21(3):143–150. 13, 15

[Oja, 1989] Oja, E. (1989). Neural networks, principal components, and subspaces. *International journal of neural systems*, 1(01):61–68. 44

[Oskouei et al., 2012] Oskouei, A. R., Heidary, H., Ahmadi, M., and Farajpur, M. (2012). Unsupervised acoustic emission data clustering for the analysis of damage mechanisms in glass/polyester composites. *Materials & Design*, 37:416–422. 44

[Ostrovsky and Johnson, 2001] Ostrovsky, L. and Johnson, P. (2001). Dynamic nonlinear elasticity in geo materials. *Rivista del Nuovo Cimento della Societa Italiana di Fisica*, 24(7):1–46. 21, 23

[Ostrovsky et al., 2019] Ostrovsky, L., Lebedev, A., Riviere, J., Shokouhi, P., Wu, C., Stuber Geesey, M. A., and Johnson, P. A. (2019). Long-time relaxation induced by dynamic forcing in geomaterials. *Journal of Geophysical Research: Solid Earth*, 124(5):5003–5013. 124, 138

[Painter and Spanias, 2000] Painter, T. and Spanias, A. (2000). Perceptual coding of digital audio. *Proceedings of the IEEE*, 88(4):451–515. 42

[Pan and Yang, 2009] Pan, S. J. and Yang, Q. (2009). A survey on transfer learning. *IEEE Transactions on knowledge and data engineering*, 22(10):1345–1359. 59

[Pashmforoush et al., 2012] Pashmforoush, F., Fotouhi, M., and Ahmadi, M. (2012). Acoustic emission-based damage classification of glass/polyester composites using harmony search k-means algorithm. *Journal of Reinforced Plastics and Composites*, 31(10):671–680. 17, 46

[Pasqualini et al., 2007] Pasqualini, D., Heitmann, K., TenCate, J. A., Habib, S., Higdon, D., and Johnson, P. A. (2007). Nonequilibrium and nonlinear dynamics in berea and fontainebleau sandstones: Low-strain regime. *Journal of Geophysical Research: Solid Earth*, 112(B1). 22

[Payan et al., 2007] Payan, C., Garnier, V., Moysan, J., and Johnson, P. (2007). Applying nonlinear resonant ultrasound spectroscopy to improving thermal damage assessment in concrete. *The Journal of the Acoustical Society of America*, 121(4):EL125–EL130. 108

[Philippidis and Aggelis, 2005] Philippidis, T. and Aggelis, D. (2005). Experimental study of wave dispersion and attenuation in concrete. *Ultrasonics*, 43(7):584–595. 14

[Prosser, 1996] Prosser, W. H. (1996). Advanced ae techniques in composite materials research. *Journal of Acoustic Emission*. 14

[Qi, 2000] Qi, G. (2000). Wavelet-based ae characterization of composite materials. *NDT & E International*, 33(3):133–144. 36

[Qian et al., 2016] Qian, K., Janott, C., Pandit, V., Zhang, Z., Heiser, C., Hohenhorst, W., Herzog, M., Hemmert, W., and Schuller, B. (2016). Classification of the excitation location of snore sounds in the upper airway by acoustic multifeature analysis. *IEEE Transactions on Biomedical Engineering*, 64(8):1731–1741. 51

[Rao and Lakshmi, 2005] Rao, M. and Lakshmi, K. P. (2005). Analysis of b-value and improved b-value of acoustic emissions accompanying rock fracture. *Current science*, pages 1577–1582. 66

[Remillieux et al., 2016] Remillieux, M. C., Guyer, R. A., Payan, C., and Ulrich, T. (2016). Decoupling nonclassical nonlinear behavior of elastic wave types. *Physical review letters*, 116(11):115501. 22

[Remillieux et al., 2017] Remillieux, M. C., Ulrich, T., Goodman, H. E., and Ten Cate, J. A. (2017). Propagation of a finite-amplitude elastic pulse in a bar of berea sandstone: A detailed look at the mechanisms of classical nonlinearity, hysteresis, and nonequilibrium dynamics. *Journal of Geophysical Research: Solid Earth*, 122(11):8892–8909. 24

[Renaud et al., 2013] Renaud, G., Rivière, J., Haupert, S., and Laugier, P. (2013). Anisotropy of dynamic acoustoelasticity in limestone, influence of conditioning, and comparison with nonlinear resonance spectroscopy. *The Journal of the Acoustical Society of America*, 133(6):3706–3718. 104

[Rice, 1980] Rice, J. (1980). Elastic wave emission from damage processes. *Journal of Nondestructive Evaluation*, 1(4):215–224. 12

[Richter, 1958] Richter, C. F. (1958). Elementary seismology, wh. *FIeeman and Company*. 66

[Rioul and Flandrin, 1992] Rioul, O. and Flandrin, P. (1992). Time-scale energy distributions: A general class extending wavelet transforms. *IEEE Transactions on Signal Processing*, 40(7):1746–1757. 39

[Rioul and Vetterli, 1991] Rioul, O. and Vetterli, M. (1991). Wavelets and signal processing. *IEEE signal processing magazine*, 8(4):14–38. 35

[Rousseeuw, 1987] Rousseeuw, P. J. (1987). Silhouettes: a graphical aid to the interpretation and validation of cluster analysis. *Journal of computational and applied mathematics*, 20:53–65. 48

[Royer and Dieulesaint, 1999] Royer, D. and Dieulesaint, E. (1999). *Elastic waves in solids I: Free and guided propagation*. Springer Science & Business Media. 6

[Rumelhart et al., 1986] Rumelhart, D. E., Hinton, G. E., and Williams, R. J. (1986). Learning representations by back-propagating errors. *Nature*, 323(6088):533–536. 55, 158

[Sagar and Prasad, 2011] Sagar, R. V. and Prasad, B. R. (2011). An experimental study on acoustic emission energy as a quantitative measure of size independent specific fracture energy of concrete beams. *Construction and Building Materials*, 25(5):2349–2357. 16, 30

[Sagar et al., 2012] Sagar, R. V., Prasad, B. R., and Kumar, S. S. (2012). An experimental study on cracking evolution in concrete and cement mortar by the b-value analysis of acoustic emission technique. *Cement and Concrete Research*, 42(8):1094–1104. 65, 68, 83

[Sagar et al., 2013] Sagar, R. V., Prasad, R., Prasad, B. R., and Rao, M. (2013). Microcracking and fracture process in cement mortar and concrete: a comparative study using acoustic emission technique. *Experimental Mechanics*, 53(7):1161–1175. 69

[Salinas et al., 2010] Salinas, V., Vargas, Y., Ruzzante, J., and Gaete, L. (2010). Localization algorithm for acoustic emission. *Physics Procedia*, 3(1):863–871. 15

[Satour et al., 2014] Satour, A., Montrésor, S., Bentahar, M., Elguerjouma, R., and Boubenider, F. (2014). Acoustic emission signal denoising to improve damage analysis in glass fibre-reinforced composites. *Nondestructive Testing and Evaluation*, 29(1):65–79. 36, 41

[Sause et al., 2012a] Sause, M., Gribov, A., Unwin, A., and Horn, S. (2012a). Pattern recognition approach to identify natural clusters of acoustic emission signals. *Pattern Recognition Letters*, 33(1):17–23. 17, 47

[Sause et al., 2012b] Sause, M., Müller, T., Horoschenkoff, A., and Horn, S. (2012b). Quantification of failure mechanisms in mode-i loading of fiber reinforced plastics utilizing acoustic emission analysis. *Composites science and technology*, 72(2):167–174. 13

[Sause et al., 2012c] Sause, M. G., Hamstad, M. A., and Horn, S. (2012c). Finite element modeling of conical acoustic emission sensors and corresponding experiments. *Sensors and Actuators A: Physical*, 184:64–71. 17

[Sause and Horn, 2010] Sause, M. G. and Horn, S. (2010). Simulation of acoustic emission in planar carbon fiber reinforced plastic specimens. *Journal of Nondestructive Evaluation*, 29(2):123–142. 11, 13, 14

[Sause and Richler, 2015] Sause, M. G. and Richler, S. (2015). Finite element modelling of cracks as acoustic emission sources. *Journal of nondestructive evaluation*, 34(1):4. 11

[Scalerandi et al., 2010] Scalerandi, M., Gliozzi, A., Bruno, C., and Antonaci, P. (2010). Nonequilibrium and hysteresis in solids: Disentangling conditioning from nonlinear elasticity. *Physical Review B*, 81(10):104114. 25, 26, 111

[Scalerandi et al., 2008] Scalerandi, M., Gliozzi, A., Bruno, C., Masera, D., and Bocca, P. (2008). A scaling method to enhance detection of a nonlinear elastic response. *Applied Physics Letters*, 92(10):101912. 23

[Scalerandi et al., 2019] Scalerandi, M., Mechri, C., Bentahar, M., Di Bella, A., Gliozzi, A., and Tortello, M. (2019). Experimental evidence of correlations between conditioning and relaxation in hysteretic elastic media. *Physical Review Applied*, 12(4):044002. 111

[Schmidhuber, 2015] Schmidhuber, J. (2015). Deep learning in neural networks: An overview. *Neural networks*, 61:85–117. 53

[Schofield, 1963] Schofield, B. (1963). Acoustic emission under applied stress. Technical report, LESSELLS AND ASSOCIATES INC WALTHAM MA. 9

[Scott, 1991] Scott, I. G. (1991). *Basic acoustic emission*, volume 6. CRC Press. 10

[Scruby et al., 1985] Scruby, C., Baldwin, G., and Stacey, K. (1985). Characterisation of fatigue crack extension by quantitative acoustic emission. *International Journal of Fracture*, 28(4):201–222. 12

[Scruby et al., 1983] Scruby, C., Wadley, H., and Hill, J. (1983). Dynamic elastic displacements at the surface of an elastic half-space due to defect sources. *Journal of Physics D: Applied Physics*, 16(6):1069. 11, 12

[Shafi et al., 2009] Shafi, I., Ahmad, J., Shah, S. I., and Kashif, F. M. (2009). Techniques to obtain good resolution and concentrated time-frequency distributions: a review. *EURASIP Journal on Advances in Signal processing*, 2009(1):673539. 34

[Shah et al., 1995] Shah, S. P., Swartz, S. E., and Ouyang, C. (1995). *Fracture mechanics of concrete: applications of fracture mechanics to concrete, rock and other quasi-brittle materials*. John Wiley & Sons. 79

[Shahidan et al., 2013] Shahidan, S., Pulin, R., Bunnori, N. M., and Holford, K. M. (2013). Damage classification in reinforced concrete beam by acoustic emission signal analysis. *Construction and Building Materials*, 45:78–86. 70, 74

[Shateri et al., 2017] Shateri, M., Ghaib, M., Svecova, D., and Thomson, D. (2017). On acoustic emission for damage detection and failure prediction in fiber reinforced polymer rods using pattern recognition analysis. *Smart Materials and Structures*, 26(6):065023. 19

[Shigeishi and Ohtsu, 2001] Shigeishi, M. and Ohtsu, M. (2001). Acoustic emission moment tensor analysis: development for crack identification in concrete materials. *Construction and Building Materials*, 15(5-6):311–319. 11, 70

[Shin et al., 2016] Shin, H.-C., Roth, H. R., Gao, M., Lu, L., Xu, Z., Nogues, I., Yao, J., Mollura, D., and Summers, R. M. (2016). Deep convolutional neural networks for computer-aided detection: Cnn architectures, dataset characteristics and transfer learning. *IEEE transactions on medical imaging*, 35(5):1285–1298. 59

[Shiotani, 2006] Shiotani, T. (2006). Evaluation of long-term stability for rock slope by means of acoustic emission technique. *Ndt & E International*, 39(3):217–228. 17

[Shiotani, 2012] Shiotani, T. (2012). Recent advances of ae technology for damage assessment of infrastructures. *Journal of Acoustic Emission*, 30. 19, 20

[Shlens, 2014] Shlens, J. (2014). A tutorial on principal component analysis. *arXiv preprint arXiv:1404.1100*. 44

[Shokouhi et al., 2017] Shokouhi, P., Rivière, J., Guyer, R. A., and Johnson, P. A. (2017). Slow dynamics of consolidated granular systems: Multi-scale relaxation. *Applied Physics Letters*, 111(25):251604. 24, 124, 138

[Shokrieh et al., 2011] Shokrieh, M., Heidari-Rarani, M., Shakouri, M., and Kashizadeh, E. (2011). Effects of thermal cycles on mechanical properties of an optimized polymer concrete. *Construction and Building Materials*, 25(8):3540–3549. 90

[Shokrieh et al., 2017] Shokrieh, M., Rezvani, S., and Mosalmani, R. (2017). Mechanical behavior of polyester polymer concrete under low strain rate loading conditions. *Polymer Testing*, 63:596–604. 64

[Sibil et al., 2012] Sibil, A., Godin, N., R'Mili, M., Maillet, E., and Fantozzi, G. (2012). Optimization of acoustic emission data clustering by a genetic algorithm method. *Journal of nondestructive evaluation*, 31(2):169–180. 47

[Sikorski, 2012] Sikorski, W. (2012). *Acoustic emission*. InTech. 30, 40

[Simonyan and Zisserman, 2014] Simonyan, K. and Zisserman, A. (2014). Very deep convolutional networks for large-scale image recognition. *arXiv preprint arXiv:1409.1556*. 56

[Snieder et al., 2016] Snieder, R., Sens-Schönfelder, C., and Wu, R. (2016). The time dependence of rock healing as a universal relaxation process, a tutorial. *Geophysical Journal International*, 208(1):1–9. 123

[Soulioti et al., 2009] Soulioti, D., Barkoula, N., Paipetis, A., Matikas, T., Shiotani, T., and Aggelis, D. (2009). Acoustic emission behavior of steel fibre reinforced concrete under bending. *Construction and Building Materials*, 23(12):3532–3536. 16, 67, 72, 74, 75, 79, 84

[Srivastava et al., 2014] Srivastava, N., Hinton, G., Krizhevsky, A., Sutskever, I., and Salakhutdinov, R. (2014). Dropout: a simple way to prevent neural networks from overfitting. *The Journal of Machine Learning Research*, 15(1):1929–1958. 58

[Stavrakas et al., 2016] Stavrakas, I., Triantis, D., Kourkoulis, S., Pasiou, E., and Dakanali, I. (2016). Acoustic emission analysis of cement mortar specimens during three point bending tests. *Latin American Journal of Solids and Structures*, 13(12):2283–2297. 69

[Suzuki et al., 1996] Suzuki, H., Kinjo, T., Hayashi, Y., Takemoto, M., Ono, K., and Hayashi, Y. (1996). Wavelet transform of acoustic emission signals. *Journal of acoustic emission*, 14:69–84. 33, 37

[Szegedy et al., 2015] Szegedy, C., Liu, W., Jia, Y., Sermanet, P., Reed, S., Anguelov, D., Erhan, D., Vanhoucke, V., and Rabinovich, A. (2015). Going deeper with convolutions. In *Proceedings of the IEEE conference on computer vision and pattern recognition*, pages 1–9. 56

[Tajbakhsh et al., 2016] Tajbakhsh, N., Shin, J. Y., Gurudu, S. R., Hurst, R. T., Kendall, C. B., Gotway, M. B., and Liang, J. (2016). Convolutional neural networks for medical image analysis: Full training or fine tuning? *IEEE transactions on medical imaging*, 35(5):1299–1312. 59

[Tang, 2000] Tang, Y. Y. (2000). *Wavelet theory and its application to pattern recognition*, volume 36. World Scientific. 36

[Ten Cate and Shankland, 1996] Ten Cate, J. A. and Shankland, T. J. (1996). Slow dynamics in the nonlinear elastic response of berea sandstone. *Geophysical Research Letters*, 23(21):3019–3022. 24

[TenCate, 2011] TenCate, J. A. (2011). Slow dynamics of earth materials: An experimental overview. *Pure and Applied Geophysics*, 168(12):2211–2219. 26, 104, 109

[TenCate et al., 2004] TenCate, J. A., Pasqualini, D., Habib, S., Heitmann, K., Higdon, D., and Johnson, P. A. (2004). Nonlinear and nonequilibrium dynamics in geomaterials. *Physical review letters*, 93(6):065501. 24

[TenCate et al., 2000a] TenCate, J. A., Smith, E., Byers, L. W., and Shankland, T. J. (2000a). Slow dynamics experiments in solids with nonlinear mesoscopic elasticity. In *AIP Conference Proceedings*, volume 524, pages 303–306. American Institute of Physics. 25

[TenCate et al., 2000b] TenCate, J. A., Smith, E., and Guyer, R. A. (2000b). Universal slow dynamics in granular solids. *Physical Review Letters*, 85(5):1020. 24, 26, 111, 123

[Teolis and Benedetto, 1998] Teolis, A. and Benedetto, J. J. (1998). *Computational signal processing with wavelets*, volume 182. Springer. 38

[Toufigh et al., 2016] Toufigh, V., Hosseinali, M., and Shirkhorshidi, S. M. (2016). Experimental study and constitutive modeling of polymer concrete's behavior in compression. *Construction and Building Materials*, 112:183–190. 80

[Toumi et al., 2017] Toumi, S., Mechri, C., Bentahar, M., Boubenider, F., and El Guerjouma, R. (2017). Characterization of microcracking in polymer concrete using multiple scattered waves under steady-state vibration conditions. *Research in Nondestructive Evaluation*, 28(1):18–27. 104

[Uddin et al., 2006] Uddin, F. A., Shigeishi, M., and Ohtsu, M. (2006). Fracture mechanics of corrosion cracking in concrete by acoustic emission. *Meccanica*, 41(4):425–442. 13

[Valenti et al., 2017] Valenti, M., Squartini, S., Diment, A., Parascandolo, G., and Virtanen, T. (2017). A convolutional neural network approach for acoustic scene classification. In *2017 International Joint Conference on Neural Networks (IJCNN)*, pages 1547–1554. IEEE. 51

[Van Den Abeele et al., 2000] Van Den Abeele, K.-A., Johnson, P. A., and Sutin, A. (2000). Nonlinear elastic wave spectroscopy (news) techniques to discern material damage, part i: nonlinear wave modulation spectroscopy (nwms). *Journal of Research in Nondestructive Evaluation*, 12(1):17–30. 23

[Van Den Abeele et al., 2001] Van Den Abeele, K. E., Sutin, A., Carmeliet, J., and Johnson, P. A. (2001). Micro-damage diagnostics using nonlinear elastic wave spectroscopy (news). *Ndt & E International*, 34(4):239–248. 104

[Van Drongelen, 2018] Van Drongelen, W. (2018). *Signal processing for neuroscientists*. Academic press. 41

[Van Loan, 1992] Van Loan, C. (1992). *Computational frameworks for the fast Fourier transform*, volume 10. Siam. 32

[Van Tittelboom et al., 2012] Van Tittelboom, K., De Belie, N., Lehmann, F., and Grosse, C. U. (2012). Acoustic emission analysis for the quantification of autonomous crack healing in concrete. *Construction and Building Materials*, 28(1):333–341. 30

[Werbos, 1974] Werbos, P. (1974). *Beyond Regression: New Tools for Prediction and Analysis in the Behavioral Sciences*. PhD thesis, Harvard University. 55

[Wold et al., 1987] Wold, S., Esbensen, K., and Geladi, P. (1987). Principal component analysis. *Chemometrics and intelligent laboratory systems*, 2(1-3):37–52. 44

[Wu et al., 2000] Wu, K., Chen, B., and Yao, W. (2000). Study on the ae characteristics of fracture process of mortar, concrete and steel-fiber-reinforced concrete beams. *Cement and Concrete Research*, 30(9):1495–1500. 69

[Yosinski et al., 2014] Yosinski, J., Clune, J., Bengio, Y., and Lipson, H. (2014). How transferable are features in deep neural networks? In *Advances in neural information processing systems*, pages 3320–3328. 60

[Zaitsev et al., 2014] Zaitsev, V., Gusev, V., Tournat, V., and Richard, P. (2014). Slow relaxation and aging phenomena at the nanoscale in granular materials. *Physical review letters*, 112(10):108302. 26

[Zaitsev et al., 2005] Zaitsev, V. Y., Gusev, V., Nazarov, V., and Castagnède, B. (2005). Interaction of acoustic waves with cracks: Elastic and inelastic nonlinearity mechanisms on different time scales. *Acoustical Physics*, 51(1):S67–S77. 23

[Zeiler and Fergus, 2014] Zeiler, M. D. and Fergus, R. (2014). Visualizing and understanding convolutional networks. In *European conference on computer vision*, pages 818–833. Springer. 51, 59

[Zelenyak et al., 2015] Zelenyak, A.-M., Hamstad, M. A., and Sause, M. G. (2015). Modeling of acoustic emission signal propagation in waveguides. *Sensors*, 15(5):11805–11822. 13

[Zhao and Liu, 2007] Zhao, Z. and Liu, H. (2007). Spectral feature selection for supervised and unsupervised learning. In *Proceedings of the 24th international conference on Machine learning*, pages 1151–1157. ACM. 43

[Zitto et al., 2012] Zitto, M. E., Piotrkowski, R., Gallego, A., and Sagasta, F. (2012). Ae wavelet processing in dynamical tests of a reinforced concrete slab. *Journal of Acoustic Emission*, 30. 36

Appendix A

Basic knowledge of neural network

In this part, with the help of a sample example, we introduce the neural network and the backpropagation algorithm in training neural network.

A.1 Artificial neural network

In general, neural networks are popular systems for pattern recognition, which are made from basic processing units (neurons), linked to each other with weighted and directed connections, such that the output of some units are inputs to others [Goodfellow et al., 2016, Géron, 2019]. The appellation 'artificial neural network' comes from the similarity between the units of these models and biological neurons.

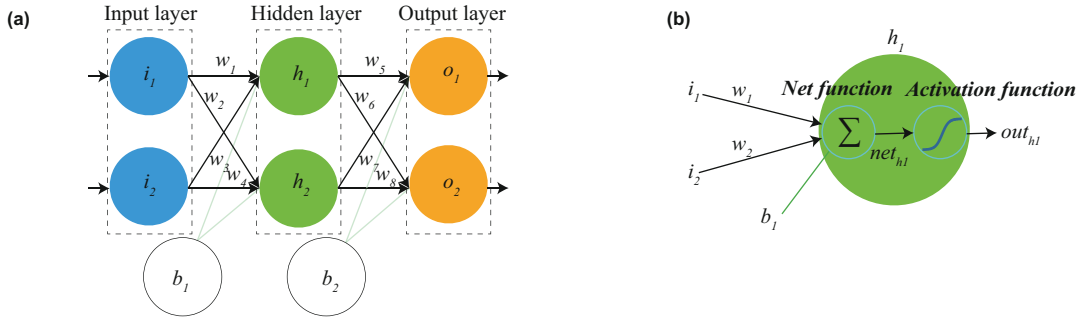

Figure A.1: (a) An example of a neural network with input layer, hidden layer and output layer. (b) The artificial neuron h_1, which computes a weighted sum of its inputs, applies an extra bias, and then an activation function.

Figure A.1(b) shows a model of an artificial neural network, which consists of three layers: input layer, hidden layer and output layer as shown in Figure A.1(a). The input features are fed to special passthrough neurons called input neurons: they output whatever input they are fed. In addition, neurons (or perceptrons) in hidden layer can be considered as the binary classifiers. As an example, Figure A.1(b) illustrates the model of an artificial neuron, the inputs and output are numbers, and each input connection is associated with a weight. The net function computes a weighted sum of its inputs and applies a bias. Then net output is fed into an activation function (such as tanh (eq: $f(x) = \tanh(x)$), sigmoid (eq: $f(x) = (1 + e^{-x})^{-1}$), etc.). In fact, a single neuron (perceptron) can be used

for simple linear binary classification. It computes a linear combination of the inputs, and if the result exceeds a threshold, it outputs the positive class. Otherwise, it outputs the negative class. For this reason, an artificial neural network can be called a multi-layer perceptrons [Rumelhart et al., 1986].

A.2 Example of training algorithm

Training a neural network consists of adjusting its parameters, the connection weights so that the model is able to perform the task at hand. We introduce the backpropagation algorithm, which consists of calculating the gradient of the error with respect to the parameters of one layer at a time, starting from the output layer and going sequentially to the input layer. In this section, the parameters in Figure A.1(a) are defined as: $i_1 = 0.05, i_2 = 0.1, w_1 = 0.15, w_2 = 0.2, w_3 = 0.25, w_4 = 0.3, w_5 = 0.4, w_6 = 0.45, w_7 = 0.5, w_8 = 0.55, b_1 = 0.35, b_2 = 0.6, target_{o1} = 0.01$ and $target_{o2} = 0.99$.

The forward propagation First, we define the total net input net_{h1} of a neuron h_1 as

$$net_{h1} = w_1 \times i_1 + w_2 \times i_2 + b_1 \times 1. \tag{A.1}$$

As shown in Figure A.1(b), we get the value of net_{h1}:

$$net_{h1} = 0.15 \times 0.05 + 0.2 \times 0.1 + 0.35 \times 1 = 0.3775. \tag{A.2}$$

To simplify the calculation, we define that all the neurons use the sigmoid function as the activation function. Then we get the output of h_1:

$$out_{h1} = \frac{1}{1 + \exp(-net_{h1})} = \frac{1}{1 + \exp(-0.3775)} = 0.593. \tag{A.3}$$

The same process is applied on h_2, we get:

$$out_{h2} = \frac{1}{1 + \exp(-net_{h2})} = 0.597. \tag{A.4}$$

We repeat this process for the output layer neurons, using the output from the hidden layer neurons as inputs. For the output o_1, we get:

$$net_{o1} = w_5 \times out_{h1} + w_6 \times out_{h1} + b_2 \times 1 = 1.1059, \tag{A.5}$$

and

$$out_{o1} = \frac{1}{1 + \exp(-out_{o1})} = 0.0751. \tag{A.6}$$

The same process applied to output neuron o_2, gives:

$$out_{o2} = \frac{1}{1 + \exp(-out_{o2})} = 0.7793. \tag{A.7}$$

For the first epoch of forward propagation, two predicted outputs (out_{o1} and out_{o2}) are computed. However, the quadratic cost function J (error) is the difference between the predicted outputs and targets which has expression as:

$$J(\mathbf{y}_n, \mathbf{t}_n) = \frac{1}{2} \sum_n \|\mathbf{y}_n - \mathbf{t}_n\|^2 . \tag{A.8}$$

where $\mathbf{y}_n$ is the component of the target vector, $\mathbf{t}_n$ is the component of the output vector. For this example, we have:

$$J_{o1} = \frac{1}{2}(target_{o1} - out_{o1})^2 = 0.2748, \tag{A.9}$$

$$J_{o2} = \frac{1}{2}(target_{o2} - out_{o2})^2 = 0.0236 \tag{A.10}$$

and

$$J_{total} = J_{o1} + J_{o2} = 0.2984, \tag{A.11}$$

The backward propagation The goal of backpropagation (BP) is to update each of the weights in the network so that the predicted output is closer to the target output, thereby minimizing the error for each output neuron and the whole output layer.

First, for weight w_5, by using gradient descent algorithm, we calculate the gradient of J_{total} with respect to w_5 which is $\frac{\partial J_{total}}{\partial w_5}$. By applying the chain rule, we get:

$$\frac{\partial J_{total}}{\partial w_5} = \frac{\partial J_{total}}{\partial out_{o1}} \times \frac{\partial out_{o1}}{\partial net_{o1}} \times \frac{\partial net_{o1}}{\partial w_5}. \tag{A.12}$$

Three partial derivative functions can be computed respectively. First, we have the equation:

$$J_{total} = \frac{1}{2}(target_{o1} - out_{o1})^2 + \frac{1}{2}(target_{o2} - out_{o2})^2, \tag{A.13}$$

then

$$\frac{\partial J_{total}}{\partial out_{o1}} = out_{o1} - target_{o1} = 0.7514 - 0.01 = 0.7414. \tag{A.14}$$

For the second partial derivative function $\frac{\partial out_{o1}}{\partial net_{o1}}$, we know that:

$$out_{o1} = \frac{1}{1 + \exp(-net_{o1})}, \tag{A.15}$$

then

$$\frac{\partial out_{o1}}{\partial net_{o1}} = out_{o1}(1 - out_{o1}) = 0.7514 \times (1 - 0.7514) = 0.1868. \tag{A.16}$$

For the third partial derivative function $\frac{\partial net_{o1}}{\partial w_5}$, by using Equation A.5, we get:

$$\frac{\partial net_{o1}}{\partial w_5} = out_{h1} = 0.5933. \tag{A.17}$$

In summary, Equation A.12 can be solve as:

$$\frac{\partial J_{total}}{\partial w_5} = 0.7414 \times 0.1868 \times 0.5933 = 0.0821. \tag{A.18}$$

To decrease error, we use the learning rate η (here, we set $\eta = 0.5$) to update w_5 to w_5^+ as:

$$w_5^+ = w_5 - \eta \times \frac{\partial J_{total}}{\partial w_5} = 0.4 - 0.5 \times 0.0821 = 0.3589. \tag{A.19}$$

This process is applied on w_6, w_7 and w_8 respectively, then we can get: $w_6^+ = 0.4086$, $w_7^+ = 0.5113$ and $w_8^+ = 0.5613$.

In backpropagation algorithm, we use the original weights, not the updated weights to update each hidden layer. For hidden layer in Figure A.1(a), we take w_1 as an example, then we get:

$$\frac{\partial J_{total}}{\partial w_1} = \frac{\partial J_{total}}{\partial out_{h1}} \times \frac{\partial out_{h1}}{\partial net_{h1}} \times \frac{\partial net_{h1}}{\partial w_1}. \tag{A.20}$$

In this equation, for term $\frac{\partial J_{total}}{\partial out_{h1}}$ we get:

$$\frac{\partial J_{total}}{\partial out_{h1}} = \frac{\partial J_{o1}}{\partial out_{h1}} + \frac{\partial J_{o2}}{\partial out_{h1}}. \tag{A.21}$$

Then we have:

$$\frac{\partial J_{o1}}{\partial out_{h1}} = \frac{\partial J_{o1}}{\partial net_{o1}} \times \frac{\partial net_{o1}}{\partial out_{h1}}. \tag{A.22}$$

For $\frac{\partial J_{o1}}{\partial net_{o1}}$, with Equation A.14 and Equation A.16, we get:

$$\frac{\partial J_{o1}}{\partial net_{o1}} = \frac{\partial J_{o1}}{\partial out_{o1}} \times \frac{\partial out_{o1}}{\partial net_{o1}} = 0.7414 \times 0.1868 = 0.1384. \tag{A.23}$$

For $\frac{\partial net_{o1}}{\partial out_{h1}}$, based on expression:

$$net_{o1} = w_5 \times out_{h1} + w_6 \times out_{h2} + b_2 \times 1, \tag{A.24}$$

we get

$$\frac{\partial net_{o1}}{\partial out_{h1}} = w_5 = 0.40. \tag{A.25}$$

Now, Equation A.22 can be solved as:

$$\frac{\partial J_{o1}}{\partial out_{h1}} = \frac{\partial J_{o1}}{\partial net_{o1}} \times \frac{\partial net_{o1}}{\partial out_{h1}} = 0.1384 \times 0.40 = 0.0553. \tag{A.26}$$

Following the same process for $\frac{\partial J_{o2}}{\partial out_{h1}}$, we get

$$\frac{\partial J_{o2}}{\partial out_{h1}} = -0.0190. \tag{A.27}$$

Therefore, Equation A.21 can be computed as:

$$\frac{\partial J_{total}}{\partial out_{h1}} = \frac{\partial J_{o1}}{\partial out_{h1}} + \frac{\partial J_{o2}}{\partial out_{h1}} = 0.0553 + (-0.0190) = 0.0363. \tag{A.28}$$

For term $\frac{\partial out_{h1}}{\partial net_{h1}}$ in Equation A.20, we use the expression as:

$$out_{h1} = \frac{1}{1 + \exp(-net_{h1})}, \tag{A.29}$$

and get

$$\frac{\partial out_{h1}}{\partial net_{h1}} = out_{h1}(1 - out_{h1}) = 0.5932(1 - 0.5933) = 0.2413. \tag{A.30}$$

For term $\frac{\partial net_{h1}}{\partial w_1}$ in Equation A.20, we use Equation A.1 and get:

$$\frac{\partial net_{h1}}{\partial w_1} = i_1 = 0.05. \tag{A.31}$$

Then Equation A.20 can be computed as:

$$\frac{\partial J_{total}}{\partial w_1} = \frac{\partial J_{total}}{\partial out_{h1}} \times \frac{\partial out_{h1}}{\partial net_{h1}} \times \frac{\partial net_{h1}}{\partial w_1} = 0.000438568. \tag{A.32}$$

Now, w_1 can be updated by η as:

$$w_1^+ = w_1 - \eta \times \frac{\partial J_{total}}{\partial w_1} = 0.15 - 0.5 \times 0.000438568 = 0.1497. \tag{A.33}$$

Repeating this for w_2, w_3, and w_4, we get $w_2^+ = 0.1995$, $w_3^+ = 0.2497$ and $w_4^+ = 0.2995$.

With these updated weights, when we fed forward the input originally $i_1 = 0.05$ and $i_2 = 0.1$, the error J is 0.2901. However, with more times of update, for example, update number $k = 100$, we get $out_{o1} = 0.1782$ and $out_{o2} = 0.8768$. Normally we define a minimum value of J_{total} to minimize the cost function (error).

Appendix B

Publications et Communications

B.1 Articles

1. X. Yu, M. Bentahar, C. Mechri, S. Montrésor, **Passive monitoring of nonlinear relaxation of cracked polymer concrete samples using acoustic emission**, *The Journal of the Acoustical Society of America (2019)*, 146(4), EL323–EL328. doi:10.1121/1.5127519

2. M. Bentahar, A. Di Bella, C. Mechri, S. Montrésor, M. Scalerandi, X.Yu, **Exploiting Slow Dynamics Effects for Damage Detection in Concrete**, *Frontiers in Built Environment (2020)*, 6. doi:10.3389/fbuil.2020.00064

B.2 Conferences

1. Acoustics '17 Boston (173rd meeting of the Acoustical Society of America), 25 - 29 June 2017 Boston, Massachusetts, USA

2. CFA (The 14th French Acoustics Congress), 23 - 27 Avril 2018, Le Havre, France

3. COFREND (3nd Doctoriale French confederation for Non Destructive Testing), 28 - 29 Mai 2018, Marne la Vallée, France

4. EWGAE (33rd European Conference on Acoustic Emission Testing), 12 - 14 September 2018, Senlis, France

5. FCAC (2nd Franco-Chinese Acoustics Conference), 29 - 31 October 2018, Le Mans, France

6. Journée Scientifique de ECND Pays de la Loire, 13 Novembre 2018, Angers, France

UNIVERSITE BRETAGNE SCIENCES LOIRE POUR L'INGENIEUR

Le Mans Université

Titre : Émission acoustique dynamique pour la caractérisation du comportement non linéaire des matériaux complexes

Mots clés : matériaux complexes (béton), quasi-statiques tests et micro-mécanismes, émission acoustique et traitement du signal, conditionnement et relaxation non-linéaire, reconnaissance des formes non-supervisée, réseau de neurones

Résumé : L'émission acoustique (EA) est reconnue pour être une technique efficace de surveillance de la santé des structures permettant de détecter la création et la propagation de microfissures dans les matériaux structuraux tels que le béton ou les composites lorsqu'ils sont soumis à des contraintes quasi-statiques. Sur la base de méthodes de traitement de signaux adéquates, différentes études ont établi des liens entre les salves d'EA et les micro-dommages créés. D'autres travaux ont montré qu'il est possible de corréler le temps de relaxation des composites et l'énergie des mécanismes d'endommagement mesurée durant la charge quasi-statique en utilisant les salves d'EA enregistrées. Cette thèse propose d'utiliser un protocole expérimental original pour détecter la relaxation non-linéaire d'échantillons de bétons à l'état intact et endommagés. Ce protocole est basé sur l'utilisation de l'EA pour capter passivement la relaxation non-linéaire d'échantillons de bétons au lieu du signal de faible amplitude habituellement utilisé dans les expériences de dynamique lente. Les résultats montrent que les méthodes de détection passives et actives conduisent à des temps de relaxation équivalents. De plus, le capteur d'EA révèle l'existence d'une 'période de silence' pendant les premières minutes de la relaxation non-linéaire après laquelle les salves d'EA commencent à être détectées. De plus, les caractéristiques des salves d'EA enregistrées pendant la relaxation passive ont montré une nette ressemblance avec celles obtenues lors de l'endommagement des mêmes échantillons, où des mécanismes de cisaillement et de compression sont impliqués. Enfin, nous notons qu'en plus de l'utilisation d'une approche de reconnaissance des formes non-supervisée pour la classification des salves d'EA, ce travail propose une nouvelle approche de classification des signaux d'EA basé sur l'image de la représentation en ondelettes continue (CWT) et le réseau de neurones convolutifs (CNN). Les résultats liés aux données d'EA dynamiques non-linéaires et quasi-statiques montrent que les deux approches de traitement du signal ont une grande précision de classification, ce qui représente un intérêt certain pour le développement de méthodes d'EA dynamiques en présence de microfissures.

Title: Dynamic acoustic emission for the characterization of the nonlinear behavior of complex materials

Keywords: complex materials (concrete), quasi-static tests and micro-mechanisms, acoustic emission and signal processing, conditioning and nonlinear relaxation, unsupervised pattern recognition, neural network

Abstract: Acoustic emission (AE) is well known to be an efficient structural health monitoring technique to detect the creation and propagation of micro-cracks within structural materials such as concrete or composites when submitted to quasi-static stresses. Based on adequate signal processing methods, different research studies have established links between the detected AE hits and the created micro-damages. Other works have shown that it is possible to correlate the relaxation time in composites and the energy of the damage mechanisms measured during the quasi-static loading using the recorded AE hits. This thesis proposes to use an original experimental protocol to probe the nonlinear relaxation of concrete samples at the intact and damaged states. This protocol is based on the use of AE to passively probe the nonlinear relaxation of concrete samples instead of the weak amplitude signal usually used in slow dynamics experiments. Results show that passive and active probing methods lead to equivalent relaxation times. Furthermore, AE probing reveals the existence of a 'silence period' during the first minutes of the nonlinear relaxation after which AE hits start to be detected. In addition, the characteristics of AE hits recorded during the passive relaxation showed a clear resemblance to those obtained during the damaging of the same samples, where shear and compression mechanisms are involved. For the clustering of the AE hits, in addition to use of an unsupervised pattern recognition approach to cluster the detected AE hits, this work proposes a novel 'image-based AE classification' approach based on continuous wavelet transform (CWT) and convolutional neural network (CNN). Results related to the nonlinear dynamic and quasi-static AE data show that both signal processing approaches have high classification accuracy, which represents a great interest in the development of dynamic AE methods in the presence of micro-cracks.